COMPOSITE OF GRAPHENE OXIDE IMPREGNATED PALM KERNEL SHELL BASED ACTIVATED CARBON FOR DYE WASTEWATER TREATMENT

TAN YAN YING

FACULTY OF ENGINEERING UNIVERSITI MALAYA KUALA LUMPUR

COMPOSITE OF GRAPHENE OXIDE IMPREGNATED PALM KERNEL SHELL BASED ACTIVATED CARBON FOR DYE WASTEWATER TREATMENT

TAN YAN YING

THESIS SUBMITTED IN FULFILMENT OF THE REQUIREMENTS FOR THE DEGREE OF DOCTOR OF PHILOSOPHY

FACULTY OF ENGINEERING UNIVERSITI MALAYA KUALA LUMPUR

UNIVERSITI MALAYA ORIGINAL LITERARY WORK DECLARATION

| Name of Candidate: Tan Yan Ying | | |
|--|--|--|
| Matric No: 17184441/3 | | |
| Name of Degree: Doctor of Philosophy | | |
| Title of Project Paper/Research Report/Dissertation/Thesis ("this Work"): Composite | | |
| of Graphene Oxide Impregnated Palm Kernel Shell Based Activated Carbon for | | |
| Dye Wastewater Treatment | | |
| | | |
| Field of Study: Advanced Materials & Technology (NEC 524: Chemical and Process) | | |
| | | |
| I do solemnly and sincerely declare that: | | |
| (1) I am the sole author/writer of this Work; | | |
| (2) This Work is original;(3) Any use of any work in which copyright exists was done by way of fair dealing | | |
| and for permitted purposes and any excerpt or extract from, or reference to or | | |
| reproduction of any copyright work has been disclosed expressly and sufficiently and the title of the Work and its authorship have been | | |
| acknowledged in this Work; | | |
| (4) I do not have any actual knowledge nor do I ought reasonably to know that the making of this work constitutes an infringement of any copyright work; | | |
| (5) I hereby assign all and every rights in the copyright to this Work to the | | |
| Universiti Malaya ("UM"), who henceforth shall be owner of the copyright in this Work and that any reproduction or use in any form or by any means | | |
| whatsoever is prohibited without the written consent of UM having been first | | |
| had and obtained; (6) I am fully aware that if in the course of making this Work I have infringed any | | |
| copyright whether intentionally or otherwise, I may be subject to legal action | | |
| or any other action as may be determined by UM. | | |
| Candidate's Signature Date: 10/4/2025 | | |
| Subscribed and solemnly declared before, | | |
| Subscribed and soleminy declared before, | | |
| Witness's Signature Date: 10/4/2025 | | |
| In the second of the secon | | |
| Name: | | |

Designation:

COMPOSITE OF GRAPHENE OXIDE IMPREGNATED PALM KERNEL SHELL BASED ACTIVATED CARBON FOR DYE WASTEWATER

TREATMENT

ABSTRACT

Dye wastewater generated from various industrial processes can lead to substantial pollution and environmental damage due to its persistent and recalcitrant nature. Among the various wastewater treatment technologies, adsorption using green and low-cost biomass-based materials stands out as a promising approach for treating dye wastewater. However, raw biomass-based adsorbents such as palm kernel shell (PKS), rubber seed shell, and coconut shell often have limitations in selectivity, recovery, and adsorption capacity, which restrict their use in treating different types of wastewater. This study aims to enhance the adsorption performance of raw PKS activated carbon (PKSAC) through the impregnation with graphene oxide (GO) and iron oxide. Physicochemical analyses revealed that after impregnation with GO and iron oxide, the ternary composite exhibited a significant increase in oxygen content (from 6.01% to 49.73%), a larger pore width (from 3.00 nm to 9.99 nm), and increased oxygenated functional groups compared to raw PKSAC. The adsorption performance of PKSAC-based adsorbents was evaluated for treating synthetic wastewater containing an anionic dye. The adsorption study demonstrated that the ternary composite performed better, achieving 99.8% color removal efficiency and an adsorption capacity of 27.3 mg/g, compared to other PKSAC-based adsorbents (60.7%-73.1%; 16.6 mg/g-19.9 mg/g) under optimum conditions. The ternary composite showed superior performance in chemical oxygen demand and color removal efficiencies, surpassing commercial activated carbons (CACs) by 28.4% and 31.9%, respectively. The reusability of the composite was confirmed over five cycles, maintaining 74.1% performance, significantly higher than CACs (30.0%). Furthermore,

the iron leaching (<0.3 mg/L) was negligible for drinking water, confirming the stability

and safety of the composite. To further improve adsorption performance, the synthesis

process of the ternary composite was optimized. This optimized ternary composite

demonstrated an adsorption capacity of 76.4 mg/g for actual industrial printing

wastewater, which was 34.5% higher than the composite before optimization (56.8 mg/g).

Experimental results indicated that adsorption using the ternary composite is

predominantly a monolayer chemisorption process. A quantum chemical analysis

revealed adsorption energies below -50 kJ/mol for all functional groups. Feature

importance analysis using machine learning revealed that the chemical properties of the

adsorbents had a more significant impact on adsorption performance than physical

properties. This study also evaluated the possibility of using the spent adsorbent in brick

formation, in addition to conducting leaching and phytotoxicity studies. In summary, the

research proved that the ternary composite developed from PKSAC is an efficient

adsorbent for treating dye wastewater, offering enhanced performance, stability, and

practicality for industrial applications.

Keywords: Adsorption; Biomass; Industrial Wastewater; Machine Learning; Quantum

Chemical Analysis

iv

KOMPOSIT GRAFIN OKSIDA DAN KARBON TERAKTIF BERASASKAN TEMPURUNG KELAPA SAWIT BAGI RAWATAN AIR SISA PEWARNA ABSTRAK

Air sisa pewarna yang dihasilkan daripada pelbagai proses industri boleh menyebabkan pencemaran dan kemusnahan alam sekitar yang ketara disebabkan oleh sifat air sisa pewarna yang persisten (memerlukan masa yang panjang untuk pelupusan) dan tahan degradasi. Antara pelbagai teknologi rawatan air sisa, penjerapan menggunakan bahanbahan biomas yang mesra alam dan berkos rendah merupakan pendekatan yang berkesan untuk merawat air sisa pewarna. Walau bagaimanapun, penjerap biomas mentah seperti tempurung kelapa sawit (PKS), tempurung biji getah dan tempurung kelapa sering menghadapi batasan dari segi kapasiti penjerapan, pemulihan dan selektiviti yang boleh menyekat keberkesanan penggunaan penjerap-penjerap biomas mentah dalam merawat pelbagai jenis air sisa pewarna. Oleh itu, kajian ini bertujuan untuk meningkatkan prestasi penjerapan karbon teraktif berasaskan tempurung kelapa sawit mentah (PKSAC) melalui pengimpregnan grafin oksida (GO) dan besi oksida. Analisis fisiko-kimia menunjukkan bahawa selepas pengimpregnan GO dan besi oksida, komposit ternari menunjukkan peningkatan ketara dalam kandungan oksigen (daripada 6.01% menjadi 49.73%), liang pori yang lebih besar (daripada 3.00 nm menjadi 9.99 nm) dan kumpulan berfungsi yang beroksigen berbanding dengan PKSAC mentah. Prestasi penjerapan berasaskan PKSAC dinilai untuk merawat air sisa sintetik yang mengandungi pewarna anionik. Kajian penjerapan menunjukkan bahawa komposit ternari mempunyai prestasi yang unggul, mencapai tahap penyingkiran warna yang lebih tinggi iaitu sebanyak 99.8% dan kapasiti penjerapan sebanyak 27.3 mg/g berbanding dengan penjerap-penjerap lain yang berasaskan PKSAC (60.7%-73.1%; 16.6 mg/g-19.9 mg/g) di bawah keadaan optimum. Komposit ternari menunjukkan prestasi yang lebih tinggi dalam tahap penyingkiran permintaan oksigen kimia (COD) dan tahap penyingkiran warna, melebihi karbon teraktif

komersial (CACs) sebanyak 28.4% dan 31.9%, masing-masing. Kebolehgunaan semula komposit ini disahkan melalui lima kitaran, iaitu mengekalkan prestasi sebanyak 74.1%, jauh lebih tinggi daripada CACs (30.0%). Selain itu, larut lesap besi adalah tidak berbahaya untuk air minuman, iaitu kurang daripada 0.3 mg/L, mengesahkan kestabilan dan keselamatan komposit ini. Bagi meningkatkan lagi prestasi penjerapan, proses sintesis komposit ternari telah dioptimumkan. Komposit ternari yang dioptimumkan ini menunjukkan kapasiti penjerapan sebanyak 76.4 mg/g untuk air sisa percetakan industri sebenar, iaitu 34.5% lebih tinggi daripada komposit sebelum dioptimumkan (56.8 mg/g). Keputusan eksperimen menunjukkan bahawa penjerapan menggunakan komposit ternari ini didominasi oleh proses kimisorpsi monolayer. Kajian kimia kuantum menunjukkan tenaga penjerapan adalah kurang daripada -50 kJ/mol untuk semua kumpulan berfungsi. Analisis kepentingan ciri melalui pendekatan pembelajaran mesin menunjukkan bahawa sifat kimia penjerap mempunyai impak yang lebih besar terhadap prestasi penjerapan berbanding dengan sifat fizikal. Kajian ini juga menilai kemungkinan penggunaan penjerap terpakai dalam pembentukan bata, selain mengkaji larut lesap besi dan fitotoksisiti. Kesimpulannya, penyelidikan ini membuktikan bahawa komposit ternari yang disintesiskan daripada PKSAC adalah penjerap yang berkesan untuk rawatan air sisa pewarna disebabkan oleh prestasinya yang lebih tinggi, stabil dan kebolehgunaan praktikal untuk diaplikasikan dalam sektor industri.

Kata Kunci: Penjerapan; Biomas; Air Sisa Industri; Pembelajaran Mesin; Analisis Kimia Kuantum

ACKNOWLEDGEMENTS

First and foremost, I extend my deepest gratitude to my supervisors, Prof. Ir. Dr. Abdul Aziz Abdul Raman, ChM. Dr. Archina Buthiyappan, and Dr. Mohd Izzudin Izzat Zainal Abidin, for their invaluable guidance, expertise, and support throughout this journey.

I am sincerely thankful to the Department of Chemical Engineering, Faculty of Engineering, Universiti Malaya, for providing a stimulating research environment and state-of-the-art facilities. I also wish to express my gratitude to every staff member of the Chemical Engineering Department for their assistance and support.

I am deeply appreciative of my colleagues and fellow graduate students who have shared their knowledge and offered mental support during this time.

I am profoundly grateful to my family for their unwavering support, understanding, and love. My heartfelt thanks go to my father, Mr. Tan Chuan Chin; my mother, Mdm. Leow Chon Koi; my sister, Yan Jing; my brother, Xuan Zhe; and Chun Tee. Their belief in me has been my greatest motivation, and their encouragement has been my source of strength. Words cannot fully express the depth of my appreciation.

This thesis would not have been possible without the collective support and encouragement of all these individuals and organizations.

TABLE OF CONTENTS

| Abs | tractiii |
|------|---|
| Abs | trakv |
| Ack | nowledgementsvii |
| Tabl | e of Contentsviii |
| List | of Figuresxiv |
| List | of Tablesxvii |
| List | of Symbols and Abbreviationsxix |
| | |
| CH | APTER 1: INTRODUCTION1 |
| 1.1 | Background Study |
| 1.2 | Problem Statement |
| 1.3 | Research Questions |
| 1.4 | Aim and Objectives of the Study5 |
| 1.5 | Scope of the Study6 |
| 1.6 | Novelty of the Study7 |
| 1.7 | Thesis Outline |
| | |
| CHA | APTER 2: LITERATURE REVIEW10 |
| 2.1 | Introduction |
| 2.2 | Characteristics of Dye Wastewater |
| 2.3 | Treatment Technology for Dye Wastewater |
| 2.4 | Biomass-Based Adsorbents |
| 2.5 | Modifications of Biomass-Based Adsorbents |
| | 2.5.1 Graphene Oxide Impregnated Biomass-Based Adsorbents |
| | 2.5.2 Iron Oxide Impregnated Biomass-Based Adsorbents |

| 2.6 | Effects | of Operational Parameters on Adsorption Process | 35 |
|------|----------|---|------|
| | 2.6.1 | Effect of Initial pH of the Solution | 35 |
| | 2.6.2 | Effect of Adsorbent Dosage | 37 |
| | 2.6.3 | Effect of Contact Time | 38 |
| | 2.6.4 | Effect of Initial Concentration of the Adsorbate | 40 |
| 2.7 | Applica | ation of Biomass-Based Adsorbent in Actual Wastewater Treatment | 41 |
| 2.8 | Adsorp | tion Mechanism using Biomass-Based Adsorbents | 51 |
| 2.9 | Stabilit | y and Reusability of the Biomass-Based Adsorbent | 54 |
| 2.10 | Applica | ation of Quantum Chemical Analysis in Adsorption Processes | 56 |
| 2.11 | Applica | ation of Machine Learning in Adsorption Processes | 59 |
| 2.12 | Summa | ary | 62 |
| | | | |
| CHA | PTER | 3: MATERIALS AND METHODOLOGY | 64 |
| 3.1 | Introdu | ection | 64 |
| 3.2 | Chemic | cals and Materials | 64 |
| 3.3 | Synthe | sis of Ternary Composite | 71 |
| | 3.3.1 | Synthesis of Graphene Oxide | 71 |
| | 3.3.2 | Synthesis of Graphene Oxide and Iron Oxide Impregnated PKSAC | 71 |
| 3.4 | Physico | ochemical Characterization of Adsorbents | 72 |
| | 3.4.1 | Brunauer-Emmett-Teller | 72 |
| | 3.4.2 | Field Emission Scanning Electron Microscopy with Energy Dispersiv | e X- |
| | | Ray | 72 |
| | 3.4.3 | Fourier Transformation Infrared | 73 |
| | 3.4.4 | Vibrating-Sample Magnetometer | 73 |
| | 3.4.5 | X-Ray Powder Diffraction | 73 |
| | 3.4.6 | Point of Zero Charge | 74 |

| | 3.4.7 Particle Size Distribution | 74 |
|------|---|------|
| 3.5 | Adsorption Performance Evaluation using PKSAC-Based Adsorbents | for |
| | Wastewater Treatment | 74 |
| 3.6 | Adsorption Study | 76 |
| 3.7 | Kinetics Study | 76 |
| 3.8 | Isotherms Study | 77 |
| 3.9 | Thermodynamics Study | 77 |
| 3.10 | Reusability Study | 77 |
| 3.11 | Leaching Study | 78 |
| 3.12 | Model Validation using Different Types of Industrial Dyes | 78 |
| 3.13 | Application in the Continuous Adsorption Process | 78 |
| 3.14 | Quantum Chemical Study | 79 |
| 3.15 | Machine Learning | 80 |
| | 3.15.1 Selection of Input Features | 80 |
| | 3.15.2 Model Training and Evaluation | 81 |
| | 3.15.3 Feature Importance Analysis | 81 |
| 3.16 | Optimization of Ternary Composite Synthesis Process | 82 |
| 3.17 | Phytotoxicity Study | 83 |
| 3.18 | Possible End-Use of Spent Adsorbents | 83 |
| 3.19 | Economic Evaluation | 85 |
| 3.20 | Safety Aspects | 85 |
| | | |
| CHA | APTER 4: RESULTS AND DISCUSSION | 95 |
| 4.1 | Introduction | 95 |
| 4.2 | Adsorption Performance Evaluation of PKSAC-Based Adsorbents using Synth | etic |
| | Wastewater | 95 |

| | 4.2.1 | Statistical Analysis | 96 |
|-----|--------|--|-------|
| | 4.2.2 | Correlation and Model Validation | 99 |
| | 4.2.3 | Model Fitting | 99 |
| | 4.2.4 | Comparison of Adsorption Performance of PKSAC-Based Adsorbents | s102 |
| 4.3 | Physic | ochemical Characteristics of PKSAC-Based Adsorbents | . 104 |
| | 4.3.1 | Textural Properties | . 104 |
| | 4.3.2 | Morphologies and Elemental Compositions | . 109 |
| | 4.3.3 | Magnetic Properties | .114 |
| | 4.3.4 | Particle Size Distribution. | .116 |
| | 4.3.5 | Crystalline Structure | .118 |
| | 4.3.6 | Point of Zero Charge | .121 |
| | 4.3.7 | Relating Physicochemical Characteristics with Adsorption Performance | ce of |
| | | PKSAC-Based Adsorbents | . 123 |
| 4.4 | Effect | of Operational Parameters on Synthetic Wastewater Adsorption u | sing |
| | Ternar | y Composite | . 125 |
| | 4.4.1 | Effect of Initial pH of the Solution | . 126 |
| | 4.4.2 | Effect of Adsorbent Dosage | . 130 |
| | 4.4.3 | Effect of Contact Time | . 131 |
| | 4.4.4 | Optimization Study | . 132 |
| 4.5 | Model | Validation of Ternary Composite | . 133 |
| | 4.5.1 | Adsorption Performance Validation using Various Dye Concentration | 133 |
| | 4.5.2 | Adsorption Performance Validation using Various Industrial Dyes | . 134 |
| | 4.5.3 | Adsorption Performance Validation using Continuous Process | . 137 |
| | 4.5.4 | Adsorption Performance Comparison with CACs | . 139 |
| 4.6 | Reusal | pility Study | . 140 |
| 47 | A dear | otion Mechanism in Treating Synthetic Wastewater | 142 |

| | 4.7.1 | Kinetics Study |
|-----|---------|--|
| | 4.7.2 | Isotherms Study |
| | 4.7.3 | Thermodynamics study |
| 4.8 | Insight | s into the Adsorption Mechanism via Computational Approaches 154 |
| | 4.8.1 | Adsorption Mechanism Evaluation via Quantum Chemical Analysis153 |
| | | 4.8.1.1 Surface Functional Groups |
| | | 4.8.1.2 Molecular Structures and Quantum Descriptors |
| | | 4.8.1.3 Effects of Functional Groups on the Adsorption Process 164 |
| | | 4.8.1.4 Comparison of Adsorption Energy |
| | 4.8.2 | Adsorption Mechanism Evaluation via Machine Learning172 |
| 4.9 | Optimi | zation of Ternary Composite Synthesis Process for the Actual Industria |
| | Wastev | water Treatment 175 |
| | 4.9.1 | Effects of Operational Parameters in Optimizing Ternary Composite |
| | | Synthesis Process |
| | | 4.9.1.1 Ratio of PKSAC/GO |
| | | 4.9.1.2 Loading Amount of Iron Oxide |
| | | 4.9.1.3 Optimization Study |
| | 4.9.2 | Effects of Adsorption Operational Parameters using Optimized Ternary |
| | | Composite |
| | | 4.9.2.1 Effect of Initial pH of the Solution |
| | | 4.9.2.2 Effect of Adsorbent Dosage |
| | | 4.9.2.3 Effect of Contact Time |
| | | 4.9.2.4 Optimization Study |
| | 4.9.3 | Mechanism Study of Optimized Ternary Composite |
| | | 4.9.3.1 Kinetics Study |
| | | 4.9.3.2 Isotherms Study |

| | | 4.9.3.3 Thermodynamics Study | .96 |
|------|-----------|---|-----|
| | 4.9.4 | Reusability Study1 | 98 |
| | 4.9.5 | Model Validation using Various Types of Actual Wastewater | 99 |
| 4.10 | Compa | rison of Physicochemical Characteristics and Adsorption Performance | of |
| | Ternary | Composite Before and After Synthesis Process Optimization2 | 201 |
| 4.11 | Econon | nic Evaluation2 | 205 |
| 4.12 | Enviro | nmental Evaluation2 | 209 |
| | 4.12.1 | Carbon Dioxide Emissions Reduction | 209 |
| | 4.12.2 | Phytotoxicity Study | 210 |
| | 4.12.3 | Leaching and Stability Study2 | 212 |
| | 4.12.4 | Possible Brick Formation using Spent Adsorbent | 212 |
| | | | |
| CHA | PTER : | 5: CONCLUSION AND RECOMMENDATIONS2 | 217 |
| 5.1 | Conclu | sion2 | 217 |
| 5.2 | Recom | mendations for Future Work2 | 218 |
| 5.3 | Contrib | outions of the Study2 | 220 |
| 5.4 | Potentia | al Applications2 | 222 |
| Refe | rences | 2 | 223 |
| List | of Public | eations and Papers Presented2 | 252 |

LIST OF FIGURES

| Figure 2.1: Literature Review Flowchart |
|---|
| Figure 2.2: Chemical Structure of Graphene Oxide |
| Figure 2.3: Post-Treatment Separation of Magnetized Adsorbents |
| Figure 2.4: Adsorption Process in Actual Wastewater Treatment Plant46 |
| Figure 2.5: Performance Comparison in Treating Synthetic and Actual Wastewater 46 |
| Figure 2.6: Adsorption Mechanisms of MB Dye onto Biomass-Based Adsorbent53 |
| Figure 3.1: Overall Methodology65 |
| Figure 3.2: PKSAC-GO-Fe Composite Synthesis Process |
| Figure 3.3: Continuous Adsorption Process using Fixed Bed |
| Figure 4.1: Predicted versus Actual Regression Plot of (a) Color Removal Efficiency and (b) Adsorption Capacity using PKSAC-GO-Fe |
| Figure 4.2: Perturbation Plots of (a) Color Removal Efficiency and (b) Adsorption Capacity using PKSAC-GO-Fe |
| Figure 4.3: Adsorption Performance Comparison of PKSAC-Based Adsorbents103 |
| Figure 4.4: Nitrogen Adsorption-Desorption of (a) PKSAC, (b) PKSAC-GO, (c) PKSAC-Fe, and (d) PKSAC-GO-Fe |
| Figure 4.5: Pore Size Distribution of PKSAC-Based Adsorbents |
| Figure 4.6: FESEM Images of (a) PKSAC, (b) PKSAC-GO, (c) PKSAC-Fe, and (d) PKSAC-GO-Fe |
| Figure 4.7: EDX Spectra of PKSAC-Based Adsorbents |
| Figure 4.8: VSM Curve of PKSAC-Based Adsorbents |
| Figure 4.9: Particle Size Distribution of PKSAC-Based Adsorbents |
| Figure 4.10: XRD Pattern of PKSAC-Based Adsorbents |
| Figure 4.11: pH _{pzc} Plot of PKSAC-Based Adsorbents |

| Figure 4.12: Interactive Effects of (a) pH and Adsorbent Dosage, (b) Adsorbent Dosage and Contact Time, and (c) Contact Time and pH on Color Removal Efficiency in Treating Anionic Dye using PKSAC-GO-Fe |
|---|
| Figure 4.13: Interactive Effects of (a) pH and Adsorbent Dosage, (b) Adsorbent Dosage and Contact Time, and (c) Contact Time and pH on Adsorption Capacity in Treating Anionic Dye using PKSAC-GO-Fe |
| Figure 4.14: Adsorption Performance Validation using Various Dye Concentration 134 |
| Figure 4.15 Adsorption Performance Validation using Various Types of Dye136 |
| Figure 4.16: Comparison between Batch and Continuous Adsorption |
| Figure 4.17: Adsorption Performance Comparison with CACs |
| Figure 4.18: Reusability of PKSAC-GO-Fe |
| Figure 4.19: Linear Kinetic Plots for (a) P-F-O, (b) P-S-O, and (c) I-P-D, and (d) Non-Linear Kinetic Plot in Treating Anionic Dye |
| Figure 4.20: Linear Isotherm Plots for (a) Langmuir, (b) Freundlich, and (c) Temkin Models, and (d) Non-Linear Isotherm Plot in Treating Anionic Dye149 |
| Figure 4.21: Van't Hoff Plot of Anionic Dye Adsorption using PKSAC-GO-Fe153 |
| Figure 4.22: FTIR Spectra of PKSAC-Based Adsorbents |
| Figure 4.23: (a) Optimized Structure, (b) HOMO and LUMO, and (c) ESP Map of AB113 Dye |
| Figure 4.24: Optimized Structures of (a) PKSAC, (b) PKSAC-GO, (c) PKSAC-Fe, and (d) PKSAC-GO-Fe |
| Figure 4.25: Optimized Structures of (a) CH (Pristine), (b) OH, (c) COH, (d) COOH, (e) COC, and (f) Fe ₃ O ₄ Functionalized Adsorbents |
| Figure 4.26: Optimized Structures of Various Adsorption Systems |
| Figure 4.27: Adsorption Energy Diagram of AB113 onto Pristine and Functionalized Adsorbents |
| Figure 4.28: Feature Importances Analysis |
| Figure 4.29: Wastewater from Printing Process |

| Figure 4.30: Interactive Effects of PKSAC/GO and Iron Oxide on the (a) Color Removal Efficiency and (b) Adsorption Capacity in Treating Actual Printing Wastewater 179 |
|--|
| Figure 4.31: pH _{pzc} of Optimized PKSAC-GO-Fe Composite |
| Figure 4.32: Interactive Effects of (a) pH and Adsorbent Dosage, (b) Adsorbent Dosage and Contact Time, and (c) Contact Time and pH on Color Removal Efficiency in Treating Actual Printing Wastewater using Optimized PKSAC-GO-Fe |
| Figure 4.33: Interactive Effects of (a) pH and Adsorbent Dosage, (b) Adsorbent Dosage and Contact Time, and (c) Contact Time and pH on Adsorption Capacity in Treating Actual Printing Wastewater using Optimized PKSAC-GO-Fe |
| Figure 4.34: Linear Kinetic Plots for (a) P-F-O, (b) P-S-O, and (c) I-P-D, and (d) Non-Linear Kinetic Plot in Treating Actual Printing Wastewater |
| Figure 4.35: Linear Isotherm Plots for (a) Langmuir, (b) Freundlich, and (c) Temkin Models, and (d) Non-Linear Isotherm Plot in Treating Actual Printing Wastewater194 |
| Figure 4.36: Van't Hoff Plot of Printing Wastewater Adsorption using Optimized PKSAC-GO-Fe |
| Figure 4.37: Reusability of Optimized PKSAC-GO-Fe |
| Figure 4.38: Adsorption Performance Validation using Various Types of Actual Wastewater |
| Figure 4.39: FESEM Images of PKSAC-GO-Fe (a) Before and (b) After Synthesis Process Optimization |
| Figure 4.40: Cost Required for COD Removal Per Day |
| Figure 4.41: Phytotoxicity Assessment of PKSAC-GO-Fe |
| Figure 4.42: Plots of (a) LOI and Water Absorption and (b) Compressive Strength of Bricks as a Function of Spent Adsorbent Composition |

LIST OF TABLES

| Table 2.1: Characteristics of Various Sources of Dye Wastewater |
|--|
| Table 2.2: Advantages and Limitations of Dye Wastewater Treatment Technologies16 |
| Table 2.3: Applications of Biomass-Based Adsorbents in Wastewater Treatment20 |
| Table 2.4: Synthesis Method and Adsorption Performance of Iron Oxide Impregnated Biomass Adsorbent |
| Table 2.5: Actual Wastewater Treatment using Biomass-Based Adsorbents47 |
| Table 2.6: Performance of Biomass-Based Adsorbents in Treating Synthetic and Actual Wastewater |
| Table 2.7: Adsorption Mechanisms of Biomass-Based Adsorbents |
| Table 2.8: Advantages and Limitations of Various Machine Learning Algorithms60 |
| Table 3.1: Chemicals and Materials Used in This Study66 |
| Table 3.2: Structure and Physicochemical Characteristics of AB113 Dye70 |
| Table 3.3: Physicochemical Characteristics of Printing Wastewater70 |
| Table 3.4: Ranges of Independent Variables with Their Coded Levels |
| Table 3.5: Ranges of PKSAC/GO and Loading Amount of Iron Oxide |
| Table 3.6: Formulation in Brick Development |
| Table 3.7: Chemicals and Materials Used with Respective Potential Hazards and Preventive Measures |
| Table 4.1: ANOVA and Polynomial Equations of PKSAC-Based Adsorbents98 |
| Table 4.2: Textural Properties of PKSAC-Based Adsorbents |
| Table 4.3: EDX Analysis of PKSAC-Based Adsorbents |
| Table 4.4: Magnetic Properties of PKSAC-Based Adsorbents |
| Table 4.5: Particle Size Distribution of PKSAC-Based Adsorbents |
| Table 4.6: Summary of Physicochemical Characteristics and Adsorption Performance of PKSAC-Based Adsorbents |

| Table 4.7: Adsorption of Anionic Dye using PKSAC-GO-Fe |
|---|
| Table 4.8: Optimization Study of PKSAC-GO-Fe |
| Table 4.9: Comparison of Batch and Continuous Process |
| Table 4.10: Kinetic Parameters of AB113 Dye Adsorption onto PKSAC-GO-Fe144 |
| Table 4.11: Isotherm Parameters of AB113 Dye Adsorption onto PKSAC-GO-Fe149 |
| Table 4.12: Thermodynamic Study of Anionic Adsorption onto PKSAC-GO-Fe154 |
| Table 4.13: Quantum Chemical Descriptors of AB113 Dye and PKSAC-Based Adsorbents |
| Table 4.14: Adsorption Energy and Bond Length |
| Table 4.15: Feature Importances of PKSAC-Based Adsorbents |
| Table 4.16: Optimization of PKSAC-GO-Fe Synthesis Process |
| Table 4.17: Optimum Synthesis Process of PKSAC-GO-Fe |
| Table 4.18: Adsorption of Printing Wastewater using Optimized PKSAC-GO-Fe182 |
| Table 4.19: Kinetic Parameters of Printing Wastewater Adsorption onto Optimized PKSAC-GO-Fe |
| Table 4.20: Isotherm Parameters of Printing Wastewater Adsorption onto Optimized PKSAC-GO-Fe |
| Table 4.21: Thermodynamic Study of Printing Wastewater Adsorption onto Optimized PKSAC-GO-Fe |
| Table 4.22: Comparison of PKSAC-GO-Fe Before and After Synthesis Process Optimization |
| Table 4.23: Economic Evaluation of PKSAC-GO-Fe Before and After Synthesis Process Optimization of PKSAC-GO-Fe |
| Table 4.24: CO ₂ Emissions from Coal-Based and PKS-Based AC Production209 |
| Table 4.25: Growth Conditions of Red Bean Seeds |
| Table 4.26: Leaching of Iron Ions into Aqueous Solution |
| Table 4.27: Properties of Brick Formed using Different Formulations214 |

LIST OF SYMBOLS AND ABBREVIATIONS

ANOVA : Analysis of Variance

CAC : Commercial Activated Carbon

COD : Chemical Oxygen Demand mg/L

CP : Counterpoise

d : Bond Length Å

DFT : Density Functional Theory

EA : Electron Affinity eV

EDX : Energy Dispersive X-Ray Spectroscopy

E_{ads} : Adsorption Energy kJ/mol

E_{adsorbent} : Total Energy of Adsorbent kJ/mol

 $E_{adsorbent+dye}$: Total Energy of Adsorbent and Dye System kJ/mol

 E_{dye} : Total Energy of Dye kJ/mol

E_{HOMO} : Highest Occupied Molecular Orbital Energy eV

E_{HOMO-LUMO} : HOMO-LUMO Energy Gap eV

E_{LUMO}: Lowest Unoccupied Molecular Orbital Energy eV

ESP : Electrostatic Potential

GO : Graphene Oxide

HOMO : Highest Occupied Molecular Orbital

IP : Ionic Potential eV

IUPAC : International Union of Pure and Applied Chemistry

LANL2DZ : Los Alamos National Laboratory 2 Double-Zeta

LUMO : Lowest Unoccupied Molecular Orbital

MSE : Mean Square Error

 pH_{pzc} : Point of Zero Charge

PKSAC : Palm Kernel Shell Activated Carbon

PKSAC-Fe : Iron Oxide Impregnated PKSAC

PKSAC-GO : GO Impregnated PKSAC

PKSAC-GO-Fe : GO and Iron Oxide Impregnated PKSAC

PKSAC/GO : Ratio of PKSAC to GO

RMSE : Root Mean Square Error

S : Global Softness eV

SDG : Sustainable Development Goal

 η : Global Hardness eV

 λ_{max} : Maximum Wavelength nm

μ : Chemical Potential eV

χ : Electronegativity eV

ω : Electrophilicity Index eV

 ΔG° : Change of Standard Gibbs Free Energy kJ/mol

ΔH° : Change of Standard Enthalpy kJ/mol

 ΔS° : Change of Standard Entropy J/mol·K

CHAPTER 1: INTRODUCTION

1.1 Background Study

Annually, around 70 million tons of synthetic dyes are produced globally, leading to significant environmental challenges from the resulting dye wastewater, which is characterized by its complex composition and recalcitrance nature (Al-Tohamy et al., 2022). Dye wastewater results in severe ecological and health impacts, negatively affecting aquatic ecosystems by reducing light penetration, which impairs photosynthesis in aquatic plants and disrupts the food chain. Additionally, dyes can be carcinogenic, toxic, and mutagenic, even at low concentrations (Cheruiyot et al., 2019; Kausar et al., 2022). The high toxicity of dyes can lead to adverse effects on human organs, including the central nervous system, brain, liver, kidneys, and reproductive systems (Kausar et al., 2022; Liu et al., 2022). Therefore, concerted efforts are needed to reduce pollution from dye wastewater.

Various treatment technologies have been developed to address the challenge of dye wastewater. Traditional methods such as flocculation, chemical coagulation, and biological treatments are often insufficient due to the recalcitrant nature of synthetic dyes. Adsorption has gained recognition as a highly versatile and effective method for dye removal due to its flexibility, simplicity, high efficiency, and production of no sludge (Ahmad et al., 2021; Du et al., 2022; Foroutan et al., 2021; Saravanan et al., 2022; Tu et al., 2023). However, conventional adsorbents are often expensive and environmentally unfriendly, driving the search for alternative precursors for adsorbent development (Shokry et al., 2019). In this context, agricultural biomass presents a promising alternative for developing green, low-cost adsorbents due to its porous, cellulosic nature and sustainable, economic advantages (Aryee et al., 2022; Yu et al., 2022).

Malaysia, the world's 2nd largest producer of oil palm, generates palm kernel shell (PKS) from the processing steps as a by-product with limited end-use. Annually, the oil palm industry produces around 4.6 million tons of dry mass PKS (Pawlak-Kruczek et al., 2020). PKS, which is rich in carbon content (18% w/w), low in ash content (<0.1% w/w), and possesses inherent porous structures, presents a promising candidate for activated carbon development (Xiang & Ghazi, 2019). A carbon-based material, graphene oxide (GO), has also attracted considerable interest as a potential adsorbent, due to its high specific surface area and carboxyl, hydroxyl, and epoxy functional groups (Orooji et al., 2018; Singh et al., 2019). There are challenges associated with the use of GO, such as difficulties in post-treatment separation, agglomeration, and stacking during application. It is therefore often necessary to modify GO to improve its properties and performance (Nasiri & Arsalani, 2018).

In this work, a ternary composite (PKSAC-GO-Fe) was synthesized through low-cost activated carbon from PKS (PKSAC) with GO and iron oxide impregnation. Ternary composites like PKSAC-GO-Fe often offer significant advantages over binary and pristine materials. The combination of PKSAC, GO, and iron oxide provides unique synergies. PKSAC contributes to sustainability, cost-effectiveness, high porosity, and a large surface area. The oxygenated functional groups on GO facilitate interactions with dye molecules through mechanisms such as hydrogen bonding, π - π stacking, and electrostatic attraction. Iron oxide adds magnetic properties, allowing the adsorbent to be easily recovered using external magnetic fields, thus improving recovery and reusability. These combined advantages make ternary composites more effective and practical in adsorption applications than pristine or binary materials.

In previous studies, the optimization of the synthesis process for the treatment of actual industrial wastewater was not adequately addressed. The underlying adsorption

mechanisms associated with the interaction between pollutants and different functionalities need to be explored when impregnating GO and iron oxide into PKSAC. However, experimental approaches alone are insufficient to fully explain these adsorption interactions. In this study, computational approaches, including quantum chemical analysis and machine learning were used to model the adsorbent-adsorbate interactions and analyze feature importance. Therefore, the experimental and computational results complement each other to avoid unbiased findings.

Moreover, environmental and economic considerations are often overlooked. In this regard, the economic feasibility study highlights the importance of optimizing the ternary composite synthesis process. On the other hand, the incorporation of spent adsorbents into brick formation contributes to the sustainability concept and mitigates potential secondary pollution. With this, the entire lifecycle of adsorbents is taken into consideration, where waste PKS are converted into adsorbents, and after the treatment processes, spent adsorbents are made into bricks. This initiative is in line with the circular economy and zero waste concepts.

1.2 Problem Statement

In recent years, considerable interest has been given to the production of activated carbon from biomass (e.g., PKSAC) attributed to its availability, environmental friendliness, and low cost. Although the physicochemical characteristics of PKSAC, such as high surface area and porosity, make it a promising adsorbent for dye wastewater treatment, recent studies have shown that the adsorption performance of raw PKSAC could be further enhanced due to its limited functionality and selectivity. In this study, different organic and inorganic materials, such as GO and metal oxides, were impregnated with raw PKSAC to improve its adsorption performance.

While carbon-based GO presents various oxygenated functional groups, it faces limitations in actual applications, including agglomeration, stacking, and difficulty in post-treatment separation. Iron oxide, on the other hand, exhibits magnetic properties, which make it easier to recover after adsorption. Hence, this study proposes the impregnation of GO and iron oxide into PKSAC to produce a ternary composite. This composite combines the strengths of three materials, including the low-cost, high surface area, eco-friendliness of PKSAC, the functionalities of GO, and the magnetic properties of iron oxide. Together, these aforementioned characteristics make it a promising adsorbent for the treatment of dye wastewater.

To maximize adsorption performance, optimizing the synthesis processes and studying the detailed adsorption mechanisms is essential. Understanding these mechanisms requires exploring the effects of impregnating GO and iron oxide into PKSAC and the interactions between pollutants and the material functionalities. However, experimental approaches alone may not fully explain these interactions. Therefore, this study employs quantum chemical analysis and machine learning techniques to gain insights into the adsorbate-adsorbent interactions, complementing experimental methods.

Additionally, the environmental and economic aspects of using the ternary composite are thoroughly investigated to ensure its practical application and sustainability. In this regards, economic evaluation, phytotoxicity study, and the potential use of spent adsorbent in brick formation were considered to develop a more sustainable and effective wastewater treatment solution.

1.3 Research Questions

This study aims to address the following research questions:

- 1. How to enhance the adsorption performance of raw AC derived from PKS?
- 2. What are the significant physicochemical characteristics of the PKSAC-based adsorbents?
- 3. Has the adsorption performance of the PKSAC-based composite improved after the modification process?
- 4. What is the underlying adsorption mechanism of the ternary composite?
- 5. Is the ternary composite more economically and environmentally viable?

1.4 Aim and Objectives of the Study

This study aims to develop a green adsorbent with enhanced adsorption performance and reusability for wastewater treatment.

- 1. To synthesize a PKSAC-based ternary composite by impregnating with graphene oxide and iron oxide.
- 2. To determine the physicochemical characteristics of the PKSAC-based composite.
- 3. To evaluate the adsorption performance of the PKSAC-based composite.
- 4. To study the adsorption mechanism of the newly developed PKSAC-based composite with synthetic dye via experimental and computational approaches.
- 5. To evaluate the economic and environmental feasibility of the PKSAC-based composite for potential real-world applications.

1.5 Scope of the Study

The main goal of this research is to develop a ternary composite by combining PKSAC, GO, and iron oxide. The synthesis process was optimized by adjusting the ratio of PKSAC to GO and the loading amount of iron oxide. The significant physicochemical properties of the PKSAC-based adsorbents, including surface area, functional groups, morphologies, elemental compositions, magnetic properties, crystalline structures, particle size distribution, and point of zero charge (pH_{pze}), were systematically analyzed. Two main responses, i.e., color removal efficiency and adsorption capacity, were evaluated to study the adsorption performance in treating synthetic and actual industrial wastewater. The effects of operational parameters, such as initial solution pH, adsorbent dosage, and contact time on the adsorption performance was investigated and optimized.

Quantum chemical analysis and machine learning approaches were employed to gain insights on the adsorption mechanisms. The chemical structures of the adsorbent and adsorbate were optimized using the Hartree-Fock (HF) and M06-2x levels with 6-31G (d, p) basis sets. On the other hand, gradient boosting algorithm was applied to study feature importance of PKSAC-based adsorbents. The environmental aspects were evaluated, emphasizing the reduction of carbon dioxide emissions, iron leaching, and phytotoxicity. The economic feasibility of using the ternary composite was also assessed. Additionally, the possible utilization of the spent adsorbent in brick production was investigated.

1.6 Novelty of the Study

This research synthesizes an innovative PKSAC-based ternary composite by impregnating PKSAC with GO and iron oxide. This novel approach contributes to the green wastewater treatment, aligning with Sustainable Development Goals (SDGs), particularly SDG 6 Clean Water and Sanitation and SDG 12 Responsible Consumption and Production.

This study integrates both experimental methods and computational techniques, including quantum chemical analysis and machine learning, to understand adsorption mechanisms. This dual approach allows for the optimization of the synthesis process and the functional design of the composite. The incorporation of computational approaches ensures an unbiased study, as conventional experimental methods alone may not fully explain the adsorption mechanisms.

The study also assesses the environmental and economic feasibility of the ternary composite, including lifecycle considerations like using spent adsorbent in brick formation, aligning with zero waste and circular economy principles, reducing carbon emissions, and exploring secondary applications. This comprehensive approach ensures the solution is both practical and sustainable.

In summary, the ternary composite developed in this study has successfully addressing existing limitations, at the same time, prioritizes sustainability. Hence, it offers a versatile, high-performance, and eco-friendly alternative to traditional wastewater treatment technologies, contributing to the future advancements in green and low-carbon wastewater treatment.

1.7 Thesis Outline

This thesis is structured into five chapters: Introduction, Literature Review, Materials and Methodology, Results and Discussion, and Conclusion and Recommendations. These chapters collectively describe the study, helping to understand the characteristics and performance of the newly developed composite. The organization of this thesis is as follows:

Chapter 1: Introduction

This chapter provides a background on the issue of dye wastewater, emphasizing the potential for green, low-cost, and efficient adsorbents. It includes the research aims and objectives, problem statement, novelty, and the scope of this study. Additionally, the chapter briefly outlines the organization of the thesis.

Chapter 2: Literature Review

The existing literature relevant to the study are reviewed in this chapter, covering the characteristics of dye wastewater, various treatment technologies, potential adsorbents, the effects of operational parameters, and adsorption mechanisms. It also summarizes key findings and identifies research gaps that the present study seeks to address.

Chapter 3: Materials and Methodology

This chapter details the materials and chemicals used in the study, as well as the equipment employed for characterizing the synthesized composite and conducting analyses. It thoroughly discusses the methods adopted, including experimental design, adsorption studies, and analytical approaches.

Chapter 4: Results and Discussion

This chapter presents the findings from this study, including physicochemical characteristics of the composite. It also examines the effects of operational parameters on color removal efficiency and adsorption capacity, discusses adsorption kinetics and isotherm models, and evaluates reusability and stability. The chapter includes analyses of variance, quantum chemical studies, machine learning technique, and the optimization of the adsorbent synthesis process for treating actual printing wastewater, as well as an assessment of the economic and environmental aspects.

Chapter 5: Conclusion and Recommendation

This chapter summarizes the major findings of the study. It also offers recommendations for future research and discusses potential applications of the developed adsorbent.

CHAPTER 2: LITERATURE REVIEW

2.1 Introduction

This chapter critically reviews relevant literature for achieving the objectives of this study. An overview of the literature review is presented in Figure 2.1.

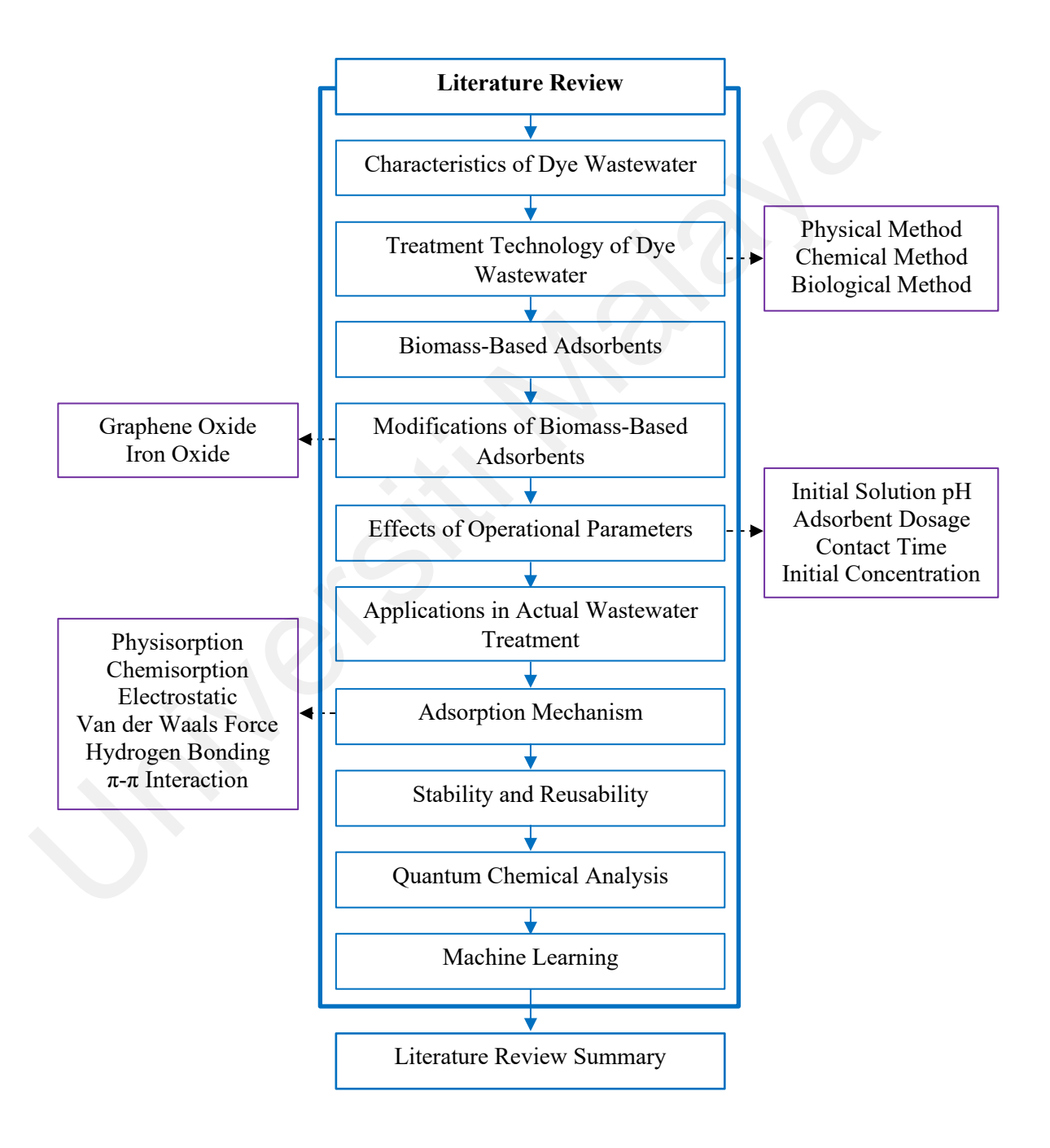


Figure 2.1: Literature Review Flowchart

2.2 Characteristics of Dye Wastewater

Many industries, including textiles, dyeing, food processing, and pharmaceuticals, face serious environmental and health challenges due to the generation of dye effluent. Among these, textile wastewater, for instance, often contains synthetic dyes, salts, heavy metals, and organic pollutants (Al-Tohamy et al., 2022; Etana et al., 2025; Khan & Malik, 2014). It is difficult to treat these dyes due to their complex aromatic structures that resist biodegradation (Periyasamy, 2024). Meanwhile, wastewater from food processing is contaminated with both natural and synthetic colorants, fats, oils, and greases, as well as organic matter. These aforementioned elements raise the levels of chemical and biological oxygen demand, which can cause receiving water bodies to become oxygen-depleted (Onet, 2010). Moreover, the active pharmaceutical ingredients, solvents, and dyes in pharmaceutical wastewater are often toxic, persistent, and capable of causing antibiotic resistance (Massima Mouele et al., 2021).

The discharge of dye wastewater has significant environmental, biological, and economic impacts. The significant coloration and turbidity are caused by the physical characteristics of the dye wastewater, such as high concentrations of dissolved organic matter and suspended particles. As a result, water bodies become recalcitrant and the aesthetic and ecological quality are negatively affected (Mahapatra & Vishwanathan, 2023). Furthermore, industrial effluents often have extreme pH values and elevated temperatures, which can harm aquatic ecosystems and hinder biological treatment processes (Dewangan et al., 2023; Rodgers, 2021). It also diminishes light penetration in water bodies, which inhibits photosynthesis in aquatic plants and hence disrupting the food chain (Hossen et al., 2022). Additionally, toxic components can accumulate in aquatic organisms, leading to bioaccumulation and biomagnification (Alsukaibi, 2022). High COD and BOD levels result in oxygen depletion, creating hypoxic conditions that can result in fish kills and a loss of biodiversity (Bhateria & Jain, 2016).

Moreover, many dyes and chemicals used in various industries (e.g., benzidine-based dyes, p phenylenediamine, azo dyes, and hexavalent chromium compounds) are mutagenic and carcinogenic. The aforementioned components are associated with significant health risks, including skin irritation, allergic contact dermatitis, occupational asthma, and respiratory issues from long-term exposure (Akhdhar, 2023; Lellis et al., 2019; Salami et al., 2023; Siddiqui et al., 2023; M. Zhang et al., 2023). The operating costs for municipalities and companies are rising as the advanced treatment procedures are required due to the complexity and fluctuation of dye wastewater. These advanced technologies are frequently expensive and resource-intensive. The typical characteristics of dye wastewater from various industrial sources are summarized in Table 2.1. As shown in Table 2.1, the composition of dye wastewater is greatly contributed by the types of compounds used during processing steps. In short, dye wastewater presents significant health, environmental, and economic challenges due to its complex composition and variability. In this regards, to develop an effective treatment technologies, aside from understanding these characteristics, continuous research and innovation are also essential to address the evolving challenges.

Table 2.1: Characteristics of Various Sources of Dye Wastewater

| Types of Dye Wastewater | Natural pH | COD (mg/L) | BOD (mg/L) | TSS (mg/L) | TDS (mg/L) | Color | References |
|-----------------------------------|------------|-------------|-------------|------------|-------------|----------------|--|
| Textile wastewater | 6.0-11.8 | 150-30000 | 80-6000 | 15-8000 | 6530-21989 | 50-2500 Pt-Co | (Ariza-Pineda et al., 2023; Dhameliya & Ambasana, 2023) |
| Food processing (sago) wastewater | 4.3-5.4 | 34000-76000 | 2560-4650 | 310-6667 | 2312-4073 | - | (Srinivasan et al., 2020) |
| Pharmaceutical wastewater | 6.7-7.4 | 23700-24500 | 11500-12100 | 9150-9240 | 15500-16700 | - | (Ramakrishna et al., 2001) |
| Pulp and paper wastewater | 2.6-9.8 | 706-2001 | 170-670 | 315-402 | 1651-2470 | 410-2802 Pt-Co | (Singh et al., 2020) |
| Printing wastewater | 8.4-9.2 | 4805-20205 | 360-940 | 1800-4150 | 3064-3190 | 0.21-2.24 Abs | (Harif et al., 2021) |
| Mining wastewater | 3.6-8.6 | 92-150 | | 2495 | 992-1349 | - | (Mike Agbesi & Ebenezer David Okwaning, 2017) |
| Leather tanning wastewater | 8.0-9.0 | 5000-5500 | 3000-3500 | 2500-3000 | - | - | (Krishanamoorthi et al., 2009) |
| Wet processing wastewater | 6-10 | 150-12000 | 80-6000 | 15-8000 | 2900-3100 | 50-2500 Pt-Co | (Ghaly et al., 2014) |

Pt-Co: Platinum-Cobalt Scale; Abs: Absorbance

2.3 Treatment Technology for Dye Wastewater

Dye wastewater is treated using a range of technologies, including biological, physical, and chemical approaches such as adsorption, flocculation, filtration, photocatalysis, advanced oxidation, chemical oxidation, activated sludge process, biofilm, and microbial fuel cell. Table 2.2 outlines the advantages and limitations of each method for comparison. Among all methods, adsorption is considered the most practical for treating dye wastewater due to its high efficiency, low material and operational costs, and ease of operation and control (Elgarahy et al., 2023). Ion-exchange resins, inorganic compounds, and coal-based activated carbon are a few examples of commercial adsorbent materials (Abuelnoor et al., 2021).

Recently, research has focused on replacing expensive and non-environmentally friendly conventional adsorbents with green and low-cost materials, which can be achieved by utilizing biomass or agricultural wastes. The term "green adsorbent" refers to low-cost adsorbents derived from renewable and abundantly available natural resources, agricultural by-products and residues, aquatic biomass, and other sources (Kyzas & Kostoglou, 2014; Thakur et al., 2022). Previously published studies have demonstrated that adsorbents developed from various biomasses can remove significant amounts of pollutants, especially after substantial modifications, offering various advantages.

Advanced oxidation processes (AOPs), such as Fenton-based reactions and photocatalysis are efficient at breaking down complex dye molecules into non-toxic substances. However, limitations such as pH range restriction, high cost and energy consumption and difficult to recover the homogeneous catalyst are to be encountered. Membrane filtration technologies, on the other hand, especially nanofiltration and ultrafiltration, show high dye removal efficiency. The integration of AOPs with

membrane filtration has demonstrated the potential to enhance degradation rates, though challenges like high cost, membrane fouling, low catalytic membrane recovery, and industrial practicability remain (C. Zhang et al., 2024).

Biological treatment methods, particularly those using microbial strains capable of producing enzymes like laccase, peroxidase, and azoreductase, have gained attraction as low-cost, eco-friendly alternatives (Ali et al., 2025). Genetically engineered microorganisms are also being explored to improve dye degradation rates (Rafeeq et al., 2023). Furthermore, photocatalysis processes that use light and catalysts to speed up a chemical reaction to degrade dye pollutants have gained significant attention. Metal oxide catalysts such as ZrO₂, TiO₂, SnO₂, CeO₂, ZrO₂, and ZnO are being studied extensively to enhance photocatalytic activity, visible light absorption and dye degradation rates through doping with rare earth elements (Kumari et al., 2023). While these methods have demonstrated considerable promise, challenges related to scalability, secondary pollution, and energy consumption still require further research and optimization to achieve widespread applications.

Table 2.2: Advantages and Limitations of Dye Wastewater Treatment Technologies

| Classification | Methods | Advantages | Limitations | References |
|----------------|--------------------|---|---|---|
| Physical | Adsorption | - Low material cost - Low operational cost - High efficiency - Easy to operate - Easy to control - No sludge - High speed - Less energy-intensive | - Difficult to recover in the post-treatment process | Aghashiri et al. (2022); (Ahmad & Ansari, 2022; Wong et al., 2018) |
| | Filtration | Simple in designEffectiveLow cost | FoulingHigh energy consumption | (Guo et al., 2016); Holkar et al. (2016); (Zheng et al., 2013) |
| | Flocculation | - Effective and simple | Non-degradable Expensive and highly toxic due to the presence of petroleum raw materials | B. Liu et al. (2018) |
| Chemical | Advanced oxidation | - Effective in dye molecule degradation | pH range restriction of the process High-cost reactants High energy consumption Difficulty in the recovery of the homogeneous catalyst (in catalytic-Fenton process) | Arzate et al. (2019); (Arzate et al., 2019; Gözmen et al., 2009); Martínez- López et al. (2019) |
| | Chemical oxidation | - Effective in organic compound removal | High chemical costUndesired by-products | Yang et al. (2019) |

Table 2.2: Continued

| Classification | Methods | Methods Advantages 1 | | References |
|----------------|-----------------------------------|--|---|---|
| | Photocatalysis | High physical-chemical stabilityEnvironment friendlyLow cost | - Low efficiency (especially for non-visible light) | Deng et al. (2019) |
| Biological | Activated sludge process Biofilm | Effective in organic compound and nutrients removal Adaptable to varying strengths of wastewater Simple procedure Low equipment requirements No secondary pollution Effective in organic compound removal | High sludge production High operational cost due to continuous aeration Sensitive to toxic loads Clogging and fouling Maintenance-intensive | (Márquez et al., 2022; Shao et al., 2020; Song et al., 2023) |
| | Microbial fuel cell | Manages influent fluctuation Produce less sludge Generates electricity Effective in treating a wide range of contaminants Low biomass production, Eliminates COD without further oxygenation | Difficult to maintain desirable results and generated power in larger systems Voltage loss due to substrate cross-conduction | (Saini et al., 2023) |

2.4 Biomass-Based Adsorbents

Solid waste is the largest source of waste in the agriculture sector. Annually, about 140 billion tons of lignocellulosic biomass waste is produced globally, accounting for 30% to 40% of all solid waste produced worldwide (Ansari et al., 2023). The improper disposal of agricultural solid waste poses significant environmental threats and harms. However, bioeconomic systems could benefit from using this waste as a raw material and transforming it into something useful (Nguyen et al., 2022; Salema et al., 2017). Compared to conventional chemical sorbents, adsorbents developed from agricultural biomass offer several advantages: they are abundantly available, biodegradable under natural conditions, and simple to collect and prepare (Anastopoulos et al., 2019; Köseoğlu & Akmil-Başar, 2015).

The organic components in agricultural biomass, such as lignin, cellulose, and hemicellulose, are key determinants of biochar's thermal conversion, composition, and structure. Functional groups present in these compounds, including hydroxyl (OH), carbonyl (C=O), methoxy (O-CH₃) and carboxyl (COOH), offer good chemical structure tunability and provide a strong basis for functionalization in adsorption (Cholico-Gonzalez et al., 2020; Du et al., 2023; W. Zhang et al., 2022). The key functions of biochar are largely determined by its properties, such as polarity and aromaticity (Han et al., 2021). The properties and adsorption performance can be significantly enhanced through suitable modifications. These includes thermal processing, physicochemical treatments, and organic and inorganic compounds impregnation. In addition, the modification process also introduces new surface functional groups that enhance bond formation, making biochar a suitable candidate as an adsorbent.

Table 2.3 depicts the application of various unmodified agricultural waste adsorbents, showing their respective removal efficiency and adsorption capacity under optimized

conditions. The color removal efficiency and adsorption capacity obtained ranged from 55.0% to 99.3% and 4.4 mg/g to 636.0 mg/g, respectively. These results indicate that biomass-derived adsorbents can remove large amounts of dyes from aqueous solutions, demonstrating their potential for actual wastewater treatment.

Malaysia, the 2nd largest producer and exporter of palm oil, contributes about 30% to global production and 37% to global exports, significantly boosting its gross domestic product. Oil palm biomass (OPB) from the palm oil industry, including oil palm trunk, palm kernel fiber, palm kernel shell, empty fruit bunch, and oil palm frond, represents 90% of the total biomass, with oil accounting for only 10%. Annually, Malaysia produces 127 million tons of OPB (Su et al., 2022). Extensive research has focused on converting OPB into useful materials, with activated carbon from PKS gaining considerable attention due to its favorable characteristics and performance in treating various pollutants. However, most previous studies have concentrated on pollutants other than dye wastewater. Converting PKS into activated carbon can lower the operational costs of the adsorption process while minimizing agricultural waste, providing dual benefits. The reviewed literature indicates that PKS-based activated carbon is a highly effective adsorbent, making it an attractive source of agricultural waste for the development of activated carbon. In summary, biomass-derived adsorbents are high-performing, cost-effective, and environmentally friendly options for the treatment of dye wastewater.

Table 2.3: Applications of Biomass-Based Adsorbents in Wastewater Treatment

| Types of Precursor | Types of Pollutant | Optimum Operational Conditions | Maximum Performance | References |
|-----------------------|---------------------------|---------------------------------------|--|-----------------------|
| Delonix regia biomass | ARS | pH = 2 | 55.0% for [ARS] _i = 10 mg/L | Aravindhan et al. |
| | | Dosage = 2 g/L | 4.4 mg/g | (2024) |
| | | Time = 60 min | | |
| Nile water algae | MB | MB: | MB: 200.0 mg/g | Moghazy et al. (2023) |
| | Cu^{2+} | Concentration = 20 mg/L | Cu ²⁺ : 153.2 mg/g | |
| | | pH = 6 | | |
| | | Dosage = 2 g/L | | |
| | | Time = 60 min | | |
| | | Cu ²⁺ : | | |
| | | Concentration = 10 and 20 mg/L | | |
| | | pH = 5.5 | | |
| | | Dosage = 2 g/L | | |
| | | Time = 60 min | | |
| Orange peel (OP) | BR46 | Concentration = 100 mg/L | 94.0% for [BR46] _i = 100 mg/L | Kapoor and Sivamani |
| | | pH = 9 | 7.4 mg/g | (2023) |
| Reed fibres | MB | Concentration = 10 mg/L | 69.6% for [MB] _i = 10 mg/L | Amri et al. (2022) |
| | | pH = 5 | 21.0 mg/g | |
| | | Time = 3 h | | |
| | | Dosage = 0.1 g | | |

Table 2.3: Continued

| Types of Precursor | Types of Pollutant | Optimum Operational Conditions | Maximum Performance | References |
|-----------------------|---------------------------|---------------------------------------|--|------------------------|
| Water hyacinth root | Reactive blue | pH = 2 | 99. 0% for [RB] _i = 50 mg/L | Teshager et al. (2022) |
| | | Dosage = 1 g/L | 128.8 mg/g | |
| | | Temperature = 22 °C | | |
| | | Speed = 200 rpm | | |
| | | Particle size = 50 μm | | |
| Antarctic yeast | RB19 | RB19: | 90.0% for [RB19] _i and [RR141] _i | Ruscasso et al. (2021) |
| Debaryomyces hansenii | RR141 | Concentration = 100 mg/L | = 100 mg/L | |
| F39A | | Dosage = 2 g/L | | |
| | | Temperature = 20 ± 1 °C | | |
| | | RR141: | | |
| | | Concentration = 100 mg/L | | |
| | | Dosage = 6 g/L | | |
| | | Temperature = 20 ± 1 °C | | |

Table 2.3: Continued

| Types of Precursor | Types of Pollutant | Optimum Operational Conditions | Maximum Performance | References |
|-------------------------|--------------------|--|------------------------|----------------------|
| Aspergillus parasiticus | CR | CR: | CR: 78.7 mg/g | Bouras et al. (2021) |
| CBS 100926 ^T | MB | Concentration = 7.2×10^{-5} mol/L | MB: 73.1 mg/g | |
| | BF | pH = 4.5 | BF: 42.7 mg/g | |
| | MGO | Time = 60 min | MGO: 35.0 mg/g | |
| | Sudan Black | MB: | Sudan Black: 24.3 mg/g | |
| | PR | Concentration = $1.6 \times 10^{-4} \text{ mol/L}$ | PR: 6.3 mg/g | |
| | | pH = 8.5 | O' | |
| | | Time = 60 min | | |
| | | BF: | | |
| | | Concentration = 1.0×10^{-4} mol/L | | |
| | | pH = 8.0 | | |
| | | Time = 60 min | | |
| | | MGO: | | |
| | | Concentration = 5.4×10^{-5} mol/L | | |
| | | pH = 8.5 | | |
| | | Time = 60 min | | |
| | | Sudan Black: | | |
| | | Concentration = $1.1 \times 10^{-4} \text{ mol/L}$ | | |
| | | pH = 8.0 | | |
| | | Time = 60 min | | |
| | | PR: | | |
| | | Concentration = 1.4×10^{-4} mol/L pH | | |
| | | = 7.5 | | |
| | | Time = 20 min | | |

Table 2.3: Continued

| Types of Precursor | Types of Pollutant | Optimum Operational Conditions | Maximum Performance | References |
|---------------------------|---------------------------|---------------------------------------|---|-------------------------|
| Cocoa shell | BB41 | pH = 6 | 90.0% for [BB41] _i = 10 mg/L | Hamadi et al. (2021) |
| | | Dosage = 4 g/L | | |
| | | Time = 45 min | | |
| | | Speed = 400 rpm | | |
| Natural safiot clay | MB | Concentration = 40 mg/L | MB: 68.5 mg/g | Kassimi (2021) |
| | SAF | pH = 12 | SAF: 45.5 mg/g | |
| | | Dosage = 30 mg | | |
| | | Temperature = 25°C | | |
| Potato peel | СВ | pH = 2.2 | 100.0 mg/g | Bouhadjra et al. (2021) |
| | | Dosage = 2 g/L | | |
| Salix alba L. (white | MB | Concentration = 150 mg/L | SA (WW): 35.5 mg/g | Gemici et al. (2021) |
| willow) | | pH = 6.4 | SB (WW): 42.7 mg/g | |
| Salix babylonica | | Dosage = 5 g/L | | |
| (weeping willow) | | Time = 240 min | | |
| | | Temperature = 15°C | | |
| Trichoderma asperellum | MG | pH = 10 | MG: 47.6 mg/g | Shanmugam et al. |
| BPL MBT1 | CV | Dosage = 1.0 g/50 mL | CV: 50.0 mg/g | (2021) |
| | | Time = 100 min | | |
| Eichhornia crassipes | RhB | - | Root: 27.2 mg/g | Saufi et al. (2020) |
| | | | Leaf: 44.6 mg/g | |
| Alkali-soluble | CR | pH = 2 | Single/binary mixture | Fatombi et al. (2019) |
| polysaccharide extracted | IC | Time = 120 min | CR: 319.1/636.0 mg/g | |
| from Carica papaya | | Temperature = 30°C | IC: 168.5/102.7 mg/g | |
| seeds | | | | |

Table 2.3: Continued

| Types of Precursor | Types of Pollutant | Optimum Operational Conditions | Maximum Performance | References |
|---------------------------|--|---------------------------------------|--|-------------------------|
| Coffee husk | CV | Concentration = 12.239 mg/L | 12.0 mg/g | Cheruiyot et al. (2019) |
| | | pH = 3 | | |
| | | Dosage = 0.25 g/50 mL | | |
| | | Time = 30 min | | |
| | | Temperature = 25° C | | |
| | | Particle size = $0.15-0.3 \text{ mm}$ | | |
| Banana peel | RB5 | pH = 3 | RB5: 49.2 mg/g | Munagapati et al. |
| | CR | Time = 180 min Temperature = 298 | CR: 164.6 mg/g | (2018) |
| | | K (25°C) | | |
| Banana peel | RhB | Dosage = 13.33 g/L | 81.1% for [RhB] _i = 25 mg/L | Singh et al. (2018) |
| | | Time = 60 min | | |
| Banana peel | MB | MB: | MB: | Stavrinou et al. (2018) |
| Cucumber peel | OG | pH = 6 | 211.9 mg/g (BP); 107.2 mg/g | |
| Potato peel | | Dosage = 1.0 g/L | (CP); 179.9 mg/g (PP) | |
| | | Time = 24 h | OG: | |
| | | OG: | 20.9 mg/g (BP); 23.6 mg/g (CP); | |
| | | pH = 2 | 40.5 mg/g (PP) | |
| | The state of the s | Dosage = 1.0 g/L | | |
| | | Time = 24 h | | |
| Aspergillus niger | AY99 | pH = 3 | 544.3 mg/g | Naskar and Majumder |
| | | Dosage = 2 g/L | | (2017) |
| | | Temperature = 30°C | | |

Table 2.3: Continued

| Types of Precursor | Types of Pollutant | Optimum Operational Conditions | Maximum Performance | References |
|---------------------|--------------------|---|--|------------------------|
| Date palm seed | CR | Concentration = 20 mg/L | 61.7 mg/g | Pathania et al. (2016) |
| | | pH = 2 | | |
| | | Dosage = 60 mg/50 mL | | |
| | | Time = 120 min | | |
| | | Temperature = 55°C | | |
| Peach shell | MB | pH = 5.5 | 76.0% for [MB] _i = 100 ppm | Marković et al. (2015) |
| | | Dosage = 400 mg/100 mL | 99.0% for [MB] $_{i} = 10 \text{ ppm}$ | |
| | | Time = 180 min | | |
| Garlic peel | DR12B | Concentration = 50 mg/L | 99.0% for [DR12B] _i = 50 mg/L | Asfaram et al. (2014) |
| | | Time = 25 min | | |
| | | Dosage = 0.2 g/50 mL | | |
| Formosa papaya seed | CV | pH = 8.0-10.0 | 86.0 mg/g | Pavan et al. (2014) |
| powder | | Dosage = 12.0 g/L | | |
| | | Time = 60.0 min | | |
| | | Temperature = 25°C | | |
| Brown macroalga | AO7 | Concentration = 50 mg/L | 35.6 mg/g | Kousha et al. (2012) |
| Stoechospermum | | pH = 2 | | |
| marginatum | | Dosage = 1 g/L | | |
| | | Time = 60 min | | |
| | | Temperature = $25\pm2^{\circ}$ C | | |
| Indian Jujuba seed | CR | pH 2 | 55.6 mg/g | Reddy et al. (2012) |
| Cotton stalk | MB | Dosage = 4 g/L | 91.2% for [MB] = 800 mg/L | Deng et al. (2011) |
| | | Time = 180 min | 147.1 mg/g | |
| | | Temperature = $308\pm2 \text{ K } (35\pm2^{\circ}\text{C})$ | | |

Table 2.3: Continued

| Types of Precursor | Types of Pollutant | Optimum Operational Conditions | Maximum Performance | References |
|--------------------|---------------------------|---------------------------------------|---------------------------------------|----------------------|
| Palm kernel fibre | MB | MB: $pH = 7.0$ | MB: 95.4 mg/g | El-Sayed (2011) |
| | CV | CV: pH = 2.4 | CV: 78.9 mg/g | |
| Cashew nutshell | CR | Concentration = 20 mg/L | 99.3% for $[CR]_i = 100 \text{ mg/L}$ | Kumar et al. (2010) |
| | | pH = 3 | 5.2 mg/g | |
| | | Dosage = 30 g/L | | |
| | | Time = 120 min | | |
| | | Temperature = 30°C | | |
| Grapefruit peel | CV | pH = 6.0 | 254.2 mg/g | Saeed et al. (2010) |
| Garlic peel | MB | Temperature = 323 K (50°C) | 142.9 mg/g | Hameed and Ahmad |
| | | | | (2009) |
| Papaya seed | MB | - | 555.6 mg/g | Hameed (2009) |
| Palm kernel shell | MB | Dosage = 1 g/L | ≈180.0 mg/g | Choong et al. (2006) |
| (purchased) | | 467 | | |

2.5 Modifications of Biomass-Based Adsorbents

In recent years, adsorption technology has advanced through innovative modifications to adsorbents, enhancing their properties and performance by altering the raw precursors (Li et al., 2022). Functionalizing raw precursors can modify physical characteristics such as hydrophilic and hydrophobic features, surface charge, pore volume, and surface area, which in turn can improve adsorption performance (Adegoke et al., 2022).

2.5.1 Graphene Oxide Impregnated Biomass-Based Adsorbents

Since its discovery in 2004, graphene, a one-atom-thick, two-dimensional (2D) carbon material, has garnered significant attention for its excellent thermal, electrical, mechanical, and optical properties, along with its high specific surface area, making it highly desirable as an adsorbent (Khalse & De, 2024). Graphene oxide (GO) (Figure 2.2) contains various functional groups, including epoxy, hydroxyl, and carboxyl groups, which contribute to adsorption processes by promoting the adsorbent-adsorbate interactions (Ricci et al., 2022). Unlike traditional carbonaceous sorbents, GO can be modified without destroying its carbonaceous hexagon structure (Fraga et al., 2020). Its notable performance in dye wastewater treatment can be attributed to its excellent chemical and physical properties (Jiang et al., 2016). However, GO's tendency to self-agglomerate and its weak separability limit its actual applications (Su et al., 2017). Hence, modifying GO with other compounds is necessary to resolve aforementioned issues.

Several studies have reported on modified GO adsorbents for wastewater treatment applications. In the study reported by Abd-Elhamid et al. (2019), a graphene oxide-activated carbon composite was developed for the removal of MB and crystal violet (CV) dyes. In the reported study, graphene oxide and activated carbon have been chemically conjugated using tetraethyl orthosilicate (TEOS). The irregular heterogeneous surface, as observed in SEM images promotes the dye adsorption and trapping. From the

experimental results, MB and CV recorded adsorption capacities of 70.0 mg/g and 147.0 mg/g for monolayer adsorption, respectively. Another similar study by Bhattacharyya et al. (2021) investigated MB dye removal using GO-activated carbon nanocomposite. It was shown that the maximum Langmuir adsorption capacity could reach 1000.0 mg/g, which is 14-fold more than the 70.0 mg/g reported by Abd-Elhamid et al. (2019). It can be seen from the scanning electron microscope (SEM) images that the pores of activated carbon and the sheet-like structure of graphene oxide are evident, which indicates both structures play an important role in MB dye adsorption.

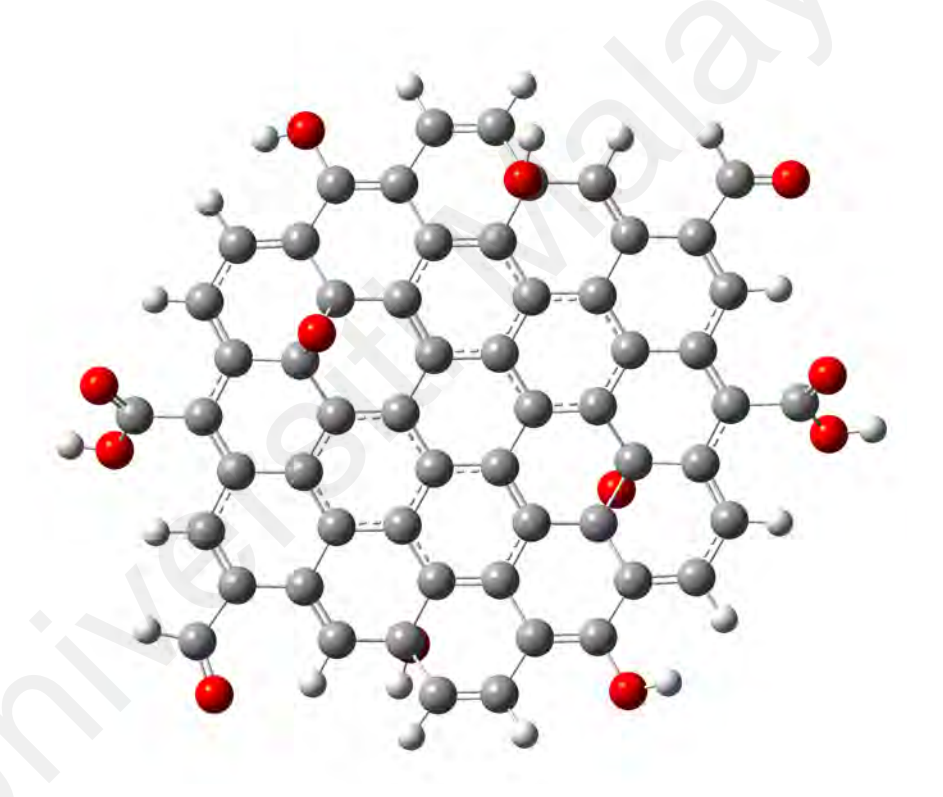


Figure 2.2: Chemical Structure of Graphene Oxide

Bhattacharyya et al. (2018) examined the removal of MB dye using graphene oxide and potato starch bio-composite cross-linked with glutaraldehyde. The developed composite was able to remove up to 90.0% of the initial dye and achieved 154.0 mg/g of adsorption capacity. On the other hand, from the study reported by S. Liu et al. (2018), a composite consisting of GO and corn straw core was synthesized for the removal of MB

dye. As a result of the addition of GO to corn straw core, the composite recorded an increase of 21.6% in removal rate, where the developed composite was able to remove up to 414.03 mg of MB dye per gram of composite when 5 wt% of GO was added.

Besides that, Wang et al. (2014) synthesized a ternary composite consisting of graphene, multi-walled carbon nanotubes (MWCNTs) and Fe₃O₄ for treating MB dye. A maximum of 65.8 mg/g of Langmuir adsorption capacity was achieved by the composite. Likewise, Almoisheer et al. (2019) reported a work in which graphene oxide is combined with silicon and carbon nanotubes and used to treat CR dye from aqueous solutions. The developed composite reveals maximum adsorption capacity (456.2 mg/g) under optimum conditions. Furthermore, a graphene oxide/activated carbon-based ternary composite for the removal of lead (II) was reported by Mojoudi et al. (2019). The nanocomposite consisting of activated carbon, graphene oxide and nanoclay was found to have a total pore volume of 1.01 m³/g with a BET surface area of 1296.00 m²/g. In short, with the incorporation of graphene oxide with various materials, the performance and characteristics of the adsorbents can be significantly enhanced, attributed to the synergic effects between them.

Incorporating GO with various materials significantly enhances the performance and characteristics of adsorbents due to synergistic effects. Despite these advancements, relatively few studies have focused on incorporating GO with biomass-based activated carbon. Therefore, further research is needed to investigate the adsorption mechanisms, properties, and performance of GO-biomass composites in treating dye wastewater.

2.5.2 Iron Oxide Impregnated Biomass-Based Adsorbents

Raw agricultural biomass often faces limitations in actual applications, especially in post-treatment separation. After adsorption processes, some adsorbents are discarded with processed sludge, causing secondary pollution (Nethaji et al., 2013). Impregnating iron oxide onto different types of biomass leverages the magnetic properties of iron oxide, facilitating easy removal from aqueous solutions (Angelova et al., 2016). Figure 2.3 shows a post-treatment separation process of magnetized adsorbents. Magnetic adsorbents, particularly iron oxide-containing materials, achieve higher adsorption performance due to surface oxygen functional groups, such as -COOH and -COH (Olusegun et al., 2023). These functional groups can facilitate hydrogen bonding between the adsorbent and adsorbate, enhancing the adsorption performance (Tatarchuk et al., 2023). Besides that, hydroxyl groups possess amphoteric properties, which could react with both acids and bases, facilitating the adsorption process (Laurent et al., 2008).

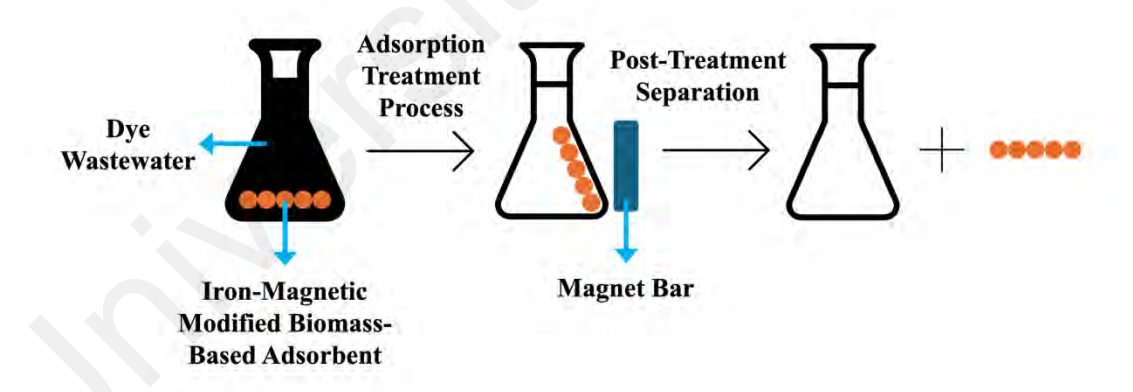


Figure 2.3: Post-Treatment Separation of Magnetized Adsorbents

Vibrating sample magnetometers (VSM) are typically used to measure the magnetic properties of developed materials. Iron oxide modified biomass can be synthesized through hydrolysis, precipitation, and other methods. Table 2.4 summarizes the synthesis methods of iron oxide modified biomass and their effectiveness in dye removal. The coprecipitation method, involving iron (II) sulfate heptahydrate (FeSO₄·7H₂O) and iron (III)

chloride hexahydrate (FeCl₃·6H₂O) with pH adjustment to alkaline conditions using sodium hydroxide (NaOH), is commonly used for synthesizing magnetized biomass adsorbents. There is a study reported by Lima et al. (2020) where magnetic materials were developed from cocoa husk (CH), peanut shell (PS), coconut mesocarp (CM) and sugarcane bagasse (SB) via single step and combustion synthesis methods. The saturation magnetizations of CH, PS, CM and SB, determined from VSM analysis, were 20.11 emu/g, 24.83 emu/g, 48.29 emu/g and 51.16 emu/g, respectively. This indicates that external magnetic fields can be used effectively to separate the adsorbents from the aqueous solution after the treatment process, avoiding the possible secondary pollution.

In Table 2.4, by-products from the first and second stages of rice milling, i.e., rice husk and rice bran have been used as precursors for the synthesis of adsorbents with magnetic properties. Based on Yang et al. (2008), rice husk was treated with 63% nitric acid to make it hydrophilic. Then, the magnetic rice husk was developed through one-step synthetization and thermal treatment at 750°C for three hours before applying to treat MB dye. The BET results revealed that with the addition of iron oxides, the surface areas were reduced to 770.00 m²/g from 826.00 m²/g. This can be explained by the deposition of iron oxides inside the pores. On the other hand, a contrastive trend was observed for rice bran-based magnetic adsorbent (Ma et al., 2020). Based on BET results, with the addition of tin dioxide (SnO₂) and iron oxide (Fe₃O₄) to the rice bran, an increase in surface area was observed from 0.59 m²/g to 0.75 m²/g, which promoted more dye adsorption.

In most of the studies, the combination of more than one method was used to modify the biomass. Based on the study of Ren et al. (2019), NaOH activation contributes to oxygen-containing groups that form hydrogen bonds with pollutants and lead to higher pore volume and surface area, which are critical properties of an adsorbent. After the magnetization process, the adsorbent tends to achieve equilibrium at a faster rate and enhances electropositivity. The developed adsorbent was able to achieve an adsorption capacity of 53.7 mg/g for removing RhB dye. Besides that, to investigate different precursors for removing RB5 dye, wood (Saroyan et al., 2017) and coconut shell (Kyzas et al., 2014) are compared. As shown by SEM analysis, both magnetized wood and coconut shell adsorbents had spongy morphologies, indicating that iron oxides are deposited on the surface. Besides that, wood-based adsorbent possesses a more porous structure compared to coconut shell-based adsorbent, which could be the reason for higher adsorption capacity (445.3 mg/g) compared to coconut shell-based adsorbent (54.8 mg/g).

In short, the addition of iron oxides to the biomass promotes the magnetic property which is beneficial for solid-liquid separation after adsorption treatment. Other than that, the adsorption capacity can also be improved significantly by adding functional groups when iron oxides are impregnated.

Table 2.4: Synthesis Method and Adsorption Performance of Iron Oxide Impregnated Biomass Adsorbent

| Types of Biomass | Synthesis Methods | Pollutant | Color Removal Efficiency | Adsorption Capacity | References |
|-----------------------|--------------------------|-----------|---------------------------------------|----------------------------|--------------------------|
| Hemp biomass | Co-precipitation | MB | - | MB: 457.6 mg/g | Akkoz and Coskun |
| | | CV | | CV: 509.3 mg/g | (2024) |
| | | MGO | | MGO: 1300.0 mg/g | |
| Chromolaena odorata | Co-precipitation | MB | - | MB: 14.4 mg/g | Ajibade and Nnadozie |
| | | BPB | | BPB: 2.7 mg/g | (2023) |
| | | RhB | | RhB: 16.5 mg/g | |
| Douglas fir biochar | Co-precipitation | BPB | 89.8% for [BPB] _i = 1000 | 448.0 mg/g | Samaraweera, Alam, et |
| | | | mg/L | | al. (2023) |
| Avocado peel | Hydrothermal | MB | - | 62.1 mg/g | Prabakaran et al. (2022) |
| Lemon wood | Co-precipitation | CV | - | 35.3 mg/g | Foroutan et al. (2021) |
| Moringa oleifera seed | Carbonization- | RB4 | - | RB4: 32.5 mg/g | Sirajudheen et al. |
| | magnetization | IC | | IC: 33.5 mg/g | (2021) |
| | | AB158 | | AB158: 35.3 mg/g | |
| Peanut shell | Co-precipitation | AF | 99.4% for $[AF]_i = 200 \text{ mg/L}$ | - | Renita et al. (2021) |
| Sugarcane bagasse | One-step synthetization | MB | - | 36.1 mg/g | Jiang et al. (2021) |
| Palm shell | Infused impregnation | MB | - | MB: 287.0 mg/g | Kittappa et al. (2020) |
| | | MO | | MO: 289.4 mg/g | |
| | | CR | | CR: 144.3 mg/g | |
| Rice bran | Co-precipitation | RB4 | - | RB4: 218.8 mg/g | Ma et al. (2020) |
| | | CV | | CV: 159.2 mg/g | |
| Egg white | Co-precipitation | MB | - | 194.0 mg/g | Vahdati-Khajeh et al. |
| | | | | | (2019) |

Table 2.4: Continued

| Types of Biomass | Synthesis Methods | Pollutant | Color Removal Efficiency | Adsorption Capacity | References |
|-----------------------|---|-----------|---|--------------------------------|-----------------------------|
| Nigella sativa L. | Co-precipitation | CBB | 85.9% for [CBB] _i = 40 mg/L | 57.3 mg/g | Abdel-Ghani et al. (2019) |
| Pineapple crown leaf | Co-precipitation | MV | \approx 94.5% for [MV] _i = 20 16.8 mg/g mg/L | | Astuti et al. (2019) |
| Rice straw | One-step synthetization | RhB | - | 53.7 mg/g | Ren et al. (2019) |
| Sargassum oligocystum | Co-precipitation | MB & MV | - 10 | MB: 60.6 mg/g MV: 59.9 mg/g | Rauf Foroutan et al. (2019) |
| Chestnut | Co-precipitation | MG | - | 311.4 mg/g | Altintig et al. (2018) |
| Peanut shell | One-step synthetization | MG | - | 195.6 mg/g | Guo et al. (2018) |
| Acorn shell | Co-precipitation | MB | - | 157.1 mg/g | Altıntıg et al. (2017) |
| Wood | Co-precipitation | RB5 | - 1 | 445.3 mg/g | Saroyan et al. (2017) |
| Brown algae Sargassum | Microwave- | AO, CV, | - | AO: 193.8 mg/g | Angelova et al. (2016) |
| horneri | synthetization | MG, MB, | | CV: 167.0 mg/g | |
| | | SO | | MG: 110.4 mg/g | |
| | | | · | MB: 158.9 mg/g | |
| | | | | SO: 144.4 mg/g | |
| Coconut shell | Concurrent activated and magnetization | AY6 | - | 13.1 mg/g | Cazetta et al. (2016) |
| Coconut shell | Co-precipitation | RB5 | - | 54.8 mg/g | Kyzas et al. (2014) |
| Hydrochar | Co-precipitation | MG | - | 476.0 mg/g | Zhu et al. (2014) |
| Rice husk | One-step synthetization + Thermal treatment | MB | - | 321.0 mg/g | Yang et al. (2008) |

2.6 Effects of Operational Parameters on Adsorption Process

The effects of four critical operational parameters on the adsorption process, including (1) initial pH of the solution, (2) adsorbent dosage, (3) contact time, and (4) initial concentration of the adsorbate, are discussed in this section. By optimizing the operational parameters will help in the development of more sustainable and efficient dye wastewater treatment processes.

2.6.1 Effect of Initial pH of the Solution

The initial pH of the solution is a critical factor in the adsorption process, as it greatly affects both the ionization state (pollutants) and the surface charge (adsorbents). Biomass-based adsorbents contain various functional groups, such as amino, hydroxyl, and carboxyl, groups. These funtionalities will undergo either deprotonation or protonation depending on the solution pH. With different changes, the adsorbate-adsorbent interactions can be significantly altered. The pH_{pze} is the pH at which the adsorbent surface is globally neutral, meaning the number of positive and negative charges is balanced. This point is greatly dependent on the electronic and chemical properties of the functional groups on the adsorbent surface (Çağlar et al., 2018). Moreover, the solution's pH also affects the structural stability and ionization degree of dye molecules, further influencing the adsorption process (Saeed et al., 2010).

At lower pH values, the increased hydrogen ions (H⁺) will protonate the surface functional groups. This results in the positively charged adsorbent surface and enhances the adsorption of anionic pollutants through electrostatic attraction. In contrast, the surface functional groups may deprotonate at higher pH ranges. The adsorption of cationic pollutants is favored in this case due to the negatively charged adsorbent surface. However, in some circumstances, the adsorption process may also be influenced by other mechanisms like ion exchange, Van der Waals interactions, and surface complexation.

Numerous studies have emphasized the significance of initial pH of the solution in the adsorption process. For example, banana peel was used by Akter et al. (2021) as an adsorbent to adsorb dyes from textile effluent. The study found that the highest adsorption performance was achieved at pH 7. This pH enables optimal interactions with dye molecules when the banana peel surface was neutral. At other pH levels, adsorption efficiency declined due to the neutralization of dye molecules of OH⁻ and H⁺ ions. Specifically, the electrostatic attraction between functional groups in the dyes (e.g., Na⁺, Cl⁻, SO₃Na⁺, -COO⁻, -O⁻) and in the adsorbent (e.g., -COOH, -OH, -NH₂, -SO₄) weaken when these groups were neutralized at acidic or alkaline pH levels, leading to reduced adsorption performance.

Similar to this, Aljeboree et al. (2023) utilized sawdust-based adsorbents for the adsorption of Congo red (an anionic dye) and methylene blue (a cationic dye). According to the study, the adsorption performance of CR peaked at acidic pH values (around pH 2). This is due to the positively charged adsorbent surface increases electrostatic attraction with the negatively charged contaminants. As the adsorbent surface deprotonated at higher pH levels, the negatively charged adsorbent and the contaminants were repelled, reducing the adsorption capacity. In contrast, MB dye performed best in the pH range of 6 to 10, most likely as a result of its cationic properties.

Similar findings have been reported in other studies. The maximum performance efficiencies of 67.3% and 88.6% at pH 6 were reported by Sen et al. (2024) for royal palm leaf sheath (RPLS) and ball-milled RPLS (BMRPLS), respectively. Experimental results have shown that the adsorption of CV is strongly pH-dependent. At higher pH ranges, lower adsorption performance is resulting from the presence of OH⁻ ions in the solution which compete with the carbon surface for binding to CV dyes. In short, one crucial factor that greatly affects the adsorption performance of biomass-based adsorbents is the initial

pH of the solution. The effectiveness of contaminants being removed from wastewater can be significantly enhanced by fully understanding the underlying mechanisms and optimizing the pH levels of the treatment process.

2.6.2 Effect of Adsorbent Dosage

Adsorbent dosage, or the amount of adsorbent material used in the adsorption process determines the number of active sites available for dye adsorption. A low adsorbent dosage might lead to rapid saturation of active sites and lead to lower removal effectiveness. At higher dosages, on the other hand, can improve dye adsorption due to the greater availability of active sites up to a limited extent. With the addition of more adsorbents beyond this point does not result in further removal as the adsorption process already reaches equilibrium (W. Zhang et al., 2020). Moreover, the particle aggregation caused by excessive adsorbent dosage might also lower the effective surface area and total adsorption efficiency.

Rhodamine B (RhB) adsorption was investigated by Kapoor et al. (2024) using AC synthesized from coconut shells. The study reported a substantial enhancement in dye removal efficiency when the adsorbent dosage was increased from 1.0 g to 2.0 g. But when the dosage was further increased from 2.0 g to 3.5 g, the efficiency dropped. This suggests excessive adsorbent led to aggregation and decreased the effective surface area. Moreover, Hashem et al. (2024) investigated the adsorption of MB with peanut shell-derived activated carbons. According to the findings, increasing the dosage of the adsorbent decreased adsorption capacity while concurrently improving removal efficiency. The initial enhancement of MB dye removal was attributed to more accessible adsorption sites. Further dosage increment, however, resulted in reduced effective surface area, particle aggregation, and unused active sites, which lowered adsorption capacity.

Another study by Algethami et al. (2024) used watermelon seed waste-based adsorbents for the adsorption of malachite green (MG). The research findings showed that the dye removal efficiency was increased from 40.0% to 94.9% when increasing the adsorbent dosage from 5 mg to 20 mg. When there was a further increment in the adsorbent dosage beyond 20 mg, there was no substantial enhancement observed. In parallel, the adsorption capacity was observed to decrease with increasing dosage. This suggests an inverse proportional relationship between adsorption capacity and adsorbent dosage. To sum up, adsorbent dosage is a critical parameter that affects the adsorption performance of biomass-based adsorbents. It appears that in the reviewed literature, where adsorption capacity tends to decrease as adsorbent dosage increases, while removal efficiency increases. Therefore, optimizing the dosage is essential for achieving maximum performance while avoiding the excessive use of adsorbent materials.

2.6.3 Effect of Contact Time

Contact time indicates how long the adsorbate interacts with the adsorbent, which is a crucial factor in the adsorption process. In general, due to the abundance of active sites on the adsorbent surface, the adsorption rate is rapid at initial. It gradually drops as time progresses until equilibrium, where, at this point, the adsorption-desorption rates are equal. This phenomenon can be explained by the initial rapid mass transfer of pollutants from the solution to the adsorbent surface, followed by a slower infiltration of pollutants into the interior of the adsorbent (Xu et al., 2019).

The solid-liquid ratio (m/V) signifies the quantity of active sites accessible for a specific pollutant concentration, is a crucial factor in adsorption rate studies (Zhang et al., 2016). Besides that, the type of adsorbent and the underlying adsorption process are additional factors that affect the adsorption rate in addition to the m/V ratio. Researchers often employ kinetic models to explain these mechanisms and connect them to the effect

of contact time. The effect of contact time using biomass-based adsorbents for treating dyes has been investigated in a number of research. For instance, Algethami et al. (2024) used a hydrochar-based adsorbent derived from watermelon seed waste to study the adsorption of MG. At initial concentrations of 25 mg/L and 50 mg/L, the study reported that the adsorption performance enhanced quickly within the first 60 minutes, reaching removal efficiencies of 56.2% and 51.6%. The removal efficiency gradually rose to 95.7% and 84.8%, respectively, between 60 and 420 minutes, and subsequently held equilibrium until 510 minutes. The rapid initial adsorption was attributed to the abundance of active sites, while the slow rate at later stages was due to site saturation.

There was another study reporting the removal of MB and CV using graphene oxideactivated carbon (GO-AC) by Abd-Elhamid et al. (2019). From the experimental findings, the color removal equilibrium for MB and CV was determined to be 40 minutes and 60 minutes, respectively. The adsorption rate was initially relatively quick due to the availability of active sites. The rate declined once these sites became saturated with pollutants. Yaqub et al. (2024) studied the adsorption of MB using tea waste and peanut shell-based adsorbents. The results reported that maximum removal was achieved at 35 minutes for tea waste-based adsorbents and 40 minutes for peanut shell-based adsorbents. Over time, the adsorption performance appeared to gradually decline, as a result of desorption. To sum up, contact time is a crucial factor that affects the adsorption performance of biomass-based adsorbents. Dye adsorption generally exhibits a similar pattern, as demonstrated by the reviewed literature, with rapid uptake at the beginning, followed by a slower rate until equilibrium is established. No further adsorption occurs after the equilibrium contact time was established. The optimum contact period, however, varies according to the adsorption mechanism, m/V ratio, and dye type. Hence, it is essential to determine the optimum contact time for ensuring efficient dye removal while minimizing operational time and costs.

2.6.4 Effect of Initial Concentration of the Adsorbate

The initial concentration of the adsorbate in the solution is an important factor that affects the adsorption process. Essentially, it determines the force that drives mass transfer between the aqueous and solid phases. At higher adsorbate concentrations, a higher adsorption rate was obtained attributed by higher driving forces, up to a certain point. Beyond this limit, there will be a decrement in adsorption capacity as the adsorption sites became saturated. In addition, the adsorption capacity is influenced by the affinity between the adsorbate molecules and the adsorbent. At higher adsorbate concentrations, the availability of active sites on the adsorbent surface becomes a limiting factor, causing the adsorption process to reach equilibrium more quickly. The concentration of the adsorbate is closely related to the adsorption isotherm, which is commonly used to understand the underlying mechanisms.

Previous studies have investigated the effect of initial adsorbate concentration on the adsorption process. For instance, Holliday et al. (2022) studied MB adsorption using pea waste-derived adsorbent. The research indicated that higher initial concentrations of MB (up to 200 mg/L) increased the adsorption capacity but decreased the removal efficiency. This is because higher dye concentrations increase the likelihood of interactions between the adsorbent and adsorbate, filling previously unoccupied adsorption sites. However, the limited number of available active sites results in a decline in removal efficiency. A similar study by Khalil et al. (2024) explores the adsorption of AO7 dye on magnetically modified orange peel-based activated carbon. The study also showed that higher dye concentrations provided a greater driving force for adsorption, which led to higher adsorption capacity. At the same time, the limited number of available adsorption sites reduced removal efficiency.

Another study by Omwoyo and Otieno (2024) investigated the MB adsorption using coconut husk cellulose. The experimental findings demonstrated a similar pattern, with removal effectiveness declining when increasing dye concentration from 30 mg/L to 100 mg/L. In conclusion, a higher initial dye concentration will lead to a stronger driving force between dye pollutants and adsorbents. Consequently, the adsorption capacity tends to increase with increasing initial dye concentration until the active sites are fully occupied with pollutants.

All in all, the adsorption process using biomass-based adsorbents is greatly influenced by several critical parameters. These parameters include the initial pH of the solution, adsorbent dosage, contact time, and initial adsorbate concentration. It is essential to optimize the aforementioned parameters for maximizing the efficiency of dye removal from the aqueous solution. In future work, the focus should be on understanding the complex interactions between these factors. Furthermore, models for predicting adsorption behavior in diverse adsorption scenarios could be developed and monitored using advanced technologies, such as artificial intelligence. The adsorption performance and sustainability of biomass-based adsorbents in wastewater treatment applications can be effectively improved and regulated through these initiatives and efforts.

2.7 Application of Biomass-Based Adsorbent in Actual Wastewater Treatment

The performance and effectiveness of an adsorbent can further be investigated through the ability of that adsorbent to treat actual wastewater which often contain numerous recalcitrant pollutants. Till date, most of the published research focus on the adsorbent performance for synthetic wastewater treatment than actual wastewater from industries. Figure 2.4 illustrates an adsorption process flow in real wastewater treatment, where processes with dotted lines are optional (Bogush et al., 2007) and Table 2.5 summarizes

different types of biomass-based adsorbents with their respective performance in treating actual wastewater.

Recently many efforts emphasized on the treatment of wastewater such as palm oil mill effluent (POME), especially in palm industry-based countries such as Indonesia and Malaysia. Wafti et al. (2017) applied the palm biomass-based activated carbon (activation temperature: 800°C) for treating POME. The adsorbent developed from empty fruit bunches (EFB) possessed a BET surface area of 937.00 m²/g and was able to remove 88.0%, 98.0% and 96.0% of BOD3, COD and suspended solid (SS) from ternary treated POME, respectively. On the other hand, maximum removals of 96.0% for color, 100.0% for total suspended solids (TSS) and COD, 97.4% for BOD and 76.7% for tannin and lignin were reported by another similar research by Mohammed and Chong (2014) using banana peel activated carbon as a biomass-based adsorbent for the treatment of POME. It was determined that banana peel activated carbon had a surface area (BET) of 875.29 m²/g. The nearly identical surface areas and removal efficiencies of the two adsorbents indicate that biomass has the potential to be a promising precursor for developing into effective adsorbents for the treatment of actual wastewater.

Besides that, Chand et al. (2015) investigated an adsorbent developed from apple pomace modified using xanthate (XMAP). The performance of XMAP adsorbent was verified by treating real wastewater from the paint, battery and pharmaceutical industries. Heavy metal ions were completely removed from wastewater by XMAP adsorbent, demonstrating the potential of XMAP as an adsorbent. Abdelfattah et al. (2016) reported the development of an adsorbent from peanut husk biomass for the removal of heavy metal ions from metal finishing processing industrial wastewater. The results showed a significant extent of heavy metal ions removal, including 100.0% of Pb (II) and 95.0% of Fe (III) ions.

Habibi et al. (2017) applied a lanthanum metal modified *Tamarix hispida* waste wood adsorbent to remove fluoride ions from glass factory wastewater. As shown in the SEM images, the developed adsorbent possesses a large porous structure. The experimental results demonstrate that more than 90.0% of the initial pollutants were effectively removed by the developed adsorbent.

Daud et al. (2020) utilized a composite adsorbent made from green mussel shell powder and coconut shell granular activated carbon to remove COD and ammoniacal nitrogen from landfill leachate. The study achieved removal efficiencies of 63.0% for ammoniacal nitrogen and 83.0% for COD under optimal conditions, which included pH 7, a contact time of 120 min, and stirring at 200 rpm, using a coconut shell granular activated carbon to green mussel shell ratio of 2.5:1.5. A main benefits of incorporating green mussel shell waste is that it can partially replace activated carbon, which reduces waste and lowers the cost of producing adsorbents.

Based on study reported by R. Foroutan et al. (2019), an adsorbent was developed from *Callinectes sapidus* biomass for Cd, Ni and Pb heavy metals removal. According to the experimental results, the monolayer adsorption capacities of Cd, Ni, and Pb were 29.2 mg/g, 29.2 mg/g and 31.4 mg/g, respectively. The adsorbent has then been applied to treat hospital wastewater at optimum conditions of 25°C using 3 g/L adsorbent under natural pH. Significant removal of various antibiotics (43.0-75.0%) and heavy metals (100.0%) were observed using the developed adsorbent.

On the other hand, according to a study by Piccin et al. (2016), chromium-tanned leather waste was used to remove color from the effluent of the leather dyeing industry. Adsorption capacity and dye removal of 148.2 mg/g and 58.0% respectively were reported in this study. Based on the study by Abdulsalam et al. (2020), sawdust of *Parkia biglobosa* treated with sulphuric acid was applied to the treatment of real textile industry

wastewater. After the acid modification, the porosity was improved, as investigated in the SEM images. The operational condition was optimized at 60°C and 15.0 hours using 1.0 g of adsorbent, which resulted in a color removal efficiency of 71.1%. There is another study by Ahmad and Hameed (2010) using acid (40 wt% H₃PO₄) modified bamboo waste adsorbent for the treatment of cotton textile mill wastewater. 93.1% of initial color of 450-650 Pt-Co and 74.0% of COD were removed using optimized bamboo waste-based adsorbent developed under activation temperature and time of 556°C and 2.3 hours with H₃PO₄ impregnation ratio of 5.24. Moreover, the efficiency and performance of sugarcane bagasse, corncobs, peanut husk, cotton sticks, and sunflower biomass as adsorbents were studied through the treatment of five different types of real textile wastewater. The reported study showed that corncobs were able to remove up to 79.0% of the dyes, which is considered a significant percentage (Bhatti, 2015). Bener et al. (2020) investigated a hybrid approach for treating real textile wastewater that included adsorption, electrocoagulation, and photo Fenton-like oxidation, with the adsorbent made from walnut shell and corncob biomass, at where maximum monolayer adsorption (63.7 mg/g) was obtained from the adsorption process itself. By this means, biomass-based adsorbents are proven to be effective at removing diverse types of actual wastewater.

The review of actual wastewater applications highlighted that biomass has high potential and is capable of being converted into adsorbents for treating actual wastewater. Adsorbents developed from biomass often possess superior properties, such as high surface areas and porous structures. These properties make them suitable to be used as precursors for the development of adsorbents. On the other hand, as synthetic wastewater is prepared according to experimental needs, the types and amounts of pollutants are known in advance. However, in the case of actual wastewater, the pollutants presented are often more complex and difficult to identify. The purpose of this section is therefore to compare and discuss the performance of biomass-based adsorbents in removing

synthetic and actual wastewater to confirm their efficiency. Table 2.6 and Figure 2.5 depict the comparison of the performance of using biomass-based adsorbents in treating synthetic and actual wastewater. By comparing the performance of xanthate modified apple pomace adsorbent in removing synthetic heavy metal ions wastewater and real wastewater from pharmaceuticals, paint and battery industries, reported by Chand et al. (2015), it can be clearly seen that, a significant adsorption capacity were achieved in the removal synthetic wastewater containing Pb (II), Cd (II) and Ni (II) ions. It was found that the maximum monolayer adsorption capacities were 178.6 mg/g for Pb (II), 112.0 mg/g for Cd (II) and 51.0 mg/g for Ni (II) ions, respectively, which are higher than actual wastewater by $\approx 9.4-42.9$, $\approx 17.1-359.9$ and $\approx 29.9-840.3$ times. On the other hand, R. Foroutan et al. (2019) used Callinectes sapidus biomass as an adsorbent for treating synthetic and real hospital wastewater reported a similar result. The adsorption capacities for the removal of Cd (II), Ni (II) and Pb (II) ions from synthetic wastewater were ≈974.3 (synthetic: 29.2 mg/g; real: 0.03 mg/g), ≈ 875.4 (synthetic: 29.2 mg/g; real: 0.03 mg/g) and ≈294.7 (synthetic: 31.4 mg/g; real: 0.11 mg/g) times higher than real hospital wastewater.

Thus, it can be concluded that higher adsorption capacity can be achieved in treating synthetic wastewater compared to actual wastewater. This can be related to the known types and amounts of pollutants present in synthetic wastewater. Furthermore, the performance of an adsorbent in treating a specific pollutant can be determined by preparing a wastewater sample containing only a single pollutant. In contrast, chemicals presented in actual wastewater are often more complex with the mixing of unknown pollutants. The mixture of various pollutants might have reactions within them and change their chemical and physical structures, which makes them more complicated to be

adsorbed. It is therefore necessary to conduct more research to study the adsorption mechanism of actual wastewater and overcome its limitations.

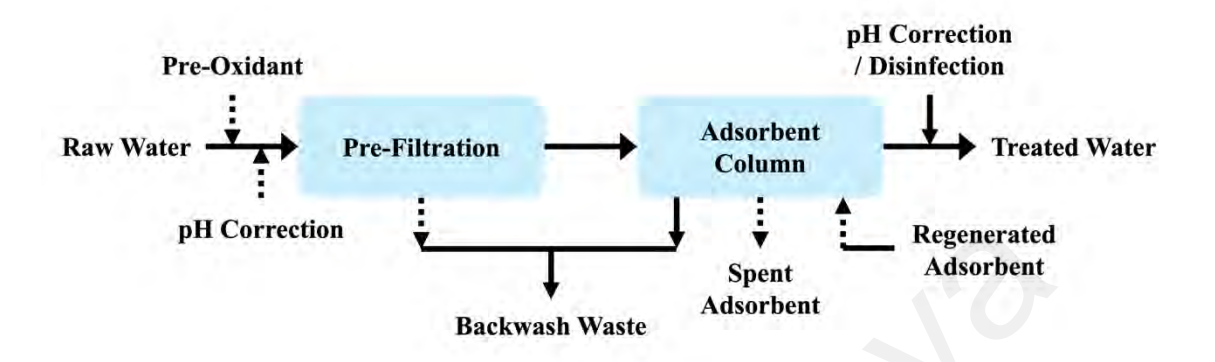


Figure 2.4: Adsorption Process in Actual Wastewater Treatment Plant

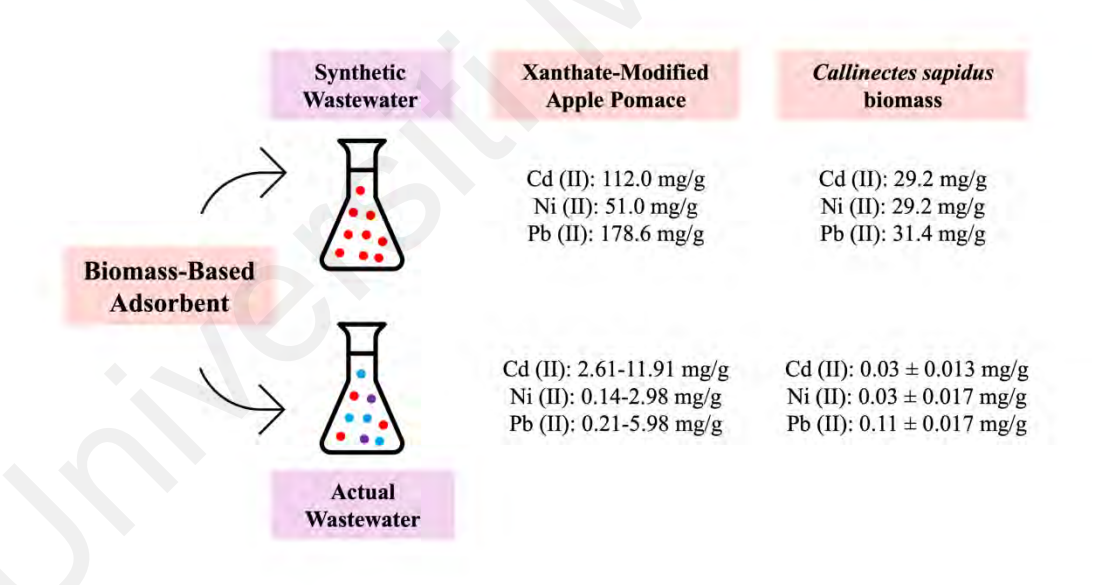


Figure 2.5: Performance Comparison in Treating Synthetic and Actual Wastewater

Table 2.5: Actual Wastewater Treatment using Biomass-Based Adsorbents

| Types of Biomass | Types of Modification | Types of Wastewater | Properties of Adsorbent | Performance | References |
|----------------------------|----------------------------------|----------------------------|--|-----------------------------|--------------------|
| Microcrystalline cellulose | HTC (urea; 240°C 4 h) | River water | SEM: Plenty of micropores | > 99.4% | H. Zhang et al. |
| | & KOH (1:3) & | Lake water | BET: 1872.30 m ² /g; 1.04 | | (2022) |
| | Calcination (800°C 2 | | m^3/g | | |
| | h) | | | | |
| Corncob biomass & | Chemical activation | Pre-treated real textile | SEM: Heterogenous | 40.0-45.0% of TOC | Bener et al. |
| walnut shell | (ZnCl ₂) & pyrolysis | wastewater | sponge-like pore structure | 8.0-10.0% of COD | (2020) |
| | (750°C) | | (corncob); cavities and gaps | 5.0-7.0% of turbidity | |
| | | | of different sizes (walnut | 35.0-40.0% of color | |
| | | * X | shell) | 20.0-25.0% of SS | |
| | | | BET: 1433.00 m ² /g; 1.09 | | |
| | | | cm ³ /g (corncob); 1364.00 | | |
| | | | m^2/g ; 1.05 cm ³ /g (walnut) | | |
| Green mussel (Perna | - | Stabilized landfill | - | 63.0% of NH ₃ -N | Daud et al. |
| viridis) shell & coconut | | leachate | | 83.0% of COD | (2020) |
| shell GAC | | | | | |
| Sawdust of Parkia | Sulphuric acid | Textile wastewater | SEM: Porous structure with | 71.1% of color | Abdulsalam et al. |
| biglobosa | treatment | | holes and openings | | (2020) |
| Callinectes sapidus | - | Hospital wastewater | SEM: Ragged, irregular and | 43.0-75.0% of | R. Foroutan et al. |
| biomass | | | porous surface with various | antibiotics | (2019) |
| | | | pores | 100.0% of heavy | |
| | | | | metals | |

Table 2.5: Continued

| Types of Biomass | Types of Modification | Types of Wastewater | Properties of Adsorbent | Performance | References |
|-------------------------|------------------------------|----------------------------|-------------------------------------|----------------------------|--------------------|
| Empty fruit bunch | Pyrolysis & physical | POME | SEM: Carbonous with | 88.0% of BOD ₃ | Wafti et al. |
| | activation (800°C) | | micropores | 98.0% of COD | (2017) |
| | | | BET: 937.00 m ² /g; 0.28 | 96.0% of SS | |
| | | | cm ³ /g | .) | |
| Tamarix hispida wasted | Lanthanum metal | Glass factory | SEM: Porous structure | > 90.0% of fluoride | Habibi et al. |
| wood | modified | wastewater | BET: 112.42 m ² /g; 0.11 | content | (2017) |
| | | | cm ³ /g | | |
| Chromium tanned leather | - | Effluent of leather | SEM: Structural fibre of | 58.0% | Piccin et al. |
| waste | | dyeing industry | collagen | 148.2 mg/g | (2016) |
| Peanut husk | - | Metal finishing for | SEM: Homogenous pore | 100.0% of Pb ²⁺ | Abdelfattah et al. |
| | | processing industrial | structures | 95.3% of Fe ³⁺ | (2016) |
| | | wastewater | | 56.4% of Cr ³⁺ | |
| | | | | 50.9% of CN ⁻ | |
| | | | | 45.4% of Cu ²⁺ | |
| | | | | 41.3% of Cd ²⁺ | |
| | | | | 38.4% of Mn ²⁺ | |
| | | | | 37.9% of Zn ²⁺ | |
| | | | | 30.0% of Co ²⁺ | |
| | | | | 23.6% of Ni ²⁺ | |
| Apple pomace | Xanthate group | Wastewater from | SEM: Amorphous and | 100.0% of Cd (II), Ni | Chand et al. |
| | introduction | pharmaceuticals, paint | uneven | (II) and Pb (II) ions | (2015) |
| | | and battery industries | | | |

Table 2.5: Continued

| Types of Biomass | Types of Modification | Types of Wastewater | Properties of Adsorbent | Performance | References |
|------------------|------------------------------|----------------------------|-------------------------------------|---------------------|---------------|
| Banana peel | Carbonization (500°C) | POME | SEM: Porous structure | 96.0% of color | Mohammed and |
| | & KOH activation & | | BET: 875.29 m ² /g | 100.0% of TSS | Chong (2014) |
| | activation (700°C) | | | 100.0% of COD | |
| | | | | 97.4% of BOD | |
| | | | | 76.7% of tannin and | |
| | | | | lignin | |
| Bamboo waste | Chemical activation | Cotton textile mill | SEM: Well-developed pores | 93.1% of color | Ahmad and |
| | (phosphoric acid) | wastewater | BET: 998.24 m ² /g; 0.69 | 74.0% of COD | Hameed (2010) |
| | | | cm ³ /g | | |
| Corncobs biomass | - | Textile wastewater | - | 79.0% of dyes | Bhatti (2015) |

Table 2.6: Performance of Biomass-Based Adsorbents in Treating Synthetic and Actual Wastewater

| Types of Riemess | Synthetic Wastewater | | Actual Wastewater | | References |
|---------------------|----------------------|---------------------|-------------------|---|----------------|
| Types of Biomass | Type Performance | | Type | Performance | References |
| Xanthate modified | Cd (II) | Cd (II): 112.0 mg/g | Wastewater from | 100.0% removal of Cd (II), Ni (II) and Pb (II) ions | Chand et al. |
| apple pomace | Ni (II) | Ni (II): 51.0 mg/g | pharmaceuticals, | | (2015) |
| | Pb (II) | Pb (II): 178.6 mg/g | paint and battery | Adsorption capacity (reanalyzed based on available | |
| | | | industries | data): | |
| | | | | Cd (II): 2.61-11.91 mg/g | |
| | | | | Ni (II): 0.14-2.98 mg/g | |
| | | | * | Pb (II): 0.21-5.98 mg/g | |
| Callinectes sapidus | Cd (II) | Cd (II): 29.2 mg/g | Hospital | 100.0% removal of Cd (II), Ni (II) and Pb (II) ions | R. Foroutan et |
| biomass | Ni (II) | Ni (II): 29.2 mg/g | wastewater | | al. (2019) |
| | Pb (II) | Pb (II): 31.4 mg/g | | Adsorption capacity (reanalyzed based on available | |
| | | | | data): | |
| | | | | $Cd (II): 0.03\pm0.013 \text{ mg/g}$ | |
| | | | | Ni (II): 0.03±0.017 mg/g | |
| | | | | Pb (II): 0.11±0.017 mg/g | |

2.8 Adsorption Mechanism using Biomass-Based Adsorbents

Adsorption-oriented processes that remove pollutants from aqueous solutions are highly dependent on their adsorption mechanism. There are several ways in which adsorption can occur, including physisorption, hydrophobic interactions, chemisorption, electrostatic interactions, Van der Waals forces, surface complexation, π - π interactions, and hydrogen bonding. In Table 2.7, various types of biomass-based adsorbents are compared in terms of their adsorption mechanisms in removing dye pollutants. As shown in Table 2.7, dye mainly adsorbs onto adsorbents via electrostatic attraction. A strong correlation exists between the surface functional groups, the pH_{pzc} of the adsorbent, and the pH of the initial solution in this mechanism. The functional groups that present on the adsorbent surface will facilitate the formation of bonds between adsorbent and adsorbate. In addition to that, when the pH < pH_{pzc}, the removal of anionic dye is favored, and the removal of cationic dye is favored when initial solution pH > pH_{pzc} (Bellaj et al., 2024; Eshghabadi & Javanbakht, 2024). While, according to the reviewed literature, most of the adsorption mechanism for dye in aqueous solution is dominated by electrostatic attraction, other mechanisms such as π - π interaction and Van der Waals force interaction were also observed. Figure 2.6 depicts the plausible adsorption interactions of a most commonly used dye, MB dye with biomass-based adsorbents.

Table 2.7: Adsorption Mechanisms of Biomass-Based Adsorbents

| Adsorbents | Pollutants | Governing Mechanisms | References |
|----------------------|------------|---|-------------------|
| DR biomass | ARS | Electrostatic attraction / hydrogen | Aravindhan et |
| | | bonding / π - π interaction | al. (2024) |
| CGLC | RhB & CR | π -π interaction/Van der Waals force | Kim et al. |
| | | | (2023) |
| MgAl/LDH- | RBV5R | Electrostatic attraction / hydrogen | Izwan |
| RSSB | | bonding / chemical complexation / | Anthonysamy et |
| | | physical adsorption / anionic | al. (2023) |
| | | exchange | |
| SWAC | MB | Electrostatic interaction / π - π | Jiang et al. |
| | | interaction / cation- π interaction | (2023) |
| BA DT | MB | Electrostatic interaction | Y. Zhang et al. |
| biofilm | MG | | (2022) |
| nAg-TC | RhB | Electrostatic attraction / hydrogen | Shaikh et al. |
| | CR | bonding / surface complexation | (2022) |
| АС-КОН | MB | AC-KOH: | Zheng et al. |
| AC-KMnO ₄ | | π - π interaction / pore diffusion | (2021) |
| | | AC-KMnO ₄ : | |
| | | Electrostatic attraction / hydrogen | |
| | | bonding / cation exchange / donor- | |
| | | receptor-effect | |
| DFPAC | MB | Electrostatic attraction / hydrogen | Jawad et al. |
| | | bonding / π - π interaction | (2021) |
| IRKC | MB | Electrostatic attraction / hydrogen | Jawad and |
| | | bonding / π - π interaction | Abdulhameed |
| | | | (2020) |
| PEI-CW | RB5 | Electrostatic attraction / hydrogen | Wong et al. |
| | CR | bonding | (2020) |
| CRHC | DGB | Electrostatic attraction / hydrogen | Jiang and Hu |
| | AB24 | bonding / competition of OH ⁻ ions | (2019) |
| | CR | | |
| CWAC | CR | Electrostatic attraction / hydrogen | Lafi et al. |
| | | bonding | (2019) |
| MSAB | APZ | Electrostatic attraction / chemical | El-Bindary et al. |
| | | reaction | (2019) |
| GCHSB | MB | Electrostatic attraction / π-π | Çağlar et al. |
| | | interaction | (2018) |
| CC | MG5 | Electrostatic attraction / hydrogen | Tran et al. |
| GS | | bonding / π - π interaction | (2017) |
| OP | | _ | |
| СРВ | LG | Electrostatic attraction | Zhao et al. |
| | | | (2017) |

Table 2.7: Continued

| Adsorbents | Pollutants | Governing Mechanisms | References |
|------------|------------|-------------------------------------|-------------------|
| MC | MB & MG | Chemisorption | Karim et al. |
| | BR46 | Electrostatic attraction / | (2017) |
| | | physisorption | |
| SD | TZ | Electrostatic attraction / Van der | Banerjee and |
| | | Waals force | Chattopadhyaya |
| | | | (2017) |
| SMFL | AB113 | Electrostatic attraction / Van der | Jain and Gogate |
| | | Waals force | (2017) |
| MLP | MB | Electrostatic attraction | Uddin et al. |
| | | | (2017) |
| MCC | MB | Electrostatic attraction | Tan et al. (2016) |
| EC | CR | Electrostatic attraction | Kaur et al. |
| GNC | | | (2013) |
| MPS | MB | Electrostatic attraction / chemical | Derakhshan et |
| | | reaction | al. (2013) |

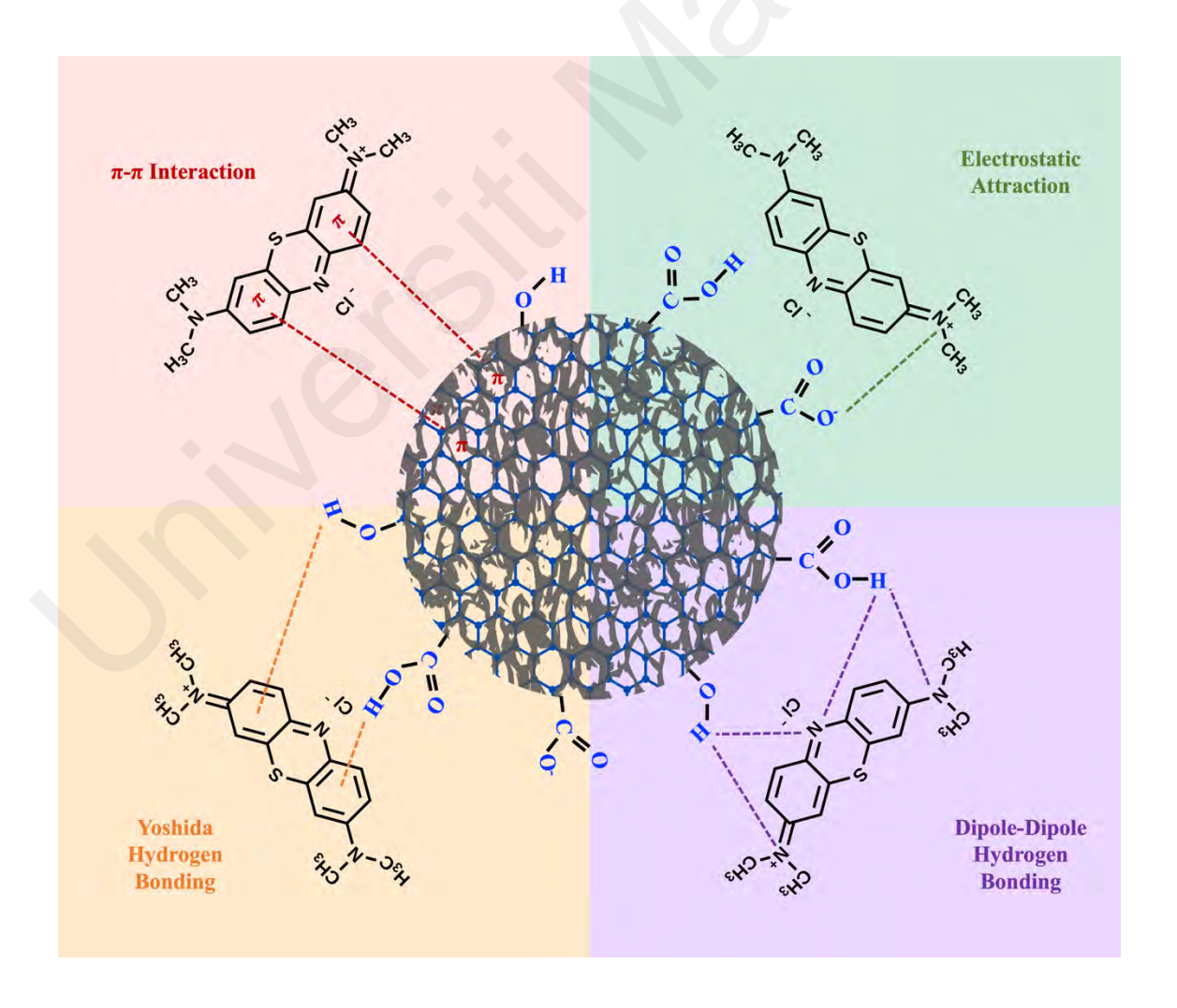


Figure 2.6: Adsorption Mechanisms of MB Dye onto Biomass-Based Adsorbent

2.9 Stability and Reusability of the Biomass-Based Adsorbent

The stability of an adsorbent is crucial because the leaching of impregnated metals can lead to secondary pollution and limit its practical application. Typically, the stability of an adsorbent is tested through leaching experiments, where minimal iron leaching (<5 mg/L) indicates strong stability of the iron oxide coating on the adsorbent (Cheng et al., 2018). Similarly, the reusability of an adsorbent is a key criterion for assessing its ability to regenerate and be reused over multiple cycles while maintaining removal efficiency and adsorption capacity. Enhancing the reusability of an adsorbent improves its cost-effectiveness and practicality in real-world applications (Sherlala et al., 2019). Magnetic properties are particularly advantageous as they facilitate easy separation after the adsorption process.

From the reviewed literature, strong acids and bases are commonly used as traditional desorption agents for regeneration studies. A recent study by Fatma et al. (2018) explored the use of 70% v/v methanol and 70% v/v ethanol as greener desorption agents, given that strong acids or bases can potentially cause secondary pollution and damage the adsorbent structure, including its active sites (Abdi et al., 2019). The presence of hydroxyl groups in both methanol and ethanol make them suitable candidates as desorbing agents. The study found that ethanol showed higher desorption efficiency, likely due to the higher partition coefficient (K_{ow}) of the hydroxyl group in ethanol (0.48) compared to methanol (0.15). A higher K_{ow} value indicates greater hydrophobicity, which enhances the bond formation between the desorption agent and dye pollutants. Additionally, ethanol has a greater molecular weight (C_2H_5OH , MW = 46.07 g/mol) compared to methanol (CH_3OH , MW = 32.04 g/mol) makes it less polar, increasing its effectiveness for non-polar dye desorption.

Various studies have examined the regeneration of biomass-based adsorbents. For instance, Omwoyo and Otieno (2024) used a 0.5 M HCl solution to desorb MB from coconut husk-based adsorbents. The experimental results showed good reusability with approximately 88.0% after three cycles. Similarly, Shanmugam et al. (2021) investigated the reusability of *Trichoderma asperellum* BPL MBT1 biomass-based adsorbents using various desorbents, which include water, HCl, and NaOH. Among those tested, 0.1 N HCl was the most effective desorbent. The significant desorptions of 69.0% for CV and 62.0% for MG suggest that ion exchange might be the predominant mechanism. In contrast, water resulted in less than 5% desorption, signifying that physisorption was not the predominant mechanism.

Waghmare et al. (2023) also reported on the regeneration of papaya peel-based adsorbent using 0.1 M NaOH and HCl solutions. After three cycles, the adsorbent maintaining 54.4% and 58.9% MB removal efficiency. Likewise, You et al. (2022) examined the reusability of rice husk-based adsorbent using 0.1 M HCl solution. After five cycles, the removal efficiency for MB and methyl violet (MV) was 43.3% and 90.6%, respectively, in a single system, and 71.7% and 68.5% in a binary system. This was attributed to the H⁺ ions in the HCl solution, which replaced adsorbed dye molecules via ion exchange and improved the porosity of the adsorbent, increasing the adsorption sites.

From the reviewed literature, biomass-based adsorbents generally exhibit good reusability, which is an indication of stability. The performance of biomass-based adsorbents is often maintained after several desorption-adsorption cycles. However, due to the possibility of secondary pollution occurring during the regeneration process, there should be a focus on using green solvents as desorption agents. Besides that, the regeneration of adsorbents should balance cost and environmental impact. Spent

adsorbents could potentially be repurposed for energy production through combustion for fuel (Waghmare et al., 2023) or for brick formation (Adazabra et al., 2023).

2.10 Application of Quantum Chemical Analysis in Adsorption Processes

Adsorption plays a crucial role in a number of fields, including environmental remediation, catalysis, and material science. It is important to design more effective adsorbents which can be achieved through an understanding of molecular-level adsorption mechanics. For example, quantum chemical studies, a well-known computational method, can be employed to investigate the reactions and processes within a system (Tu & Laaksonen, 2010). It uses computational chemistry methods to solve the Schrödinger equation and describes the behavior of electrons in molecules. The reactivity of adsorbates and adsorbents, electronic structure, and binding energies can be determined through quantum chemical studies.

Quantum chemical studies primarily employ Density Functional Theory (DFT) to calculate the reactivity and behavior of chemical species. DFT methods are commonly employed due to their precision and comparability to experimental findings. Specifically, M06 functionals are widely used among the several DFT functionals due to their exceptional accuracy (Walker et al., 2013).

Thermodynamic descriptors, directly related to the feasibility of a process, include Gibbs free energy, entropy, enthalpy, and heat capacity. A reaction is spontaneous and thermodynamically feasible when ΔG° and ΔH° are negative. The general equations for calculating Gibbs free energy and enthalpy are shown in Eq. 2.1 and Eq. 2.2.

$$\Delta G^{\circ} (298 K) = \sum_{product} \Delta_f G^{\circ}_{product} - \sum_{reactant} \Delta_f G^{\circ}_{reactant}$$
 (2.1)

$$\Delta H^{\circ} (298 K) = \sum_{product} \Delta_f H^{\circ}_{product} - \sum_{reactant} \Delta_f H^{\circ}_{reactant}$$
 (2.2)

The dipole moment, highest occupied molecular orbital (HOMO) energy (E_{HOMO}), and lowest unoccupied molecular orbital (LUMO) energy (E_{LUMO}) are the main descriptors in quantum chemical studies. Those aforementioned descriptors can be used to derive additional descriptors like the HOMO-LUMO energy gap ($E_{HOMO-LUMO}$), chemical potential (μ), electrophilicity index (ω), global hardness (η), electronegativity (χ), electron affinity (EA), global softness (S), and ionization potential (IP) (Asghar, 2016; M. M. Bello, 2019).

The E_{HOMO-LUMO} gives an indication of the reactivity of interacting molecules. The tendency of a species to accept and donate electrons is denoted as electrophilicity index and chemical potential, respectively. Electronegativity indicates the tendency of a species to attract a shared pair of electrons. Global softness and hardness represent the reactivity and stability of a species (Ghashghaee, Azizi, & Ghambarian, 2020; Souza, Carvalho, Vieira, Silva, & Brasil, 2018; Yang & Parr, 1985). The quantum descriptors can be computed using Eq. 2.3 to Eq. 2.10.

$$IP = -E_{HOMO} \tag{2.3}$$

$$EA = -E_{LUMO} (2.4)$$

$$E_{HOMO-LUMO} = E_{HOMO} - E_{LUMO} = IP - EA \tag{2.5}$$

$$\mu = \left(\frac{E_{HOMO} + E_{LUMO}}{2}\right) = -\left(\frac{IP + EA}{2}\right) \tag{2.6}$$

$$\omega = \left[\frac{\left(\frac{E_{HOMO} + E_{LUMO}}{2} \right)^2}{E_{LUMO} - E_{HOMO}} \right] = \left[\frac{\left(\frac{IP + EA}{2} \right)^2}{IP + EA} \right]$$
 (2.7)

$$\chi = -\left(\frac{E_{HOMO} + E_{LUMO}}{2}\right) = \left(\frac{IP + EA}{2}\right) \tag{2.8}$$

$$\eta = \left(\frac{E_{LUMO} - E_{HOMO}}{2}\right) = \left(\frac{IP - EA}{2}\right) \tag{2.9}$$

$$S = \left(\frac{1}{\eta}\right) = \left(\frac{2}{E_{LUMO} - E_{HOMO}}\right) = \left(\frac{2}{IP - EA}\right)$$
 (2.10)

Adsorption mechanisms between adsorbents and adsorbates are currently the focus of quantum chemical studies. For example, Malik, Dahiya, & lata (2017), used coconut husk to remove heavy metals. Based on quantum analysis, coconut husk was determined to be an electron-rich donation site. Besides that, Gao, Li, Yang, Li, & Yang (2019) also employed quantum chemical studies to investigate the elimination of ofloxacin using lignin-based adsorbents. Based on the reported findings, it demonstrates that quantum chemical methods can predict adsorption mechanisms based on electrostatic potential changes in molecules.

In addition, the adsorption of different pollutants using various adsorbents has been studied recently using quantum chemical techniques. As an example, Zhao et al. (2024) investigated carbon dioxide (CO₂) adsorption on N-doped activated carbon using DFT. The analysis showed that N-doping enhanced CO₂ selectivity over oxygen (O₂) by 3.7 times when conducted at B3LYP and M06-2x levels. Bhardwaj et al. (2024) modeled the structure of GO adsorbents before and after thiol group functionalization (GO-MBT) at the B3LYP level. Based on the experimental findings, functionalized adsorbents showed enhanced adsorption performance, which is in good agreement with quantum simulations, where a reduced HOMO-LUMO energy gap was observed. It was supported by enhanced polarizability and chemical reactivity after functionalization. A study by Bouabbaci et al. (2024) studied the adsorption of MG dye on a pine bark-based adsorbent. The adsorption mechanism of MG dye was found to involve the -OH and -COOH functional groups, as revealed by quantum analysis data.

In short, quantum chemical analysis provides a deep understanding of adsorption mechanisms at the molecular level, at the same time, offers valuable insights into the design and optimization of adsorbents. In quantum chemical analysis, the density of states, geometric structure, binding energy, and charge distribution are among the critical parameters. The implementation of quantum chemical analysis has facilitated a more comprehensive understanding of a wide range of adsorption processes, including gas adsorption, heavy metal ion adsorption, and organic dye adsorption using a variety of adsorbents.

2.11 Application of Machine Learning in Adsorption Processes

The integration of machine learning into the adsorption process using biomass-based adsorbents has become a trend recently. Table 2.8 summarizes the benefits, drawbacks, and training methods of four widely used algorithms. These algorithms include decision trees, random forests, gradient boosting, and artificial neural networks. Compared to other commonly used algorithms, Gradient Boosting Models (GBMs) have emerged as highly effective due to their ability to handle complex, nonlinear data and deliver precise predictions. Besides that, it can also offer significant advantages in understanding the importance of by allowing the linkage and relating various inputs, such as adsorbent properties and operational conditions with desirable outputs, such as removal efficiency and adsorption capacity.

Table 2.8: Advantages and Limitations of Various Machine Learning Algorithms

| Algorithms | Training style | Advantages | Limitations | References |
|---------------------------|---------------------------------|--|---|--|
| Decision tree | Hierarchical Single-threaded | Easy to interpret and visualizeHandles categorical and numerical data | Difficult to modify Performs poorly on complex datasets High cost for large trees | (Gulati et al., 2016) |
| Random forest | Parallel | Handles large datasets well Resistant to overfitting Measures feature importance Provides transparency in the decision making process | Less interpretable due to bagging Computationally expensive for large datasets | (Khan et al., 2024; Salman et al., 2024) |
| Gradient boosting | Sequential | High accuracy for complex, nonlinear data Ability to handle large datasets Effective feature importance ranking Handles categorical data without encoded them as numerical values | Requires hyperparameter tuning Time consuming for large datasets | (Khan et al., 2024; Malek et al., 2022) |
| Artificial neural network | Iterative Parallel Black-box | Suitable for very large and complex datasets Captures nonlinear relationships effectively | Risk of overfittingHigh computationDifficult to interpret the "black-box" model | (Maier et al., 2023; Mas & Flores, 2008) |

GBMs have been successfully implemented in various adsorption studies to evaluate and predict the efficiency of adsorbents. It was also used to ascertain the relative significance of various features. A study by Kobayashi and Yoshida (2021) utilized physicochemical characteristics and molecular descriptors to develop a quantitative structure-property relationship (QSPR) model that accurately predicted the soil adsorption coefficient (K_{oc}) using LightGBM, a variant of GBM. It was shown that GBMs can be used to predict critical parameters such as K_{oc} in environmental chemistry.

In addition, Bentéjac et al. (2021) reported a comparative analysis of GBMs for evaluating the performance of various GBM variants. Their findings indicate that CatBoost achieved the highest generalization accuracy, with XGBoost and LightGBM following closely behind. These models exhibit outstanding capabilities to manage large and complicated datasets, which are essential for adsorption studies. The ability of GBMs to determine the significance of features is also advantageous for adsorption research. For example, Mazaheri et al. (2017) optimized the removal of MB and cadmium ions using natural walnut carbon implementing boosted regression trees (BRT). The sensitivity analysis demonstrated that the most critical factors were adsorbent mass and pH.

Gradient boosting models not only identify critical features but also optimize adsorption processes by accurately predicting adsorption capacities. A study by Ali et al. (2021) on asphaltene adsorption using MgO nanoparticles demonstrated that GBMs provided highly accurate predictions compared to other machine learning (ML) algorithms. Moreover, H. Yang et al. (2021) applied GBMs to predict soil adsorption capacities for heavy metals and mapped their global distribution. The Shapley additive explanation method was employed to rank feature importance. It is illustrated that GBMs are effective in environmental risk assessment and management. The use of GBMs in the adsorption process has proven to be highly effective in analyzing and predicting

adsorption performance. Moreover, it can also identify the relative importances of various operational parameters of the adsorption process and adsorbent characteristics. In short, through the application of machine learning, the optimization of adsorption processes is facilitated which provides critical insights that guide experimental and industrial applications.

2.12 Summary

Dye wastewater poses a serious risk to human health and the environment, which requires innovative and efficient treatment methods. Due to numerous advantages such as low cost, high efficiency, and ease of use, adsorption has become the preferred method for treating dye effluents. This study presents a novel approach by synthesizing a ternary PKSAC-based ternary composite that is impregnated with GO and iron oxide. This ternary composite has addressed a number of the drawbacks of conventional adsorbents.

The novelty of this study lies in its multidisciplinary approach to advanced adsorption technology. The ternary composite successfully combines the high surface area and eco-friendliness of PKSAC, the functionalities of GO and the magnetic properties of iron oxide. This synergistic integration enhances the adsorption performance, at the same time, facilitates efficient post-treatment separation and ensures reusability.

The initial pH of the solution, adsorbent dosage, contact time, and adsorbate concentration are among the important operational parameters that affect the adsorption of dye wastewater. AB113 dye has been chosen as the model dye for this study due to its widespread use in real-world applications and a relatively lack of research on it compared to other dyes.

Machine learning and quantum chemistry techniques are also used in this work. The predominating adsorption mechanisms are analyzed by quantum chemistry studies which

offer molecular-level insights into the interactions between adsorbents and adsorbates. Machine learning further supported it via the quantification of various operational parameters through feature importance analysis. Furthermore, the entire lifecycle of the adsorbent is also considered. The proposed application of spent adsorbents in brick formation highlights its alignment with circular economy principles, transforming waste into valuable products and promoting environmental sustainability.

With the development of a novel ternary composite with enhanced adsorption performance and actual practicability, this study contributes to a more eco-friendly and sustainable technology for treating dye wastewater. The predominant adsorption mechanisms can be identified by combining machine learning and quantum chemistry studies with experimental findings. In summary, this research opens opportunities in the circular economy, transforming waste into useful materials and promoting environmental sustainability.

CHAPTER 3: MATERIALS AND METHODOLOGY

3.1 Introduction

This chapter details the materials and methods used in the research. The synthesis of the PKSAC-GO-Fe composite, including improved Hummers' and co-precipitation methods, is described. Various characterization techniques were employed to study the significant physicochemical characteristics of the synthesized composite and confirm its successful development. The effects of operational parameters, such as initial solution pH, adsorbent dosage, and contact time, were studied and optimized for treating synthetic wastewater. The performance of the ternary composite was further validated at various initial dye concentrations, continuous process, using various industrial dyes, and compared with commercial activated carbons. Quantum chemical analysis was conducted to investigate the role of various functional groups in the adsorption process. In parallel, machine learning was utilized to perform feature importance analysis. After optimizing the ratio of PKSAC/GO and the amount of iron oxide loading, the performance of the composite was tested using actual industrial printing wastewater. The physicochemical characteristics and adsorption performance of the PKSAC-GO-Fe composite before and after synthesis process optimization are compared and discussed. Additionally, the economic and environmental considerations of using the PKSAC-GO-Fe composite were evaluated. The overall methodology of this research is illustrated in Figure 3.1.

3.2 Chemicals and Materials

The chemicals, materials, and wastewater samples utilized in this study are summarized in Table 3.1, including their respective properties and applications. All chemicals were of analytical grade and used without further purification, and the samples were prepared using deionized water. The physicochemical characteristics of AB113 are summarized in Table 3.2, while Table 3.3 depicts those of the actual industrial printing wastewater.

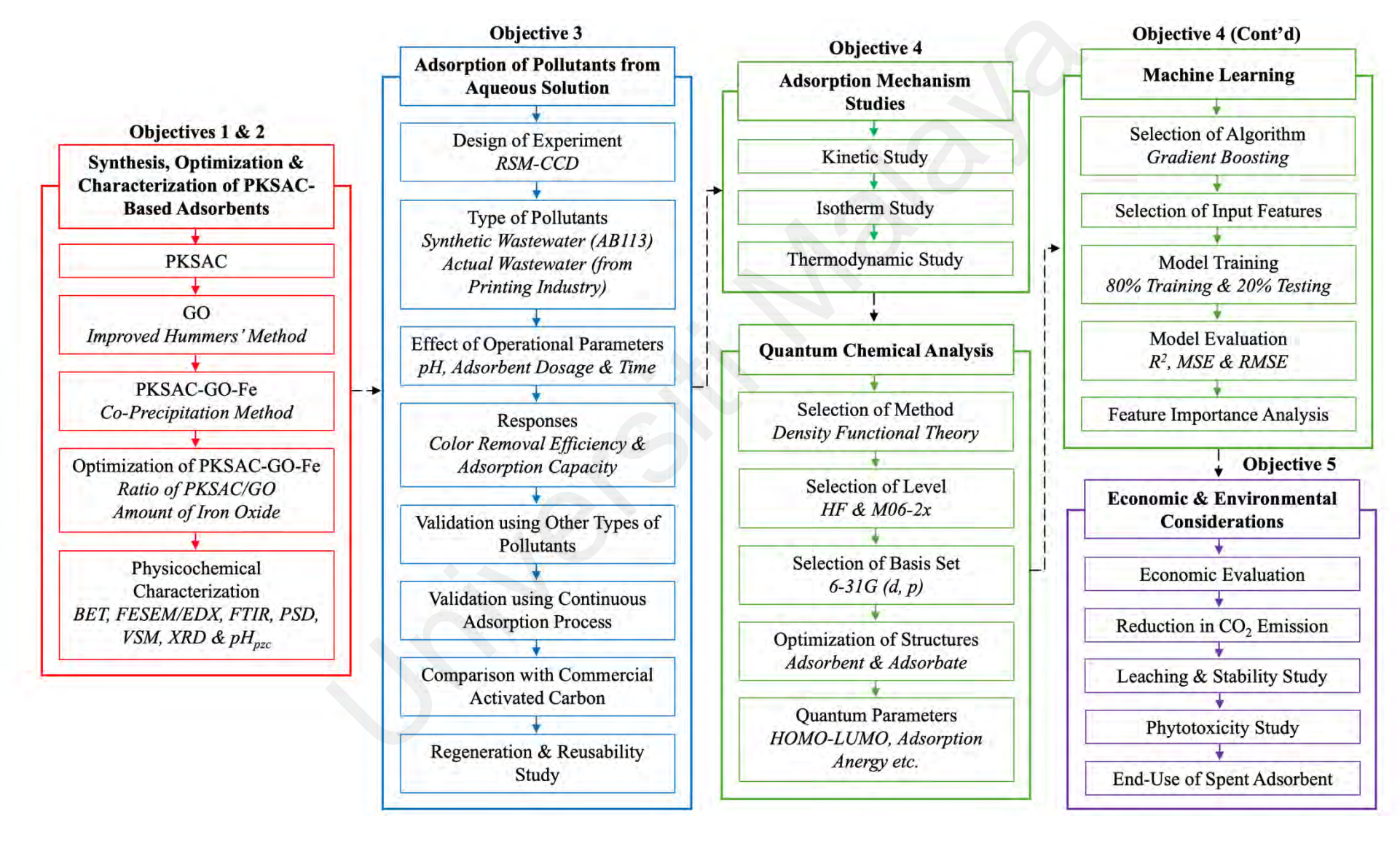


Figure 3.1: Overall Methodology

Table 3.1: Chemicals and Materials Used in This Study

| Chemicals / Materials | Molecular Formula | CAS Number | Properties | Applications |
|------------------------------------|--------------------------------------|------------|-------------------------|-----------------------|
| Palm kernel shell activated carbon | - | - | Particle size: < 250 μm | Composite development |
| | | | Form: powder | |
| | | | Activation: physical | |
| Graphite powder | - | 7782-42-5 | MW: 12.01 g/mol | Composite development |
| | | | Particle size: < 20 μm | |
| | | | Form: powder | |
| Red brick powder | - | - | Form: powder | Brick development |
| Commercial activated carbon 1 | - | - | Biomass-based AC | Comparison |
| | | | Form: granular | |
| Commercial activated carbon 2 | - | - | Therapeutic grade AC | Comparison |
| | | | Form: powder | |
| Commercial activated carbon 3 | С | 7440-44-0 | MW: 12.01 g/mol | Comparison |
| | | | Chemically pure | |
| | | | Form: powder | |
| Red bean seed | - | - | - | Phytotoxicity study |
| Iron (II) chloride tetrahydrate | FeCl ₂ ·4H ₂ O | 13478-10-9 | MW: 198.81 g/mol | Composite development |
| | | | Purity: ≥ 98.0% | |
| Iron (III) chloride hexahydrate | FeCl ₃ ·6H ₂ O | 10025-77-1 | MW: 270.33 g/mol | Composite development |
| | | | Purity: ≥ 98.0% | |
| Acetic acid | CH ₃ COOH | 64-19-7 | MW: 65.05 g/mol | Composite development |
| | | | Purity: > 99.5% | _ |
| Hydrochloric acid | HC1 | 7647-01-0 | MW: 36.46 g/mol | Composite development |
| | | | Purity: 35-38% | pH adjustment |

Table 3.1: Continued

| Chemicals / Materials | Molecular Formula | CAS Number | Properties | Applications |
|------------------------|---|------------|--------------------------|-------------------------|
| Sulphuric acid | H ₂ SO ₄ | 7664-93-9 | MW: 98.08 g/mol | Composite development |
| | | | Purity: 95-98% | pH adjustment |
| Ammonium hydroxide | NH ₄ OH | 1336-21-6 | MW: 35.04 g/mol | Composite development |
| | | | Purity: 24-26% | |
| Sodium hydroxide | NaOH | 1310-73-2 | MW: 40.00 g/mol | pH adjustment |
| | | | Form: pellets | |
| | | | Purity: ≥ 99.0% | |
| Hydrogen peroxide | H ₂ O ₂ | 7722-84-1 | MW: 34.01 g/mol | Composite development |
| | | | Concentration: 30% | |
| | | | Purity: 30-31% | |
| Potassium permanganate | KMnO ₄ | 7722-64-7 | MW: 158.04 g/mol | Composite development |
| | | | Purity: ≥ 99.0% | |
| Potassium chloride | KC1 | 7440-09-7 | MW: 74.56 g/mol | pH _{pzc} study |
| | | | Purity: ≥ 99.0% | |
| Ethanol | C ₂ H ₅ OH | 64-17-5 | MW: 46.07 g/mol | Composite development |
| | | | Purity: > 99.5% | Desorption study |
| Acid blue 113 | C ₃₂ H ₂₁ N ₅ Na ₂ O ₆ S | 3351-05-1 | MW: 681.66 g/mol | Adsorption study |
| | | | Dye content: 50% | |
| Methylene blue | C ₁₆ H ₁₈ ClN ₃ S | 61-73-4 | MW: 319.86 g/mol | Validation |
| | | | Dye content: $\geq 85\%$ | |
| Rhodamine B | C ₂₈ H ₃₁ ClN ₂ O ₃ | 81-88-9 | MW: 479.02 g/mol | Validation |
| | | | Dye content: $\geq 95\%$ | |
| Methyl orange | C ₁₄ H ₁₄ N ₃ NaO ₃ S | 547-58-0 | MW: 327.33 g/mol | Validation |
| | | | Dye content: 85% | |

Table 3.1: Continued

| Chemicals / Materials | Molecular Formula | CAS Number | Properties | Applications |
|--------------------------------|---|------------|--------------------------|------------------|
| Remazol brilliant blue R | C ₂₂ H ₁₆ N ₂ Na ₂ O ₁₁ S ₃ | 2580-78-1 | MW: 626.54 g/mol | Validation |
| | | | Dye content: 40-65% | |
| Acid yellow 17 | $C_{16}H_{10}Cl_2N_4Na_2O_7S_2$ | 6359-98-4 | MW: 551.29 g/mol | Validation |
| | | | Dye content: 60% | |
| Reactive blue 4 | $C_{23}H_{14}Cl_2N_6O_8S_2$ | 13324-20-4 | MW: 637.43 g/mol | Validation |
| | | | Dye content: 35% | |
| Reactive red 120 | C44H24Cl2N14O20S6Na6 | 61951-82-4 | MW: 1469.98 g/mol | Validation |
| | | | Dye content: $\geq 50\%$ | |
| Reactive black 5 | C ₂₆ H ₂₁ N ₅ Na ₄ O ₁₉ S ₆ | 17095-24-8 | MW: 991.82 g/mol | Validation |
| | | | Dye content: 55% | |
| Malachite green | C ₅₂ H ₅₄ N ₄ O ₁₂ | 2437-29-8 | MW: 927.02 g/mol | Validation |
| | | | Dye content: $\geq 90\%$ | |
| Amaranth | $C_{20}H_{11}N_2Na_3O_{10}S_3$ | 915-67-3 | MW: 604.47 g/mol | Validation |
| | | | Dye content: 85-95% | |
| Printing wastewater | - | - | COD: 597 mg/L | Adsorption study |
| | | | Natural pH: 7.2 | |
| | | | Type: raw wastewater | |
| Plastic fabrication wastewater | - | - | COD: 7380 mg/L | Validation |
| | | | Natural pH: 7.4 | |
| | | | Type: raw wastewater | |
| Landfill leachate | - | - | COD: 424 mg/L | Validation |
| | | | Natural pH: 9.1 | |
| | | | Type: raw wastewater | |

Table 3.1: Continued

| Chemicals / Materials | Molecular Formula | CAS Number | Properties | Applications |
|-----------------------|-------------------|------------|----------------------------|--------------------------------|
| Batik wastewater | - | - | COD: 1576 mg/L | Validation |
| | | | Natural pH: 11.9 | |
| | | | Type: raw wastewater | |
| Textile wastewater | - | - | COD: 199 mg/L | Validation |
| | | | Natural pH: 3.7 | |
| | | | Type: raw wastewater | |
| POME | - | - | COD: 579 mg/L | Validation |
| | | | Natural pH: 8.7 | |
| | | | Type: biologically treated | |
| | | | wastewater | |
| COD cell | - | - | Range: 25-1500 mg/L | Pollutant degradation analysis |
| | | | Method: photometric | |
| Filter paper | - | | Type: ashless 150 | Filtration |
| | 4 | | Diameter: 11 cm | |
| Syringe filter | - | - | Type: Nylon (non-sterile) | Filtration |
| | | | Diameter: 25 mm | |
| | | | Pore size: 0.45 μm | |
| Parafilm | - | - | - | Prevent samples contamination |

CAS: Chemical Abstracts Service; COD: Chemical Oxygen Demand; MW: Molecular Weight

Table 3.2: Structure and Physicochemical Characteristics of AB113 Dye

| Type of Synthetic Wastewater | Acid Blue 113 |
|--------------------------------------|--|
| Color index number (CI) | 26360 |
| CAS number | 3351-05-1 |
| Abbreviation | AB113 |
| Synonyms | CI 26360; Coomassie ZRN; Acid Cyanine 5R; |
| | Navy Blue 5R; Erionyl Navy R; C.I. Acid blue |
| | 113; Tracidcyanine 5R; Conacid Blue AAC; |
| | Covalene Navy 2R |
| Chemical structure | |
| | |
| Formula | $C_{32}H_{23}N_5Na_2O_6S_2$ |
| Maximum wavelength (λ_{max}) | 566 nm |
| Molecular weight | 681.65 g/mol |
| Pictogram(s) | ! ¥2 |

Table 3.3: Physicochemical Characteristics of Printing Wastewater

| Type of Actual Industrial Wastewater | Printing Wastewater |
|---|-----------------------------------|
| pH in nature | 7.2 |
| Total dissolved solids | 22 mg/L |
| Electrical conductivity | 44 μS/cm |
| Salt concentration | 25 mg/L |
| Maximum wavelength (λ_{max}) | 291 nm |
| Chemical oxygen demand | 597 mg/L |
| Visible color | Dark blue |
| Provider | A packaging and printing company |
| | located in Kulim, Kedah, Malaysia |

3.3 Synthesis of Ternary Composite

A ternary composite of GO and iron oxide impregnated PKSAC (PKSAC-GO-Fe) was synthesized in two steps. GO was synthesized using an enhanced Hummers' method while PKSAC-GO-Fe was developed following the co-precipitation method reported by Taher et al. (2018) and Sherlala et al. (2019).

3.3.1 Synthesis of Graphene Oxide

Firstly, graphite powder (3 g) was added to concentrated H₂SO₄ (70 mL) and stirred vigorously (10 min; 1000 rpm) using a magnetic stirrer with hot plates (model: WiseStir[®] SMHS-6). Then, 9.0 g of KMnO₄ were added slowly for an hour. The steps above were carried out in an ice bath to control the mixture temperature. After that, the mixture was stirred for half an hour at 40°C. Then, 150 mL of deionized water was added, and the mixture was heated to 95°C and stirred for another 15 min. After 15 min, 500 mL of deionized water was added and 15 mL of H₂O₂ was added dropwise to stop the reaction. The resultant solids (GO) were filtered and washed using a 10% HCl solution. The synthesized GO was dried at 70°C for 48 hours and kept in an airtight container.

3.3.2 Synthesis of Graphene Oxide and Iron Oxide Impregnated PKSAC

To synthesize PKSAC-GO-Fe, GO (1.0 g) was dispersed into a mixture containing CH₃COOH (2%) and HCl (5 mL) and sonicated for 30 min (model: Hielscher Ultrasound Technology UP400S). Then, 1 g of PKSAC was added and underwent half an hour of sonication. Then FeCl₃·6H₂O and FeCl₂·4H₂O were added in a molar ratio of 2:1 and the mixture was sonicated again for another 30 min. The mixture was stirred overnight (about 12 hours) and then on the next day, 0.1 M of NH₄OH solution was added dropwise at 25°C to raise the suspension to pH 8.0 and again sonicated for 30 min. After 12 hours, the resultant PKSAC-GO-Fe solids were collected using an external magnetic field. The solids were washed with deionized water and ethanol, and then dried for 24 hours at 60°C.

A simple graphical flowchart of overall steps in synthesizing PKSAC-GO-Fe composite is shown in Figure 3.2.

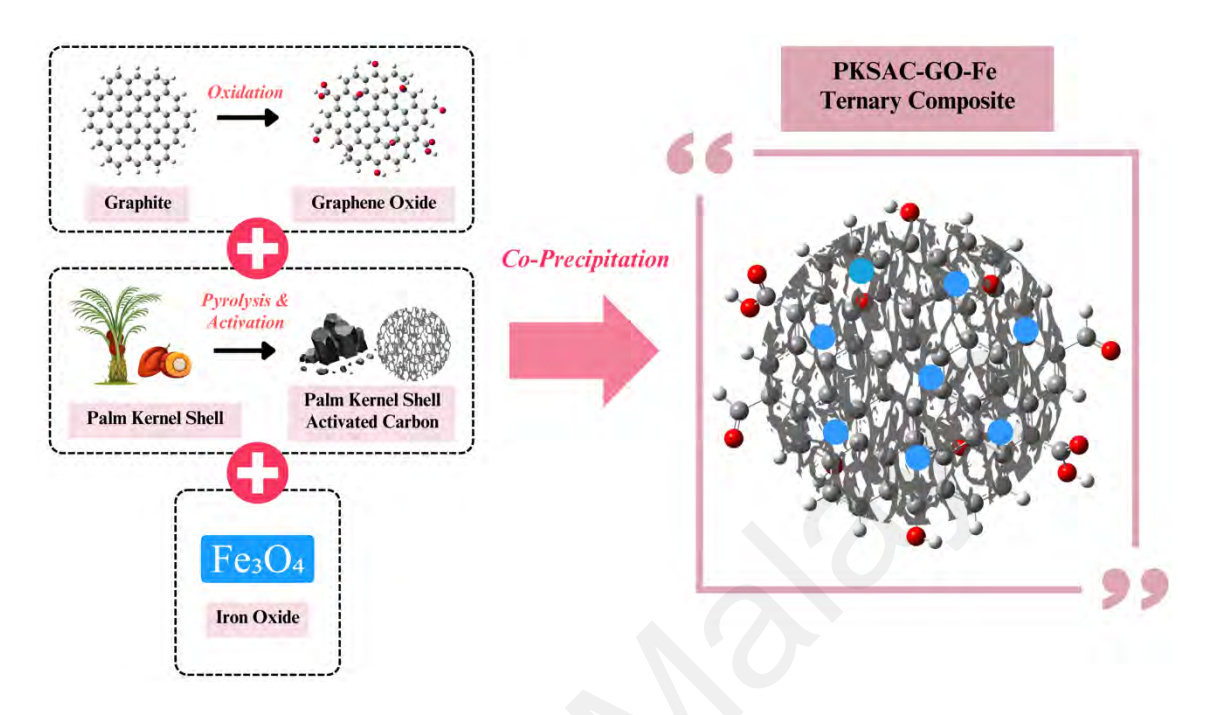


Figure 3.2: PKSAC-GO-Fe Composite Synthesis Process

3.4 Physicochemical Characterization of Adsorbents

3.4.1 Brunauer-Emmett-Teller

N₂ adsorption/desorption isotherms of the adsorbents were measured at 77 K using a Micrometrics ASAP 2020 system (software: MicroActive 2.00; model: TRISTAR II 3030 Kr V4.01) following the Brunauer-Emmett-Teller (BET) and Barrett-Joyner-Halenda (BJH) methods. The textural properties of the adsorbents including surface areas and pore structures, were obtained from BET and BJH analyses.

3.4.2 Field Emission Scanning Electron Microscopy with Energy Dispersive X-Ray

The morphology and chemical composition of the adsorbents were studied using field emission scanning electron microscopy with energy dispersive X-ray (FESEM/EDX) analysis. Magnified images were produced by FESEM through sample scanning with an electron beam while the elemental composition of the adsorbents was determined by EDX

via detecting X-rays emitted during electron beam bombardment. In this study, FESEM/EDX analysis was conducted using an FEI Quanta 200 FESEM system (software: Microscope XT), which operates in a low vacuum environment.

3.4.3 Fourier Transformation Infrared

The surface functional groups of the adsorbents were studied using a PerkinElmer Spectrometer (model: Frontier Lake Shore 7400 Series) with infrared light ranging from 550 to 4000 cm⁻¹. FTIR analysis was performed through three consecutive scans.

3.4.4 Vibrating-Sample Magnetometer

The magnetic properties of a sample are routinely characterized using a vibrating-sample magnetometer (VSM) as a function of temperature, magnetic field, and time. VSM operates based on Faraday's Law of Induction, where the electric field is measured by varying the magnetic field. In this study, a VSM system (model: Lake Shore 7400 Series, version 4.6.0) with a maximum field, field increment, and ramp rate of 8000 Oe, 200 Oe, and 20 Oe/second, respectively, was used to examine the magnetic properties of the materials.

3.4.5 X-Ray Powder Diffraction

X-ray powder diffraction (XRD) analysis is based on constructive interference between monochromatic X-rays and a crystalline sample. The X-rays diffract through the sample and are detected as the beam and detector rotate through a range of angles. In this study, XRD analysis was conducted to investigate the presence of crystalline phases in the composite using a D8 Advance X-Ray Diffractometer-Bruker AXS (software: DIFFRAC plus -EVA ICDD Powder Diffraction File Database) with 40 kV and 40 mA CuK $_{\alpha}$ radiation at ambient temperature.

3.4.6 Point of Zero Charge

The pH_{pzc} is the pH at which the adsorbent surface is globally neutral, meaning there is no net charge at that pH. In this study, the pH_{pzc} of the adsorbents was identified using the method reported by Bach et al. (2018). Adsorbent (1 g/L) was added to a 0.1 M KCl solution with different initial pH values (ranging from pH 2 to 13). The mixture was shaken for 10 min and left for over 24 hours to establish equilibrium. The initial and final solution pH values were used to determine pH_{pzc}.

3.4.7 Particle Size Distribution

A particle size analyzer (model: Malvern Mastersizer 2000 version 5.60, UK) was used to study the particle size distribution (PSD) of the adsorbents. Particle size distribution analysis provides various information on the particle sizes range with their relative abundances in adsorbent samples.

3.5 Adsorption Performance Evaluation using PKSAC-Based Adsorbents for Wastewater Treatment

Response surface methodology-central composite design (RSM-CCD) was employed to design the experiments, study, and optimize the interactive effect of three independent operational parameters: initial pH of the solution (pH 3-11), adsorbent dosage (1-5 g/L) and contact time (2-6 h). In this study, Design-Expert® Software (Version 13; Stat-Ease, Inc., USA) was used to implement RSM-CCD design, with the three adsorption parameters as independent variables, as depicts in Table 3.4.

The RSM-CCD approach allows for the efficient performance of a large number of experiments, up to five factors, to study the interactions between operational parameters (Gadekar & Ahammed, 2019). The essential empirical runs required were determined using Eq. 3.1.

$$n_{exp} = l^k + 2k + c_p \tag{3.1}$$

Where n_{exp} is the number of experiments; l is the number of levels; k is the number of factors, and c_p is the number of replicates of center points. In this study, 20 sets of experiments were conducted for each type of adsorbent.

The CCD design model can be expressed as shown in Eq. 3.2.

$$Y = \beta_o + \sum_{i=1}^n \beta_i X_i + \sum_{i=1}^n \beta_{ii} X_i^2 + \sum_{i=1}^{n-1} \sum_{j=i+1}^n \beta_{ij} X_i X_j + \varepsilon$$
 (3.2)

Where Y is the response; β_o is the constant coefficient; β_i is the linear coefficient; β_{ii} is the quadratic coefficient; β_{ij} is the interaction coefficient, and ε is the random error. X_i and X_j are the coded values of the independent variables.

Two responses, namely color removal efficiency and adsorption capacity, were considered in this study. The ranges of operational parameters were determined based on preliminary one-factor-at-a-time experiments and literature studies.

Table 3.4: Ranges of Independent Variables with Their Coded Levels

| Indonandant | | | | Levels | | |
|--------------------------|------|-----|----------|------------|--------------|------|
| Independent Variables | Unit | -α | Low (-1) | Medium (0) | High (+1) | +α |
| рН | - | 1.7 | 3 | 7 | 11 | 12.3 |
| Adsorbent dosage | g/L | 0.4 | 2 | 6 | 10 | 5.6 |
| Contact time | h | 1.4 | 2 | 4 | 6 | 6.6 |

3.6 Adsorption Study

The performance of adsorbents in removing AB113 dye was evaluated through a batch adsorption process. A 20 mL solution of 100 mg/L AB113 dye was placed in an Erlenmeyer flask. The solution pH was adjusted accordingly with the addition of 0.1 M acidic (H_2SO_4) and alkaline (NaOH) solutions. A predetermined amount of adsorbent was then added, and the sample was covered with cling film to avoid contamination. The sample was shaken at 200 rpm using a rotary orbital shaker (model: Lab Companion SI-300) for a predetermined time. Afterward, the color changes were measured using a UV spectrophotometer (model: Spectroquant® Pharo 300) at maximum wavelength (λ_{max}) of 566 nm, after filtering the solution with a syringe filter (Nylon; non-sterile; 0.45 μ m; 25 mm). The efficiency of color removal and adsorption capacity were calculated using Eq. 3.3 to Eq. 3.5.

Color removal efficiency (%) =
$$\frac{Absorbance_{initial} - Absorbance_{final}}{Absorbance_{initial}} \times 100$$
 (3.3)

Adsorption capcity_t
$$(mg/g) = \frac{(c_o - c_t)v}{w}$$
 (3.4)

Adsorption capcity_e
$$(mg/g) = \frac{(C_o - C_e)V}{W}$$
 (3.5)

Where C_o , C_t , and C_e are the AB113 dye concentrations at initial stage, at time t, and at equilibrium (mg/L), respectively; V is the sample solution volume (L), and W is the adsorbent dosage (g).

3.7 Kinetics Study

The adsorption kinetics study was conducted to understand the adsorption dynamics of pollutants. Three widely used models, namely pseudo-first-order (P-F-O), pseudo-second-order (P-S-O), and intra-particle diffusion (I-P-D) models, were employed to determine the controlling mechanism of the adsorption process. The kinetics studies were

conducted under the optimum conditions. The final dye concentration over time was measured, and the data obtained were fitted to different kinetics models.

3.8 Isotherms Study

Adsorption isotherm models are used to estimate the maximum monolayer adsorption capacity of an adsorbent (Wang & Guo, 2020; Zhou et al., 2022). They are significant when designing an adsorption system and offer valuable insights into the adsorption mechanism. In this study, three isotherm models were considered: Langmuir, Freundlich, and Temkin.

3.9 Thermodynamics Study

A thermodynamic study was conducted to assess the effect of temperature on the adsorption process. The nature of the adsorption process was proposed based on thermodynamic parameters, including changes in enthalpy (ΔS°), Gibbs free energy (ΔG°), and entropy (ΔH°). This study was conducted over a temperature range of 25°C to 65°C.

3.10 Reusability Study

In the reusability study, five adsorption-desorption cycles were conducted. The spent adsorbent was regenerated using a 70% v/v ethanol solution as a green desorption agent (Fatma et al., 2018). In order to maximize recovery, the procedure started with a magnetic bar followed by centrifugation process (model: HERMLE Z206A) at 6000 rpm for five minutes. After the adsorbent was collected, it was agitated with ethanol and afterwards rinsed with deionized water. The ethanol-treated adsorbent was dried overnight at 60°C before being reused in the next cycle. Color removal efficiency and adsorption capacity were recorded for each cycle. Despite a 5-10% adsorbent loss per cycle, the adsorbent dosage for wastewater treatment was maintained at the optimal level for consistency.

3.11 Leaching Study

The iron leaching test was conducted to access the potential release of iron species from iron oxide-containing adsorbents, including PKSAC-Fe, PKSAC-GO-Fe, and optimized PKSAC-GO-Fe. The procedure was carried out in compliance with established standards BS EN 12457-2 (Zandi et al., 2007). The iron oxide-containing adsorbents (1 g/L) were immersed in ultrapure water at ambient temperature for 24 hours with intermittent agitation facilitating uniform interactions between the adsorbent and the solution. After that, the collected leachate was filtered through a syringe filter (0.45 µm) to remove any particulates matter or solids. The concentration of iron species in the leachate was quantified using inductively coupled plasma mass spectrometry (ICP-MS) (model: ICP Optima 7000 DV, Perkin Elmer). A blank solution of ultrapure water was used as a control to assess possible background contamination.

3.12 Model Validation using Different Types of Industrial Dyes

The capability of PKSAC-GO-Fe composite in removing different types of dye was validated using ten different dyes including MB, RhB, methyl orange (MO), remazol brilliant blue R (RBBR), acid yellow 17 (AY17), reactive blue 4 (RB4), reactive red 120 (RR120), reactive black 5 (RB5), MG, and amaranth. The aforementioned dyes were selected due to their widely used in many different industries and are therefore indicative of typical pollutants present in industrial effluent.

3.13 Application in the Continuous Adsorption Process

To explore the practical application of PKSAC-GO-Fe in industrial wastewater treatment, both continuous and batch adsorption studies were compared to evaluate its suitability for different processes. The performance of batch and continuous adsorption processes, specifically in terms of chemical oxygen demand (COD) removal efficiency, color removal efficiency, and adsorption capacity, was studied. The continuous adsorption

study followed the method outlined by Mahamadi et al. (2019). The experiments were conducted using a glass cylinder with an internal diameter of 12 mm and a length of 250 mm, which served as an adsorption column. The PKSAC-GO-Fe composite (0.5 g) was packed into the adsorption column. A consistent flow rate of 1.5 mL/min was maintained using a peristaltic pump to simulate continuous flow. Tests were performed with an initial AB113 concentration of 500 mg/L at a pH of 7.5. Samples of the treated solutions were collected at the exit point and analyzed using a UV spectrophotometer, as illustrated in Figure 3.3.

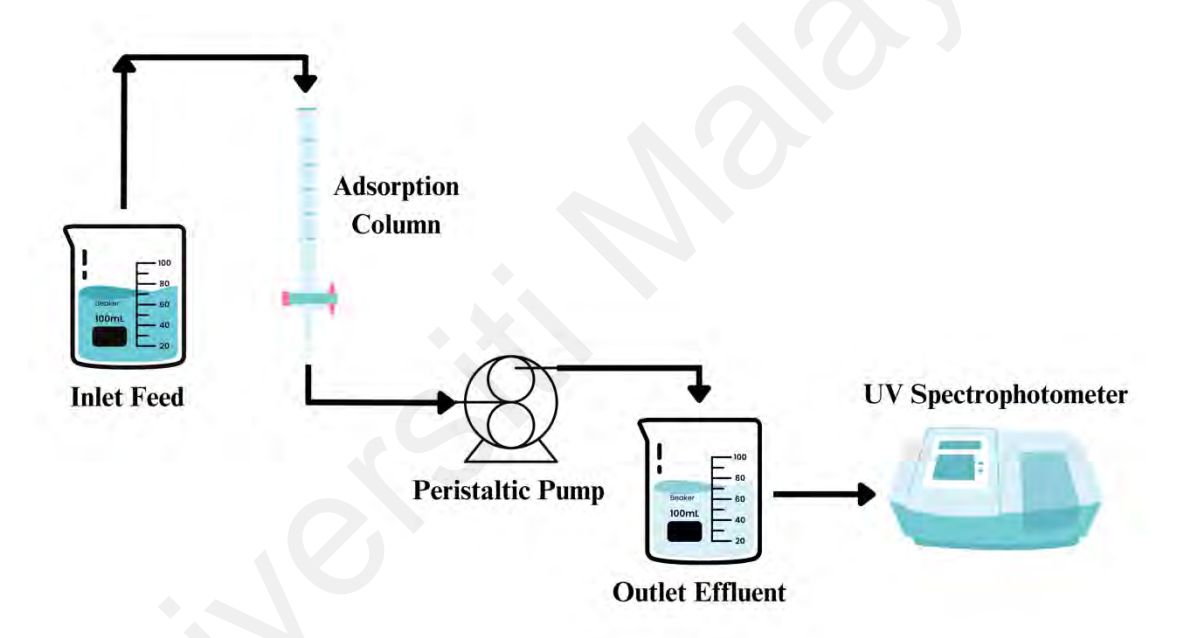


Figure 3.3: Continuous Adsorption Process using Fixed Bed

3.14 Quantum Chemical Study

A quantum chemical study was conducted using the Gaussian 09W software package (Gaussian, Inc., USA), with initial geometries of the molecules developed using the GaussView 05 visualization program (Gaussian, Inc., USA). Energy calculations and geometry optimization of the dye molecule and adsorbent composite were performed using the HF and M06-2x levels with the 6-31G (d, p) basis set. For molecules containing

Fe, HF, and M06-2x methods in GEN mode (LANL2DZ for Fe atoms and 6-31G (d, p) for other atoms) were employed.

It is proven in the previous studies that the reactivity of a molecule depends on its functional group rather than its size (Supong et al., 2019). Therefore, in this study, an adsorbent structure with 4 fused benzene rings was used, considering a pristine adsorbent (CH) and various surface functional groups presented on PKSAC-GO-Fe composite, including OH, COH, COOH, COC, and Fe₃O₄. The adsorption energy (E_{ads}) of the AB113 dye and various functionalized adsorbents was calculated using Eq. 3.6. The counterpoise (CP) method was used to estimate the basis set superposition error (BSSE) (Wazzan et al., 2019).

Vazzan et al., 2019).
$$E_{ads} = E_{adsorbent+dye} - (E_{adsorbent} + E_{dye})$$
(3.6)

Where $E_{adsorbent+dye}$ is the total energy of adsorbent and dye system; $E_{adsorbent}$ is the total energy of adsorbent, and E_{dye} is the total energy of dye. An E_{ads} of greater than -30 kJ/mol (less negative) indicates a physisorption process, while an E_{ads} lower than -50 kJ/mol (more negative) indicates a chemisorption process. Stronger adsorption is depicted by a more negative E_{ads} value.

3.15 Machine Learning

3.15.1 Selection of Input Features

There are three main categories of input parameters for the adsorption process. (1) Operational parameters of the adsorption processes include initial pH of the solution, adsorbent dosage, contact time, dye concentration, and temperature. (2) The chemical properties of PKSAC-based adsorbents like pH_{pzc} and elemental composition, specifically the relative composition of carbon (C), oxygen (O), and iron (Fe). (3) The physical properties of PKSAC-based adsorbents, i.e., BET surface area, pore volume, pore

diameter, and Sauter mean diameter. Color removal efficiency and adsorption capacity were the two responses evaluated.

3.15.2 Model Training and Evaluation

The dataset was preprocessed and then split into two subsets: 80% for training and 20% for testing (Hafsa et al., 2020). The coefficient of determination (R²), mean square error (MSE), and root mean square error (RMSE) were used to evaluate the performance of the regression model. An ideal model would have low MSE and RMSE values, as well as an R² value close to 1. This indicates high accuracy and minimal prediction errors. The evaluation equations are shown in Eq. 3.7 to Eq. 3.9.

$$R^{2} = 1 - \frac{\sum_{i=1}^{N} (Y_{i}^{exp} - Y_{i}^{pred})^{2}}{\sum_{i=1}^{N} (Y_{i}^{exp} - Y_{ave}^{pred})^{2}}$$
(3.7)

$$MSE = \frac{1}{N} \sum_{i=1}^{N} \left(Y_i^{exp} - Y_i^{pred} \right)^2$$
(3.8)

$$RMSE = \sqrt{\frac{1}{N} \sum_{i=1}^{N} \left(Y_i^{exp} - Y_i^{pred} \right)^2}$$
(3.9)

where Y_i^{exp} , Y_i^{pred} , and Y_{ave}^{pred} represent the experimental, predicted, and average of the experimental values, respectively, and N is the total number of samples.

3.15.3 Feature Importance Analysis

After training the model, a feature importance analysis was performed to determine the contribution of each parameter to the adsorption performance. This analysis examines the reduction in the model's prediction error when a particular feature is used. Features with higher importance scores are those that significantly impact the adsorption performance, thus providing insights into which operational conditions and adsorbent characteristics are more critical (Yadav et al., 2025).

3.16 Optimization of Ternary Composite Synthesis Process

The synthesis process of PKSAC-GO-Fe composite was optimized by considering two parameters: the ratio of PKSAC/GO and the loading amount of iron oxide. RSM-CCD was used to design and optimize these parameters. The experimental ranges are provided in Table 3.5. First, *a* gram of GO was added into an acidic solution (2% CH₃COOH; 5 mL HCl) and sonicated for half an hour using an ultrasonic processor (model: Hielscher Ultrasound Technology UP400S). Then *b* gram of PKSAC was added and sonicated for half an hour. After that, *c* g of FeCl₃·6H₂O and *d* g of FeCl₂·4H₂O (corresponding to the desired iron oxide loading) were added in a molar ratio of 2:1 and stirred overnight. NH₄OH was added dropwise to raise the mixture to an alkaline pH range, facilitating the deposition of iron oxide, followed by another 30 min sonication. The resultant solid (PKSAC-GO-Fe) from different formulations was rinsed with water and ethanol before being dried in an oven.

Table 3.5: Ranges of PKSAC/GO and Loading Amount of Iron Oxide

| | | | Levels | | |
|-----------------------|-----------|-------------|---------------|--------------|-----------|
| Independent Variables | -α | Low (-1) | Medium (0) | High (+1) | +α |
| PKSAC/GO | 0.08/0.92 | 0.2/0.8 | 0.5/0.5 | 0.8/0.2 | 0.92/0.08 |
| Iron oxide | 8.8% | 15.0% | 30.0% | 45.0% | 51.2% |

PKSAC + GO = 2 g

The optimized PKSAC-GO-Fe composite was comprehensively characterized using FTIR, FESEM/EDX, BET, VSM, PSD, XRD, and pH_{pzc} analyses. It was then applied to treat printing wastewater, an actual industrial wastewater, to study the color removal efficiency and adsorption capacity. The pH, adsorbent dosage, and contact time were optimized. The adsorption mechanisms of printing wastewater using the optimized PKSAC-GO-Fe were studied through adsorption kinetics, isotherms, and thermodynamics. The reusability of the optimized composite was also evaluated. The composite was further validated using various types of actual dye wastewater, including

those from plastic fabrication, POME, landfill leachate, textile, and batik industries. Additionally, the performance of PKSAC-GO-Fe before and after optimization was compared in terms of physicochemical characteristics, performance, and economic feasibility.

3.17 Phytotoxicity Study

The phytotoxicity study was conducted based on the approach described by Miyah et al. (2023). The purpose of this study is to assess how PKSAC-GO-Fe-treated dye solutions affect seed germination and the growth of following seedlings over a period of seven days. In this study, red bean seeds were selected as the test species. Cotton-lined containers were prepared for seed germination. There are three different groups: (1) seeds germinated in ultrapure water (control), (2) seeds germinated in the untreated dye solution, and (3) seeds germinated in the PKSAC-GO-Fe-treated dye solution.

An equal number of red bean seeds (25 seeds) were placed in each container. The containers were placed in a controlled environment with consistent air, temperature, and light conditions. The germination rate and growth conditions of the red bean seeds were monitored daily for seven consecutive days. The seed germination rate (SGR) (Eq. 3.10) and overall seedling health are recorded.

$$SGR = \frac{Germinated\ seeds\ number}{Tested\ seeds\ number} \times 100$$
(3.10)

3.18 Possible End-Use of Spent Adsorbents

The possible replacement of red brick powder in brick development using spent adsorbents up to 15% by weight was studied according to the methodologies reported by Adazabra et al. (2023) and Faria et al. (2012). Alternative brick samples were prepared

by incorporating varying compositions of spent adsorbent (5%, 10%, and 15%) into the brick mixture, with 0% composition serving as the control (Table 3.6). The spent adsorbent was obtained from previous adsorption experiments conducted on wastewater samples. The samples were dried for 24 hours at 110°C to remove any moisture content before being used in the brick production process. The moisture content of the red brick powder-spent adsorbent mixture was set to 7%, calculated as the ratio of moisture mass to dry mass. Rectangular bricks (21.5 mm x 9.6 mm x 7.0 mm) were prepared at a laboratory scale and then calcinated at 1000°C for 6 hours after air-drying at room temperature for one day.

Table 3.6: Formulation in Brick Development

| Formulation | Red Brick Powder (%) | Spent Adsorbent (%) |
|----------------------|----------------------|---------------------|
| RB100-SA00 (control) | 100 | 0 |
| RB95-SA05 | 95 | 5 |
| RB90-SA10 | 90 | 10 |
| RB85-SA15 | 85 | 15 |

The loss on ignition (LOI) of the alternative brick samples was determined using Eq. 3.11.

$$LOI(\%) = \frac{Weight_{dry \, sample} - Weight_{calcinated \, sample}}{Weight_{dry \, sample}} \times 100$$
(3.11)

Water absorption (WA) values of the fired brick samples were determined by immersing the samples in water for 24 hours, after which they were removed, and the wet weights were recorded. The water absorption percentage was calculated using Eq. 3.12.

$$WA (\%) = \frac{Weight_{wet \, sample} - Weight_{dry \, sample}}{Weight_{dry \, sample}} \times 100$$
(3.12)

The compressive strength of the fired brick samples was evaluated through mechanical tests. The ramp rate of 2.5 kN/min was applied to the samples until complete cleavage occurred. The maximum load applied before cleavage per sample surface area (MPa) was

recorded as the compressive strength. The mechanical strength machine and software used were INSTRON 4469 and INSTRON Series IX Automated Materials Tester Version 7.24.00, respectively.

3.19 Economic Evaluation

An economic evaluation of PKSAC-GO-Fe was conducted before and after the synthesis process optimization, comparing it to CACs based on chemical and material costs, overhead expenses, yield, and adsorption performance. To assess feasibility, a case study was carried out in an industrial wastewater treatment setting. The study examined the effectiveness of PKSAC-GO-Fe and CACs in removing COD to meet Malaysia's Standard A Discharge Standard for Industrial Effluent, with a COD level of $\leq 80 \text{ mg/L}$ (Environmental Quality (Industrial Effluents) Regulations 2009).

3.20 Safety Aspects

Safety aspects were carefully considered throughout the laboratory work to prevent possible accidents during experiments. Due to the use of various chemicals, safety data sheets (SDS) were reviewed beforehand to ensure proper precautions and measures were taken. Additionally, personal protective equipment (PPE) including laboratory coats, face masks, latex gloves, covered shoes, and protective goggles were worn at all times. Table 3.7 summarizes the chemicals used in this study along with their respective potential hazards and preventive measures.

Table 3.7: Chemicals and Materials Used with Respective Potential Hazards and Preventive Measures

| Chemicals / Materials | Hazards | Classifications - Category | Safeguards |
|---|--|---|---|
| Palm kernel shell activated carbon / commercial activated carbon Graphite powder | Flammable dust Causes serious eye irritation May cause respiratory irritation and lung damage under prolonged exposure Causes serious eye irritation | Eye irritation - 2A Specific target organ toxicity following single exposure - 3 Flammable - 1 Eye irritation - 2A Specific target organ toxicity following | - Wear PPE Avoid dust formation Wear PPE Ensure adequate ventilation. |
| | - May cause respiratory irritation | single exposure - 3 | - Avoid dust formation. |
| Red brick powder | Causes skin irritation Causes eye irritation May cause respiratory irritation May cause cancer May cause damage to respiratory system through prolonged or repeated exposure | Skin irritation - 2 Eye irritation - 2B Single exposure (respiratory) - 3 Repeated exposure (respiratory) - 2 Carcinogenicity - 1A | Wear PPE. Ensure adequate ventilation. Do not breathe dust. Wash hands and exposed skin thoroughly after handling. |
| Iron (II) chloride tetrahydrate (FeCl ₂ ·4H ₂ O) | May be corrosive to metals.Harmful if swallowed.Causes serious eye damage. | Corrosive to metal - 1 Acute oral toxicity - 4 Serious eye damage/eye irritation - 1 | Wear PPE. Ensure adequate ventilation. Wash thoroughly after handling. Minimize dust generation and accumulation. |

Table 3.7: Continued

| Chemicals / Materials | Hazards | Classifications - Category | Safeguards |
|--|---|--|--|
| Iron (III) chloride hexahydrate (FeCl ₃ ·6H ₂ O) | Harmful if swallowed. Causes skin irritation. May cause an allergic skin reaction. Causes serious eye damage. May cause damage to organs through prolonged or repeated exposure. | Acute oral toxicity - 4 Skin corrosion/irritation - 2 Serious eye damage/eye irritation - 1 Skin sensitization - 1 Specific target organ (kidney, liver, blood) toxicity - (repeated exposure) - 2 | Wear PPE. Ensure adequate ventilation. Wash thoroughly after handling. Minimize dust generation and accumulation. |
| Acetic acid (CH ₃ COOH) | - Causes severe skin burns and eye damage. | - Skin corrosion - 1B | Wear PPE.Wash thoroughly after handling.Keep away from heat, sparks, and flame. |
| Hydrochloric acid (HCl) | Causes eye and skin burns. Causes digestive and respiratory tract burns. May be fatal if inhaled or swallowed. Repeated or prolonged exposure may cause erosion of exposed teeth. Corrosive to metal. | Corrosive to metals - 1 Acute inhalation toxicity - 3 Skin corrosion/irritation - 1B Serious eye damage/eye irritation - 1 Specific target organ toxicity - single exposure - 3 | Wear PPE. Wash thoroughly after handling. Store in a cool, dry, well-ventilated area away from incompatible substances. |

Table 3.7: Continued

| Chemicals / Materials | Hazards | Classifications - Category | Safeguards |
|--|-------------------------------|--|--|
| Sulphuric acid (H ₂ SO ₄) | - May be corrosive to | - Skin corrosion - 1A | - Wear PPE. |
| | metals. | - Serious eye damage - 1 | - Wash thoroughly after handling. |
| | - Causes severe skin burns | - Corrosive to metals - 1 | - Do not store near combustible |
| | and eye damage. | | materials. |
| | - Causes serious eye | | |
| | damage. | | |
| Ammonium hydroxide | - Causes severe skin burns | - Skin corrosion - 1B | - Wear PPE. |
| (NH ₄ OH) | and eye damage. | - Acute hazards to the aquatic environment - | - Store in cool, dry and well- |
| | - May cause respiratory | 1 | ventilated areas, with containers |
| | irritation. | - Specific target organ toxicity following | tightly closed. |
| | - Very toxic to aquatic life. | single exposure - 3 | |
| Sodium hydroxide | - May be corrosive to | - Serious eye damage - 1 | - Wear PPE. |
| (NaOH) | metals. | - Corrosive to metals - 1 | - Wash thoroughly after handling. |
| | - Causes severe skin burns | - Skin corrosion - 1B | - Store in a tightly closed container. |
| | and eye damage. | | - Store in a cool, dry, well- |
| | - Causes serious eye | | ventilated area away from |
| | damage. | | incompatible substances. |
| Hydrogen peroxide | - Harmful if swallowed or | - Acute oral toxicity - 4 | - Wear PPE. |
| (H_2O_2) | if inhaled. | - Acute inhalation toxicity - 4 | - Wash hands after handling. |
| | - Causes serious eye | - Serious eye damage/eye irritation - 1 | - Keep from contact with oxidizing |
| | damage. | | materials. |
| | | | - Store in a cool, dry, well- |
| | | | ventilated area away from |
| | | | incompatible substances. |

Table 3.7: Continued

| Chemicals / Materials | Hazards | Classifications - Category | Safeguards |
|--------------------------|------------------------------|--|-----------------------------------|
| Potassium permanganate | - May intensify fire. | - Oxidizing - 2 | - Wear PPE. |
| (KMnO ₄) | - Oxidizer. | - Irritant Acute toxicity (oral, dermal, | - Wash thoroughly after handling. |
| | - Harmful if swallowed. | inhalation) - 4 | - Keep away from heat/sparks/open |
| | - Causes severe skin burns | - Chronic hazards to the aquatic environment | flames/hot surfaces. |
| | and eye damage. | -1 | |
| | - Causes serious eye | - Acute hazards to the aquatic environment - | |
| | damage. | 1 | |
| | - Very toxic to aquatic life | - Skin corrosion - 1B | |
| | with long lasting effects. | - Serious eye damage - 1 | |
| Potassium chloride (KCl) | - May be harmful if | - Skin irritation - 2 | - Wear PPE. |
| | swallowed. | - Eye irritation - 2A | - Minimize dust generation and |
| | - Causes serious eye | | accumulation. |
| | irritation. | | - Store in a cool, dry place. |
| | - Causes skin irritation. | | |
| | - Toxic to terrestrial | | |
| | vertebrates. | | |

Table 3.7: Continued

| Chemicals / Materials | Hazards | Classifications - Category | Safeguards |
|--|--|--|--|
| Ethanol (C ₂ H ₅ OH) | Highly flammable liquid and vapor. Toxic if swallowed. May cause drowsiness or dizziness. May damage fertility or the unborn child. May cause damage to organs through prolonged or repeated exposure. | Flammable liquids - 2 Toxic acute toxicity (oral, dermal, inhalation) - 3 Health hazard reproductive toxicity - 2 Specific target organ toxicity following repeated exposure - 2 Irritant Specific target organ toxicity following single exposure - 3 | Wear PPE. Ensure adequate ventilation. Wash thoroughly after handling. Keep away from heat, sparks, and flame. Avoid breathing dust/fume/gas/mist/vapours/spray. |
| COD cell | May be corrosive to metals. Toxic in contact with skin. Causes severe skin burns and eye damage. May cause damage to organs (kidney) through prolonged or repeated exposure. Very toxic to aquatic life with long lasting effects. | Corrosive to metals - 1 Acute dermal toxicity - 3 Skin corrosion/irritation - 1A Serious eye damage/eye irritation - 1 Specific target organ toxicity - repeated exposure (kidney) - 2 Hazardous to the aquatic environment - acute hazard - 1 Hazardous to the aquatic environment - chronic hazard - 1 | Wear PPE. Avoid release to the environment. |

Table 3.7: Continued

| Chemicals / Materials | Hazards | Classifications - Category | Safeguards |
|-----------------------|---|--|---|
| Acid blue 113 (AB113) | Dust may cause irritation and inflammation of eyes. Prolonged or repeated contact may cause skin irritation. Harmful if swallowed. May cause gastrointestinal irritation with nausea, vomiting and diarrhea. May cause irritation of the respiratory tract. | Skin sensitization - 1 Eye irritation - 2 Hazardous to the aquatic environment - long-term chronic hazard - 3 Hazardous to the aquatic environment - acute hazard - 2 | Wear PPE. Ensure adequate ventilation. Preserve in tight and light-resistant containers. Avoid release to the environment. |
| Methylene blue (MB) | Causes skin irritation. Causes eye irritation. May cause respiratory irritation. May cause cancer. May cause damage to respiratory system through prolonged or repeated exposure. | Skin irritation - 2 Eye irritation - 2A Specific target organ toxicity - single exposure - 3 Acute toxicity (oral, dermal, inhalation) - 4 | Wear PPE. Prevent from reaching drains, sewer or waterway. Minimize dust generation and accumulation. |

Table 3.7: Continued

| Chemicals / Materials | Hazards | Classifications - Category | Safeguards |
|---------------------------------|--|--|---|
| Rhodamine B (RhB) | Harmful if swallowed. Causes serious eye irritation. Harmful to aquatic life with long lasting effects. | Acute toxicity (oral) - 4 Hazardous to the aquatic environment - acute hazard - 3 Hazardous to the aquatic environment - chronic hazard - 3 Eye irritation - 2A | Wear PPE. Prevent from reaching drains, sewer or waterway. Minimize dust generation and accumulation. |
| Methyl orange (MO) | - Toxic if swallowed. | - Acute toxicity (oral) - 3 | Wear PPE. Wash skin thoroughly after handling. Do not eat, drink or smoke when using this product. |
| Remazol brilliant blue R (RBBR) | | 3 | - Wear PPE. |
| Acid yellow 17 (AY17) | Harmful if swallowed. May cause stomach discomfort. Respiratory irritation. May cause irritation to eyes. May cause skin irritation in sensitive individuals. Possible risks of irreversible effects. | | - Wear PPE. |

Table 3.7: Continued

| Chemicals / Materials | Hazards | Classifications - Category | Safeguards |
|------------------------------|---|---|---|
| Reactive blue 4 (RB4) | - Causes serious eye irritation. | - Eye irritation - 2A | Wear PPE.Wash skin thoroughly after handling. |
| Reactive red 120 (RR120) | May cause an allergic skin reaction. May cause allergy or asthma symptoms or breathing difficulties if inhaled. | | Wear PPE. Ensure adequate ventilation. Avoid breathing dust/fume/gas/mist/vapours/spray. Avoid dust formation. Remove all sources of ignition |
| Reactive black 5 (RB5) | May cause an allergic skin reaction. May cause allergy or asthma symptoms or breathing difficulties. | Respiratory sensitization - 1Skin sensitization - 1 | Wear PPE.Avoid breathing dust/fume/gas/mist/vapors/spray. |
| Malachite green (MG) | Toxic if swallowed. Causes serious eye damage. Suspected of damaging fertility. Suspected of damaging the unborn child. Very toxic to aquatic life with long lasting effects. | Acute toxicity (oral) - 3 Serious eye damage/eye irritation - 1 Reproductive toxicity - 2 Hazardous to the aquatic environment - acute hazard - 1 Hazardous to the aquatic environment - chronic hazard - 1 | Wear PPE. Wash skin thoroughly after handling. Do not eat, drink or smoke when using this product. Avoid release to the environment. |

Table 3.7: Continued

| Chemicals / Materials | Hazards | Classifications - Category | Safeguards |
|-----------------------|-------------------------------|--|-----------------------------------|
| Amaranth | - Toxic if swallowed. | - Acute toxicity (oral) - 3 | - Wear PPE. |
| | - Causes serious eye | - Serious eye damage/eye irritation - 1 | - Wash thoroughly after handling. |
| | damage. | - Reproductive toxicity - 2 | - Do not eat, drink or smoke when |
| | - Suspected of damaging | - Hazardous to the aquatic environment - | using this product. |
| | fertility or the unborn | acute hazard - 1 | |
| | child. | - Hazardous to the aquatic environment - | |
| | - Very toxic to aquatic life. | chronic hazard - 1 | |
| | - Very toxic to aquatic life | | |
| | with long lasting effects. | | |

PPE: Personal protective equipment

CHAPTER 4: RESULTS AND DISCUSSION

4.1 Introduction

This chapter presents the experimental and computational results obtained from this study. It starts with a comparison of PKSAC-based adsorbents, which emphasizes their adsorption performance and physicochemical characteristics. After that, the effects of operational parameters for treating synthetic wastewater are analyzed and optimized. Various dye concentrations, industrial dyes, continuous processes, and commercial activated carbons are used to validate the RSM-CCD model. In addition, the study investigates the reusability of the adsorbent. The predominant adsorption mechanism is confirmed through both experimental and computational methods. The synthesis process of the ternary composite is then optimized for treating actual industrial wastewater. The effects of operational parameters on the treatment of industrial wastewater are also examined and optimized. A comparison is made between the adsorption performance and physicochemical characteristics of the ternary composite before and after synthesis process optimization. Finally, economic and environmental evaluations are conducted.

4.2 Adsorption Performance Evaluation of PKSAC-Based Adsorbents using Synthetic Wastewater

Activated carbon derived from PKS is denoted as a potential adsorbent due to its high surface area and porous structure. This study focuses on impregnating graphene oxide (GO) and iron oxide into PKSAC. It is to enhance the physicochemical characteristics and adsorption performance of PKSAC-based adsorbents. The effectiveness of PKSAC-based adsorbents in color removal efficiency and adsorption capacity for treating synthetic wastewater containing anionic AB113 dye is compared statistically using analysis of variance (ANOVA).

4.2.1 Statistical Analysis

In experimental studies where numerous conditions are evaluated, the ANOVA statistical method is beneficial for identifying significant differences between the means of more than two independent groups (Alsharief et al., 2024). In this study, an ANOVA was conducted for PKSAC-based adsorbents in terms of color removal efficiency and adsorption capacity, as summarized in Table 4.1.

All PKSAC-based adsorbents exhibit p-values < 0.0001 for both adsorption capacity and color removal efficiency, as indicated in Table 4.1. These values are significantly lower than the 0.05 threshold (α = 0.05 or 95% confidence). The results indicate that all the developed models are highly significant (Ariza-Pineda et al., 2023). The R² and adjusted R² values for raw PKSAC were 0.7393 and 0.6904 for color removal efficiency, and 0.8352 and 0.7912 for adsorption capacity, respectively. Moreover, PKSAC demonstrated adequate precision values of 12.4595 for color removal efficiency and 13.9482 for adsorption capacity, which are greater than 4. This suggests that the models are reasonably reliable and accurate in forecasting the adsorption capacity and color removal efficiency when treating synthetic wastewater with raw PKSAC.

After the impregnation of GO into raw PKSAC, the R² value for color removal efficiency increased by 15.2%, from 0.7393 to 0.8515, and the adjusted R² increased by 13.4%, from 0.6904 to 0.7829 for the PKSAC-GO composite. The R² value increased by 2.3%, from 0.8352 to 0.8545, and the adjusted R² increased by 1.4%, from 0.7912 to 0.8025 for the adsorption capacity. These enhancements signify that GO impregnation into raw PKSAC effectively improved the RSM-CCD model for adsorption performance prediction. In comparison to raw PKSAC and the PKSAC-GO composite, the R² and adjusted R² values of PKSAC-Fe significantly increased with the addition of iron oxide. For instance, as compared to raw PKSAC, the R² and adjusted R² of PKSAC-Fe were

0.9187 and 0.8897 for color removal efficiency and 0.8965 and 0.8689 for adsorption capacity, respectively, showing improvements of 24.3%, 28.9%, 7.3%, and 9.8%. In addition, the R² and adjusted R² values of PKSAC-Fe increased by 24.3% and 28.9% for color removal efficiency, and by 7.3% and 9.8% for adsorption capacity compared to PKSAC-GO.

The highest improvement was observed with the combined impregnation of GO and iron oxide to raw PKSAC. The R² and adjusted R² values reached 0.9793 and 0.9698 for color removal efficiency, and 0.9653 and 0.9493 for adsorption capacity, respectively for PKSAC-GO-Fe composite. The high R² values make the models developed by RSM-CCD highly suitable for future analysis and prediction (Poddar et al., 2023). Furthermore, the models were validated by high adequate precision values of 28.9682 for color removal efficiency and 28.0190 for adsorption capacity. In short, the combination of PKSAC, GO, and iron oxide in the PKSAC-GO-Fe composite showed the highest improvements, with significant increases in R² values and model precision, making it the most effective modification.

Table 4.1: ANOVA and Polynomial Equations of PKSAC-Based Adsorbents

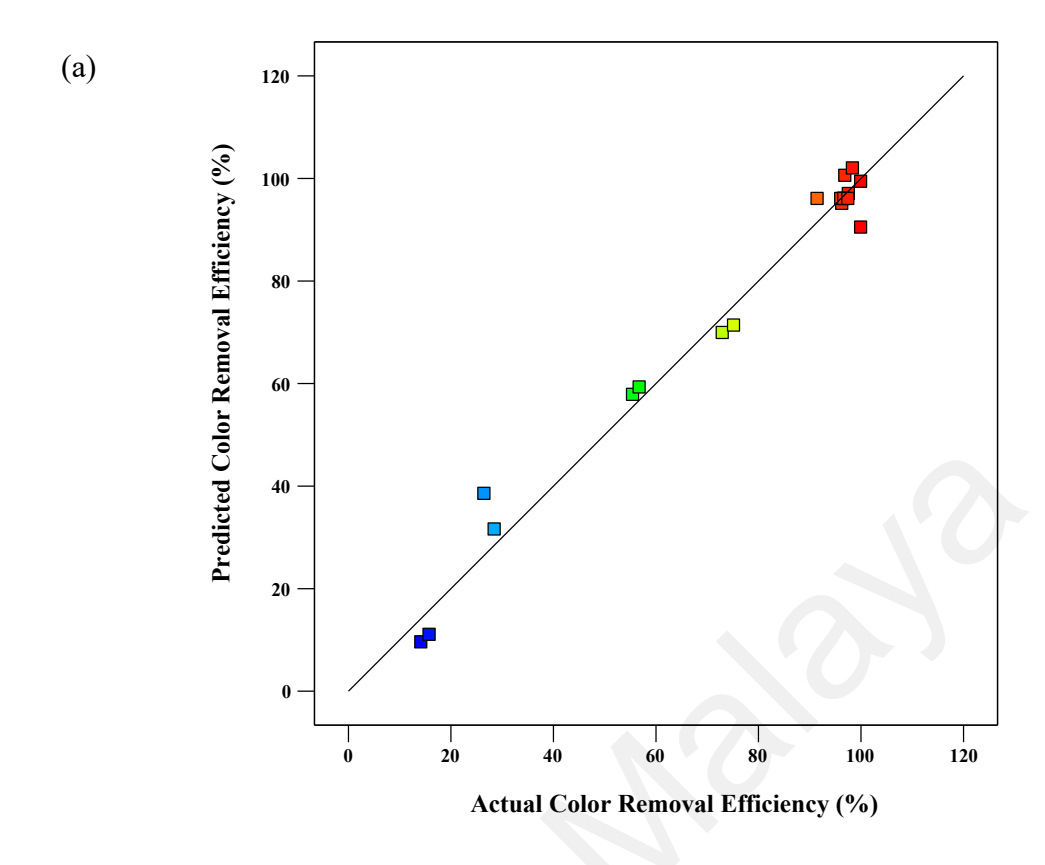
| Adsorbents | Responses | F- Value | p- Value | R ² | Adjusted R ² | Adequate Precision | Polynomial Equations | Eq. |
|-------------|------------------|-------------|-------------|----------------|-------------------------|--------------------|---|-----|
| PKSAC | Color removal | 15.12 | <0.0001 | 0.7393 | 0.6904 | 12.4595 | 9.9914 – 1.6537 pH + 14.9985 adsorbent dosage + 3.8773 contact time | 4.1 |
| | efficiency | | | | | | | |
| | Adsorption | 19.00 | < 0.0001 | 0.8352 | 0.7912 | 13.9482 | 87.8092 – 7.1016 pH – 15.9041 adsorbent dosage + | 4.2 |
| | capacity | | | | | | 0.6741 contact time + 1.5375 pH × adsorbent dosage | |
| PKSAC-GO | Color | 12.42 | 0.0001 | 0.8515 | 0.7829 | 12.2459 | 92.2920 – 19.5388 pH + 15.6933 adsorbent dosage + | 4.3 |
| | removal | | | | | | 2.6056 contact time + 1.2453 pH × adsorbent dosage + | |
| | efficiency | | | | | | $0.9242 \text{ pH}^2 - 2.1560 \text{ adsorbent } dosage^2$ | |
| | Adsorption | 16.44 | < 0.0001 | 0.8545 | 0.8025 | 15.0155 | 113.9057 – 14.0749 pH – 17.4958 adsorbent dosage + | 4.4 |
| | capacity | | | | | | 0.9674 contact time + 1.5172 pH × adsorbent dosage + | |
| | | | | | | | 0.5116 pH^2 | |
| PKSAC-Fe | Color | 31.66 | < 0.0001 | 0.9187 | 0.8897 | 20.4974 | 88.5821 – 10.3823 pH +16.2808 adsorbent dosage + | 4.5 |
| | removal | | | | | | 1.2976 contact time + 1.4109 pH × adsorbent dosage – | |
| | efficiency | | | | | | 2.8999 adsorbent dosage ² | |
| | Adsorption | 32.48 | < 0.0001 | 0.8965 | 0.8689 | 17.9805 | 122.9713 – 10.4664 pH – 22.5941 adsorbent dosage + | 4.6 |
| | capacity | | | | | | 0.3710 contact time + 2.1438 pH × adsorbent dosage | |
| PKSAC-GO-Fe | Color | 102.72 | < 0.0001 | 0.9793 | 0.9698 | 28.9682 | 26.6284 + 7.3440 pH + 33.3363 adsorbent dosage + | 4.7 |
| | removal | | | | | | 0.3625 contact time + 0.5500 pH × adsorbent dosage – | |
| | efficiency | | | | | | 1.1024 pH ² – 4.5540 adsorbent dosage ² | |
| | Adsorption | 60.30 | < 0.0001 | 0.9653 | 0.9493 | 28.0190 | 105.6720 – 1.8880 pH – 28.5226 adsorbent dosage + | 4.8 |
| | capacity | | | | | | 0.2149 contact time + 1.5875 pH × adsorbent dosage – | |
| | | | | | | | $0.4641 \text{ pH}^2 + 1.5356 \text{ adsorbent dosage}^2$ | |

4.2.2 Correlation and Model Validation

The correlations between predicted and experimental runs for color removal efficiency and adsorption capacity using the PKSAC-GO-Fe composite are shown in Figure 4.1. Higher and lower performance levels are indicated by the red and blue colored data points, respectively. The data points of all runs are well-distributed along the straight line, indicating an excellent correlation for the model developed for color removal efficiency and adsorption capacity. This strong correlation indicates that the model accurately predicts outcomes based on experimental data. As depicted in Figure 4.2, the perturbation plots show that the initial pH of the solution and the adsorbent dosage have a more significant effect on the responses than contact time. This is indicated by the steep curvature in the plot, highlighting that initial solution pH and adsorbent dosage are critical factors influencing the adsorption performance within the design space (Uba et al., 2022).

4.2.3 Model Fitting

Polynomial equations are frequently used to represent the relationship between responses (color removal efficiency and adsorption capacity) and independent parameters (pH, adsorbent dosage, and contact time). The polynomial equations developed for PKSAC-based adsorbents, after excluding insignificant terms to enhance model fitness, are summarized in Table 4.1. (Eq. 4.1 to Eq. 4.8) in terms of actual factors. The quality of the polynomial model equation was statistically assessed by parameters such as R² values, p-value, and adequate precision. The polynomial equations show how independent factors and their interactions influence adsorption performance. A positive term indicates a beneficial effect on a response, while a negative term suggests a detrimental effect (Malenga et al., 2022). These equations offer accurate predictions of adsorption performance using PKSAC-based adsorbents within the investigated range.



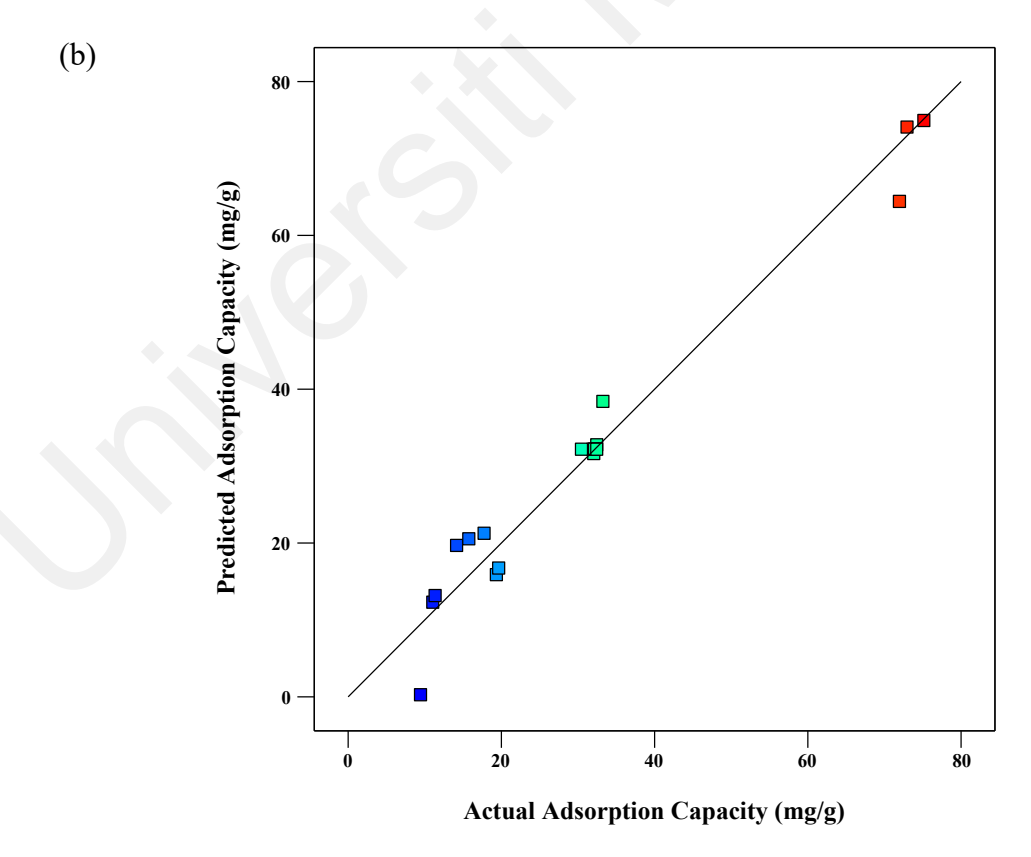
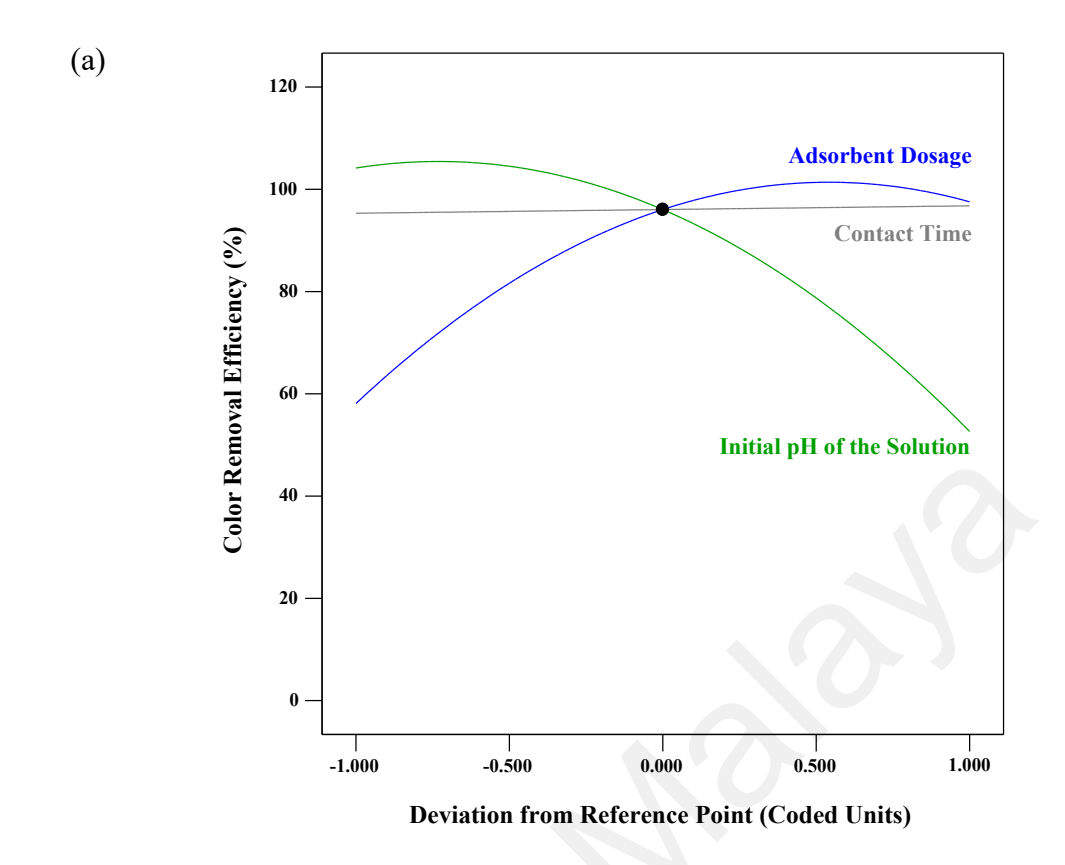


Figure 4.1: Predicted versus Actual Regression Plot of (a) Color Removal Efficiency and (b) Adsorption Capacity using PKSAC-GO-Fe



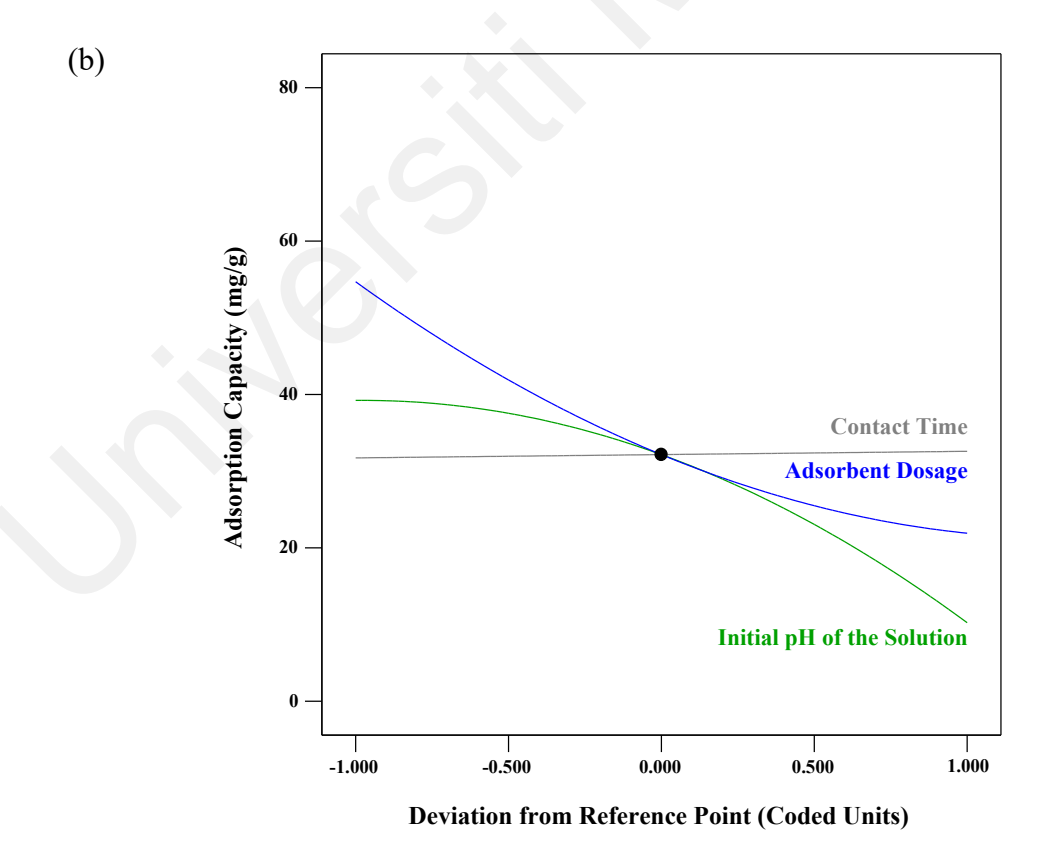


Figure 4.2: Perturbation Plots of (a) Color Removal Efficiency and (b) Adsorption Capacity using PKSAC-GO-Fe

4.2.4 Comparison of Adsorption Performance of PKSAC-Based Adsorbents

To evaluate the effects of impregnating GO and iron oxide into PKSAC, the adsorption performance in terms of color removal efficiency and adsorption capacity of PKSAC-based adsorbents was studied and compared in the treatment of synthetic wastewater containing anionic AB113 dye. Figure 4.3 presents a comparison of the adsorption performance of various PKSAC-based adsorbents under similar operational conditions.

For the raw material, PKSAC demonstrated a color removal efficiency of 43.2% and an adsorption capacity of 11.8 mg/g. After impregnation with GO, the resulting PKSAC-GO showed significant improvements with a color removal efficiency of 66.0% and an adsorption capacity of 18.0 mg/g. This corresponds to enhancements of 52.8% in color removal efficiency and 52.5% in adsorption capacity. The improvement observed with the addition of GO can be attributed to the additional oxygenated functional groups provided by GO, which facilitate stronger adsorbate-adsorbent bonds. These findings are consistent with earlier research by Brito et al. (2023), Z. Yang et al. (2021), Ndagijimana et al. (2021), and Bhattacharyya et al. (2021), which reported that activated carbon/graphene oxide composites performed better at adsorption than raw activated carbon.

When iron oxide was added to raw PKSAC, PKSAC-Fe exhibited a color removal efficiency of 73.1% and an adsorption capacity of 19.9 mg/g. This represents that the color removal efficiency and adsorption capacity have increased by 69.2% and 68.6%, respectively, compared to raw PKSAC. This result is in line with previous studies by Rao Vaddi et al. (2024) and Wu et al. (2024), which also reported enhanced adsorption performance with the addition of iron oxide. The ternary composite of PKSAC-GO-Fe demonstrated outstanding performance among all PKSAC-based adsorbents, with a color removal efficiency of 99.8% and an adsorption capacity of 27.3 mg/g. Compared to raw

PKSAC, color removal efficiency and adsorption capacity improvements are 131.0% and 131.4%, respectively. The synergistic effects of PKSAC with large surface area, GO with various oxygenated functional groups, and iron oxide with magnetic and catalytic properties are contributing to the exceptional performance of PKSAC-GO-Fe.

To sum up, the PKSAC-GO-Fe ternary composite demonstrates excellent performance in both color removal efficiency and adsorption capacity, outperforming raw PKSAC and other modified PKSAC-based adsorbents. This highlights the significance of modifications and impregnations in enhancing the adsorption performance of raw materials.

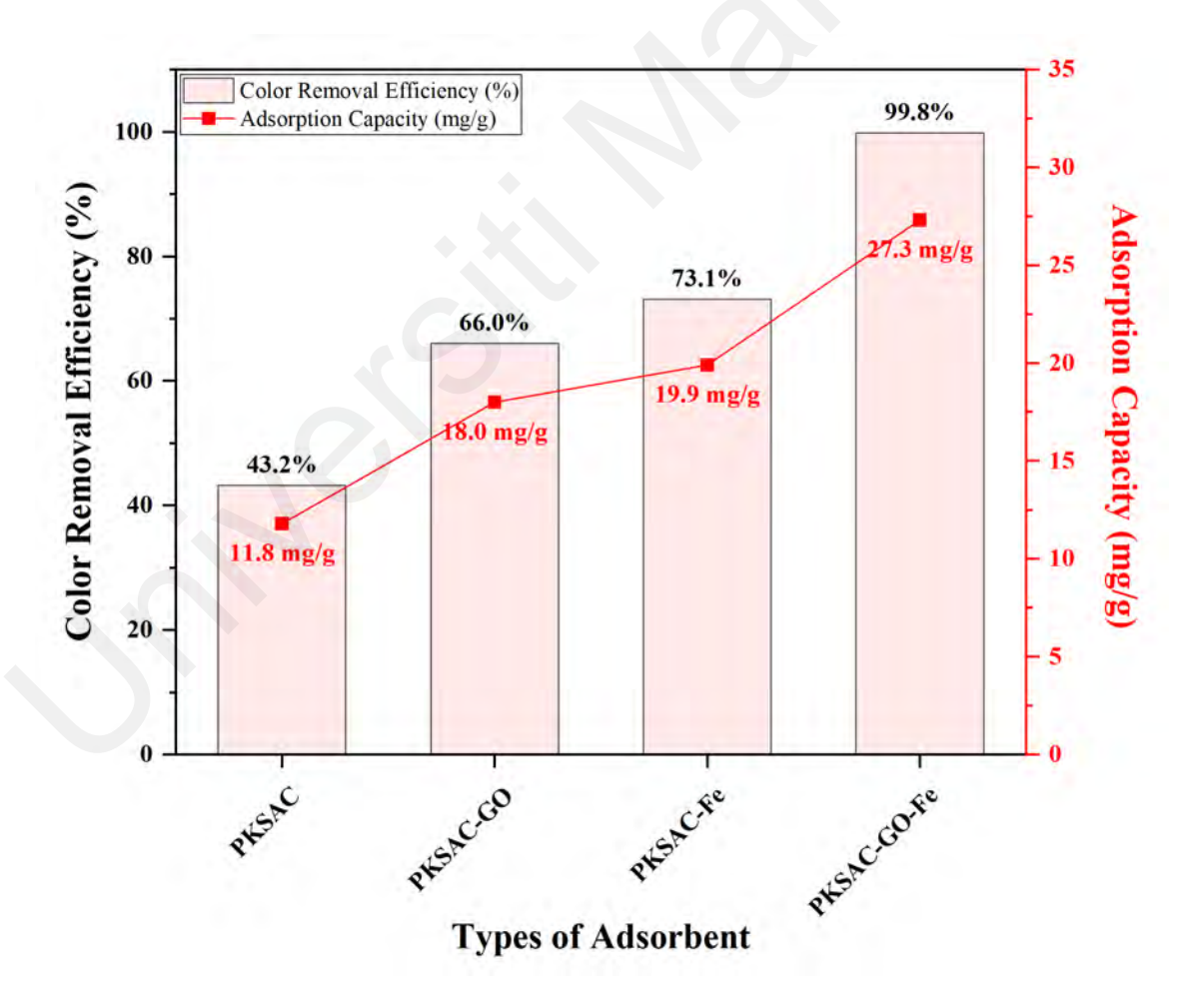


Figure 4.3: Adsorption Performance Comparison of PKSAC-Based Adsorbents

4.3 Physicochemical Characteristics of PKSAC-Based Adsorbents

In this study, the significant physicochemical characteristics of PKSAC-based adsorbents that contribute to the adsorption performance in wastewater treatment were analyzed and compared. In the following sections, the characteristics include textural properties, morphologies, elemental compositions, magnetic properties, particle size distribution, crystalline structure, and point of zero charge are discussed in detail.

4.3.1 Textural Properties

The textural properties of PKSAC-based adsorbents were studied using BET and BJH analyses. The pore volume, surface areas, and pore size of the PKSAC-based adsorbents are provided in Table 4.2, while nitrogen adsorption-desorption isotherms and pore size distribution plots are shown in Figures 4.4 and 4.5.

At low relative pressures (P/P_o < 0.1), all samples show a sharp increase in nitrogen adsorption, indicating the presence of micropores. On the other hand, the mesoporosity of PKSAC-based adsorbents is evidenced by the hysteresis loops in the adsorption/desorption isotherms (Wei et al., 2022). This is further supported by the average pore widths, which range between 3.00 and 9.99 nm, within the typical mesopore range of 2 to 50 nm (Taguchi & Schüth, 2005). This observation suggests both microporosity and mesoporosity are present in the PKSAC-based adsorbent with mesoporous dominance (Gallios et al., 2017; Y. Liu et al., 2020).

The nitrogen adsorption-desorption isotherms of all PKSAC-based adsorbents exhibit Type IV isotherms (IUPAC classification), characterized by hysteresis loops due to capillary condensation in mesopores. For raw PKSAC and PKSAC-GO, the hysteresis loops align with H4 characteristics, signifying a dominance of narrow slit-shaped mesopores. After iron oxide impregnation, the hysteresis loop type transitions to H3 for PKSAC-Fe and PKSAC-GO-Fe. The formation of wedge-shaped mesopores is likely due

to partial blocking or structural modification of smaller mesopores by deposited iron oxide particles (Kalenskii et al., 2023).

For raw PKSAC, very high BET and Langmuir surface areas of 915.41 m²/g and 1013.81 m²/g were obtained, respectively. These high surface area values indicate significant porosity, which is crucial for effective adsorption processes. These values are comparable to the BET surface area of palm kernel shell activated carbon reported by Jumasiah et al. (2005), which was 1088 m²/g. However, after the impregnation of GO into PKSAC, the PKSAC-GO composite demonstrated BET and Langmuir surface areas of 708.72 m²/g and 779.66 m²/g, respectively, representing reductions of 22.6% and 23.1% compared to raw PKSAC. The decrease in surface area is attributed to the addition of GO, which has a lower surface area (BET: 192.24 m²/g; Langmuir: 269.82 m²/g) compared to raw PKSAC. Similarly, after the impregnation of iron oxide (BET: 98.45 m²/g; Langmuir: 103.29 m²/g), the BET and Langmuir surface areas of PKSAC-Fe decreased by 54.0% and 54.3%, respectively, from 915.41 m²/g to 420.82 m²/g and from 1013.81 m²/g to 463.80 m²/g, compared to raw PKSAC. Additionally, the pore volume decreased by 19.5%, from 0.41 cm³/g to 0.33 cm³/g after iron oxide impregnation. These reductions are due to the coverage of some pores on the PKSAC surface (Duan et al., 2020). The finding is similar to Cao and Zhang (2020), which reported that with the increasing amount of iron loading on activated carbon covered the micropores and hence decreased the overall pore volume and surface area.

For the PKSAC-GO-Fe composite, after the impregnation of both GO and iron oxide, the BET and Langmuir surface areas were determined to be 280.39 m²/g and 309.97 m²/g, respectively. These values are the lowest among all PKSAC-based adsorbents. The further reduction in surface areas is due to the additional coating of iron oxide on the PKSAC-GO surface, which blocks some pores, as supported by FESEM analysis. Despite

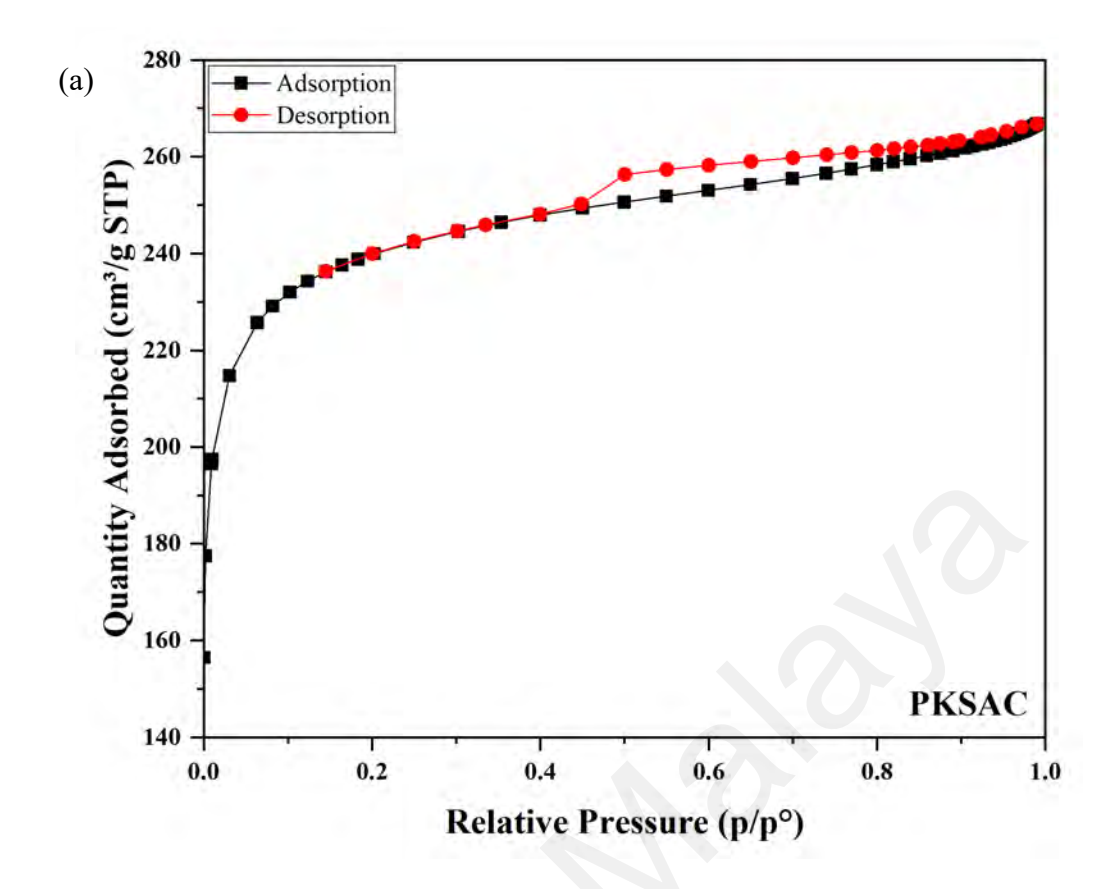
the reduced surface areas, the PKSAC-GO-Fe composite still possesses higher surface areas compared to similar adsorbents reported by Sherlala et al. (2019) (152.38 m^2/g), Liu et al. (2019) (190.28 m^2/g), Abdi et al. (2019) (226 m^2/g), Gao et al. (2019) (53.83 m^2/g) and Hosseinzadeh and Ramin (2018) (132.9 m^2/g).

Notably, although the surface area and pore volume of the PKSAC-GO-Fe were reported to be decreased after the impregnation of GO and iron oxide, there was no reduction in its adsorption capacity. It is in line with Yongde Liu et al. (2020), which indicates that physisorption is not the primary mechanism. Kinetic analysis of the aforementioned study suggests that chemisorption is the rate-limiting step. The primary interactions are π - π , electrostatic, hydrogen bonding, and π -cation interactions. Besides that, other studies further confirm that impregnation improves adsorbent-adsorbate interactions and therefore enhances the adsorption performance due to surface functionalities and active sites (Brito et al., 2023; Wang et al., 2020; Zabneva et al., 2012).

In short, the textural properties of PKSAC-based adsorbents show decreased surface area does not bring detrimental effects on adsorption performance. Hence, it is suggested that rather than physical adsorption, the adsorption process is most likely dominant by chemical interactions.

Table 4.2: Textural Properties of PKSAC-Based Adsorbents

| Parameter | BET Surface Area (m²/g) | Langmuir Surface Area (m²/g) | BJH Average Pore Width (nm) | Pore Volume (cm³/g) |
|-------------|----------------------------|------------------------------------|-----------------------------------|------------------------|
| PKSAC | 915.41 | 1013.81 | 3.00 | 0.41 |
| PKSAC-GO | 708.72 | 779.66 | 4.66 | 0.36 |
| PKSAC-Fe | 420.82 | 463.80 | 6.04 | 0.33 |
| PKSAC-GO-Fe | 280.39 | 309.97 | 9.99 | 0.35 |



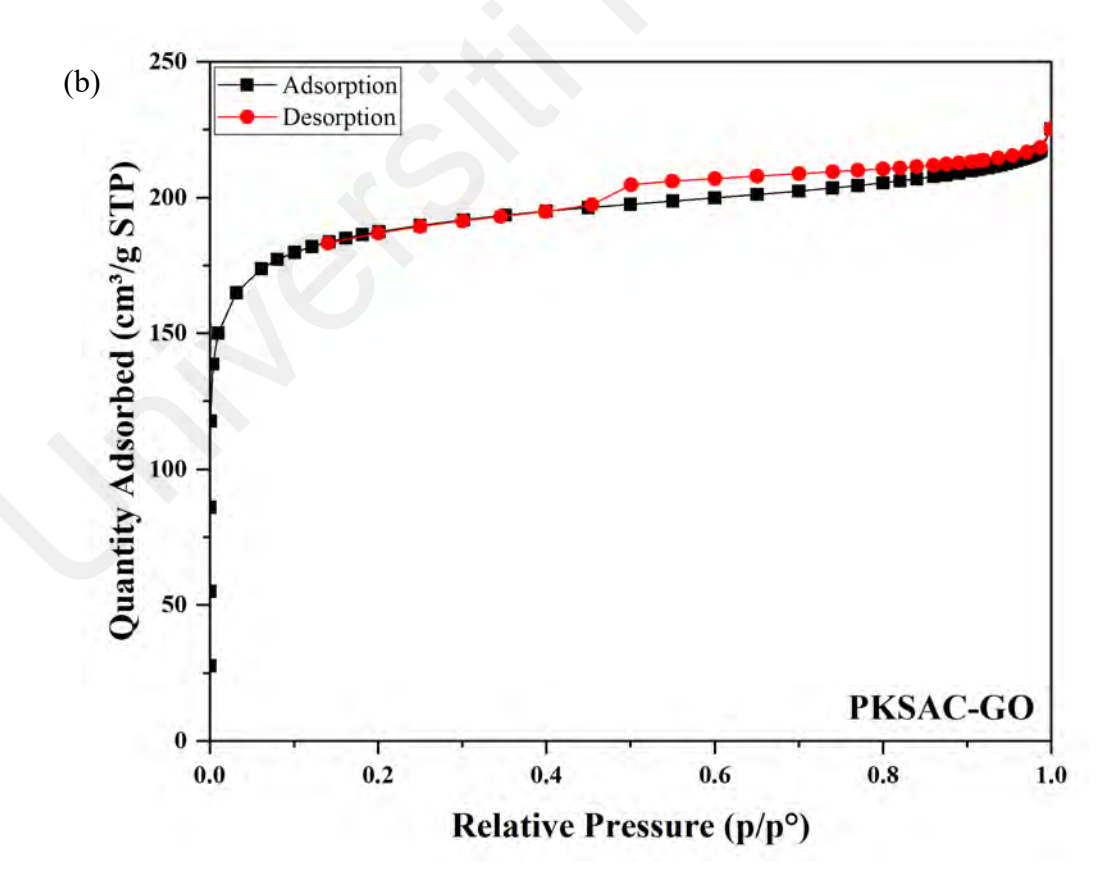
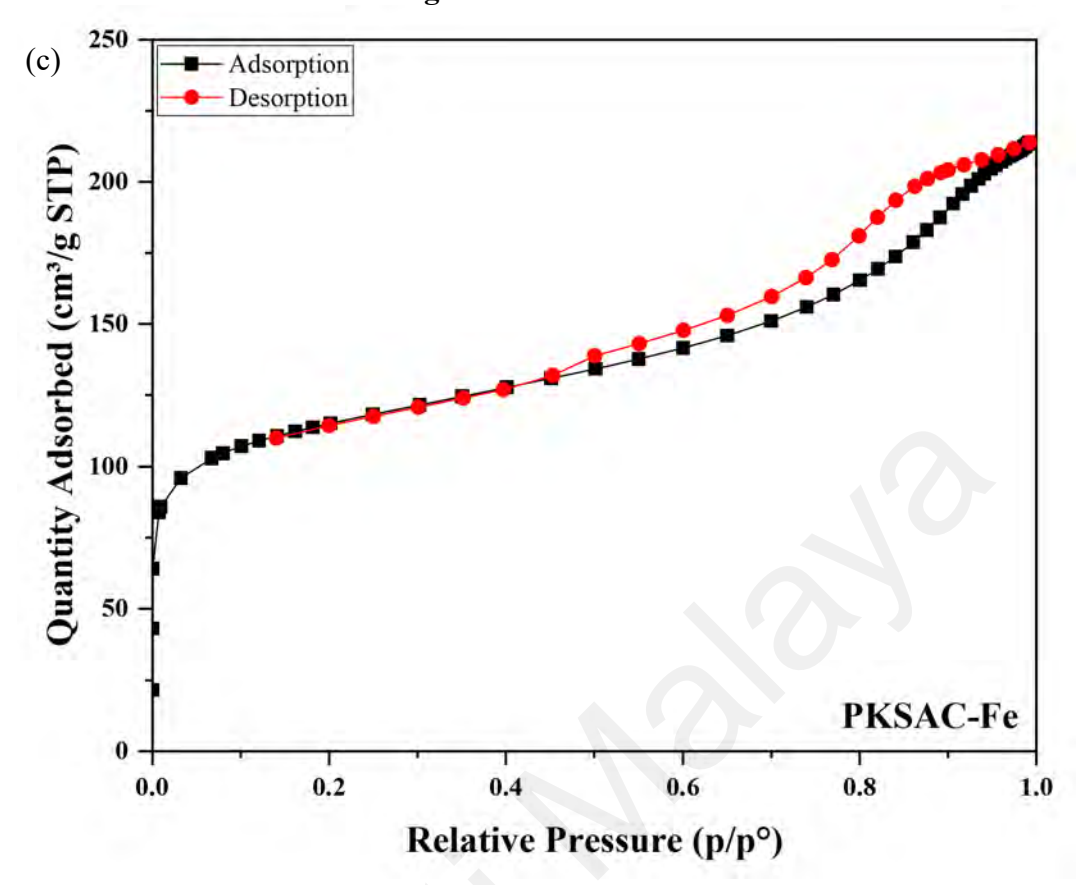
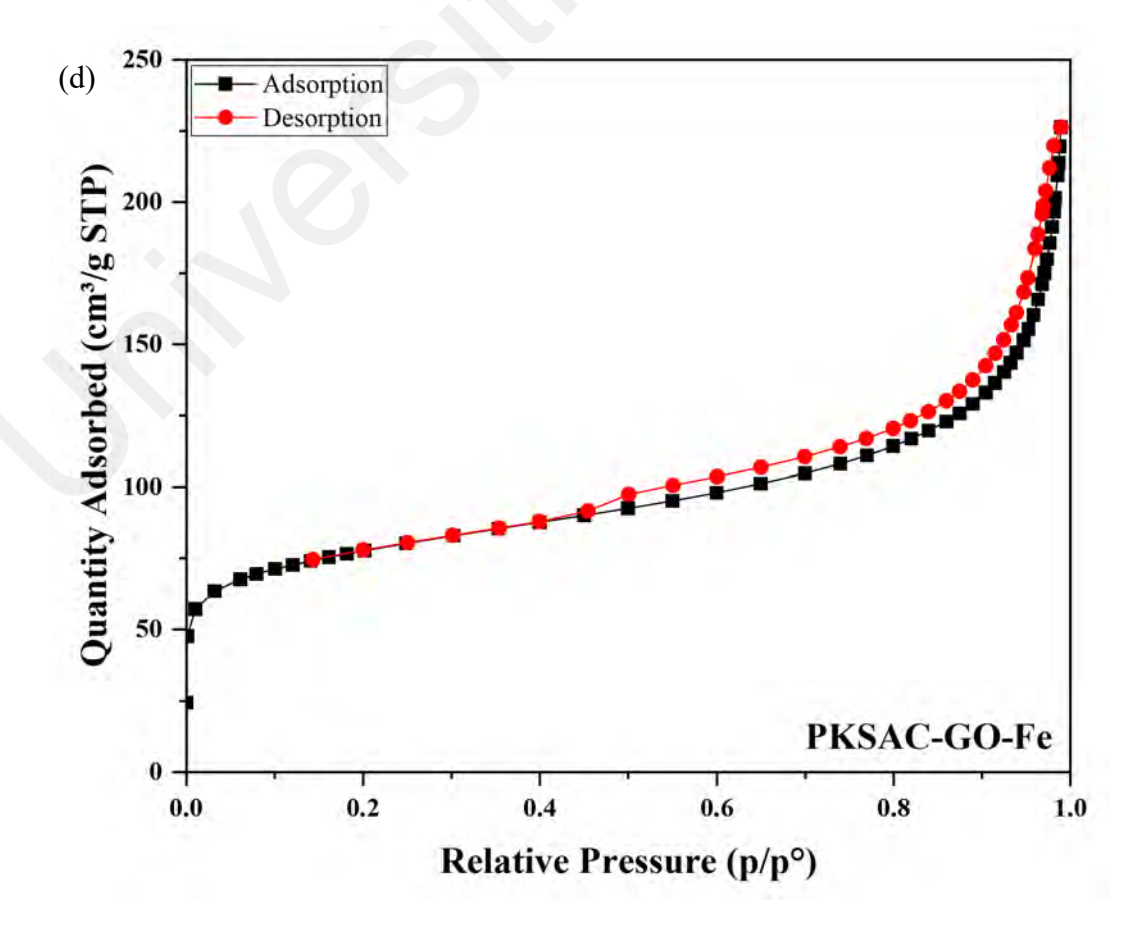


Figure 4.4: Nitrogen Adsorption-Desorption of (a) PKSAC, (b) PKSAC-GO, (c) PKSAC-Fe, and (d) PKSAC-GO-Fe

Figure 4.4: Continued





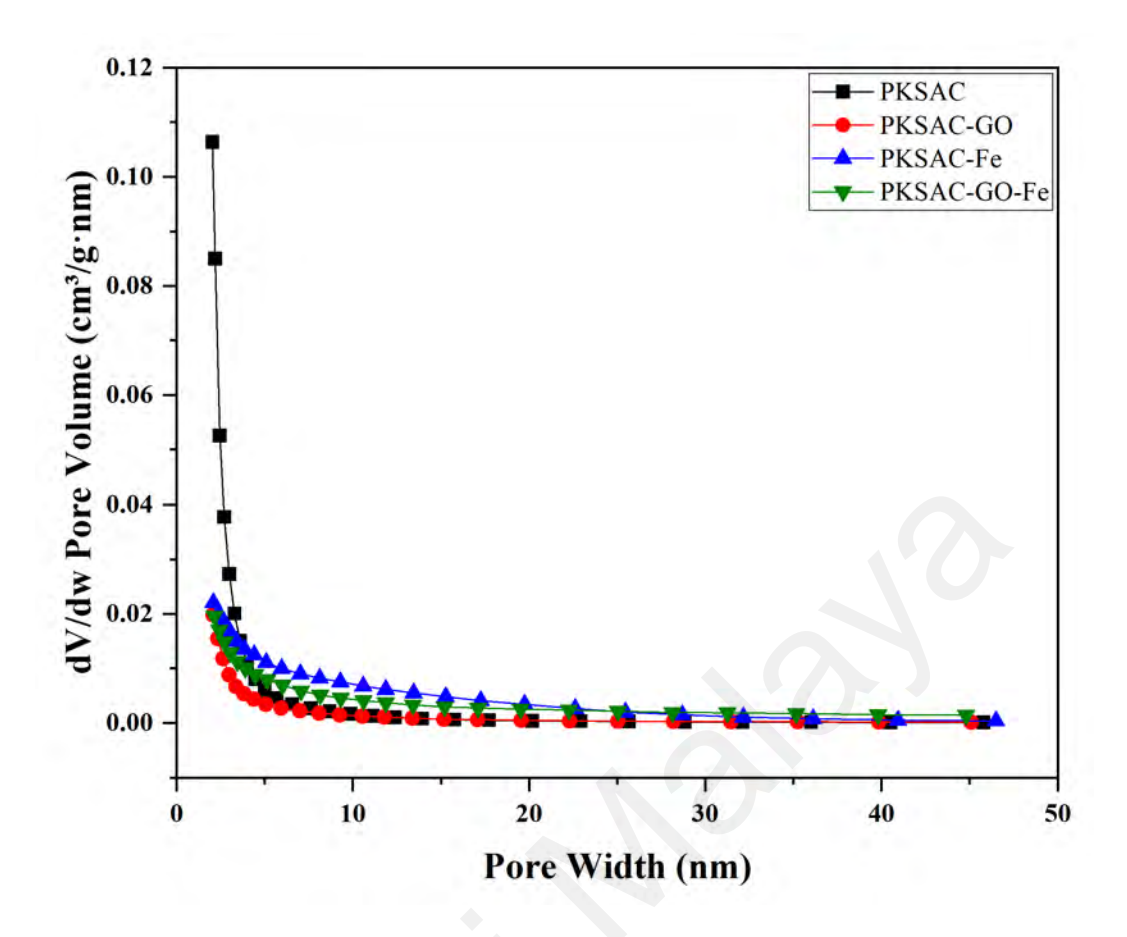


Figure 4.5: Pore Size Distribution of PKSAC-Based Adsorbents

4.3.2 Morphologies and Elemental Compositions

The surface morphologies of PKSAC-based adsorbents (Figure 4.6) were evaluated using FESEM analysis. For raw PKSAC, the FESEM image (Figure 4.6 (a)) shows a highly porous, heterogeneous, and irregular surface (Xiang & Ghazi, 2019). This is attributed to the activation process during PKSAC development, which creates a network of porous structures. These pores contribute to a large surface area, as supported by BET analysis, which makes them an excellent adsorbent for various applications.

After the impregnation of GO into raw PKSAC, the FESEM image shows that a sheet-like structure was also observed beside the porous structure of PKSAC. The presence of a sheet-like structure signifies the successful impregnation of GO into PKSAC. On the other hand, for PKSAC-Fe, the impregnation of iron oxide into PKSAC adds an

agglomerated structure in addition to the existing porous structure. This modification maintains the porous structure of PKSAC while adding the unique properties of iron oxide (Pang et al., 2020).

In the case of PKSAC-GO-Fe, the FESEM image shows a combination of porous, sheet-like, and agglomerated structures, which indicates the successful impregnation of both GO and iron oxide into PKSAC. The composite integrates the properties of all three materials, resulting in enhanced adsorption performance. In short, the FESEM analysis effectively illustrates the surface morphologies of various PKSAC-based adsorbents, confirming the successful impregnation of graphene oxide and iron oxide into the raw PKSAC.

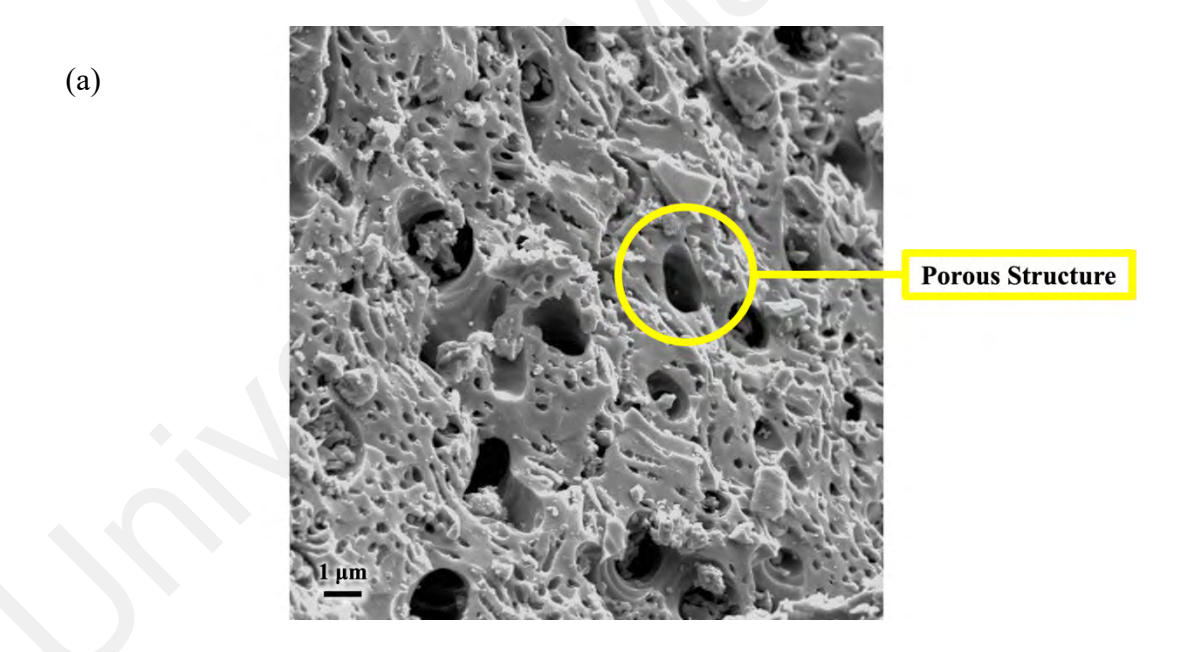


Figure 4.6: FESEM Images of (a) PKSAC, (b) PKSAC-GO, (c) PKSAC-Fe, and (d) PKSAC-GO-Fe

Figure 4.6: Continued

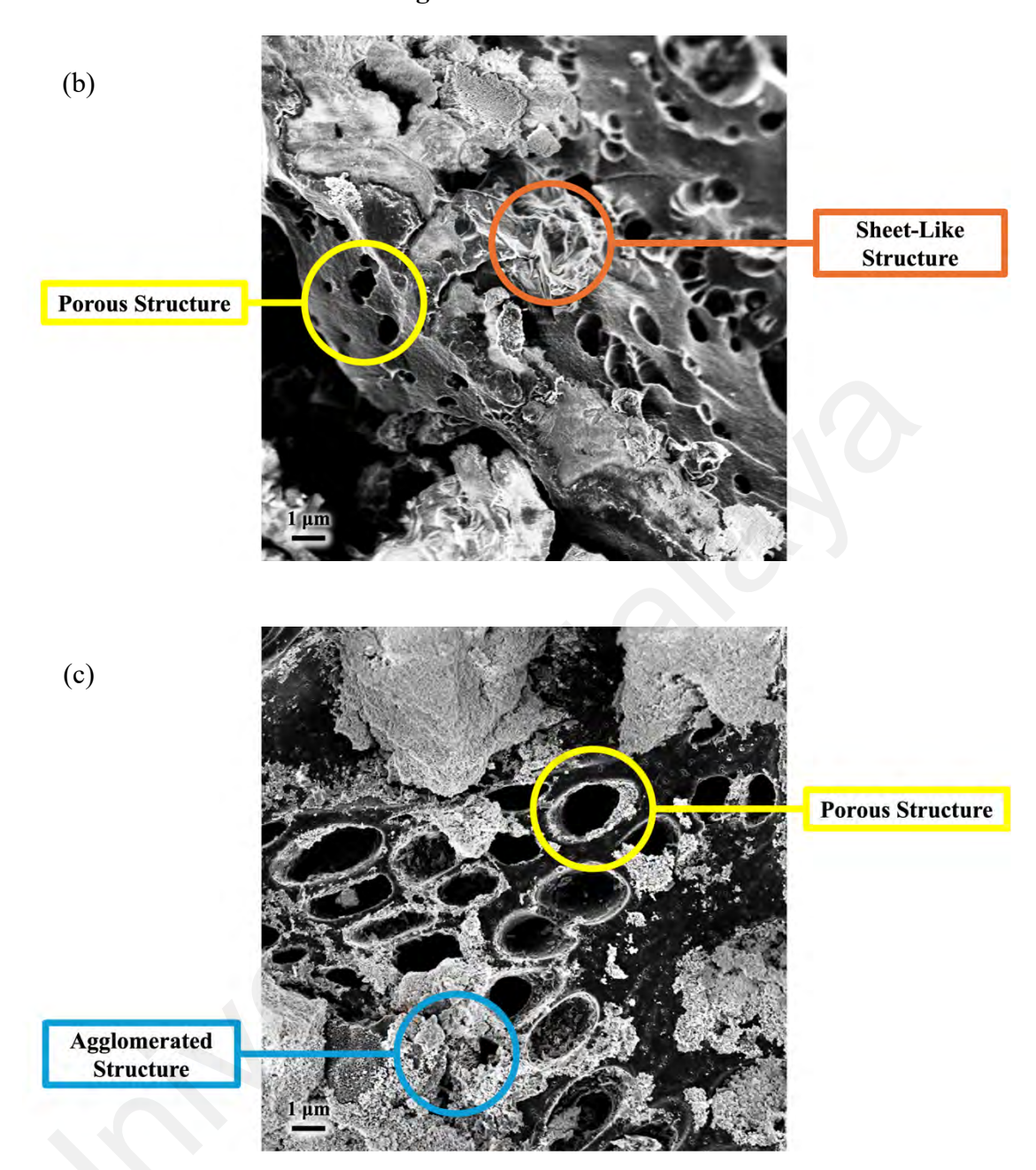
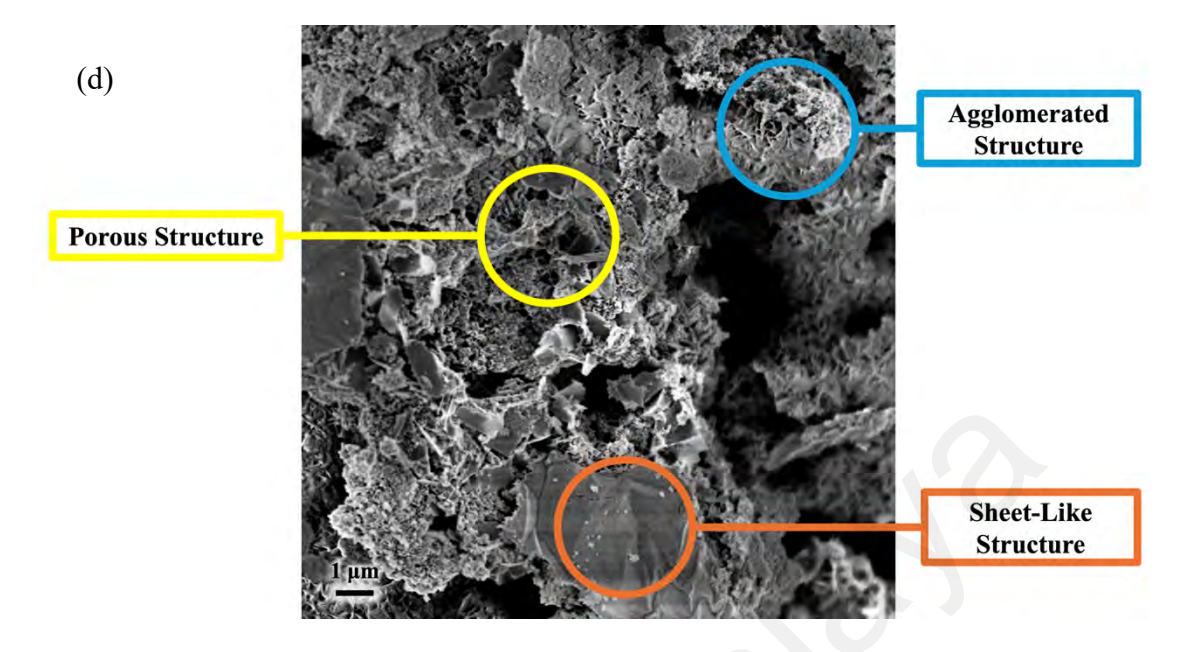


Figure 4.6: Continued



Additionally, EDX analysis reveals the elemental compositions of PKSAC-based adsorbents, as depicted in Table 4.3 and Figure 4.7. The raw PKSAC is composed of 93.99% carbon and 6.01% oxygen. After impregnating GO into PKSAC, the carbon composition decreases by 4.1%, from 93.99% to 90.18%, while the oxygen composition increases by 63.4%, from 6.01% to 9.82%. These changes are attributed to the impregnation of GO, which has a higher oxygen-to-carbon ratio (59.32% carbon and 37.07% oxygen) due to its abundance of oxygenated functional groups. In the case of PKSAC-Fe, the impregnation of iron oxide introduces 7.81% iron. Additionally, the oxygen composition increases significantly by 318.1%, from 6.01% to 25.13%, indicating successful iron oxide impregnation. At the same time, the carbon composition decreases by 28.7%, from 93.99% to 67.06%, likely due to the iron oxide deposition on the surface of PKSAC, covering some carbon atoms. For the PKSAC-GO-Fe composite, the oxygen composition of 49.73% is the highest among all the PKSAC-based adsorbents, with increments of 727.5% compared to PKSAC (6.01%), 406.4% compared to PKSAC-GO (9.82%), and 97.9% compared to PKSAC-Fe (25.13%), respectively. The presence of

15.25% iron and the higher atomic percentage of oxygen confirms the successful impregnation of both GO and iron oxide into PKSAC. The lower carbon composition of 35.02% in PKSAC-GO-Fe is likely due to the coverage of carbon atoms by iron oxide, which was also observed in the EDX analysis for PKSAC-Fe.

In short, FESEM/EDX analysis offers a comprehensive view of the surface morphologies and elemental compositions of PKSAC-based adsorbents. The FESEM images show the successful impregnation of GO and iron oxide into raw PKSAC. This was indicated by the presence of porous (PKSAC), sheet-like (GO), and agglomerated (iron oxide) structures in the ternary composite. The EDX analysis further confirmed the successful impregnation of these materials by showing changes in their elemental compositions.

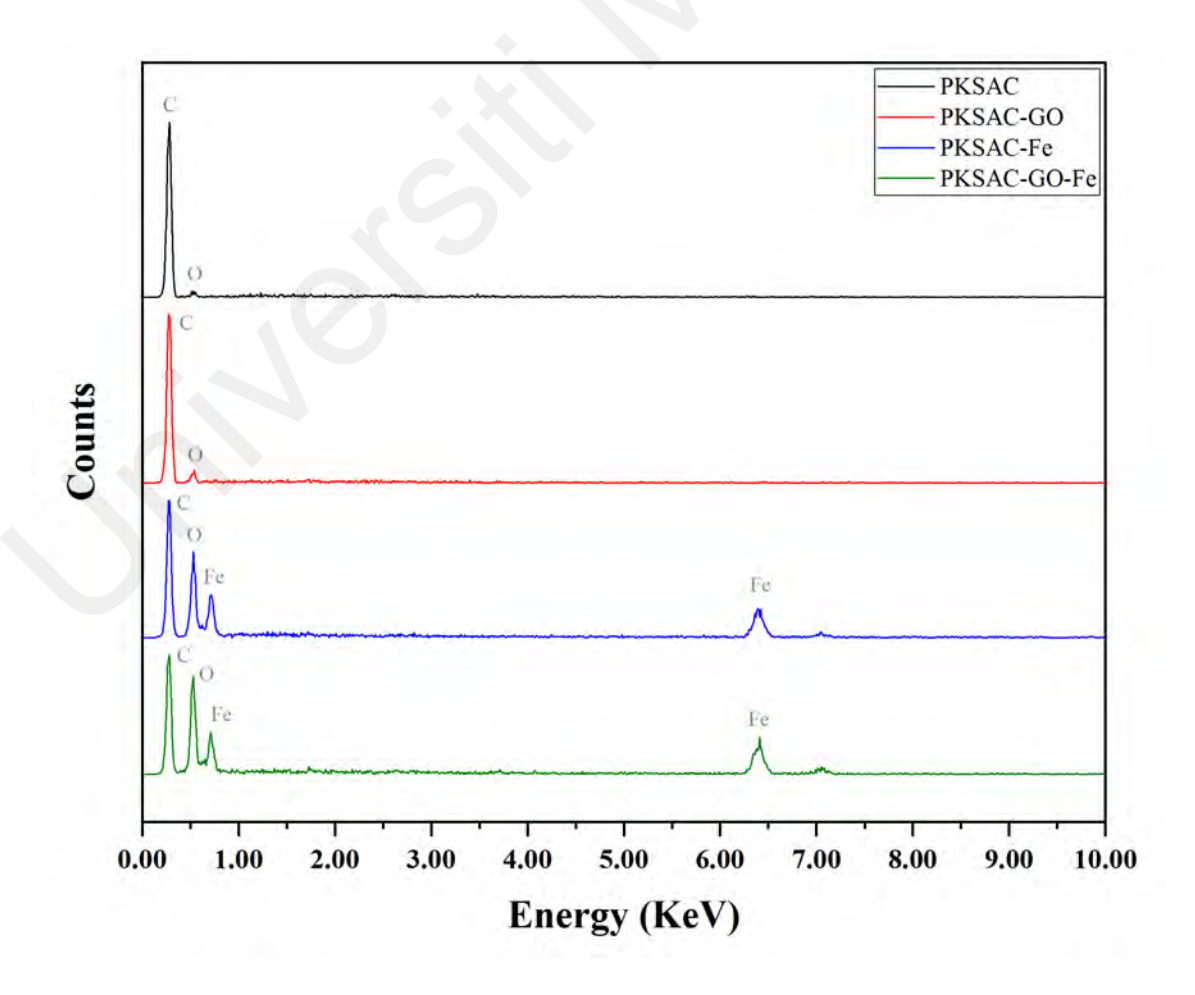


Figure 4.7: EDX Spectra of PKSAC-Based Adsorbents

Table 4.3: EDX Analysis of PKSAC-Based Adsorbents

| Adsorbents | Atomic (%) | | | | |
|-------------|------------|--------|-------|--|--|
| Ausorbents | Carbon | Oxygen | Iron | | |
| PKSAC | 93.99 | 6.01 | - | | |
| PKSAC-GO | 90.18 | 9.82 | - | | |
| PKSAC-Fe | 67.06 | 25.13 | 7.81 | | |
| PKSAC-GO-Fe | 35.02 | 49.73 | 15.25 | | |

4.3.3 Magnetic Properties

The magnetic properties of PKSAC-based adsorbents were examined using VSM analysis, with results presented in Figure 4.8 and Table 4.4. Saturation magnetization, coercivity, and retentivity are the three essential parameters in VSM analysis. Saturation magnetization indicates the strength of the magnetic properties, coercivity reveals the material's resistance to demagnetization, and retentivity indicates the capacity of materials to remain magnetized even in the absence of a magnetic field (Sharma et al., 2024).

The saturation magnetization of raw PKSAC and PKSAC-GO was determined to be 1.41 emu/g and 1.06 emu/g, respectively, according to VSM analysis. These negligible values can be related to the non-magnetic nature of both PKSAC and GO. The iron oxide impregnation into raw PKSAC, however, significantly enhances the saturation magnetization from 1.41 emu/g to 24.37 emu/g. This can be attributed to the magnetic properties contributed by iron oxide.

In the case of PKSAC-GO-Fe, a magnetization of 33.74 emu/g indicates excellent magnetic properties, which is higher than some previous studies (Abdi et al., 2019; Gao et al., 2019; Hosseinzadeh & Ramin, 2018). The coercivity of 45.094 G shows the excellent resistance of PKSAC-GO-Fe to demagnetizing, and 3.0817 emu/g retentivity indicates that the composite can maintain its magnetism in the absence of a magnetic

field. The PKSAC-GO-Fe composite shows good magnetic properties, which is essential for post-treatment separation by an external magnetic field.

In summary, the VSM analysis shows that iron oxide impregnation greatly improves the magnetic properties of PKSAC-based adsorbents. The PKSAC-GO-Fe composite shows excellent magnetic properties, with high saturation magnetization, coercivity, and retentivity. These characteristics are crucial for facilitating the efficient separation of adsorbents from treated water using an external magnetic field, making the PKSAC-GO-Fe composite a promising material for practical wastewater treatment applications.

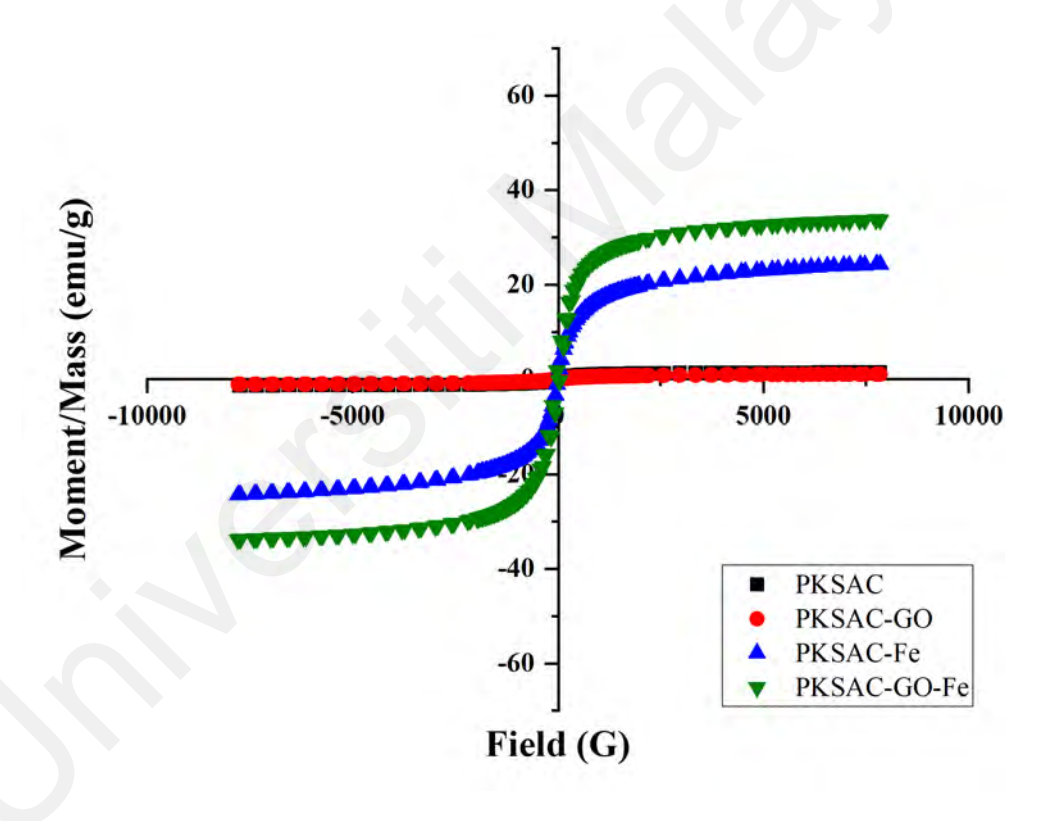


Figure 4.8: VSM Curve of PKSAC-Based Adsorbents

Table 4.4: Magnetic Properties of PKSAC-Based Adsorbents

| Adsorbents | Coercivity (G) | Magnetization (emu/g) | Retentivity (emu/g) |
|-------------|----------------|-----------------------|---------------------|
| PKSAC | 20.13 | 1.41 | 0.06 |
| PKSAC-GO | 54.72 | 1.06 | 0.08 |
| PKSAC-Fe | 2.08 | 24.37 | 0.11 |
| PKSAC-GO-Fe | 45.09 | 33.74 | 3.08 |

4.3.4 Particle Size Distribution

PSD analysis provides insights into the range and distribution of particle sizes within a material. There are several important parameters in PSD analysis. The particle sizes at which 10%, 50%, and 90% of the cumulative particle volume falls are denoted as d_{10%}, d_{50%}, and d_{90%}, respectively. Moreover, the Sauter mean diameter is a weighted average particle size based on the surface area of the particles, which reveals the effective particle size of a material. The results of PSD analysis for PKSAC-based adsorbents are shown in Table 4.5 and Figure 4.9.

Based on PSD analysis, for PKSAC, the particle size distribution shows d_{10%} at 93.22 μm, d_{50%} at 425.58 μm, and d_{90%} at 704.04 μm. The Sauter mean diameter was determined to be 78.30 μm, indicating ample surface area for adsorption. The aforementioned values are consistent with previously reported activated carbon derived from palm kernel fiber (Kundu et al., 2014). After the impregnation of GO into PKSAC, the PKSAC-GO composite shows a distribution of d_{10%} at 39.44 μm, d_{50%} at 299.31 μm, and d_{90%} at 494.82 μm. These values are determined to be lower than those of raw PKSAC by approximately 57.7%, 29.7%, and 29.7%, respectively. This phenomenon can be attributed to the exfoliation of PKSAC and GO during the synthesis process of the composite, which involves sonication and an acidic environment (Yan et al., 2014). For PKSAC-Fe, after the impregnation of iron oxide, the particle size distribution shows d_{10%} at 10.34 μm, d_{50%} at 55.81 μm, and d_{90%} at 158.15 μm, which are lower by 88.9%, 86.9%, and 77.5%, respectively compared to PKSAC. Smaller particle sizes observed in PKSAC-Fe could be attributed to the uniform dispersion of iron oxide onto PKSAC, in addition to the effects of sonication and an acidic environment.

The PKSAC-GO-Fe composite shows a particle size distribution with $d_{10\%}$ at 14.99 μ m, $d_{50\%}$ at 392.31 μ m, and $d_{90\%}$ at 989.17 μ m. Compared to raw PKSAC, PKSAC-GO,

and PKSAC-Fe, the d_{90%} value of PKSAC-GO-Fe is higher by approximately 40.5%, 99.9%, and 525.5%, respectively. This increment can be explained by the larger particles formation within the ternary composite. The larger particles lead to a higher tendency for rapid settling and facilitate the efficient separation of particles from the supernatant after the treatment processes (Bhattacharyya et al., 2018). Besides that, the PSD curve of PKSAC-GO-Fe (Figure 4.9) also displays the characteristics of all components, further confirming the presence of PKSAC, GO, and iron oxide in the ternary composite. To sum up, the PSD analysis reveals the particle size distribution of PKSAC-based adsorbents, where the impregnation of GO and iron oxide into PKSAC results in smaller particles for PKSAC-GO and PKSAC-Fe, and larger composite particles for PKSAC-GO-Fe.

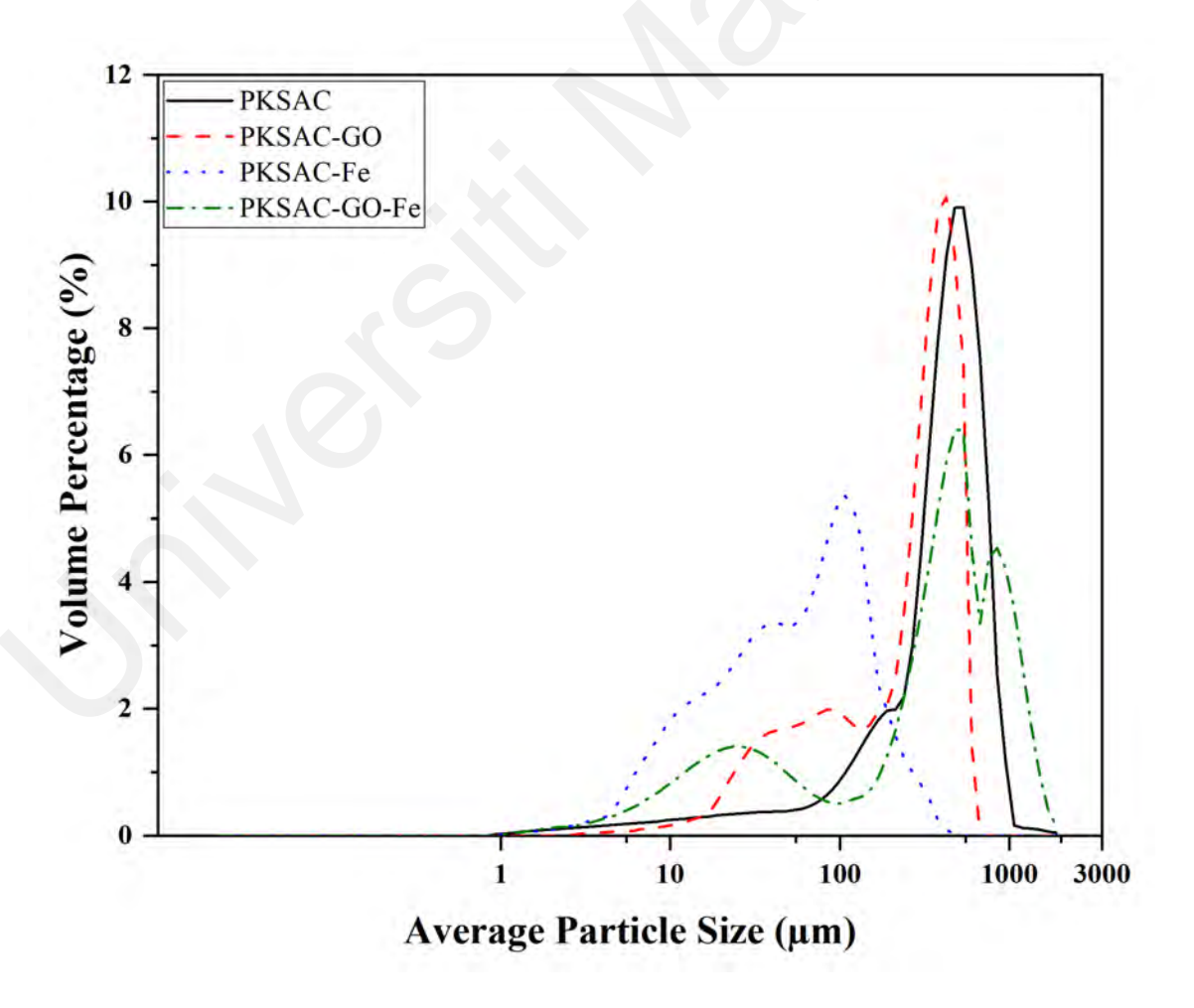


Figure 4.9: Particle Size Distribution of PKSAC-Based Adsorbents

Table 4.5: Particle Size Distribution of PKSAC-Based Adsorbents

| Adsorbents | d _{10%} (μm) | d _{50%} (μm) | d _{90%} (μm) | Sauter Mean Diameter (µm) |
|-------------|-----------------------|-----------------------|-----------------------|------------------------------|
| PKSAC | 93.22 | 425.58 | 704.04 | 78.30 |
| PKSAC-GO | 39.44 | 299.31 | 494.82 | 98.81 |
| PKSAC-Fe | 10.34 | 55.81 | 158.15 | 25.06 |
| PKSAC-GO-Fe | 14.99 | 392.31 | 989.17 | 41.77 |

4.3.5 Crystalline Structure

The crystalline structure of PKSAC-based adsorbents in this study was investigated using XRD analysis, as depicted in Figure 4.10. The crystalline phases found in the PKSAC-based adsorbents were identified by examining the diffraction peaks and their 20 values. The International Centre for Diffraction Data (ICDD), previously denoted as the Joint Committee on Powder Diffraction Standards (JCPDS), is used to identify the phases present in the XRD spectra. As shown in Figure 4.10, the amorphous structure of raw PKSAC is indicated by broad peaks with no sharp features. This is a typical structure of PKSAC, as an activated carbon mainly consists of disordered carbonaceous materials, which known for its high surface area and porosity rather than crystallinity. Peaks observed around 26.0° and 44.0° are assigned to the (002) and (100) planes and correspond to planar graphite and amorphous structures, respectively. These peaks signify that the carbon layers with disordered structures are presence in the raw PKSAC (Sukhbaatar et al., 2021).

After impregnating GO into raw PKSAC, the peak of the PKSAC-GO composite combines the characteristics of both PKSAC and GO. In addition to the broad peak at 26.0° which is linked to the graphitic carbon from PKSAC, there is an additional peak at 11.7° which corresponds to the interlayer spacing of GO (Thangappan et al., 2014). This peak aligns with JCPDS card no. 75-1621, which is the JCPDS data for GO. The peaks of PKSAC and GO coexist in the PKSAC-GO composite, suggesting that the individual

components maintain their individual structures and indicating successful composite formation.

After the impregnation of iron oxide into PKSAC, the XRD pattern of PKSAC-Fe shows peaks for both PKSAC and iron oxide. Peaks at 30.2°, 35.8°, 57.5°, and 63.1° confirm the presence of iron oxide, which correspond to the (220), (311), (511), and (440) planes of Fe₃O₄. The aforementioned peaks align well with the JCPDS standard for iron oxide (JCPDS card no. 75-0033), which confirms the presence of iron oxide in the composite. This indicates that iron oxide is impregnated into PKSAC without significantly altering its original structure. Besides that, the broad peak of carbon indicates that the amorphous nature of PKSAC is maintained in the composite.

On the other hand, when both GO and iron oxide are impregnated into PKSAC, the PKSAC-GO-Fe composite exhibits peaks consistent with all three components. The presence of all characteristic peaks suggests the successful impregnation of GO and iron oxide into PKSAC. The impregnation process maintains their structural properties without causing significant changes to their structures. In short, XRD analysis provided critical insights into the crystalline structure of PKSAC-based adsorbents. PKSAC showed amorphous characteristics, GO exhibited peaks indicating a layered structure, and iron oxide displayed clear crystalline peaks. All PKSAC-based composites successfully retained the crystalline features of the individual materials, confirming the successful synthesis and impregnation of the components while maintaining their individual characteristics.

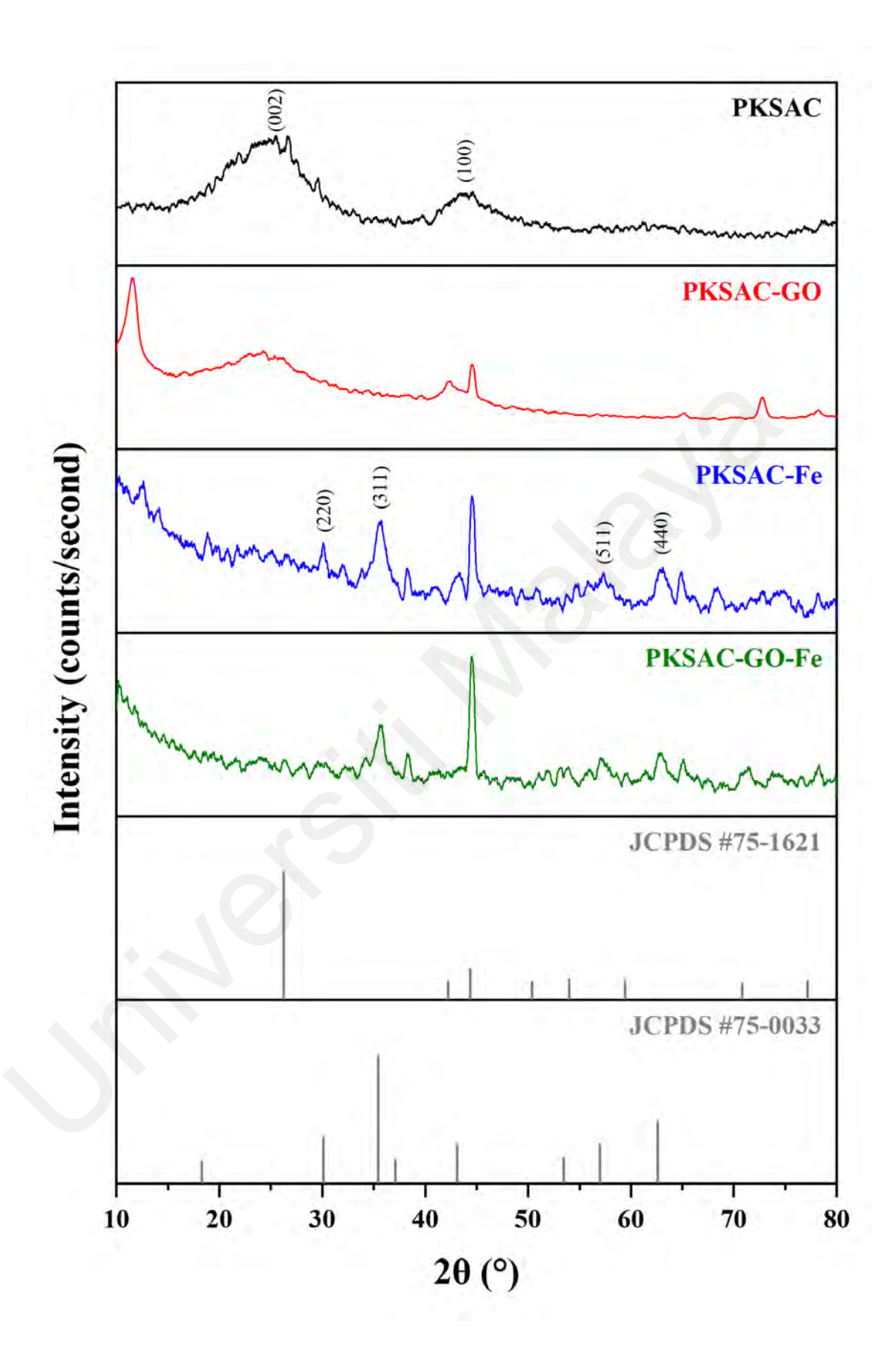


Figure 4.10: XRD Pattern of PKSAC-Based Adsorbents

4.3.6 Point of Zero Charge

The pH_{pzc} is a critical parameter for understanding the surface charge properties of PKSAC-based adsorbents. The pH_{pzc} is the pH at which the adsorbent surface has no net charge. At pH values above the pH_{pzc}, the surface is negatively charged, while below the pH_{pzc}, it becomes positively charged. This characteristic influences the adsorption behavior of the material towards different ionic species, making it essential for optimizing adsorbents for various applications. Figure 4.11 illustrates the pH_{pzc} plots for PKSAC-based adsorbents.

For raw PKSAC, the pH_{pzc} is determined to be at pH 8.4, meaning the surface charge of PKSAC is neutral at this pH. Below pH 8.4, the surface becomes positively charged, enhancing the adsorption of negatively charged (anionic) species. Conversely, above pH 8.4, the surface becomes negatively charged, promoting the adsorption of cationic species. When GO is impregnated into PKSAC to form the PKSAC-GO composite, the pH_{pzc} shifts significantly from pH 8.4 to pH 3.0. This shift is due to the impregnation of GO, which has a lower pH_{pzc} (pH 2.1), thereby affecting the overall pH_{pzc} of the composite. As a result, the surface of PKSAC-GO is neutral at a much lower pH, altering its adsorption characteristics. Similarly, for the PKSAC-Fe composite, after the impregnation of iron oxide into PKSAC, the pH_{pzc} is determined to be at pH 7.2, lower than the pH_{pzc} of raw PKSAC (pH 8.4) due to the addition of iron oxide (pH 6.4). The combination of PKSAC and iron oxide results in a composite with an intermediate pH_{pzc}, which is nearly neutral.

For the PKSAC-GO-Fe composite, the pH_{pzc} is around pH 5.6. This value represents an average of the pH_{pzc} values of PKSAC (pH 8.4), GO (pH 2.1), and Fe (pH 6.4). When the solution pH is below 5.6, the surface will be positively charged, enhancing the adsorption of anionic pollutants. This observation aligns with experimental results, which

show higher performance under acidic conditions. However, significant removal at solution pH values above the pH_{pzc} was also observed, indicating that electronic interaction is not the sole predominant mechanism in the adsorption process. Other factors, such as chemical interactions and surface functional groups, also contribute to the overall adsorption performance. A study by Abdi et al. (2019) reported that a magnetic graphene oxide-modified composite with a similar pH_{pzc} of 5.4, supporting these findings. In summary, the pH_{pzc} analysis reveals how the GO and iron oxide impregnation alters the surface charge properties of PKSAC-based adsorbents. The pH_{pzc} values shift significantly depending on the materials combined, affecting the adsorption behavior towards different ionic species.

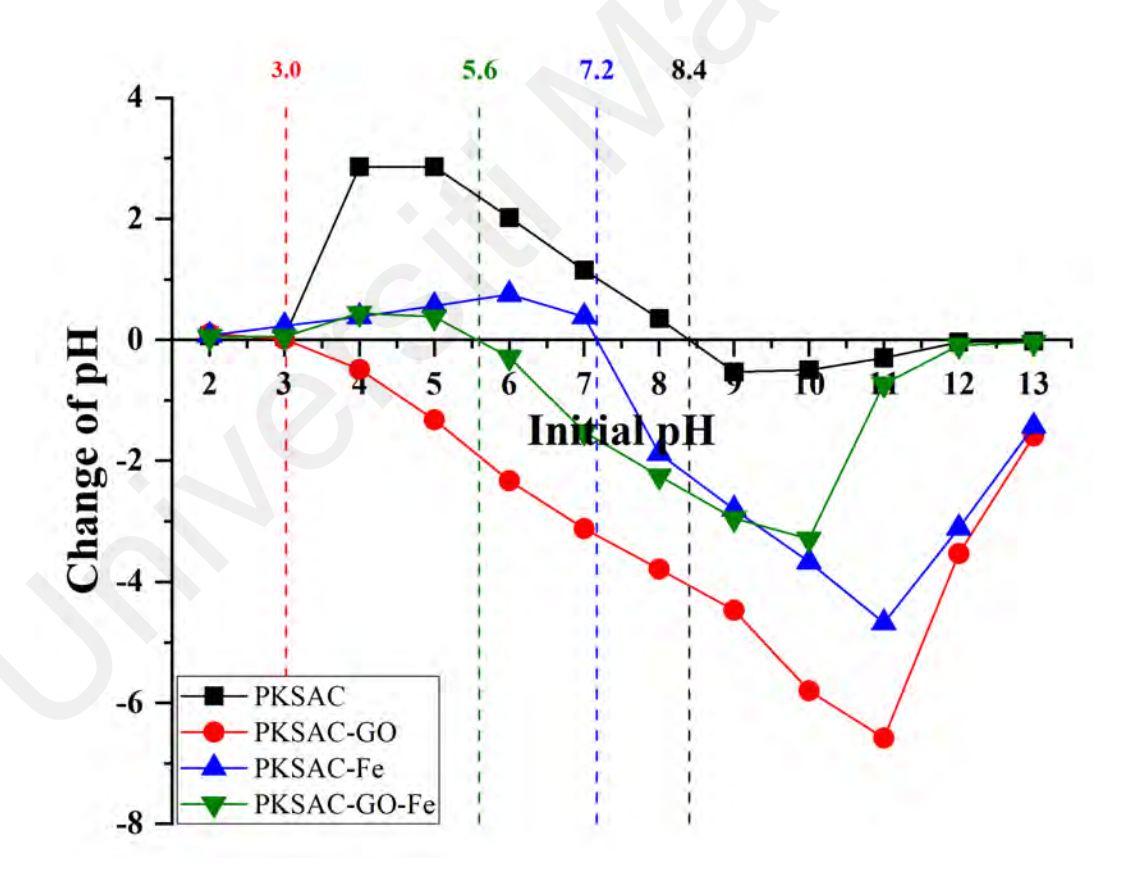


Figure 4.11: pH_{pzc} Plot of PKSAC-Based Adsorbents

4.3.7 Relating Physicochemical Characteristics with Adsorption Performance of PKSAC-Based Adsorbents

The physicochemical characterization of PKSAC-based adsorbents revealed significant relationships between their characteristics and adsorption performance, as summarized in Table 4.6. Textural analysis showed that reduced surface areas (PKSAC-GO-Fe: 280.39 $\,\mathrm{m}^2/\mathrm{g}$; PKSAC: 915.41 $\,\mathrm{m}^2/\mathrm{g}$) and pore volumes were due to the introduction of a lower surface area of GO and pore blockage by depositing iron oxide particles. The color removal efficiency and adsorption capacity, however, were not inhibited by the lower surface area, indicating that chemisorption mechanisms played a more predominant role than physisorption in the adsorption process. This is further supported by EDX analysis, which demonstrated increased oxygen content (PKSAC-GO-Fe: 49.73%; PKSAC: 6.01%) with iron incorporation (15.25%). These changes suggest enhanced surface functionalities provided by oxygenated groups of GO and Fe-O bonds of iron oxide. These functionalities in turn facilitate the adsorbent-adsorbate interactions (e.g., hydrogen bonding, π - π interactions).

The presence of porous, sheet-like, and agglomerated morphologies in the FESEM image of the ternary composite confirmed the successfully impregnation of GO and iron oxide into raw PKSAC. Besides that, XRD analysis further signifies the presence of graphite and Fe₃O₄ phases in the ternary composite. PKSAC-GO-Fe has a significant saturation magnetization of 33.74 emu/g. With this, secondary pollution can be minimized through efficient post-treatment separation using an external magnetic field. The PSD results demonstrated that the bigger particle size of PKSAC-GO-Fe (d_{90%}: 989.17 μm) facilitated the faster separation process. In addition, pH_{pzc} of PKSAC-GO-Fe (pH 5.6) indicated surface charge shifting after GO and iron oxide impregnation, aligning with adsorption trends where anionic pollutants have higher performance under acidic

conditions, although non-electrostatic interactions also play a role, where significant removal was also achieved at higher pH ranges.

The physicochemical characterization is very important to understand how impregnation alters the properties of PKSAC-based adsorbents. The changes recorded after impregnation are directly related to the adsorption performance of PKSAC-based adsorbents, which are essential for designing adsorbents with desired functionalities and optimized performance.

Table 4.6: Summary of Physicochemical Characteristics and Adsorption Performance of PKSAC-Based Adsorbents

| Parameter | PKSAC | PKSAC- | PKSAC- | PKSAC- | |
|--------------------------------------|--------|--------|--------|--------|--|
| rarameter | TRSAC | GO | Fe | GO-Fe | |
| Physicochemical Characteristics | | | | | |
| BET surface area (m ² /g) | 915.41 | 708.72 | 420.82 | 280.39 | |
| Average pore diameter (nm) | 3.00 | 4.66 | 6.04 | 9.99 | |
| Carbon (C) (%) | 93.99 | 90.18 | 67.06 | 35.02 | |
| Oxygen (O) (%) | 6.01 | 9.82 | 25.13 | 49.73 | |
| Iron (Fe) (%) | - | | 7.81 | 15.25 | |
| Magnetization (emu/g) | - | - | 24.37 | 33.74 | |
| pH_{pzc} | 8.4 | 3.0 | 7.2 | 5.6 | |
| Adsorption Performance | | | | | |
| Color removal efficiency (%) | 43.2 | 66.0 | 73.1 | 99.8 | |
| Adsorption capacity (mg/g) | 11.8 | 18.0 | 19.9 | 27.3 | |

4.4 Effect of Operational Parameters on Synthetic Wastewater Adsorption using Ternary Composite

Based on the experiment sets suggested by RSM-CCD, the performance of PKSAC-GO-Fe ternary composite in treating synthetic wastewater containing an anionic dye was evaluated in terms of color removal efficiency and adsorption capacity. As in Table 4.7, complete color removal efficiency (100.0%) was achieved under two different conditions: (i) at an initial solution pH of 1.7 using 3 g/L of adsorbent for 4 hours, and (ii) at pH 7 using 5.6 g/L of adsorbent for 4 hours. Additionally, the highest adsorption capacity of 75.2 mg/g was achieved using 1 g/L of the adsorbent at pH 3 for a contact time of 6 hours. The interactive effects of operational parameters were studied, and these interactions were illustrated in 2D plots in the following sections.

Table 4.7: Adsorption of Anionic Dye using PKSAC-GO-Fe

| Run | Initial pH of the Solution | Adsorbent Dosage (g/L) | Time (h) | Color Removal Efficiency (%) | Adsorption Capacity (mg/g) |
|-----|-------------------------------|---------------------------|-------------|------------------------------------|----------------------------------|
| 1 | 7.0 | 3.0 | 4.0 | 96.6 | 32.2 |
| 2 | 11.0 | 1.0 | 2.0 | 14.2 | 14.2 |
| 3 | 3.0 | 5.0 | 2.0 | 96.9 | 19.4 |
| 4 | 7.0 | 3.0 | 4.0 | 96.7 | 32.2 |
| 5 | 7.0 | 3.0 | 4.0 | 96.1 | 32.0 |
| 6 | 11.0 | 1.0 | 6.0 | 15.8 | 15.8 |
| 7 | 7.0 | 3.0 | 6.6 | 97.6 | 32.5 |
| 8 9 | 1.7 | 3.0 | 4.0 | 100.0 | 33.3 |
| 9 | 7.0 | 0.4 | 4.0 | 26.5 | 72.0 |
| 10 | 7.0 | 5.6 | 4.0 | 100.0 | 17.8 |
| 11 | 7.0 | 3.0 | 1.4 | 96.3 | 32.1 |
| 12 | 11.0 | 5.0 | 6.0 | 56.8 | 11.4 |
| 13 | 12.3 | 3.0 | 4.0 | 28.5 | 9.5 |
| 14 | 3.0 | 1.0 | 2.0 | 73.0 | 73.0 |
| 15 | 3.0 | 1.0 | 6.0 | 75.2 | 75.2 |
| 16 | 11.0 | 5.0 | 2.0 | 55.5 | 11.1 |
| 17 | 7.0 | 3.0 | 4.0 | 91.5 | 30.5 |
| 18 | 7.0 | 3.0 | 4.0 | 96.7 | 32.2 |
| 19 | 3.0 | 5.0 | 6.0 | 98.4 | 19.7 |
| 20 | 7.0 | 3.0 | 4.0 | 97.5 | 32.5 |

4.4.1 Effect of Initial pH of the Solution

The initial pH of the solution is crucial in the adsorption process because the adsorbent surface charge can be protonated or deprotonated in the presence of protons and electrons. In this study, the effect of pH, ranging from 3 to 11, was investigated. Figure 4.12 shows the 2D plots of the interaction between operational parameters for color removal efficiency. As shown in Figure 4.12 (a), the color removal efficiency decreases from 70.7% to 10.5% when the solution pH is increased from pH 3 to 11 at a contact time of 4 hours using 1 g/L of PKSAC-GO-Fe. However, when the PKSAC-GO-Fe dosage is increased by 140.0% from 1 to 2.4 g/L, the color removal efficiency increases by 62.2% from 49.8% to 80.8% even under slightly alkaline conditions (around pH 8).

The effect of solution pH can be explained by considering the pH_{pzc} of the PKSAC-GO-Fe composite. The pH_{pzc} of PKSAC-GO-Fe is 5.6, indicating that its surface is positively charged below pH 5.6 and negatively charged above this value. Since AB113 is an anionic dye, there will be electrostatic attraction below the pH_{pzc} and electrostatic repulsion above the pH_{pzc}. Thus, higher removal efficiency was achieved under acidic conditions based on the experimental results. However, significant adsorption was also observed under alkaline conditions, suggesting that the adsorption of AB113 using PKSAC-GO-Fe is not solely dominated by electrostatic interactions.

For example, in the study by Mosoarca et al. (2020), the adsorbent exhibited a similar pH_{pzc} of 5.8. Experimental results showed that the adsorption capacity remained relatively consistent between pH 6 and 12 when removing cationic methylene blue dye. However, a significant adsorption capacity was also observed at pH levels below the pH_{pzc}, indicating that electrostatic interactions were not the sole mechanism driving the adsorption process. Additional mechanisms, such as chemical reactions between the adsorbent and dye molecules, π - π interactions, hydrogen bonding, and other interactions,

also play a significant role (Cemin et al., 2021; Han et al., 2011; Pang et al., 2017; Yadav et al., 2022). These results indicate that excellent color removal efficiency can be achieved within a wide range of pH using PKSAC-GO-Fe, which is advantageous for practical applications, as the pH of actual wastewater can vary greatly.

On the other hand, Figure 4.13 (a) illustrate the interaction between initial solution pH and adsorbent dosage on the adsorption capacity of PKSAC-GO-Fe in treating AB113 dye. As shown in Figure 4.13 (a), PKSAC-GO-Fe achieves the highest adsorption capacity under acidic conditions. The adsorption capacity decreases gradually as the solution pH increases from 3 to 11. This observation is consistent with the nature of the AB113 dye, which is an anionic dye and favors adsorption when the solution pH is less than the pH_{pzc} (5.6). Similar findings were reported by Jain et al. (2020b).

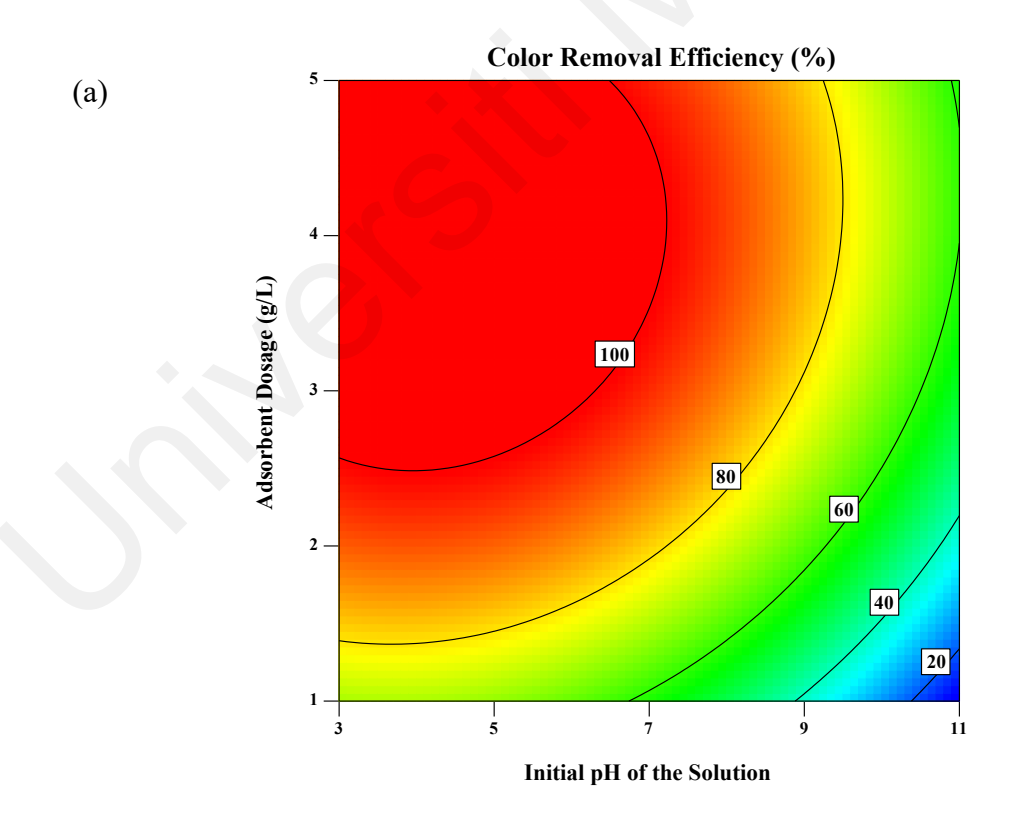
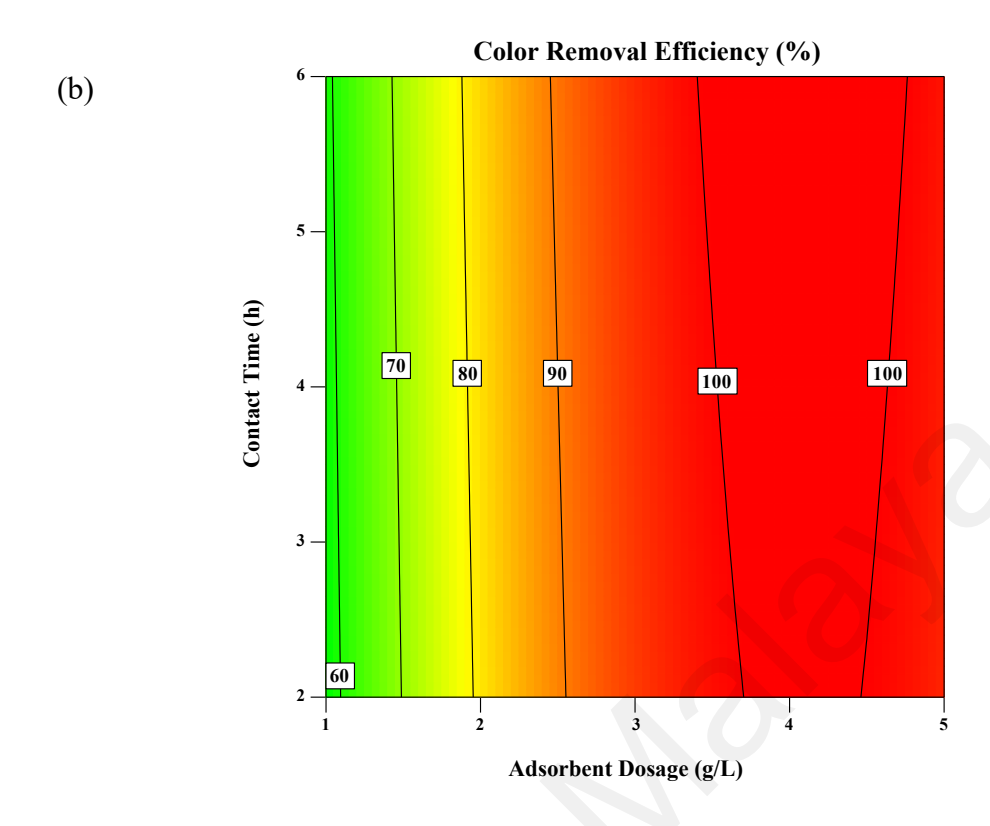
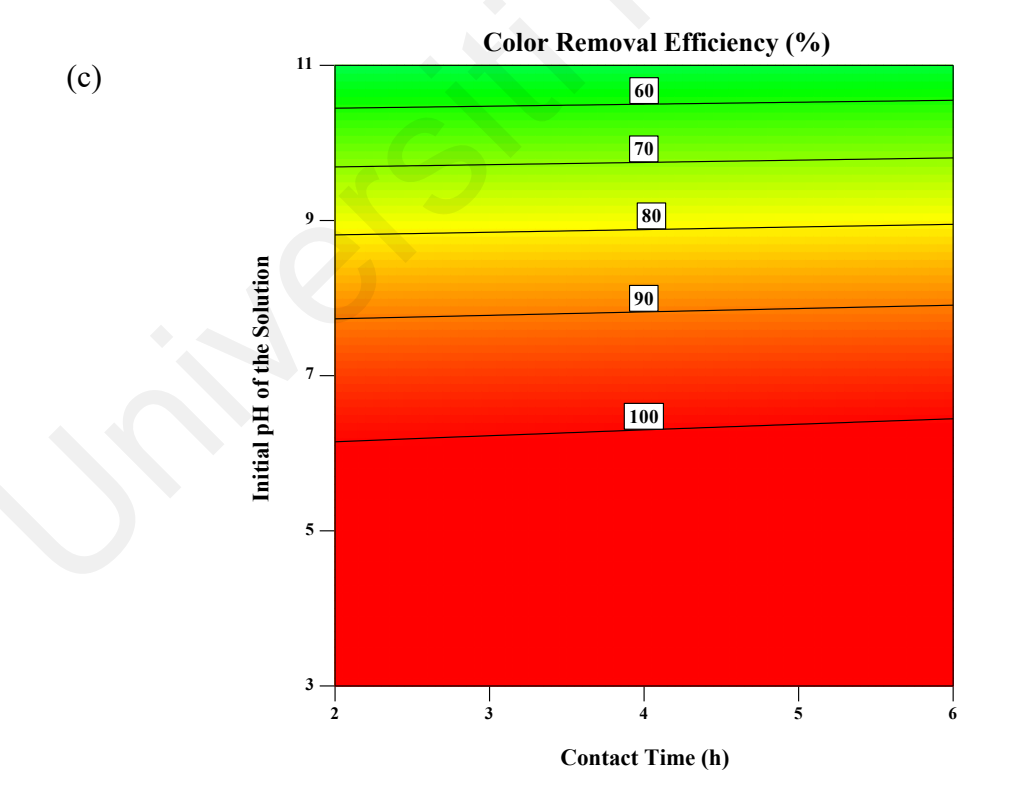
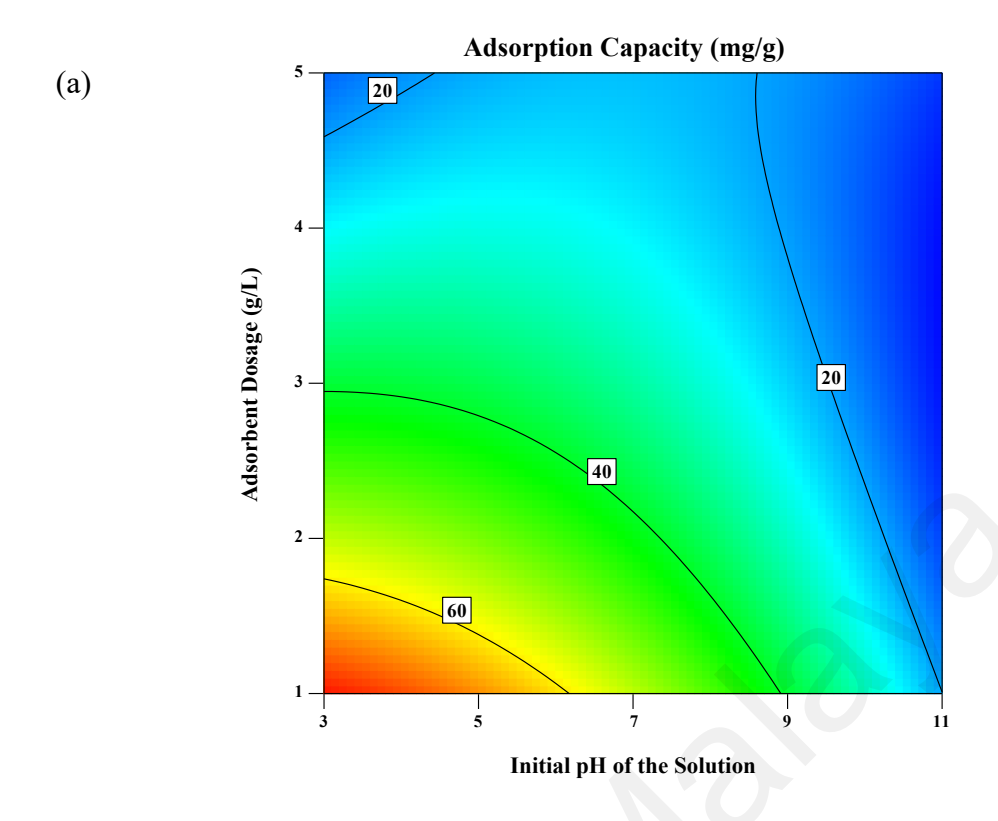


Figure 4.12: Interactive Effects of (a) pH and Adsorbent Dosage, (b) Adsorbent Dosage and Contact Time, and (c) Contact Time and pH on Color Removal Efficiency in Treating Anionic Dye using PKSAC-GO-Fe

Figure 4.12: Continued







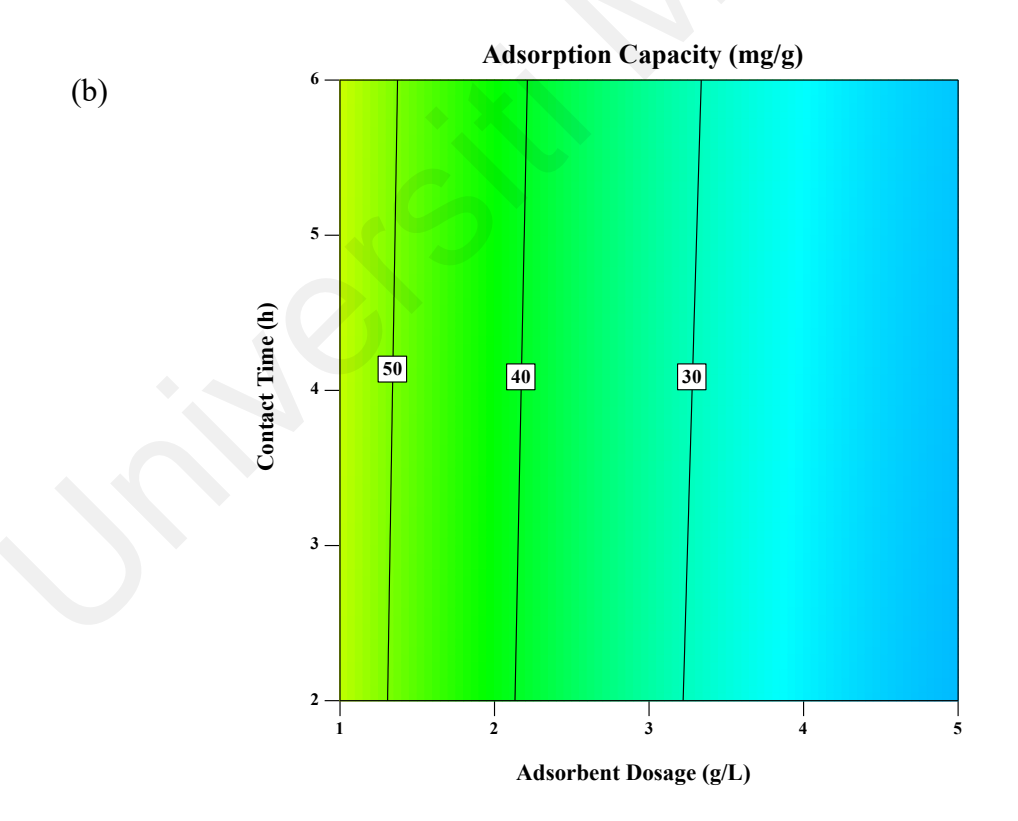
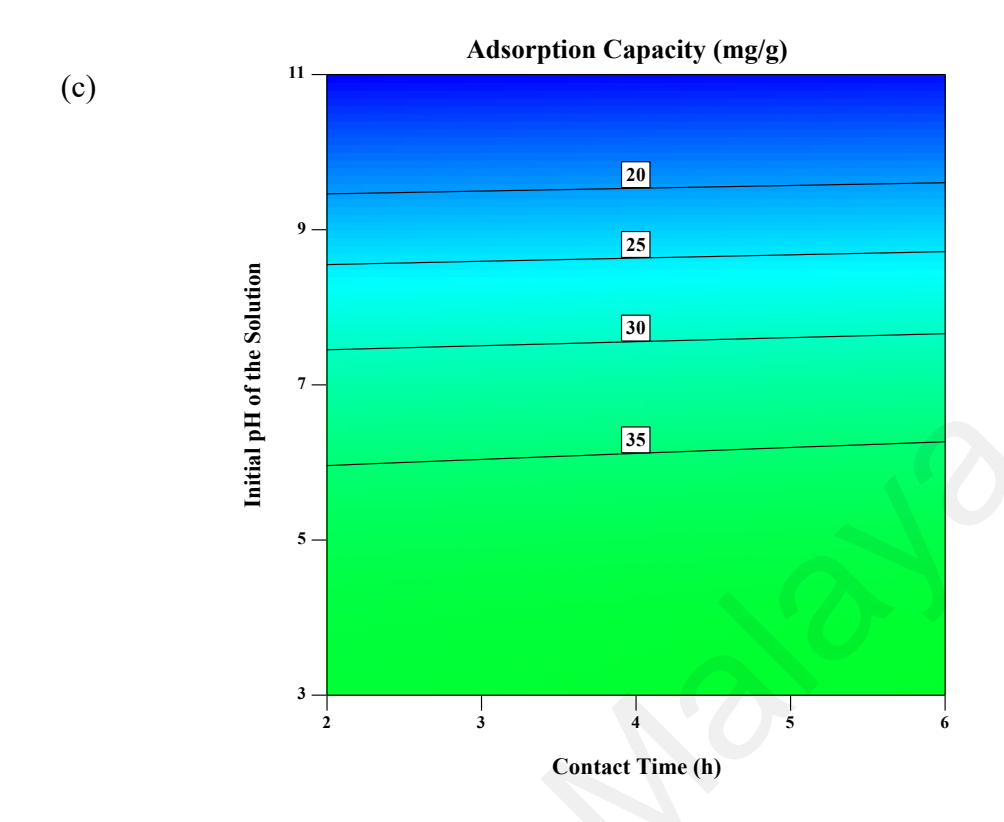


Figure 4.13: Interactive Effects of (a) pH and Adsorbent Dosage, (b) Adsorbent Dosage and Contact Time, and (c) Contact Time and pH on Adsorption Capacity in Treating Anionic Dye using PKSAC-GO-Fe

Figure 4.13: Continued



4.4.2 Effect of Adsorbent Dosage

The effect of PKSAC-GO-Fe dosage on color removal efficiency was investigated by varying the dosage from 1 to 5 g/L. Color removal efficiency increased gradually from 58.2% with 1 g/L of PKSAC-GO-Fe to 100% with 3.5 g/L at pH 7 and a contact time of 4 hours (Figure 4.12 (b)). Besides that, Figure 4.12 (a) show that complete color removal efficiency is achieved with only 2.5 g/L of PKSAC-GO-Fe at pH 3. However, at pH 7, the system required 3.5 g/L of PKSAC-GO-Fe to achieve complete color removal efficiency, which is 40.0% higher. Increasing the adsorbent dosage above 3.5 g/L had little additional effect on color uptake, possibly because the system had reached adsorption equilibrium. This increase can be attributed to increasing the adsorbent dosage enhances color removal efficiency because it provides more binding sites. As the adsorbent dosage increases, more active sites become available for dye molecules

interaction, thereby enhancing adsorption and resulting in greater dye uptake (Djelloul et al., 2017; Pandey et al., 2025).

Figure 4.13 (b), on the other hand, illustrates the effect of PKSAC-GO-Fe dosage and contact time on adsorption capacity. The adsorption capacity decreased by 59.9% from 54.6 to 21.9 mg/g as the PKSAC-GO-Fe dosage increased from 1 to 5 g/L at pH 7 and a contact time of 4 hours. According to the adsorption capacity equation, the denominator, which is the adsorbent dosage, has a predominant effect on the adsorption capacity. Consequently, this increases in adsorbent dosage results in a decrease in the adsorption capacity of the PKSAC-GO-Fe composite. This trend can be attributed to the partial filling of pores with adsorbate and the overcrowding of adsorbent particles, which causes aggregation and reduces the effective surface area available for adsorption (Samaraweera, Rivera, et al., 2023).

4.4.3 Effect of Contact Time

The contact time for the adsorption process was varied from 2 to 6 hours to assess its impact on AB113 dye adsorption. It was observed that contact time had a less significant effect compared to the initial solution pH and adsorbent dosage, as demonstrated in Figures 4.12 (b) and (c) for color removal efficiency and Figures 4.13 (b) and (c) for adsorption capacity. For example, color removal efficiency increased slightly from 57.5% to 58.9% (a 1.4% increase) when the contact time was extended from 2 to 6 hours at pH 7 using 1 g/L of PKSAC-GO-Fe (Figure 4.12 (b)). Similarly, at pH 3, the adsorption capacity increased marginally from 38.8 to 39.7 mg/g (a 0.9 mg/g increase) with the same 4-hour increase in contact time, as shown in Figure 4.13 (c).

The limited impact of contact time can be attributed to the fact that most of the AB113 dye adsorption onto PKSAC-GO-Fe occurred within the first two hours of the process. Initially, numerous active sites are available for adsorption, but as the process continues,

these sites become occupied by dye molecules, leading to a reduced uptake rate with extended contact time (Sen et al., 2024). The findings align well with the kinetics study. Therefore, within the investigated range, contact time does not significantly affect color removal efficiency and adsorption capacity.

4.4.4 Optimization Study

An optimization study was conducted for the PKSAC-GO-Fe to verify the predicted optimized values that suggested by RSM-CCD with the experimental values, as summarized in Table 4.8. The high confidence levels indicate that the model developed using RSM-CCD can be used to predict the performance of the PKSAC-GO-Fe composite in treating AB113 dye accurately for both color removal efficiency and adsorption capacity. The optimum conditions selection is determined by adsorption parameters, such as the initial pH of the solution, adsorbent dosage, and contact time. For instance, the highest adsorption capacity (75.2 mg/g) is predicted to be achieved under acidic conditions (pH 3) with a lower PKSAC-GO-Fe dosage (1 g/L) and a longer contact time (6 hours). On the other hand, the highest color removal efficiency can be achieved at an extreme pH of 1.7 using 3 g/L of adsorbent for 4 hours. Hence, it is important to balance these parameters during the selection of optimum conditions, at the same time, considering economic, environmental, and practical aspects.

An initial pH of 7.5 using 3.7 g/L of adsorbent with a contact time of 2.1 hours were selected as the optimum conditions for treating AB113 using PKSAC-GO-Fe in this study. The pH value of 7.5 aligns with the average discharge standard A in Malaysia (pH 6.0 to 9.0), according to the Malaysian Environmental Law. With this, it eliminates the need for additional chemicals usage for adjusting the wastewater pH after the adsorption process, which reduces operating costs and minimizes the potential environmental impact.

Table 4.8: Optimization Study of PKSAC-GO-Fe

| Initial pH of the Solution | Adsorbent Dosage (g/L) | Time | e Color Remov Efficiency (% | | Adsorption Capacity (mg/g) | |
|----------------------------|---------------------------|------|--------------------------------|------|-------------------------------|------|
| the Solution | Dosage (g/L) | (h) | Pred. | Exp. | Pred. | Exp. |
| 7.5 | 3.7 | 2.1 | 100.0 | 99.8 | 25.7 | 27.3 |

Pred.: Predicted; Exp.: Experimental

4.5 Model Validation of Ternary Composite

4.5.1 Adsorption Performance Validation using Various Dye Concentration

The PKSAC-GO-Fe composite was tested with AB113 dye at initial concentrations ranging from 50 mg/L to 500 mg/L, in increments of 50 mg/L, to examine the effect of initial dye concentration. The experiments were conducted under optimum conditions: pH 7.5, 3.7 g/L of PKSAC-GO-Fe, with a contact time of 2.1 hours at room temperature and pressure.

As shown in Figure 4.14, complete color removal efficiency (100.0%) was achieved at an initial dye concentration of 50 mg/L. As the dye concentration increased gradually to 500 mg/L, the color removal efficiency dropped by 37.3% (from 100% to 62.7%). The reduction in color removal efficiency is attributed to the limited availability of active sites for dye binding, as the adsorbent dosage remained constant when the pollutant amount increased with dye concentration. At higher dye concentrations, the adsorption sites became saturated, causing a shortage of active sites and therefore reducing color removal efficiency (Khalil et al., 2024). This finding is consistent with previous studies (Algethami et al., 2024; Wang et al., 2022).

The adsorption capacity of the PKSAC-GO-Fe, in contrast, was determined to be increased from 13.7 mg/g at an initial dye concentration of 50 mg/L to 85.7 mg/g at 500 mg/L. This more than six-fold increase in adsorption capacity can be explained by the stronger driving force created by higher dye concentrations, which helps the AB113 dye molecules overcome mass transfer resistance between the aqueous and solid phases (Lai

et al., 2019; Wenxiang Zhang et al., 2020). Additionally, higher dye concentrations increase the number of collisions between AB113 dye molecules and the PKSAC-GO-Fe composite, thereby enhancing adsorption capacity.

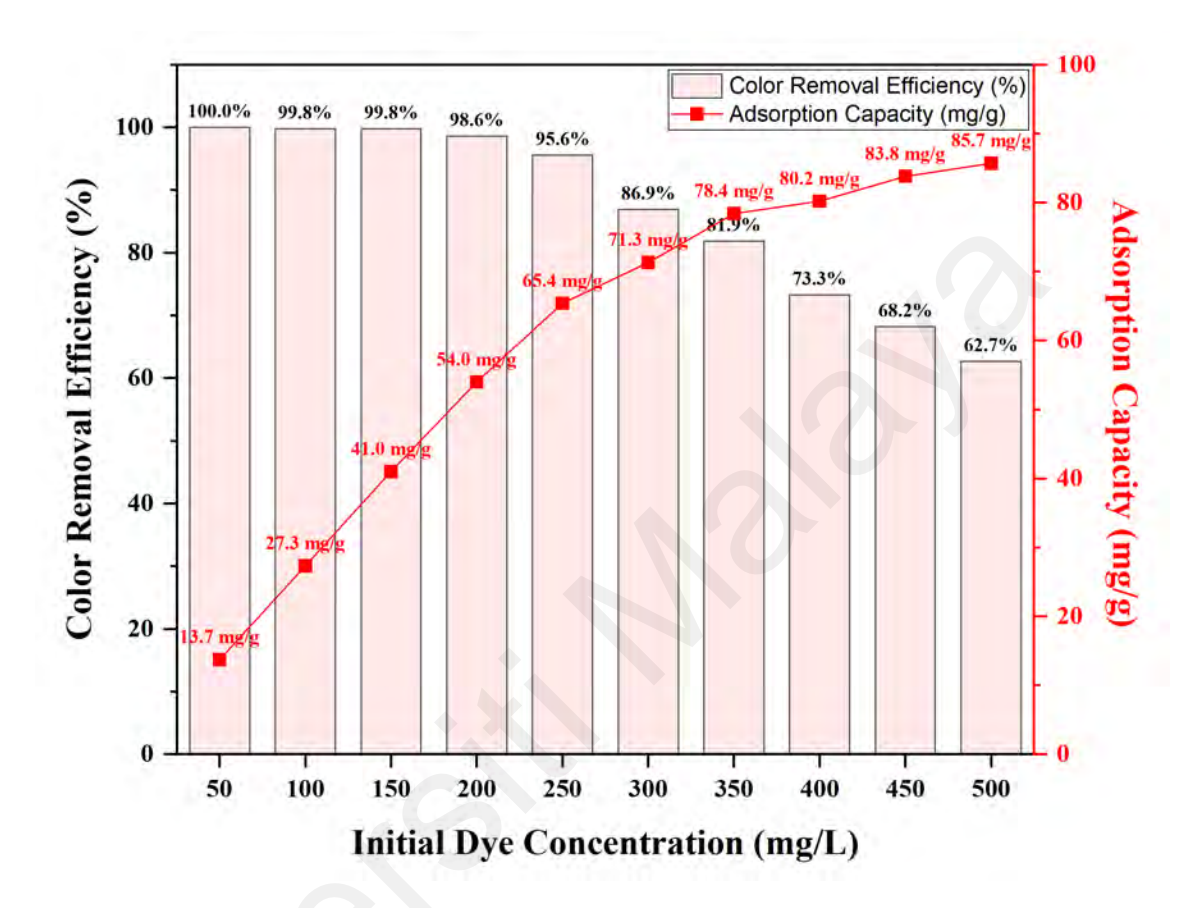


Figure 4.14: Adsorption Performance Validation using Various Dye Concentration

4.5.2 Adsorption Performance Validation using Various Industrial Dyes

To evaluate the broad applicability of the PKSAC-GO-Fe composite, its performance was validated using various industrial dyes under the optimum conditions previously determined for AB113 dye removal (pH 7.5, 3.7 g/L, 2.1 h). Ten different dyes were selected to represent a wide range of industrial applications, including MB, RhB, MO, RBBR, AY17, RB4, RR120, RB5, MG, and Amaranth. These dyes are commonly used in industries such as textiles, food processing, pharmaceuticals, and aquaculture, making them representative of real-world wastewater treatment scenarios.

When treating AB113 using the ternary composite, the results showed a color removal efficiency of 99.8%, an adsorption capacity of 27.3 mg/g, and a chemical oxygen demand (COD) reduction of 58.0%. As shown in Figure 4.15, the average COD reduction for the ten dyes using PKSAC-GO-Fe was 20.1%, ranging from 1.5% for RR120 to 52.6% for MB. MG also achieved a similar COD reduction of 52.5%. The average values for color removal efficiency and adsorption capacity were 47.3% (ranging from 9.2% to 92.9%) and 12.9 mg/g (ranging from 2.5 mg/g to 25.4 mg/g), respectively. The lowest color removal efficiency and adsorption capacity were observed for RhB and MO, while the highest were observed for MB.

The experimental results indicate that COD reduction does not directly correlate with color removal efficiency and adsorption capacity. For example, as shown in Figure 4.15, RB4 achieved a high color removal efficiency of 89.4% and an adsorption capacity of 24.4 mg/g, but only 7.2% COD reduction was observed. This discrepancy can be attributed to various factors, including the chemical composition of the dye solution, competitive adsorption, pH, ionic strength, and adsorption kinetics. Additionally, the differences in performance can be linked to the physicochemical characteristics of PKSAC-GO-Fe, such as surface area, pore size distribution, and functional groups, which interact differently with each dye type. Molecular characteristics and interactions, such as charge distribution, the presence of functional groups, and their positions, also influence the affinity of dyes toward PKSAC-GO-Fe, leading to varying performance outcomes.

The optimal conditions for AB113 dye were chosen in the validation process as a representative benchmark due to its industrial relevance and structural complexity. With this, it ensures consistency in testing and allows meaningful comparisons under identical conditions. The variations in molecular structures, charge distributions, and functional

group interactions cause differences in the adsorption performance, as indicated by experimental results (Zeeshan et al., 2025). In this regard, the optimization of adsorption conditions and the synthesis process should be focused in order to enhance the performance of PKSAC-GO-Fe in treating various dyes. Besides that, alternative treatment technologies, such as hybrid adsorption systems, or coupling with other treatment methods, such as photocatalysis, could also contribute to an increase in overall efficiency.

In summary, this validation study using various industrial dyes provides valuable insights into optimizing adsorption processes and understanding the complex interactions between adsorbents and pollutants. Besides that, the adsorption performance can still be improved via adsorption conditions and synthesis process optimization, as well as coupling with different treatment technologies.

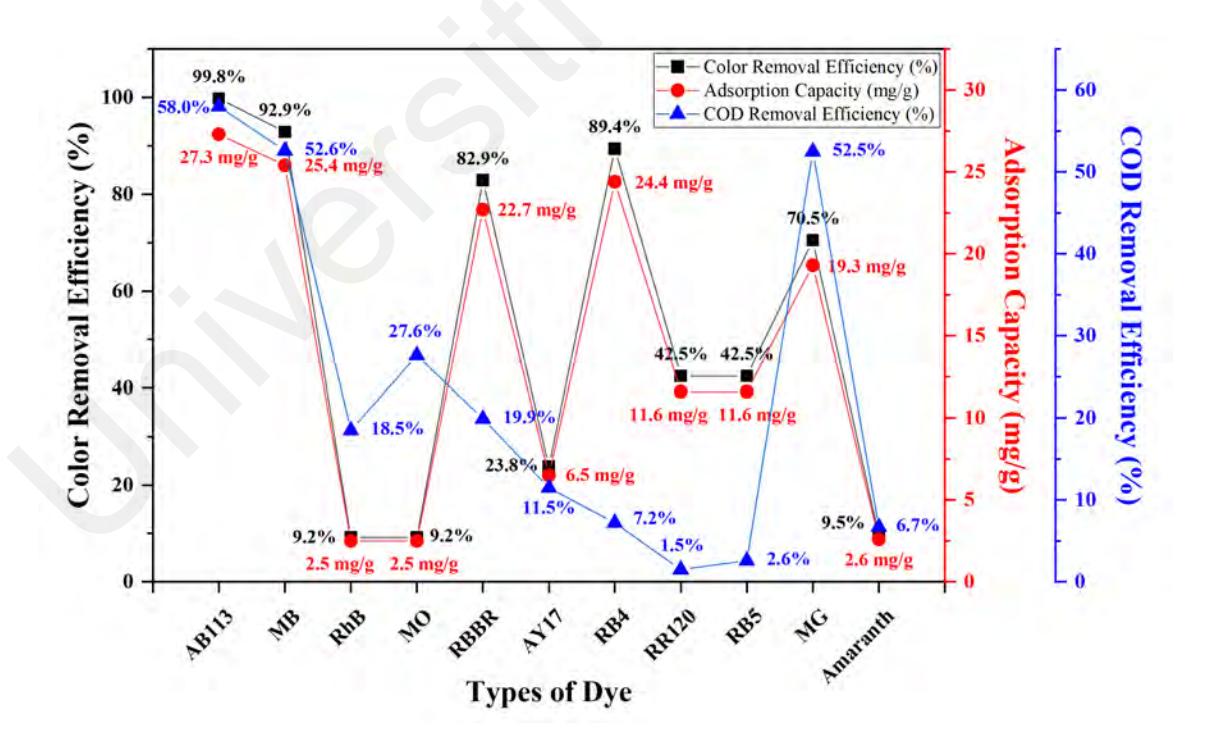


Figure 4.15 Adsorption Performance Validation using Various Types of Dye

4.5.3 Adsorption Performance Validation using Continuous Process

In this work, the performance of PKSAC-GO-Fe was validated through continuous processes to study the suitability of the ternary composite for different operational settings. In a continuous process, the wastewater is passed through a column packed with adsorbents under non-equilibrium conditions, whereas the batch process generally involves immersing adsorbents in the wastewater until equilibrium is reached. They are often being applied in different settings depending on wastewater treatment requirements. The batch processes are simpler and more suitable for small-scale operations whilst continuous processes are better suited for large-scale applications since they can process large volumes of effluent efficiently and consistently (Juela et al., 2022).

The experimental results indicate that continuous processes exhibit comparable adsorption performance to batch adsorption processes, as shown in Table 4.9 and Figure 4.16. Only slight differences of 0.5% and 0.7% were observed in color removal efficiency and rate constant between batch and continuous processes. The results suggest that the PKSAC-GO-Fe composite can effectively be applied to both processes, depending on treatment goals. However, a lower COD removal efficiency of 65.4% was observed in the continuous process, which is 13.3% lower than that achieved in the batch process (75.4%). This is due to the entire surface of the adsorbents being available immediately in batch processes, and hence interacting with the dye pollutants uniformly. In contrast, the residence time of dyes might be limited by the bed height in the continuous processes (Jain et al., 2020a).

Based on experimental results, the PKSAC-GO-Fe composite showed favorable performance under different adsorption settings. In short, batch and continuous processes are often selected according to various considerations, such as specific industrial needs, regulatory requirements, and economic factors.

Table 4.9: Comparison of Batch and Continuous Process

| Parameter | Batch | Continuous |
|------------------------------|-----------|-----------------------|
| Operational conditions | 500 mg/L | 500 mg/L |
| | pH 7.5 | pH 7.5 |
| | 0.5 g | 0.5 g |
| | 13.3 min | 1.5 mL/min (13.3 min) |
| | 20 mL | 20 mL |
| Color removal efficiency (%) | 99.7% | 99.3% |
| Adsorption capacity (mg/g) | 19.9 mg/g | 19.9 mg/g |
| COD removal efficiency (%) | 75.4% | 65.4% |
| Rate constant (mg/g min) | 1.50 | 1.49 |

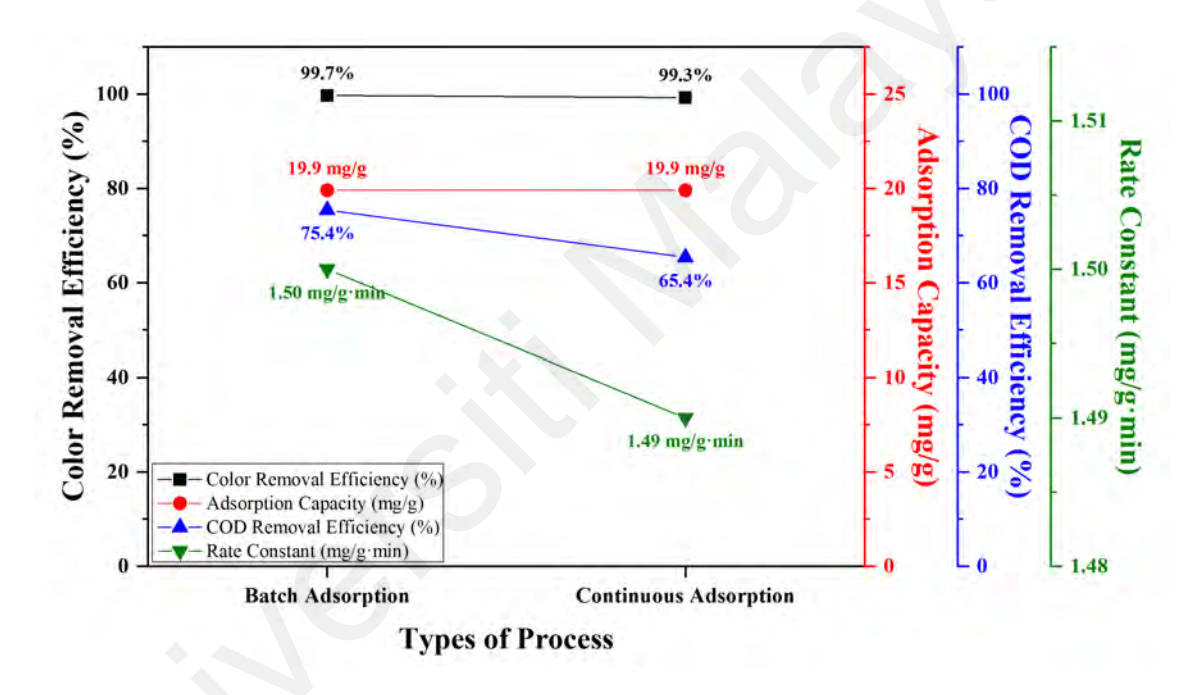


Figure 4.16: Comparison between Batch and Continuous Adsorption

4.5.4 Adsorption Performance Comparison with CACs

This section compares the performance of PKSAC-GO-Fe with several commercially available activated carbons (CACs). This includes the assessment and comparison of color removal efficiency, adsorption capacity, COD removal efficiency, and reusability. The CACs chosen for comparison were (1) CAC obtained from biomass, (2) CAC for therapeutic applications, and (3) CAC in chemically pure forms.

As shown in Figure 4.17, under optimum conditions (pH 7.5, adsorbent dosage of 3.7 g/L, for a duration of 2.1 hours), PKSAC-GO-Fe showed a color removal efficiency of 99.8%, which was significantly higher than those of the CACs by 56.7%, 19.9%, and 19.2% for CAC 1 (43.2%), CAC 2 (79.9%), and CAC 3 (80.6%) respectively. Furthermore, the adsorption capacity of PKSAC-GO-Fe reached 27.3 mg/g, exceeding the average performance of CACs by 32.1%. The COD reduction achieved by PKSAC-GO-Fe was 58.0%, which was higher than CACs by 51.6%, 18.4%, and 15.3%, respectively.

Reusability is another important parameter for practical industrial applications. An adsorbent with high reusability has the ability to maintain high performance across multiple adsorption-desorption cycles, which makes it a promising option for long-term wastewater treatment. Besides that, it also reduces the environmental impact and operational costs associated with their disposal and replacement. After the end of the fifth regeneration cycle, the PKSAC-GO-Fe composite maintained up to 74.0% of its original performance, whereas the CACs maintained an average of only 30.0% of their original performance under similar operational conditions.

In short, the experimental results show that PKSAC-GO-Fe performs better than CACs in terms of adsorption performance and reusability, which makes it a superior choice for industrial wastewater treatment applications.

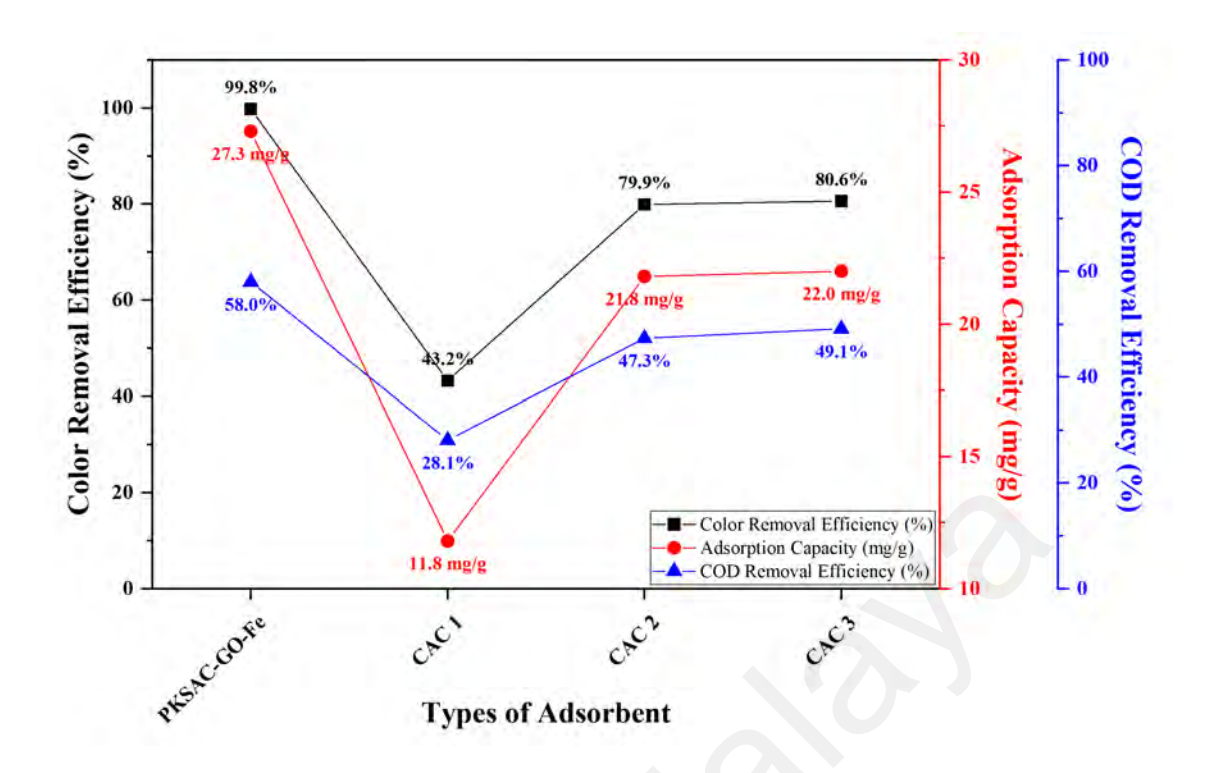


Figure 4.17: Adsorption Performance Comparison with CACs

4.6 Reusability Study

The reusability study explains the adsorbent's stability and ability to be regenerated after adsorption (Van Tran et al., 2019). The reusability study was carried out under optimal conditions (pH 7.5 and 2.1h using 3.7 g/L of PKSAC-GO-Fe). Figure 4.18 shows that color removal efficiency decreased from 99.8% in the first cycle to 74.0% in the fifth cycle. The gradual reduction in color removal efficiency was due to the dye not being fully desorbed from the surface of the PKSAC-GO-Fe (Bhattacharyya et al., 2018). However, the PKSAC-GO-Fe still achieved more than 70% of color removal efficiency after the fifth cycle, signifying the excellent reusability and stability of the PKSAC-GO-Fe. Based on industrial aqueous applications, the adsorbent typically results in 20-70% utilization of the original total pore volume before being considered spent (*International Filtration News*, 2009). Hence, based on the reusability study, the ternary composite can be utilized up to 5-15 cycles, depending on effluent standards requirements.

Besides that, the reusability of PKSAC-GO-Fe is higher than surfactant modified fallen leaves adsorbent using the same dye solution (AB113 dye) (Jain & Gogate, 2017). A reduction of 2.1% of color removal was recorded for PKSAC-GO-Fe at the third cycle, which is six-times lower compared to 12.1% of color removal reduction of surfactant modified fallen leaves. In short, the ability of PKSAC-GO-Fe to be reused for several cycles is a merit for operational cost reduction in industrial applications.

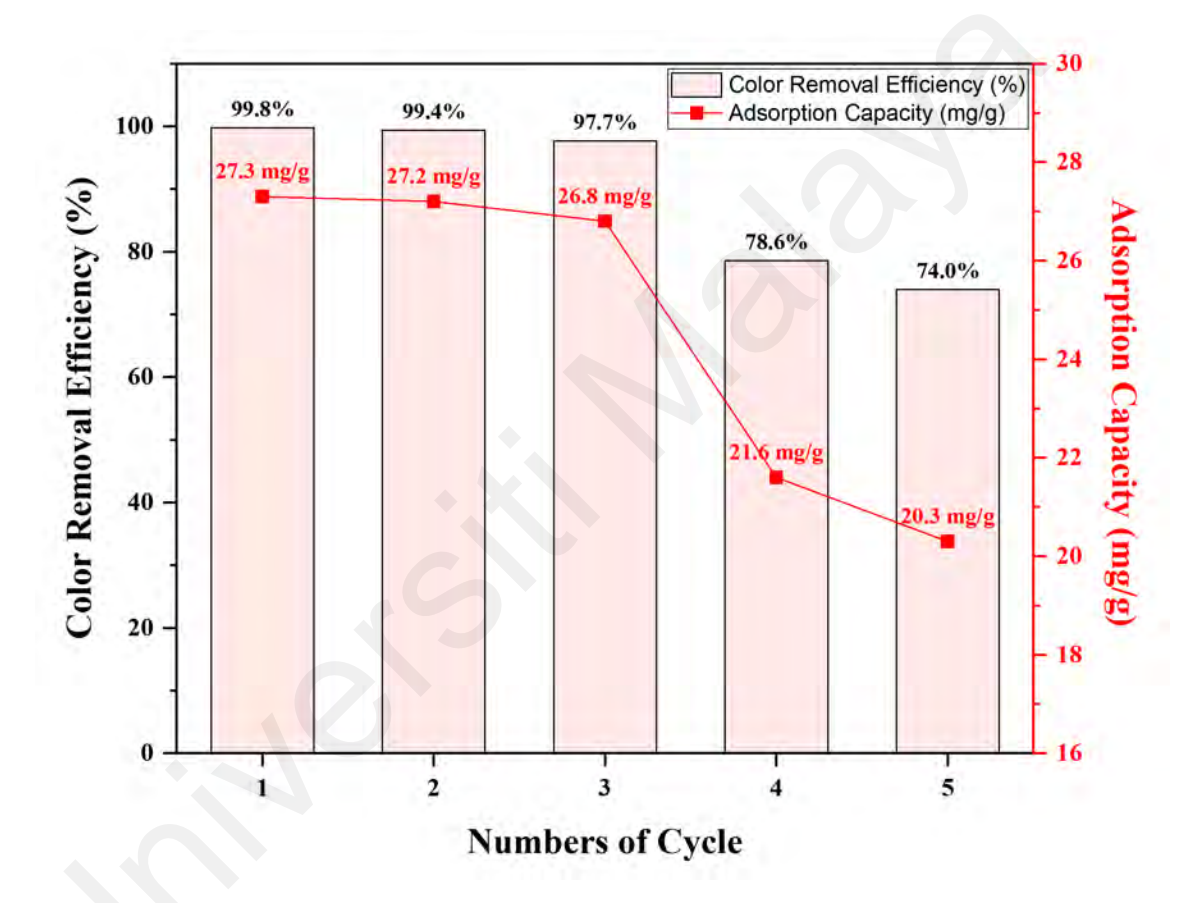


Figure 4.18: Reusability of PKSAC-GO-Fe

4.7 Adsorption Mechanism in Treating Synthetic Wastewater

4.7.1 Kinetics Study

Adsorption kinetics was studied to determine the rate of AB113 adsorbed as well as its mechanism (Aljeboree et al., 2017). To study the kinetics model for the adsorption of AB113 dye onto PKSAC-GO-Fe, three most commonly used models, pseudo-first-order (P-F-O), pseudo-second-order (P-S-O) and intra-particle diffusion (I-P-D) models, were used. Eq. 4.9 to Eq. 4.13 represent the P-F-O, P-S-O and I-P-D models, respectively, in both linear and non-linear expressions.

(a) Pseudo-First-Order

Non-linear:

$$q_t = q_e(1 - e^{-k_1 t}) (4.9)$$

Linear:

$$\log(q_e - q_t) = -\frac{k_1}{2.303}t + \log q_e \tag{4.10}$$

(b) Pseudo-Second-Order

Non-linear:

$$q_t = \frac{k_2 q_e^2 t}{q_e k_2 t + 1} \tag{4.11}$$

Linear:

$$\frac{t}{q_t} = \frac{1}{q_e}t + \frac{1}{k_2 q_e^2} \tag{4.12}$$

(c) Intra-Particle Diffusion

$$q_t = k_i t^{1/2} + c (4.13)$$

Where q_e and q_t are the adsorbed adsorbate per weight of adsorbent at equilibrium and at time t (mg g⁻¹); k_1 and k_2 are the rate constant for P-F-O (min⁻¹) and P-S-O (g mg⁻¹ min⁻¹).; t is donated as adsorption contact time; k_i (mg g⁻¹ min^{-0.5}) represents the rate coefficient of intra-particle diffusion; c (mg g⁻¹) is the constant of boundary layer thickness.

The results of the kinetic parameters are summarized in Table 4.10, and the graphs of the three different models are provided in Figure 4.19. From the experimental results, the adsorption of AB113 dye onto PKSAC-GO-Fe is best described by the P-S-O model, as indicated by the highest R² value. The linear and non-linear P-S-O models have R² values of 0.9988 and 0.9890, respectively. The predicted adsorption capacities for the linear (27.9 mg/g) and non-linear (26.9 mg/g) P-S-O models closely match the experimental value of 27.3 mg/g, with 2.2% and 1.5% differences. In contrast, the P-F-O model shows less agreement, with predicted capacities for linear and non-linear of 15.4 mg/g and 25.9 mg/g, respectively, with 55.7% and 5.3% differences, further supporting the validity of the P-S-O model (Ouettar et al., 2023).

These results suggest that the adsorption of AB113 dye onto PKSAC-GO-Fe is likely controlled by chemisorption. This finding is in line with the physicochemical characterization and adsorption performance observed in this study. As an example, although there is a reduction in surface area after the impregnation of GO and iron oxide into PKSAC, the adsorption performance was not hindered. In addition, there is a significant adsorption performance observed even when the solution pH is greater than the pH_{pzc}, which indicates that the adsorption process is predominant by chemisorption. These results are consistent with previous research on the adsorption of various synthetic dyes (Al-Odayni et al., 2023; Kapoor & Sivamani, 2023; Shaikh et al., 2022).

Table 4.10: Kinetic Parameters of AB113 Dye Adsorption onto PKSAC-GO-Fe

| Kinetic Model | Parameter | Unit | Linear | Non-Linear |
|---------------|-------------------|--|--------|------------|
| Experimental | qe (experimental) | mg g ⁻¹ | 27.3 | |
| P-F-O | \mathbf{k}_1 | min ⁻¹ | 0.05 | 0.18 |
| | $q_{\rm e}$ | mg g ⁻¹ | 15.4 | 25.9 |
| | \mathbb{R}^2 | - | 0.7861 | 0.9725 |
| P-S-O | \mathbf{k}_2 | g mg ⁻¹ min ⁻¹ | 0.01 | 0.01 |
| | q_{e} | mg g ⁻¹ | 27.9 | 26.9 |
| | \mathbb{R}^2 | - | 0.9988 | 0.9890 |
| I-P-D | k _i | mg g ⁻¹ min ^{-0.5} | 0.62 | 1.74 |
| | c | - | 20.29 | 10.01 |
| | \mathbb{R}^2 | - | 0.9771 | 0.6773 |

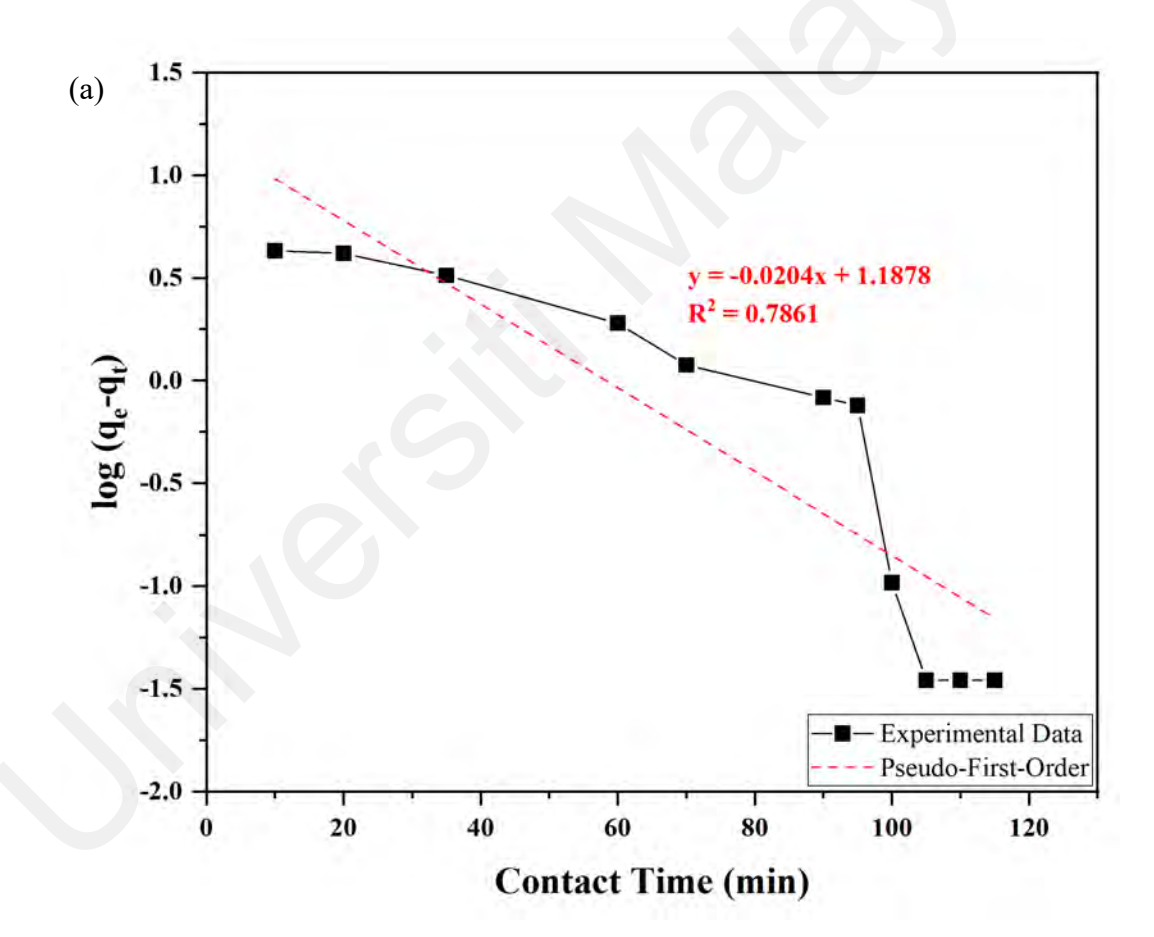
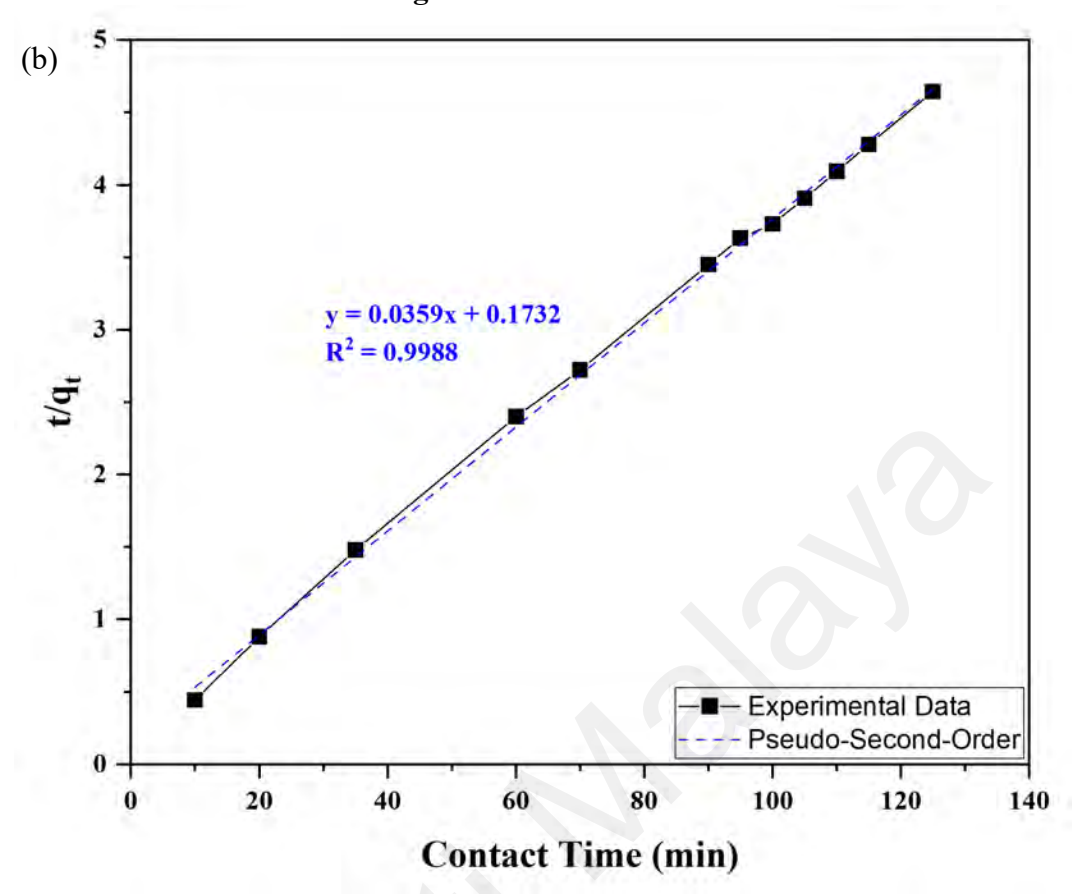
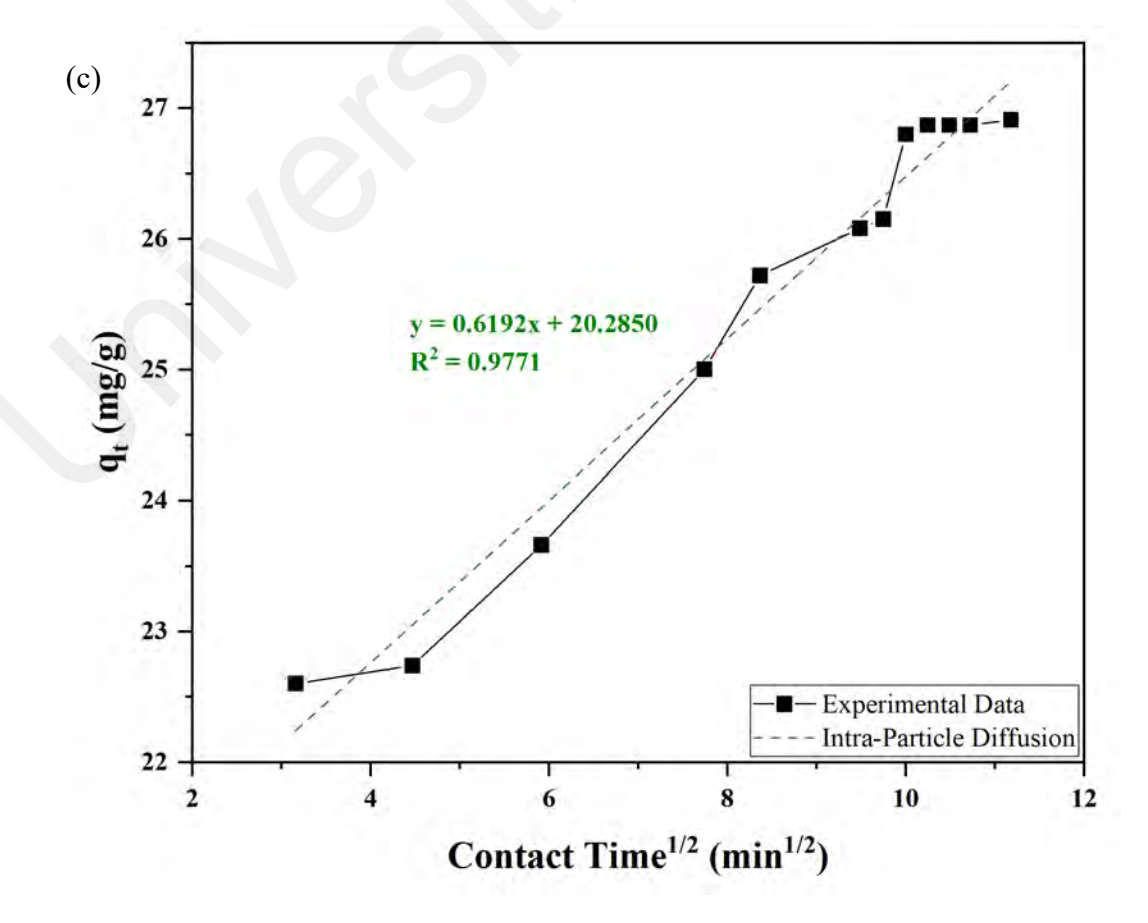


Figure 4.19: Linear Kinetic Plots for (a) P-F-O, (b) P-S-O, and (c) I-P-D, and (d) Non-Linear Kinetic Plot in Treating Anionic Dye

Figure 4.19: Continued





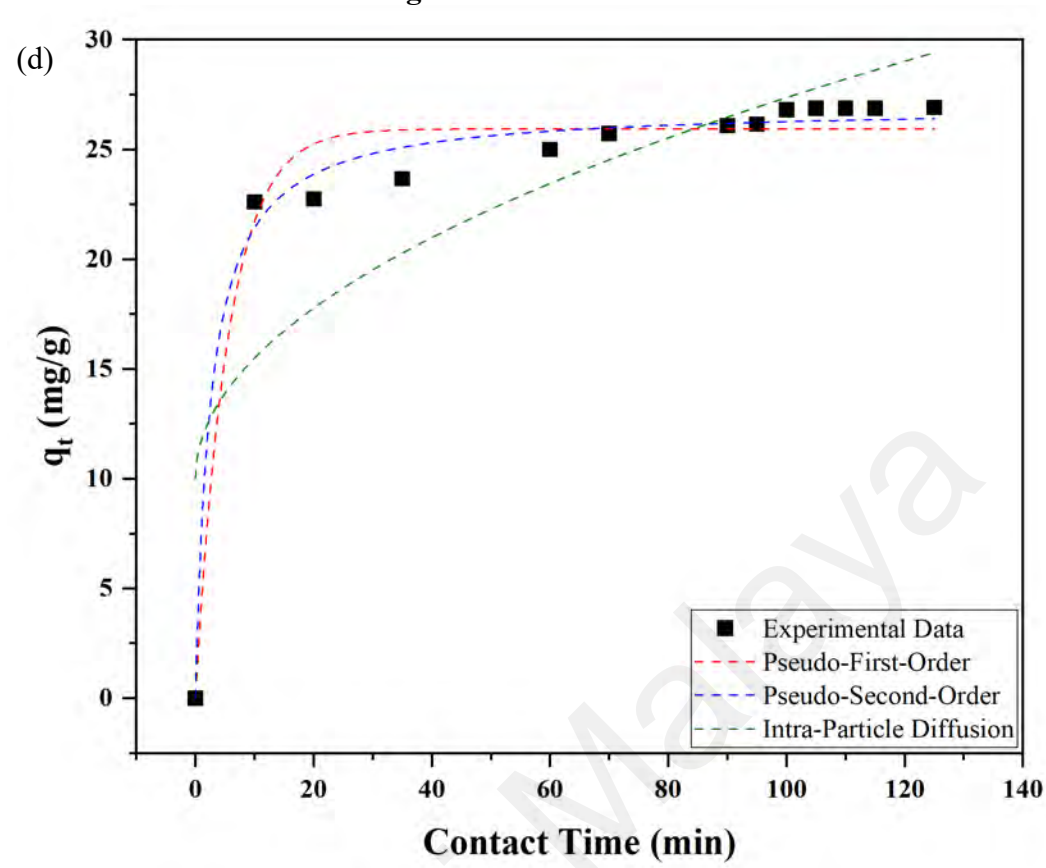


Figure 4.19: Continued

4.7.2 Isotherms Study

The isotherm models usually give essential information regarding maximum monolayer adsorption capacity as well as an adsorbent's mechanism, surface properties and affinity (Wang & Guo, 2020; Zhou et al., 2022). Three well-known isotherms, Langmuir (Langmuir, 1918), Freundlich (Swearingen, 1932) and Temkin (Temkin & Pyzhev, 1940), were used to study the behavior of AB113 dye adsorbed onto PKSAC-GO-Fe composite. Eq. 4.14 to Eq. 4.21 represent the non-linear and linear Langmuir, Freundlich and Temkin isotherms, respectively.

(a) Langmuir

Non-linear:

$$q_e = \frac{Q_{max}K_LC_e}{(1+K_LC_e)} \tag{4.14}$$

Linear:

$$\frac{c_e}{q_e} = \left(\frac{1}{Q_{max}}\right)C_e + \left(\frac{1}{Q_{max}K_L}\right) \tag{4.15}$$

The separation factor, R_L is a crucial parameter in the Langmuir isotherm model which reveals the favorability of the adsorption process. Eq. 4.16 was used to obtain R_L value.

$$R_L = \frac{1}{1 + K_L C_o} \tag{4.16}$$

 R_L value of $0 \le R_L \le 1$ indicates the adsorption process is desirable.

(b) Freundlich

Non-linear:

$$q_e = K_F(C_e)^{\frac{1}{n}} (4.17)$$

Linear:

$$\log q_e = \frac{1}{n} \log C_e + \log K_F \tag{4.18}$$

(c) Temkin

Non-linear:

$$q_e = B \ln A C_e \tag{4.19}$$

Linear:

$$q_e = B \ln C_e + B \ln A \tag{4.20}$$

$$B = \frac{RT}{b} \tag{4.21}$$

Where Q_{max} is the maximum amount of adsorbate adsorbed per weight of adsorbent at monolayer (mg/g); K_L (L/mg) and K_F (mg¹⁻ⁿ Lⁿ g⁻¹) are Langmuir constant and Freundlich constant, respectively; B (no unit) and A (L/g) are constants for heat of sorption and equilibrium binding, respectively; B is adsorption heat (J/mol).

Among the three isotherm models, the Langmuir model exhibited the highest R^2 values of 0.9982 and 0.9965 for linear and non-linear models, respectively, indicating that the adsorption of AB113 dye on PKSAC-GO-Fe dominated by monolayer adsorption, as depicted in Table 4.11 and Figure 4.20. The high Q_{max} for the linear (87.0 mg/g) and non-linear (136.7 mg/g) models indicates a desirable adsorption capacity of PKSAC-GO-Fe as an adsorbent. The K_L for the linear and non-linear models were 0.1933 and 0.0036, respectively. Additionally, the R_L values of $0 < R_L < 1$ (0.01 and 0.36) signify the favorability of AB113 dye adsorption using PKSAC-GO-Fe. These results suggest that PKSAC-GO-Fe exhibits significant adsorption capacities, surpassing previous studies on dye removal using various adsorbents (Ghaedi et al., 2022; Waghmare et al., 2023; Wong et al., 2020).

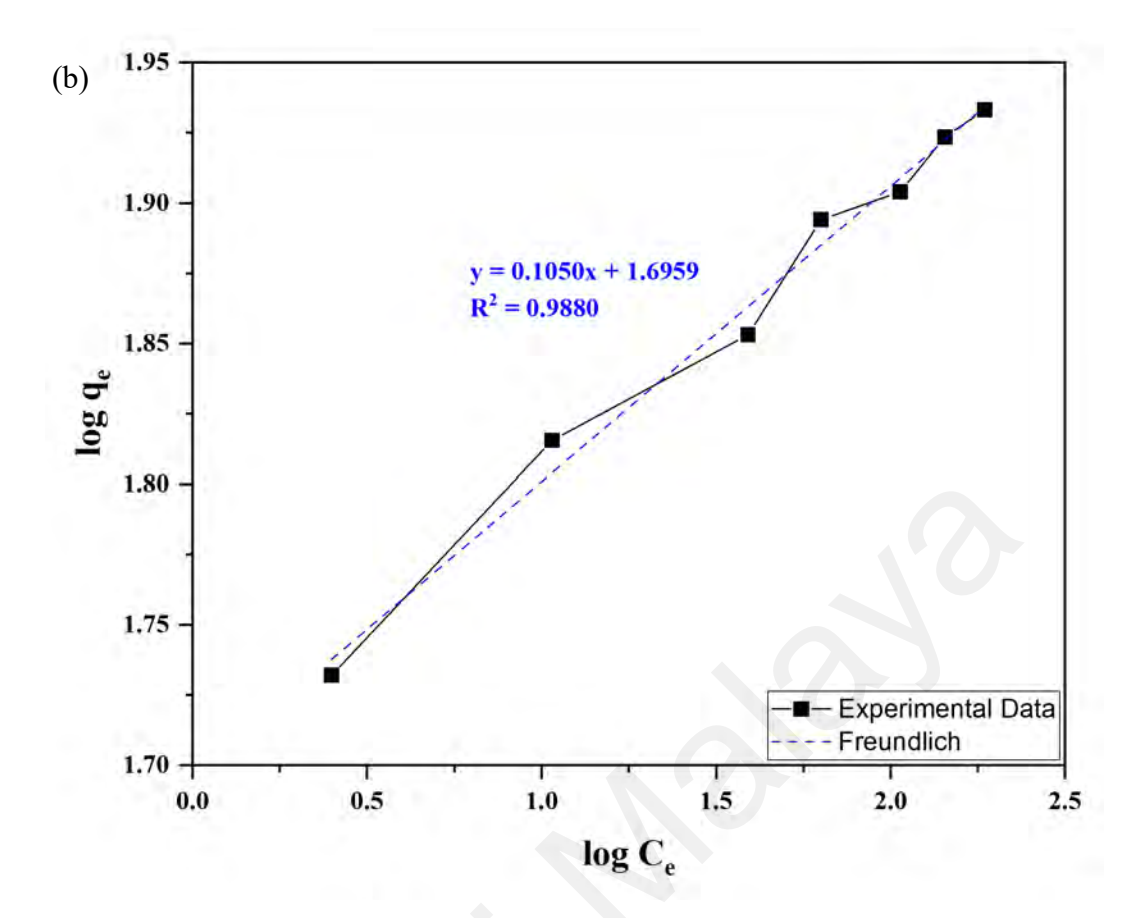
For the Freundlich isotherm analysis, the n values of 9.52 and 2.17 (1 < n < 10) suggest that adsorption is favorable (Pessoa et al., 2024). In the case of the Temkin isotherm model, the b values were determined to be 342.32 and 71.51 J/mol for linear and non-linear models, respectively. In summary, the AB113 adsorption data using PKSAC-GO-Fe best fit the isotherm models in the following sequence for the linear model: Langmuir > Freundlich > Temkin. For the non-linear model, the sequence is Langmuir > Temkin > Freundlich. Since the adsorption of AB113 on PKSAC-GO-Fe fits well into the Langmuir and P-S-O models, the adsorption process can be considered predominantly as monolayer chemisorption (Wong et al., 2020).

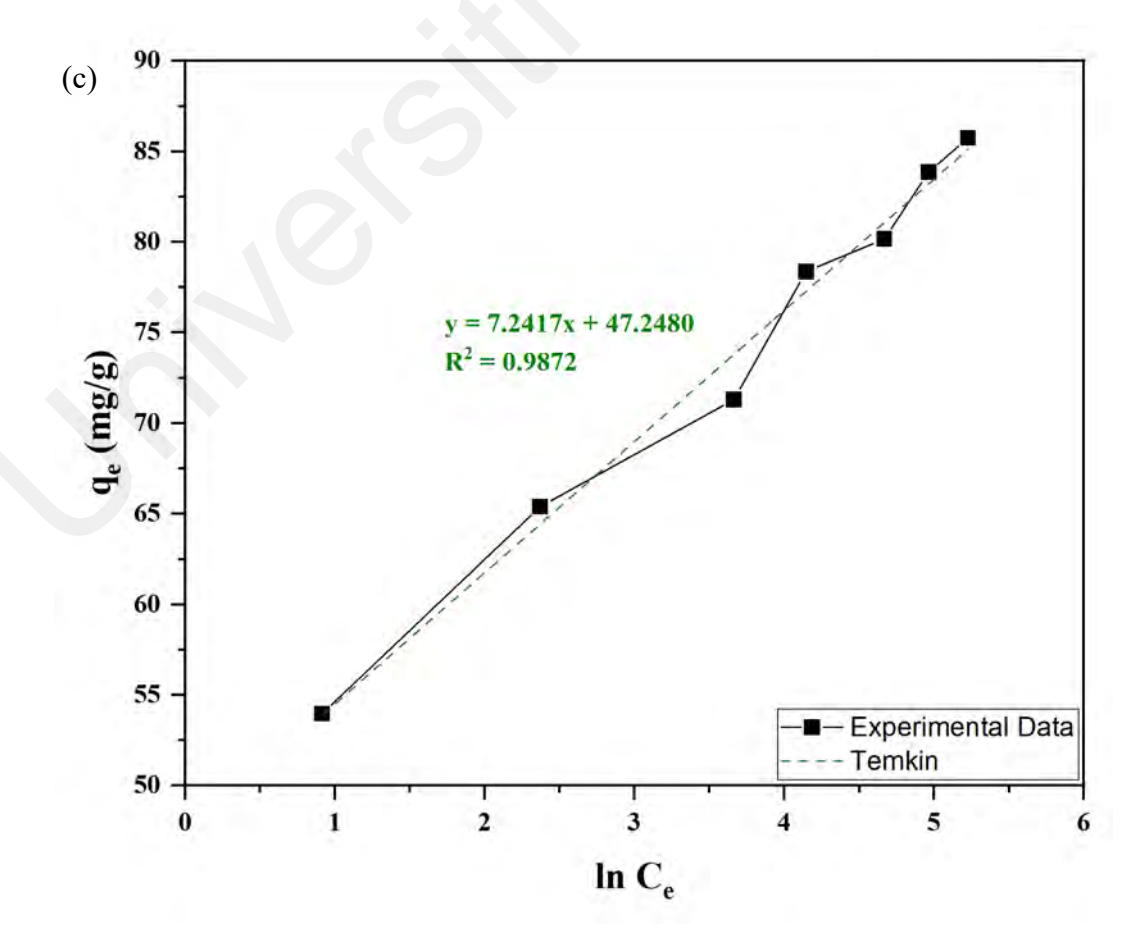
Table 4.11: Isotherm Parameters of AB113 Dye Adsorption onto PKSAC-GO-Fe

| Isotherm Model | Parameter | Unit | Linear | Non-Linear |
|----------------|------------------|---------------------|--------|------------|
| Langmuir | Q _{max} | mg g ⁻¹ | 87.0 | 136.7 |
| | K_{L} | L mg ⁻¹ | 0.1933 | 0.0036 |
| | $R_{ m L}$ | - | 0.01 | 0.36 |
| | \mathbb{R}^2 | - | 0.9982 | 0.9965 |
| Freundlich | K_{F} | $mg^{1-n}L^ng^{-1}$ | 49.65 | 5.01 |
| | n | - | 9.52 | 2.17 |
| | \mathbb{R}^2 | - | 0.9880 | 0.9932 |
| Temkin | A | L g ⁻¹ | 681.59 | 0.03 |
| | В | - | 7.24 | 34.19 |
| | ь | J mol ⁻¹ | 342.32 | 71.51 |
| | \mathbb{R}^2 | - | 0.9872 | 0.9963 |

Figure 4.20: Linear Isotherm Plots for (a) Langmuir, (b) Freundlich, and (c) Temkin Models, and (d) Non-Linear Isotherm Plot in Treating Anionic Dye

Figure 4.20: Continued





100 (d) 80 60 qe (mg/g) 20 **Experimental Data** Langmuir Freundlich Temkin 100 200 300 400 500 $C_e (mg/L)$

Figure 4.20: Continued

4.7.3 Thermodynamics study

The temperature effect on the adsorption processes can be related to thermodynamics study. The thermodynamics parameters can be determined from Eq. 4.22 to Eq. 4.24.

$$\Delta G^{\circ} = -RT \ln K_c \tag{4.22}$$

$$K_c = \frac{c_s}{c_e} \tag{4.23}$$

$$\ln K_c = \left(\frac{\Delta S^{\circ}}{R}\right) - \left(\frac{\Delta H^{\circ}}{RT}\right) \tag{4.24}$$

Where K_c is equilibrium constant; C_s and C_e are equilibrium dye concentration on adsorbent and in bulk solution respectively (mg/L); R is ideal gas constant (8.314 $\frac{J}{mol \cdot K}$) and T is temperature of adsorption process (K).

In this study, the thermodynamic study was conducted by varying the temperature from 298.15 K (25°C) to 338.15 K (65°C) in 10 K (10°C) intervals. The thermodynamic results of PKSAC-GO-Fe is shown in Figure 4.21 and Table 4.12. Experimental results revealed that color removal efficiency and adsorption capacity decreased from 78.6% (64.4 mg/g) to 50.2% (41.1 mg/g) as the temperature increased from 25°C to 65°C. In addition, according to Figure 4.21, the positive slope of the AB113 adsorption on PKSAC-GO-Fe indicates that the process is exothermic. The thermodynamic parameters governing the adsorption process provide insights into the spontaneity, randomness, and heat exchange associated with the adsorption phenomenon. These parameters were obtained from van't Hoff plots. In this study, the Δ H°, Δ S°, and Δ G° of AB113 dye adsorption using PKSAC-GO-Fe were determined to be -16.47 kJ/mol, -43.17 J/mol·K, and -3.82 to -1.96 kJ/mol, respectively.

The negative value of ΔH° (-16.47 kJ/mol) indicates that the adsorption process is exothermic, meaning the adsorption of AB113 dye onto PKSAC-GO-Fe releases heat to the surroundings. This exothermic nature implies that the interactions between dye molecules and the adsorbent surface are predominantly driven by attractive forces such as Van der Waals interactions, hydrogen bonding, or chemical bonding. The negative entropy change ($\Delta S^{\circ} = -43.17 \text{ J/mol·K}$) suggests a decrease in randomness or disorderliness during the adsorption process. This decrease in entropy could be attributed to the ordering of dye molecules on the surface of the adsorbent or the restriction of their freedom of movement after the adsorption process (Ahmad & Danish, 2022).

Although the decrease in entropy, the adsorption processes remain favorable, as indicated by the negative Gibbs free energy values (ΔG°). The negative values of ΔG° suggest that the adsorption process is thermodynamically favorable within the studied range. A negative ΔG° implies that the adsorption process is spontaneous, indicating that

the interactions between AB113 dye and PKSAC-GO-Fe are favorable in terms of both enthalpy and entropy contributions. Moreover, more negative ΔG° values indicate a more spontaneous adsorption process at specific temperatures and vice versa (Bello et al., 2019). The results obtained were in line with those reported in previous studies (Dixit et al., 2024; Kapoor & Sivamani, 2023; Kumbhar et al., 2022). In summary, the adsorption of AB113 onto PKSAC-GO-Fe is denoted as a spontaneous and exothermic process. In hot regions, such as Malaysia, shallow wastewater ponds can reach temperatures of 32-35°C (AlMomani & Örmeci, 2020). Hence, from another point of view, the experimental results indicate that PKSAC-GO-Fe achieves a significant removal rate at the aforementioned temperature range, as well as at slightly lower and higher temperatures.

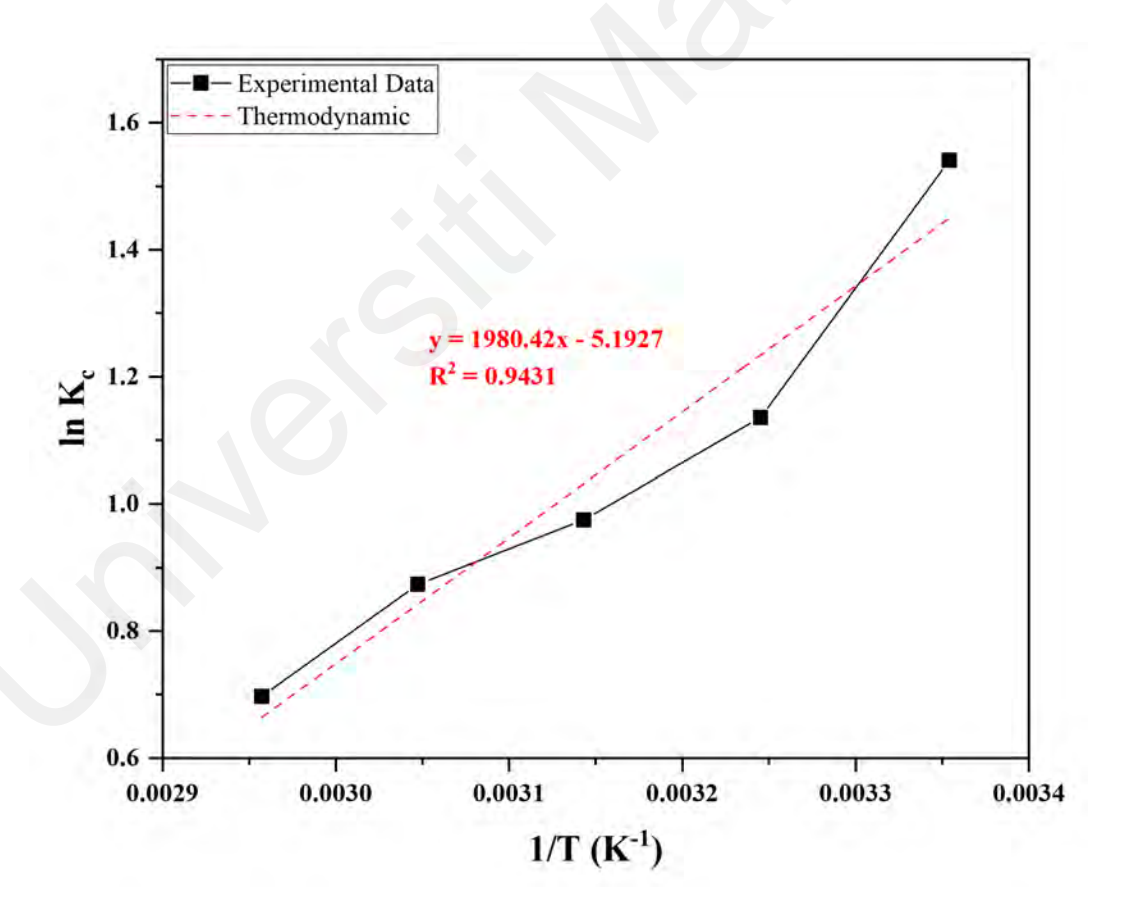


Figure 4.21: Van't Hoff Plot of Anionic Dye Adsorption using PKSAC-GO-Fe

Table 4.12: Thermodynamic Study of Anionic Adsorption onto PKSAC-GO-Fe

| T (K) | ΔG° (kJ/mol) | ΔH° (kJ/mol) | ΔS° (J/mol·K) |
|--------|--------------|--------------|---------------|
| 298.15 | -3.82 | -16.47 | -43.17 |
| 308.15 | -2.91 | | |
| 318.15 | -2.58 | | |
| 328.15 | -2.38 | | |
| 338.15 | -1.96 | | |

4.8 Insights into the Adsorption Mechanism via Computational Approaches

Recent advances in computational approaches, like quantum chemical analysis and machine learning, have provided substantial insights about adsorption phenomena at the molecular level, which in turn aid in optimizing wastewater processes. In this work, the focus is given to the adsorption mechanism of synthetic wastewater onto PKSAC-GO-Fe composite.

Quantum chemical analysis can be used to investigate the interactions between dye molecules and various functional groups on the adsorbent surface. An overview of the adsorption process can be obtained by calculating the adsorption energy between pollutants and different functional groups on the adsorbent surface. It also provides comprehensive details on the electronic properties of various molecules. The electrophilicity index, chemical hardness, softness, and HOMO-LUMO energy are some of the quantum parameters that are analyzed for predicting the reactivity and stability of various molecules. These calculations were performed using DFT, which provides a microscopic view of the adsorption process, and at the same time, emphasizes the role of electronic configurations and molecular interactions.

Besides that, machine learning algorithms have emerged as effective approaches for modeling and predicting various processes, including adsorption. It can identify specific patterns and relationships between various inputs and outputs through experimental and computational data training, which are not readily apparent through traditional analysis.

With this, it facilitates adsorption prediction and optimization under various conditions. Moreover, machine learning can also be accurately used to study the weightage of each physicochemical characteristic and operational condition in the adsorption process through feature importance analysis. The detailed adsorption mechanism of AB113 dye on PKSAC-GO-Fe composite can therefore be revealed through the integration of quantum chemical analysis and machine learning, as well as being complemented by experimental results. This dual approach not only enhances the understanding of fundamental interactions but also promotes the development of high-performance adsorbents for wastewater treatment applications.

4.8.1 Adsorption Mechanism Evaluation via Quantum Chemical Analysis

One of the essential techniques in quantum chemistry is DFT, which provide insights into stability and reactivity of molecules based on various quantum descriptors such as E_{HOMO}, E_{LUMO}, dipole potential, chemical hardness, softness, electrophilicity etc. In this study, all computations were performed using Gaussian 09 software, employing the HF and M06-2x methods with the 6-31G(d, p) basis set, and the GEN method when iron atoms were involved. Besides that, the adsorption energy between dye molecule and functional groups present on adsorbent surface are studied, where the adsorption mechanism, i.e., predominant adsorption process can be deducted.

4.8.1.1 Surface Functional Groups

FTIR analysis was performed to examine the surface functional groups of PKSAC-based adsorbents, with the resulting spectra displayed in Figure 4.22. For PKSAC, peaks observed at 3000, 2919, 2845, and 2740 cm⁻¹ are related to the vibrations of C-H bonds. Additional peaks at 3411 and 1414 cm⁻¹ represent the O-H bending of hydroxyl groups. The presence of carboxylic acids in PKSAC is indicated by peaks at 3258 and 2630 cm⁻¹, corresponding to O-H stretching modes, and a peak at 1809 cm⁻¹ related to C=O

stretching vibrations. Peaks at 974 and 710 cm⁻¹ are due to C=C bending. These groups likely result from the residual carbonization of lignocellulosic components of palm kernel shells during the synthesis process (Opoku et al., 2021). From the FTIR spectrum, it can be deduced that -OH and -COOH functional groups are present in the raw PKSAC.

There are some alterations observed in the FTIR spectra after the impregnation process. As an example, the FTIR spectrum of the PKSAC-GO composite combined peaks from both PKSAC and GO after the impregnation of GO into PKSAC, and hence signifies the PKSAC-GO composite was successfully synthesized. In addition to the peaks contributed by PKSAC, additional peaks were observed at 1133 cm⁻¹ (C-O from tertiary alcohol), 1217 cm⁻¹ (epoxy C-O-C groups), and 1739 cm⁻¹ (aldehyde C=O groups), along with a peak at 2806 cm⁻¹ (aldehyde C-H groups). Therefore, it is suggested that in addition to the -OH and -COOH groups from PKSAC, additional functional groups contributed by GO impregnation were observed, including aldehyde and epoxy groups (Hosseinzadeh & Ramin, 2018; Joshi et al., 2022).

In addition to the original peaks of raw PKSAC, PKSAC-Fe exhibits a peak in the 550-750 cm⁻¹ range after iron oxide impregnation. This peak, representing metal-oxygen stretching vibrations (Fe-O), confirms that iron oxide has been successfully impregnated into PKSAC (Algethami et al., 2024; Husain et al., 2021; Pang et al., 2020). On the other hand, the FTIR analysis of PKSAC-GO-Fe revealed all significant peaks from PKSAC, GO, and iron oxide. The presence of all of these functional groups in the ternary composite is evidence that the impregnation of both GO and iron oxide into raw PKSAC was successful. This resulted in an improvement in the adsorption performance, which is in line with the experimental results. Overall, FTIR analysis provides valuable insights into the functional groups of PKSAC-based adsorbents, confirming the successful synthesis and combination of various materials in PKSAC-based adsorbents.

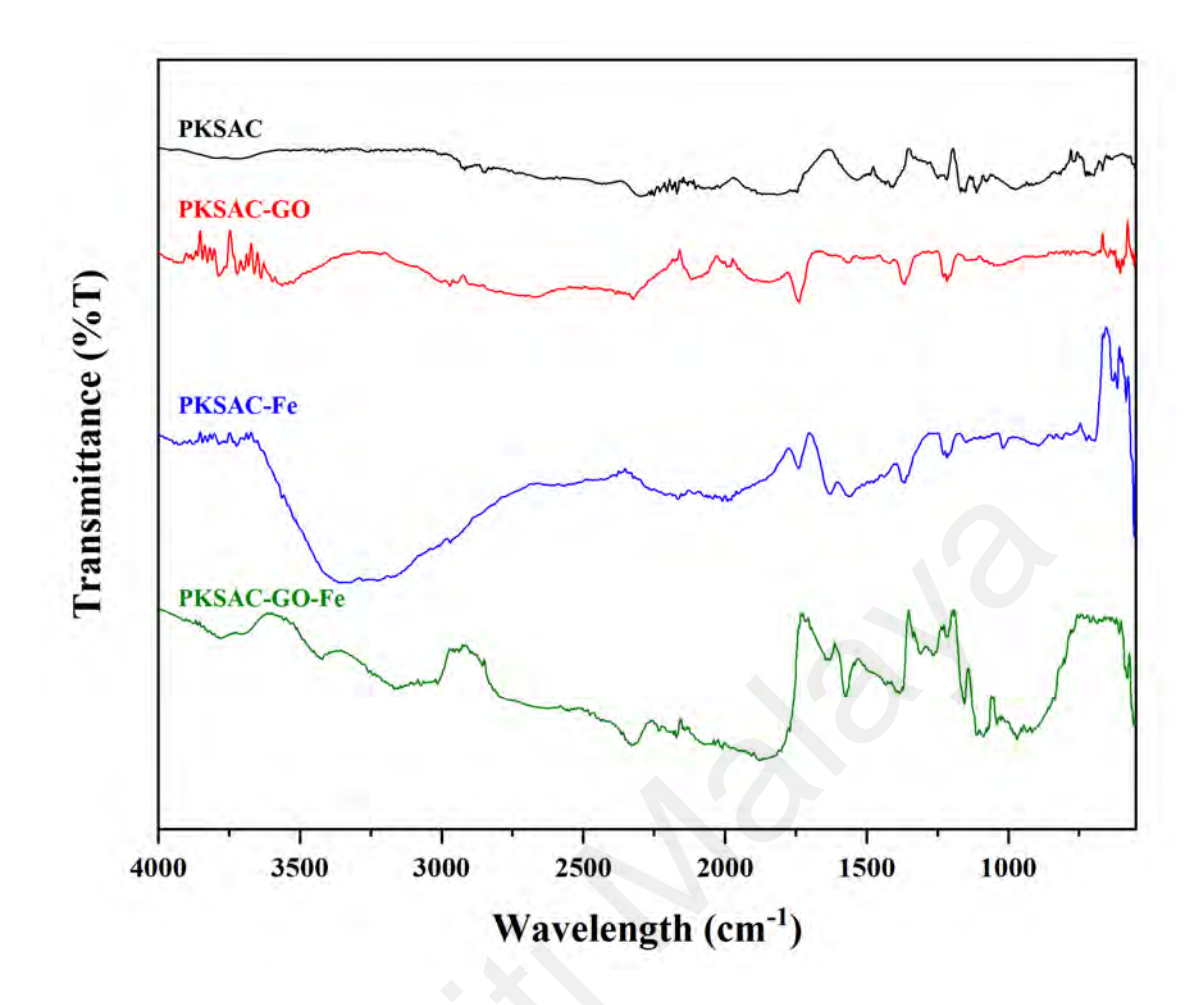


Figure 4.22: FTIR Spectra of PKSAC-Based Adsorbents

4.8.1.2 Molecular Structures and Quantum Descriptors

Quantum descriptors play a crucial role in interpreting the stability and reactivity of PKSAC-based adsorbents. Table 4.13 presents key quantum chemical descriptors for the AB113 dye and various PKSAC-based adsorbents, including PKSAC, PKSAC-GO, PKSAC-Fe, and PKSAC-GO-Fe. Those quantum descriptors are obtained after the optimization of each geometry structure. On the other hand, Figure 4.23 displays the optimized AB113 structure, molecular boundary orbital (HOMO and LUMO), and electrostatic potential (ESP) map while the optimized structures of PKSAC-based adsorbents are showed in Figure 4.24. In each structure, gray represents C atoms, white represents H atoms, red represents O atoms, yellow represents S atoms, and blue represents N atoms.

 E_{HOMO} represents the ability to donate electrons, with higher (less negative) values suggesting better electron-donating capability. E_{LUMO} represents the ability to accept electrons, with lower values suggesting better electron-accepting ability, contributing to higher reactivity. The $E_{HOMO-LUMO}$ gap indicates the reactivity of the molecule, with smaller gaps suggesting higher reactivity. EA measures the energy released when an electron is added to the LUMO. IP measures the energy required to remove an electron from the HOMO. Chemical potential reflects the tendency of electrons to escape from the molecule. Negative values indicate stability. The higher χ value suggesting a stronger ability to attract electrons. Electronegativity reflects the ability of a molecule to attract electrons. Chemical hardness measures resistance to electron cloud deformation. Higher values indicate less reactivity. Softness is the inverse of hardness. Higher values indicate higher reactivity. Electrophilicity index quantifies the ability of a molecule to accept electrons. Higher values indicate better electron-accepting capability and high reactivity.

As shown in Table 4.13, the AB113 dye exhibits a E_{HOMO} of -2.33 eV and E_{LUMO} of 1.66 eV suggest that the dye has a balanced ability to donate and accept electrons, making it moderately reactive. The E_{HOMO-LUMO} gap of 3.99 eV further indicates this moderate reactivity. The E_{HOMO-LUMO} gap was found to be within the ranges of other types of dye investigated previously (Bellaj et al., 2024; Ibrahim et al., 2024; Miyah et al., 2023). Figure 4.23 illustrates that the LUMO density distribution is primarily concentrated on the aniline groups, while the HOMO density distribution is centered on the naphthalene group and near the edge of the dye structure. The ESP map indicates that the electrophilic active sites for AB113 dye are located at the sulfonate groups (Miyah et al., 2023).

The PKSAC-based adsorbents, including PKSAC, PKSAC-GO, PKSAC-Fe, and PKSAC-GO-Fe, display varying degrees of stability and reactivity based on their quantum chemical descriptors. PKSAC exhibits a total energy of -2443.20 a.u., indicating

moderate stability. Its E_{HOMO} of -5.93 eV and E_{LUMO} of -1.88 eV suggest a higher electron-donating and accepting ability, with an $E_{HOMO-LUMO}$ gap of 4.05 eV. The IP and EA of 5.93 eV and 1.88 eV, respectively, support its moderate reactivity. After the impregnation of GO into PKSAC, PKSAC-GO displayed a total energy of -5490.64 a.u., shows an enhancement of 124.7% compared to raw PKSAC, which demonstrating GO impregnation can significantly increase the stability of the adsorbent. The E_{HOMO} of -5.91 eV and E_{LUMO} of -3.01 eV, coupled with an $E_{HOMO-LUMO}$ gap of 2.91 eV, indicate a higher reactivity. Its lower chemical hardness (η) of 1.45 eV and higher softness (S) of 0.69 eV confirm its higher reactivity, and an electrophilicity index (ω) of 6.85 eV suggests a strong electron-accepting capability, compared to raw PKSAC.

Besides that, for PKSAC-Fe, after the impregnation of iron oxide into PKSAC, the composite shows a total energy of -3113.93 a.u., indicates a lower stability compared to PKSAC-GO, but still determined to be more stable than raw PKSAC by 27.5%. On the other hand, the E_{HOMO-LUMO} gap of 4.20 eV, suggesting lower reactivity compared to PKSAC-GO (2.91 eV) by 30.7%. The moderate chemical potential (μ) of -3.94 eV and electronegativity (γ) of 3.94 eV align with its overall moderate reactivity properties. Among all PKSAC-based adsorbents, after the impregnation of GO and iron oxide into raw PKSAC, PKSAC-GO-Fe stands out with the lowest energy value of -6161.47 a.u., indicating the highest stability among the adsorbents, surpassing PKSAC, PKSAC-GO, and PKSAC-Fe by 152.2%, 12.2%, and 97.9%, respectively. Its E_{HOMO} of -6.12 eV and E_{LUMO} of -4.04 eV suggest strong electron-donating and accepting abilities, with an $E_{HOMO-LUMO}$ gap of 2.07 eV indicating high reactivity. The lowest chemical potential (μ) of -5.08 eV and highest electronegativity (χ) of 5.08 eV signify its strong reactivity and stability. The highest electrophilicity index (ω) of 12.44 eV further confirms its superior electron-accepting ability, making it the most effective adsorbent for AB113 dye removal, aligning with the experimental results.

The total energy represents the stability of the molecule, where a lower energy values, indicates higher stability. AB113 dye has an energy of -2752.68 a.u., while PKSAC-based adsorbents have energies ranging from -2443.20 a.u. to -6161.47 a.u. The lowest energy is observed for PKSAC-GO-Fe (-6161.47 a.u.), indicating its highest stability among all PKSAC-based adsorbents. The sequence of total energy and E_{HOMO-LUMO} energy gap of PKSAC-based adsorbents are as below:

Total energy:

E_{HOMO-LUMO} gap:

In short, the quantum chemical descriptors indicate that the impregnation of GO and iron oxide into PKSAC significantly enhances the stability and reactivity of the adsorbent. PKSAC-GO-Fe composite, with its lowest energy value and highest reactivity indicators, stands out as the most effective adsorbent for pollutants removal.

Table 4.13: Quantum Chemical Descriptors of AB113 Dye and PKSAC-Based Adsorbents

| Descriptors | AB113 | PKSAC | PKSAC-GO | PKSAC-Fe | PKSAC-GO-Fe |
|-----------------------------|----------|----------|----------|----------|-------------|
| Total energy (a.u.) | -2752.68 | -2443.20 | -5490.64 | -3113.93 | -6161.47 |
| E _{HOMO} (eV) | -2.33 | -5.93 | -5.91 | -6.04 | -6.12 |
| E _{LUMO} (eV) | 1.66 | -1.88 | -3.01 | -1.84 | -4.04 |
| E _{HOMO-LUMO} (eV) | 3.99 | 4.05 | 2.91 | 4.20 | 2.07 |
| IP (eV) | 2.33 | 5.93 | 5.91 | 6.04 | 6.12 |
| EA (eV) | -1.66 | 1.88 | 3.01 | 1.84 | 4.04 |
| μ (eV) | -0.33 | -3.91 | -4.46 | -3.94 | -5.08 |
| χ (eV) | 0.33 | 3.91 | 4.46 | 3.94 | 5.08 |
| η (eV) | 1.99 | 2.03 | 1.45 | 2.10 | 1.04 |
| S (eV) | 0.50 | 0.49 | 0.69 | 0.48 | 0.96 |
| ω (eV) | 0.03 | 3.77 | 6.85 | 3.70 | 12.44 |

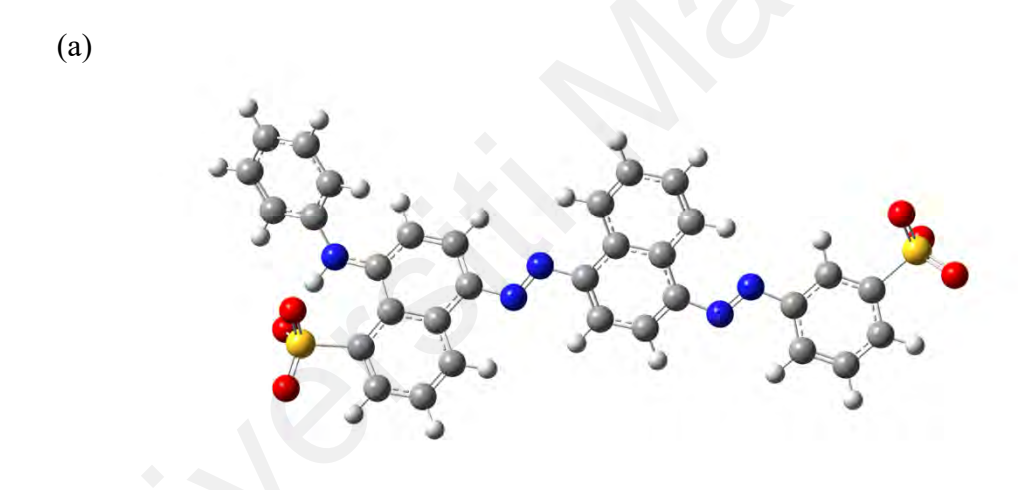
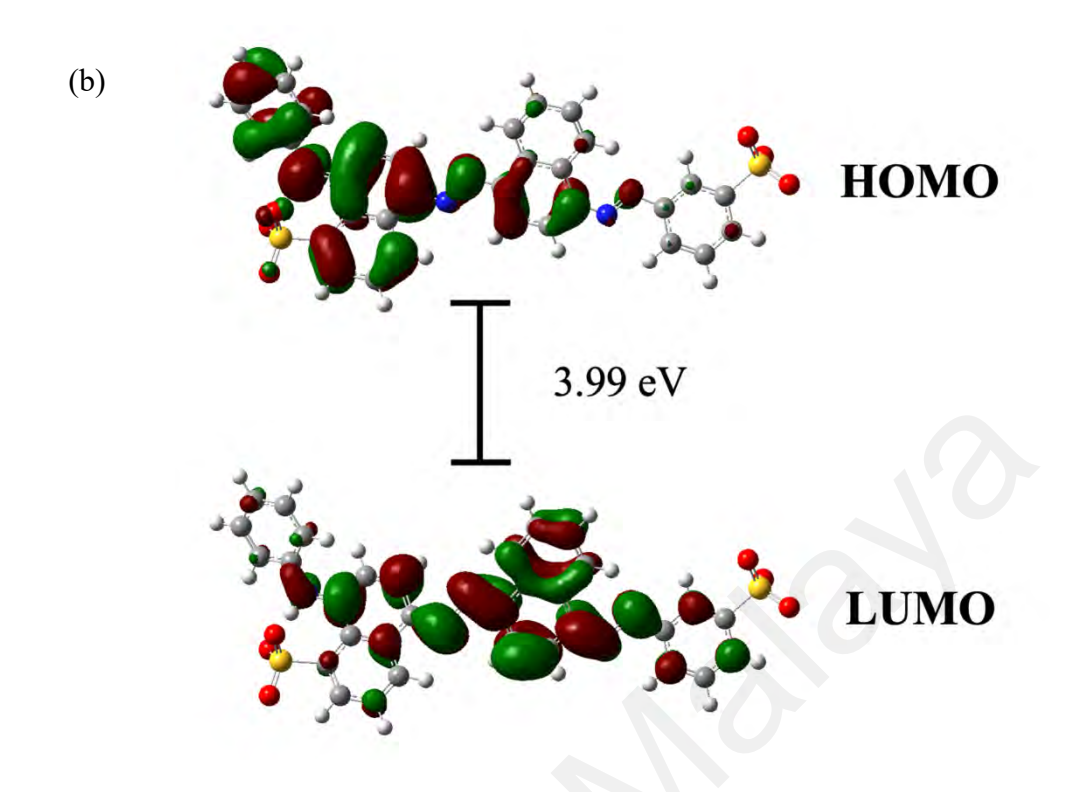
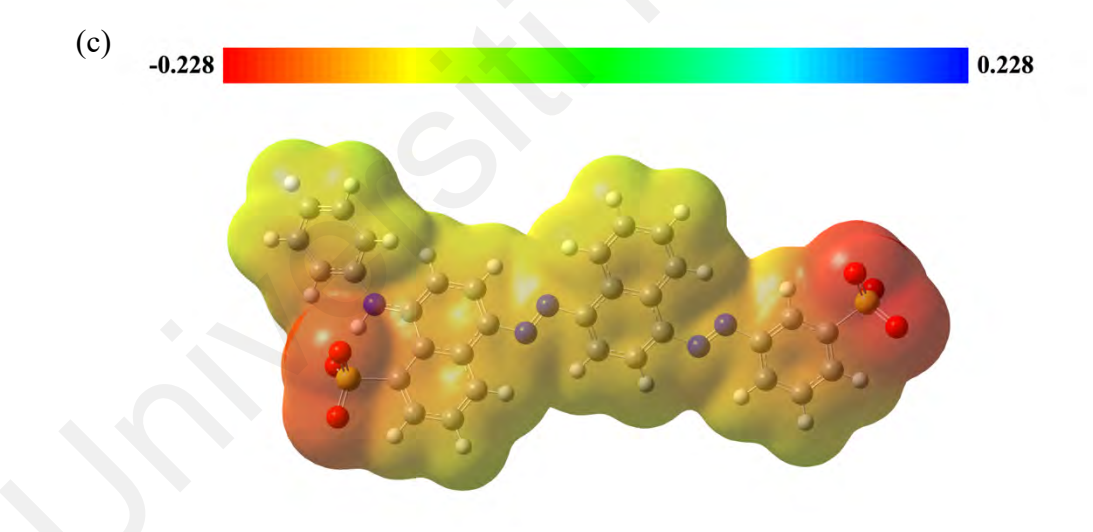


Figure 4.23: (a) Optimized Structure, (b) HOMO and LUMO, and (c) ESP Map of AB113 Dye

Figure 4.23: Continued





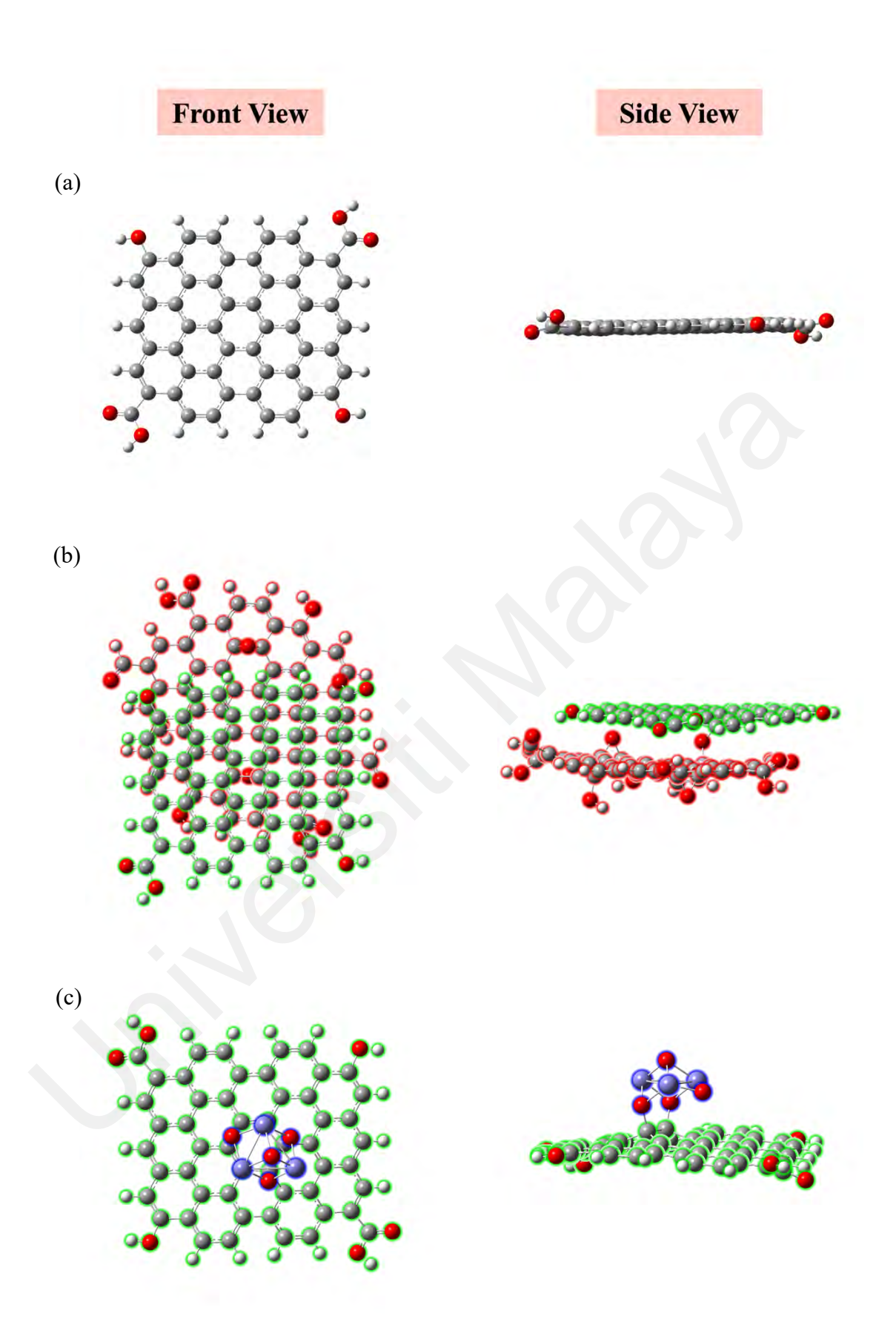
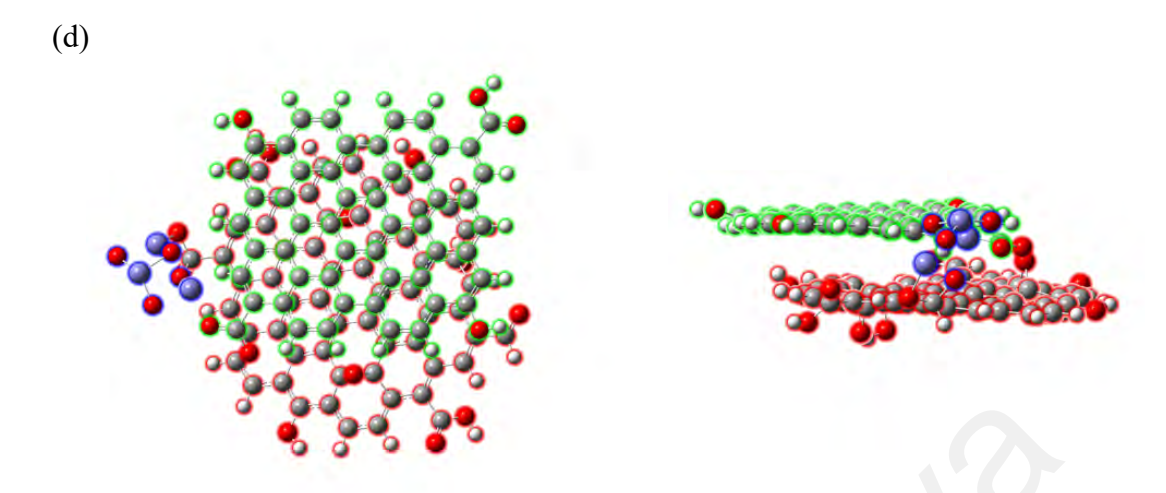


Figure 4.24: Optimized Structures of (a) PKSAC, (b) PKSAC-GO, (c) PKSAC-Fe, and (d) PKSAC-GO-Fe

Figure 4.24: Continued



4.8.1.3 Effects of Functional Groups on the Adsorption Process

To study the adsorption mechanism of AB113 dye on the PKSAC-GO-Fe surface, a quantum approach was employed, focusing on the various functional groups on the adsorbent. FTIR analysis identified several functional groups on the PKSAC-GO-Fe surface, including hydroxyl (OH), aldehyde (COH), carboxyl (COOH), ether (COC), and Fe₃O₄ groups. These functional groups, contributed by PKSAC, GO, and iron oxide, serve as active sites for dye adsorption. In this study, DFT calculations were performed to study the interactions between dye molecules and the functional groups on PKSAC-GO-Fe, to assess the effects and importances of different functional groups in dye adsorption. Figure 4.25 shows the optimized structures of pristine and various functionalized adsorbents.

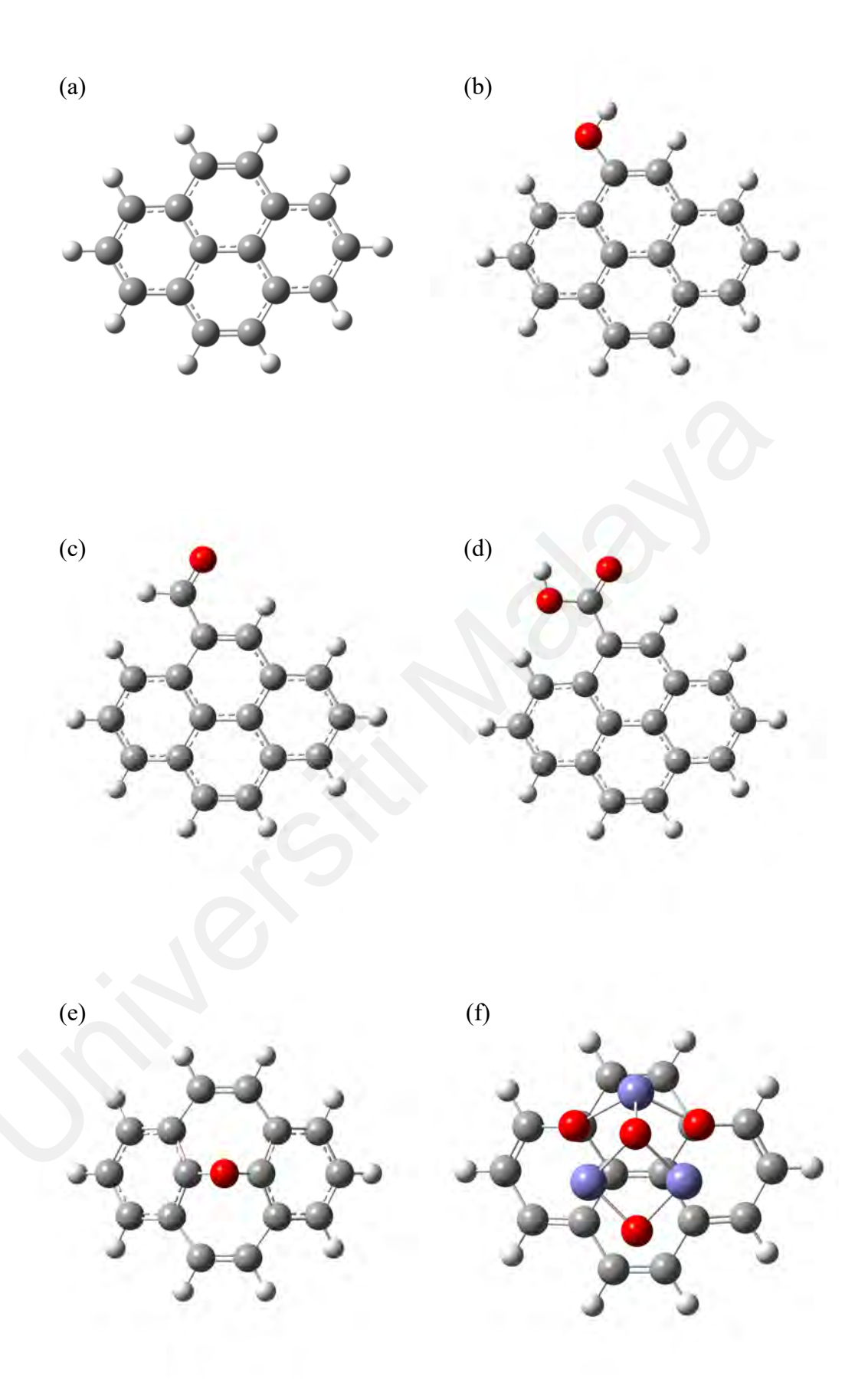


Figure 4.25: Optimized Structures of (a) CH (Pristine), (b) OH, (c) COH, (d) COOH, (e) COC, and (f) Fe₃O₄ Functionalized Adsorbents

Multiple interactions are involved in the adsorption of AB113 on PKSAC-GO-Fe, including electrostatic interactions, electron donor-acceptor mechanisms, π - π interactions between aromatic π systems, and hydrogen bonding. Hydrogen bonding, in particular, is a key interaction type contributing to the adsorption process. This study focused on the hydrogen bonding interactions between AB113 and the oxygenated functional groups on the PKSAC-GO-Fe surface using a quantum approach. As a control, the interaction of AB113 with a pristine adsorbent (with all C-H bonds at the edges) was considered and compared to functionalized adsorbents. Figure 4.26 shows the optimized structures of AB113 dye with various functionalized adsorbents, and Table 4.14 provides bond distances and adsorption energies.

Table 4.14: Adsorption Energy and Bond Length

| Adsorption Systems | Adsorption Energy (kJ/mol) | Bond Length (Å) | |
|--------------------------------------|----------------------------|-----------------|--|
| AB113-CH | -52.12 | 2.22 Å | |
| AB113-OH | -103.86 | 1.56 Å | |
| AB113-COH | -70.92 | 2.18 Å | |
| AB113-COOH | -103.39 | 1.44 Å | |
| AB113-COC | -70.69 | 2.25 Å | |
| AB113-Fe ₃ O ₄ | -118.59 | 1.98 Å | |

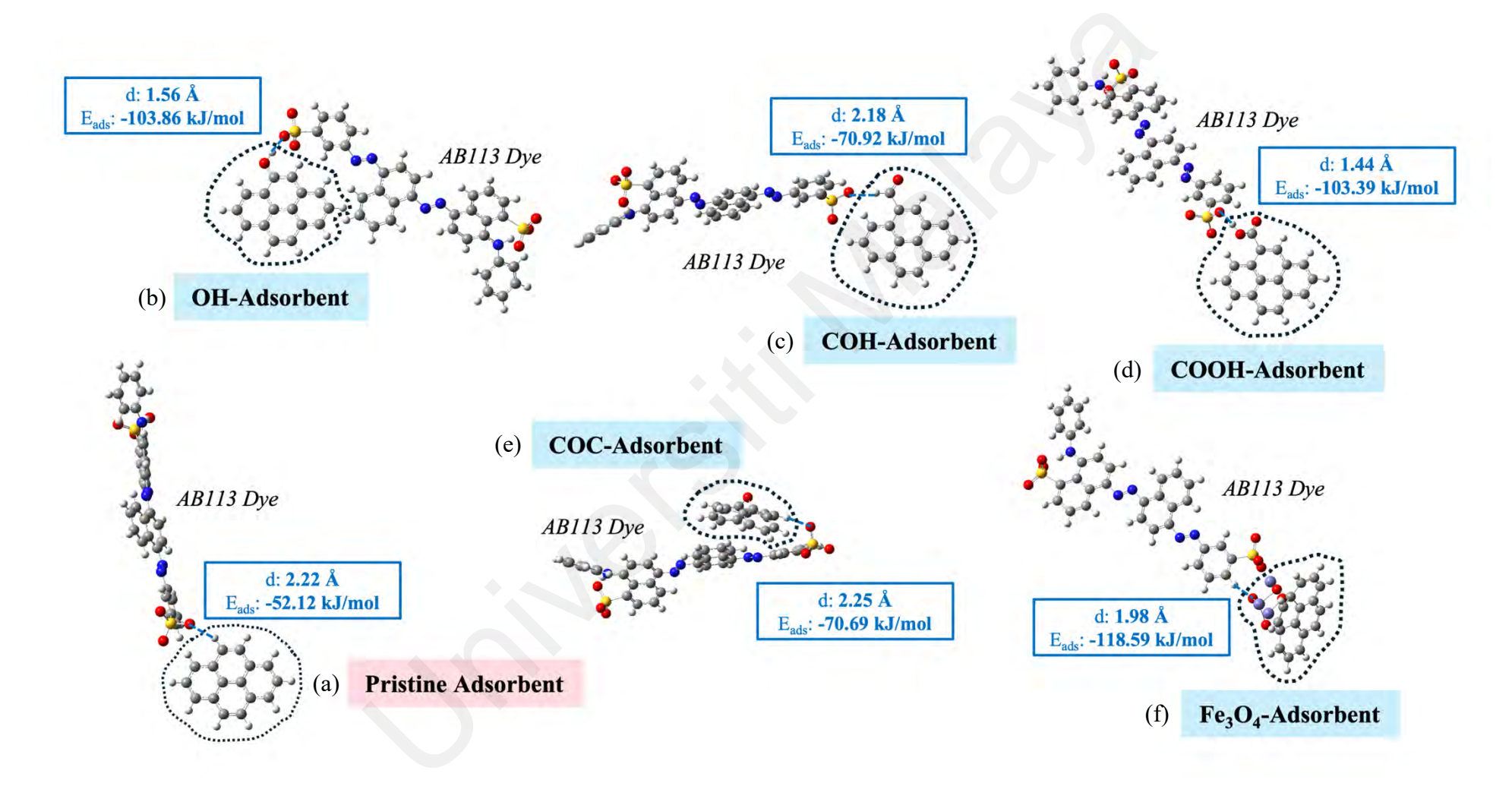


Figure 4.26: Optimized Structures of Various Adsorption Systems

(a) Pristine CH Adsorbent

As a control, the pristine adsorbent with all edges saturated with C-H groups was considered. The interaction between AB113 and the pristine (CH) adsorbent involved the formation of a hydrogen bond between the O atom from the sulfur trioxide (SO₃) group of AB113 and the H atom of the adsorbent. The optimized structure of the AB113-CH interaction is shown in Figure 4.26 (a). The C-H bond distance of the pristine adsorbent increased from 1.08647 Å to 1.08856 Å, indicating bond weakening due to electron cloud shifting towards the adsorption site. The hydrogen bond distance was 2.22 Å, with an adsorption energy of -52.12 kJ/mol, indicating a favorable chemisorption process. As seen in Table 4.14, the adsorption energy between AB113 and the pristine adsorbent was the lowest among all, highlighting the importance of functionalizing the adsorbent to enhance adsorption performance.

(b) OH Functionalized Adsorbent

AB113 interacts with the OH functionalized adsorbent through hydrogen bonding, as shown in Figure 4.26 (b). The hydrogen bond formed between the H atom from the adsorbent (O-H bond) and the oxygen atom of SO₃ (from AB113). The bond lengths of O-H and S-O elongated from 0.96398 Å to 1.01058 Å and 1.47398 Å to 1.50039 Å, respectively, indicating electron density shift towards the hydrogen bond. The hydrogen bond distance was 1.56 Å, with an adsorption energy of -103.86 kJ/mol, indicating strong chemisorption. This adsorption energy is the highest among all functionalized adsorbents, underscoring the importance of introducing hydroxyl groups to enhance adsorption performance.

(c) COH Functionalized Adsorbent

The interaction between AB113 and COH functionalized adsorbent is shown in Figure 4.26 (c). The O atom of AB113 interacts with the H atom of the COH functionalized

adsorbent, resulting in the elongation of the S-O bond distance from 1.47571 Å to 1.48351 Å, and the C-H bond length of COH increased from 1.08510 Å to 1.08517 Å. These changes indicate bond weakening due to stronger hydrogen bond formation. The AB113-COH bond distance was 2.18 Å, with an adsorption energy of -70.92 kJ/mol, indicating favorable chemisorption. The adsorption energy between AB113 and COH was significantly stronger than that of the pristine adsorbent by 36.1% (from -52.12 kJ/mol to -70.92 kJ/mol).

(d) COOH Functionalized Adsorbent

AB113 interacts with the COOH functionalized adsorbent through two hydrogen bonds, as shown in Figure 4.26 (d). One hydrogen bond forms between the H atom of COOH and the O atom of SO₃ from AB113, while the other forms between the O atom of COOH and the H of the benzene ring where SO₃ is bonded. The bond length of O-H from -COOH increased from 0.96965 Å to 1.04889 Å. The C-H bond length from the AB113 molecule also elongated from 1.08581 Å to 1.08818 Å. The bond distances were 1.44 Å and 2.29 Å, respectively. The adsorption energy of the AB113-COOH interaction was -103.39 kJ/mol, indicating strong chemisorption, highlighting the favorable interaction between AB113 and the COOH functionalized adsorbent. Additionally, the adsorption energy between AB113 and the COOH functionalized adsorbent was double that of the pristine adsorbent, emphasizing the importance of functionalizing the adsorbent to enhance performance.

(e) COC Functionalized Adsorbent

Figure 4.26 (e) illustrates the interaction between the AB113 dye molecule and the COC functionalized adsorbent. The AB113 molecule and the COC functionalized adsorbent were arranged in parallel, with one of the C-H edges of the -COC functionalized adsorbent deviating towards the SO₃ of AB113. The hydrogen bond was formed between the

hydrogen atom of the COC functionalized adsorbent (C-H) and the oxygen atom of SO₃ in AB113. The C-H bond length of the COC functionalized adsorbent elongated from 1.08757 Å to 1.08965 Å, indicating electron density shift towards the hydrogen bond. The hydrogen bond distance was 2.25 Å, and the adsorption energy was -70.69 kJ/mol, indicating chemisorption.

(f) Fe₃O₄ Functionalized Adsorbent

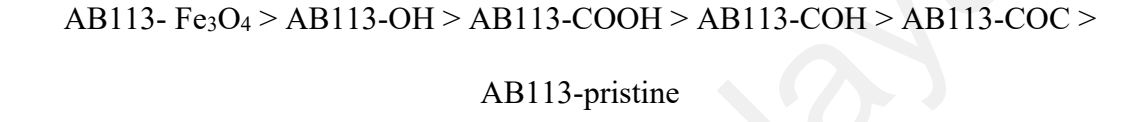
Figure 4.26 (f) depicts the interaction between the AB113 dye molecule and Fe₃O₄. The hydrogen atom of the benzene ring in the AB113 dye molecule, where the SO₃ group is bonded, forms a reaction with Fe₃O₄. A hydrogen bond is established between the hydrogen atom of the AB113 dye molecule and the oxygen atom of Fe₃O₄. The hydrogen bond distance is 1.98 Å, with an adsorption energy of -118.59 kJ/mol, indicating a chemisorption process.

4.8.1.4 Comparison of Adsorption Energy

Quantum calculations revealed that introducing various functional groups such as OH, COOH, COH, COC, and Fe₃O₄ on the adsorbent surface via impregnation of GO and iron oxide significantly enhanced the bonding and adsorption energy between the adsorbent and adsorbate, aligning well with experimental results.

A comparison of the adsorption energies of AB113 when interacting with both pristine and variously functionalized adsorbents was conducted, as illustrated in Figure 4.27. Among the different functional groups, Fe₃O₄ had the highest adsorption energy of -118.59 kJ/mol, followed by OH and COOH (-103.86 kJ/mol and -103.39 kJ/mol, respectively), suggesting stronger interactions compared to COH (-70.92 kJ/mol) and COC (-70.69 kJ/mol) functionalized adsorbents. It is noteworthy that all the functionalized adsorbents exhibited stronger adsorption energies than the pristine adsorbent (-52.12 kJ/mol), which aligns with experimental findings that adsorption

performance improves with the impregnation of GO and iron oxide into raw PKSAC. Additionally, from the quantum analysis, it is deduced that, in addition to the magnetic properties provided by the iron oxide impregnation, Fe₃O₄ significantly enhanced the adsorption of AB113 dye. This is consistent with experimental results, where higher adsorption performance was attained for PKSAC-Fe compared to raw PKSAC. All adsorption energies were lower than -50 kJ/mol, indicating a chemisorption process, consistent with adsorption kinetics studies. The interaction strengths ranked as follows:



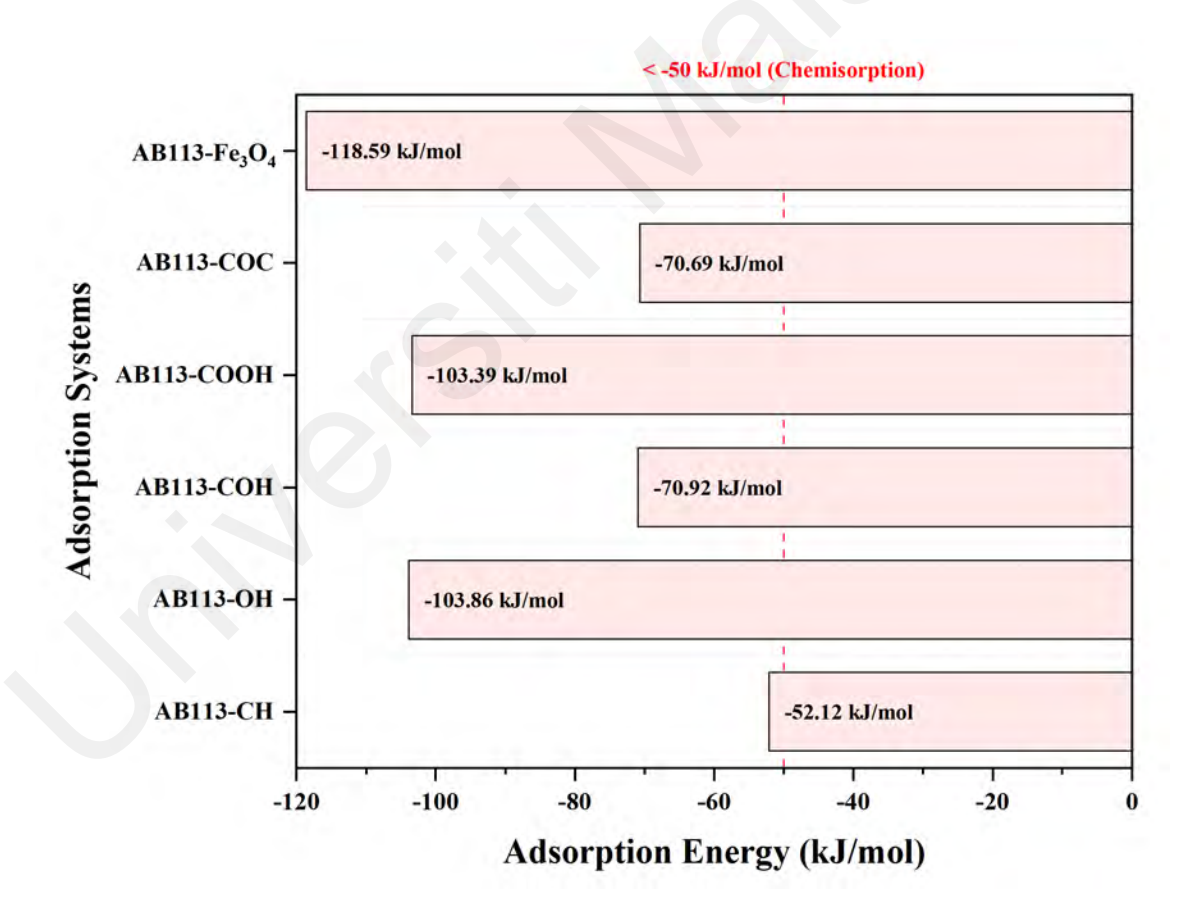


Figure 4.27: Adsorption Energy Diagram of AB113 onto Pristine and Functionalized Adsorbents

The quantum method has revealed the effects of a variety of surface functional groups on adsorption processes. This provides a comprehensive understanding of the electronic structures of dye molecules as well as the functional groups that are found on the surface of adsorbents. The results of both experimental and quantum studies showed strong correlations with one another, which indicates that the incorporation of a variety of functional groups into the adsorbent results in a substantial improvement in adsorption performance. This is achieved by forming stronger adsorbent-adsorbate bonds. Besides that, quantum chemical analysis has also confirmed that the predominant mechanism of PKSAC-GO-Fe is chemisorption. In short, quantum chemical analysis can be used to design and synthesize adsorbents with optimum surface functional groups and enhanced adsorption performance.

4.8.2 Adsorption Mechanism Evaluation via Machine Learning

In this work, a feature importance analysis was conducted to study the adsorption of AB113 dye using PKSAC-based adsorbents. The algorithm used was a gradient boosting machine learning model. The results are presented in Table 4.15 and Figure 4.28, which provide information on each parameter affecting the adsorption process. The model achieved a high R^2 value ($R^2 = 0.9590$) and MSE and RMSE values of 13.96 and 3.74, respectively, demonstrating superior predictive capability compared to previous literature (Zhao et al., 2023).

Operational parameters collectively have the most substantial effect on the adsorption process, contributing a total weightage of 85.53% to the overall importance. The adsorbent dosage was determined to be the most influential, with a weightage of 43.60% among all operational parameters. This indicates that the amount of adsorbent used in an adsorption process plays the most critical role that affects adsorption performance. It was followed by the initial pH of the solution, with a weightage of 32.75%. These findings

are consistent with the perturbation curve (Figure 4.2), where a steeper slope signifies their dominance in influencing adsorption performance. Contact time, dye concentration, and temperature, on the other hand, also contribute to the overall performance of the adsorption process. The weightages were determined to be 1.01%, 6.97%, and 1.20%, respectively. These results align with a previous study by Mazaheri et al. (2017), which also identified adsorbent dosage and pH as the most significant factors in the adsorption process.

In addition, the analysis indicates that the chemical properties of PKSAC-based adsorbents have a more significant effect on the adsorption process than their physical properties. The total weightage for chemical properties is 8.43%, with carbon content being the highest contributor (weightage of 3.63%). The pH_{pze}, oxygen content, and iron content of the PKSAC-based adsorbents are also important, with weightages of 1.47%, 1.65%, and 1.68%, respectively. This suggests that the chemical composition of the adsorbents, which affects their surface chemistry and interaction with pollutants, is critical for effective adsorption. Physical properties, such as BET surface area, pore diameter, pore volume, and Sauter mean diameter, contribute to a total weightage of 6.04%, which is 28.4% lower than the chemical properties of PKSAC-based adsorbents. Among these, pore diameter (weightage of 2.89%) and BET surface area (weightage of 1.44%) are more significant compared to pore volume (weightage of 1.08%) and Sauter mean diameter (weightage of 0.63%). The results signify that while the physical properties of the adsorbents do play a role in the adsorption process, they are less significant compared to chemical properties and operational parameters.

The feature importance analysis revealing the predominance of chemical properties and the significant effects of pH and adsorbent dosage indicated that chemisorption is the main mechanism. Strong chemical bonds are formed between the dye molecules and the

adsorbent surface during the chemisorption process. This type of process is therefore heavily dependent on the surface chemistry and functional groups of the adsorbents. The interactions at the molecular level are vital for the adsorption process, as indicated by the high importance of chemical properties like pH_{pzc} and elemental composition. In summary, the feature importance analysis demonstrates the significance of operational parameters, particularly adsorbent dosage and pH, in the adsorption of AB113 dye using PKSAC-based adsorbents. Chemical properties, especially surface chemistry and elemental composition, are determined to be more influential than physical properties like surface area and pore size. These findings reveal that the adsorption mechanism is predominantly chemisorption, driven by chemical interactions between the pollutant and the adsorbent surface. The results are well aligned with adsorption kinetic and quantum chemical analysis.

Table 4.15: Feature Importances of PKSAC-Based Adsorbents

| Category | Parameter | Weightage | Total Weightage |
|-------------|----------------------|-----------|-----------------|
| Physical | BET surface area | 1.44% | 6.04% |
| properties | Pore diameter | 2.89% | |
| | Pore volume | 1.08% | |
| | Sauter mean diameter | 0.63% | |
| Chemical | pH_{pzc} | 1.47% | 8.43% |
| properties | Carbon content | 3.63% | |
| | Oxygen content | 1.65% | |
| | Iron content | 1.68% | |
| Operational | рН | 32.75% | 85.53% |
| parameters | Adsorbent dosage | 43.60% | |
| | Contact time (h) | 1.01% | |
| | Dye concentration | 6.97% | |
| | Temperature | 1.20% | |

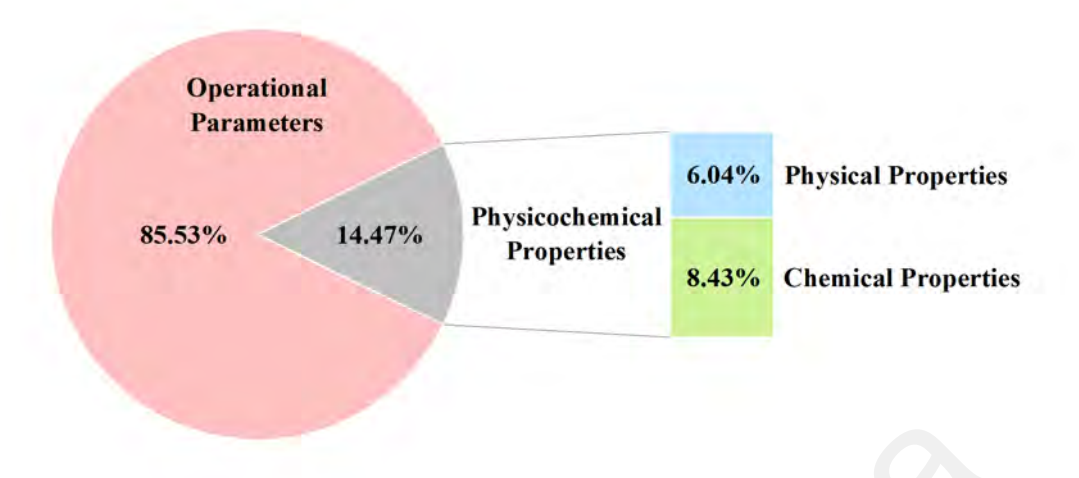


Figure 4.28: Feature Importances Analysis

4.9 Optimization of Ternary Composite Synthesis Process for the Actual Industrial Wastewater Treatment

Printing wastewater poses a significant environmental concern due to the large volumes produced and the complex mix of contaminants (Sayin et al., 2022). These effluents often include high levels of coloration and organic content. A significant amount of wastewater is produced during the manufacturing process in the printing industry, which encompasses a wide range of sectors including commercial printing, packaging, and textiles. The process of generating and treating printing wastewater is shown in Figure 4.29 (Naveed et al., 2006). It is estimated that the printing industry produces millions of liters of wastewater annually worldwide. Therefore, treating printing wastewater is crucial for ensuring public health, protecting the environment, complying with regulations, and promoting sustainable industrial practices.

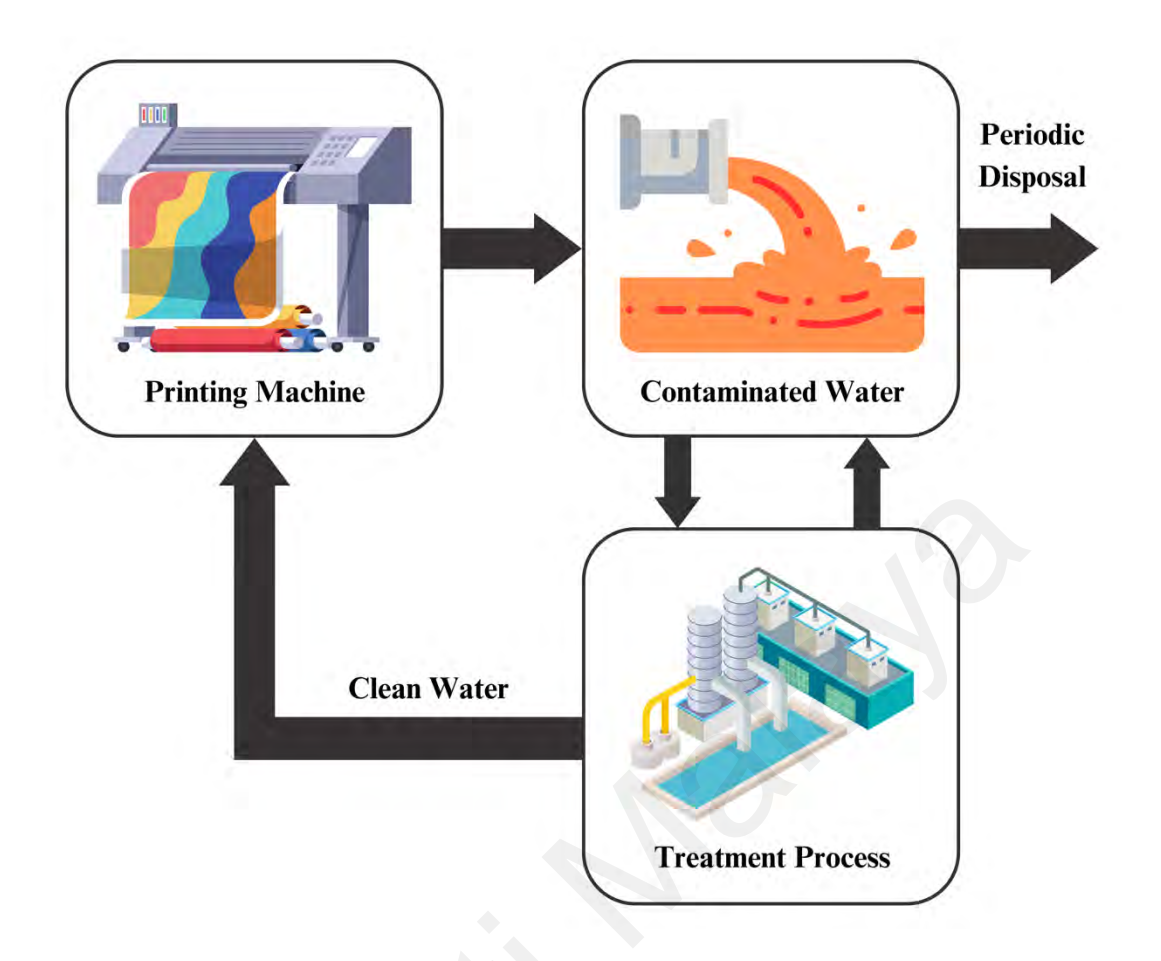


Figure 4.29: Wastewater from Printing Process

4.9.1 Effects of Operational Parameters in Optimizing Ternary Composite Synthesis Process

In this work, the optimization of PKSAC-GO-Fe synthesis process for the treatment of actual printing wastewater was conducted by varying the ratio of PKSAC/GO and the iron oxide loading amount. The PKSAC/GO ratio was varied from 0.2/0.8 to 0.8/0.2, and the iron oxide loading was adjusted between 15% and 45%. The performance of PKSAC-GO-Fe in treating actual industrial printing wastewater in terms of color removal efficiency and adsorption capacity is summarized in Table 4.16.

Among the different formulations tested, the PKSAC-GO-Fe composite synthesized with a PKSAC/GO ratio of 0.2/0.8 and an iron oxide loading of 45% demonstrated the highest performance. This optimized composite achieved a color removal efficiency of

61.7% and an adsorption capacity of 49.5 mg/g using 3.7 g/L of optimized PKSAC-GO-Fe at pH 7.5 for 2.1 hours.

Table 4.16: Optimization of PKSAC-GO-Fe Synthesis Process

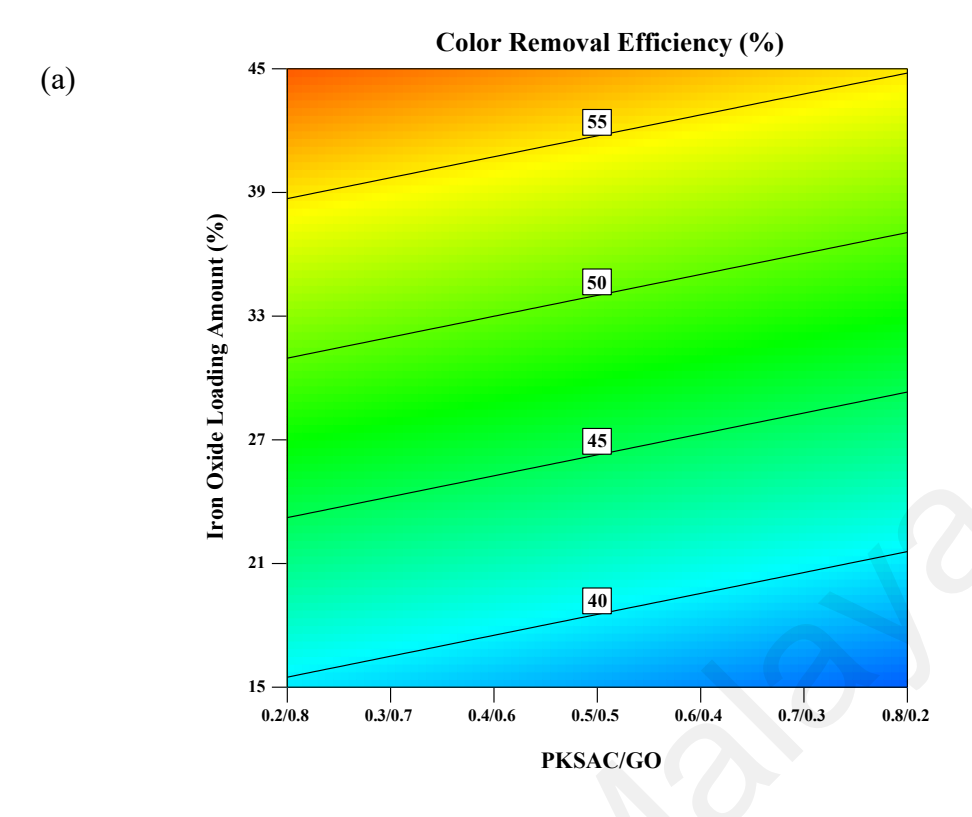
| Run PKSAC/GO | | Iron Oxide (%) | Color Removal | Adsorption | |
|--------------|-----------|------------------|----------------|-----------------|--|
| Kuli | r KSAC/GO | 11011 Oxide (76) | Efficiency (%) | Capacity (mg/g) | |
| 1 | 0.5/0.5 | 30.0 | 45.0 | 36.1 | |
| 2 | 0.2/0.8 | 45.0 | 61.7 | 49.5 | |
| 3 | 0.8/0.2 | 45.0 | 53.2 | 42.7 | |
| 4 | 0.5/0.5 | 30.0 | 49.9 | 40.1 | |
| 5 | 0.8/0.2 | 15.0 | 33.3 | 26.7 | |
| 6 | 0.08/0.92 | 30.0 | 49.7 | 39.9 | |
| 7 | 0.5/0.5 | 30.0 | 45.7 | 36.7 | |
| 8 | 0.5/0.5 | 51.2 | 60.6 | 48.6 | |
| 9 | 0.2/0.9 | 15.0 | 38.0 | 30.5 | |
| 10 | 0.92/0.08 | 30.0 | 47.9 | 38.5 | |
| 11 | 0.5/0.5 | 8.8 | 36.6 | 29.4 | |
| 12 | 0.5/0.5 | 30.0 | 45.8 | 36.8 | |
| 13 | 0.5/0.5 | 30.0 | 48.9 | 39.3 | |

4.9.1.1 Ratio of PKSAC/GO

The effects of PKSAC/GO and iron oxide loading amounts in the PKSAC-GO-Fe synthesis process on color removal efficiency and adsorption capacity for treating actual printing wastewater are illustrated in Figure 4.30. The PKSAC/GO ratio significantly influences the surface properties and adsorption performance of the composite. PKSAC provides a high surface area and pore structure, which are crucial for adsorption processes. Conversely, GO offers functional groups that enhance interactions with pollutants and improve dispersibility in aqueous solutions.

As shown in Figure 4.30, increasing the PKSAC/GO ratio from 0.2/0.8 to 0.5/0.5 resulted in a decrease in color removal efficiency and adsorption capacity from 39.7% and 31.9 mg/g to 37.8% and 30.3 mg/g, respectively, with a constant iron oxide loading of 15%. Further increasing the PKSAC/GO ratio from 0.5/0.5 to 0.8/0.2 led to an

additional decrease in color removal efficiency and adsorption capacity to 35.8% and 28.7 mg/g, respectively. This trend was consistent across different iron oxide loading amounts. For example, with a 30% iron oxide loading, color removal efficiency and adsorption capacity decreased from 49.4% (39.7 mg/g) to 45.5% (36.4 mg/g). A similar decreasing trend was investigated with a 45% iron oxide loading, where the adsorption performances were 59.1% (47.4 mg/g) and 55.1% (44.2 mg/g) for PKSAC/GO ratios of 0.2/0.8 and 0.8/0.2, respectively. This can be explained by, at a lower PKSAC/GO ratio (0.2/0.8), the higher amount of GO enhances the hydrophilicity of the composite and increases the number of active sites available for pollutant binding due to oxygen-containing functional groups of GO. Conversely, a higher PKSAC content (0.8/0.2) provides more pores but potentially reduces the overall functionality of the composite, leading to decreased adsorption efficiency. Excessive PKSAC may also cause adsorbent surface aggregation, further reducing color removal efficiency and adsorption capacity (Hossain & Park, 2016). Additionally, the complex nature of printing wastewater may require more GO, which contains a variety of functional groups compared to PKSAC. Therefore, a balanced ratio is essential for maximizing both surface area and functionality, with the 0.2/0.8 ratio being optimum for treating printing wastewater.



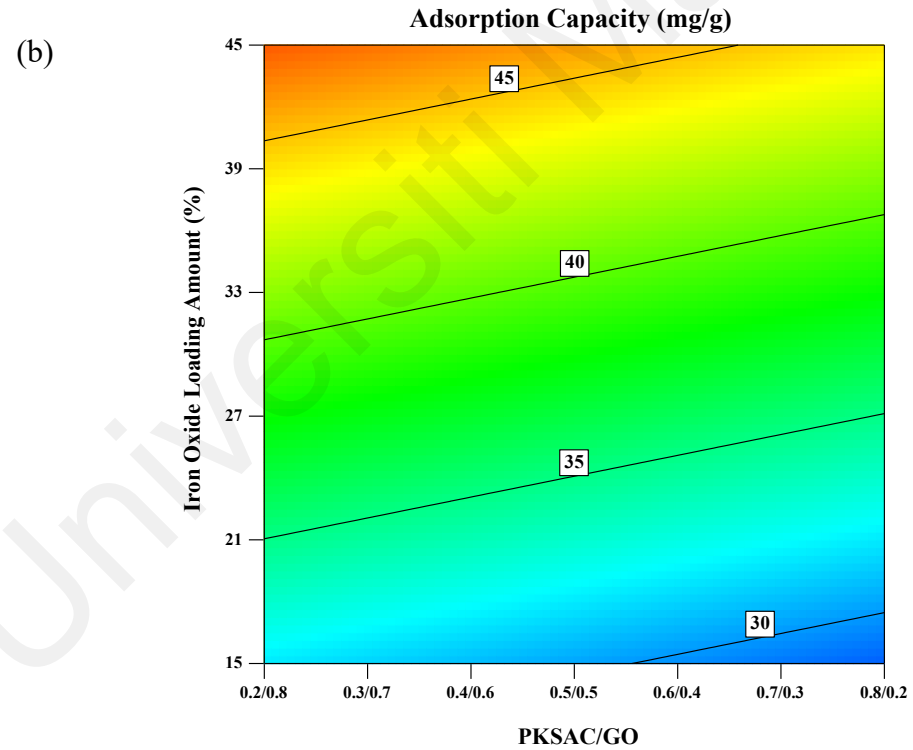


Figure 4.30: Interactive Effects of PKSAC/GO and Iron Oxide on the (a) Color Removal Efficiency and (b) Adsorption Capacity in Treating Actual Printing Wastewater

4.9.1.2 Loading Amount of Iron Oxide

The loading amount of iron oxide affects the magnetic properties and surface chemistry of the adsorbent. Increasing the iron oxide content enhances the magnetic separability of the adsorbent, which is advantageous for practical applications. However, excessive iron oxide can lead to particle agglomeration, reducing the available surface area for adsorption (Yi et al., 2020; N. Zhang et al., 2024). In this study, the iron oxide loading on the composite varied from 15% to 45%, and the performance in treating printing wastewater was studied (Figure 4.30).

From Figure 4.30, color removal efficiency of printing wastewater increased from 37.8% to 57.0% when the iron oxide loading increased from 15% to 45% at a PKSAC/GO ratio of 0.5/0.5. Similarly, the adsorption capacity followed the same trend, increasing from 30.3 mg/g to 45.7 mg/g under similar synthesis conditions. This increase in color removal efficiency and adsorption capacity with higher iron oxide content can be related to the synergistic effect that improves the performance of the PKSAC-GO-Fe composite (Chen et al., 2009). However, when the iron oxide content increased further to 51.2%, a reduction in color removal efficiency and adsorption capacity was observed, likely due to the excess iron oxide causing changes in pore distribution and accessible adsorption sites (Cheng et al., 2019).

Hence, a 45% iron oxide loading was found to be optimum. This high iron oxide content provided sufficient magnetic properties for easy separation without significantly hindering the surface area and porosity. Lower iron oxide loadings (15%) did not offer the same level of magnetic separability and were less effective in pollutant adsorption due to fewer active sites available on the adsorbent surface.

4.9.1.3 Optimization Study

The predicted and experimental values under optimum conditions were compared to confirm the suitability and accuracy of the RSM-CCD model to evaluate and predict the adsorbent synthesis process, as shown in Table 4.17. Under optimum conditions of PKSAC/GO ratio of 0.2/0.8 and 45% iron oxide loading, the predicted results for color removal efficiency and adsorption capacity were 59.1% and 47.4 mg/g, respectively in treating printing wastewater. The color removal efficiency and adsorption capacity achieved experimentally were determined to be 61.7% and 49.5 mg/g, respectively. By comparing the predicted and experimental values, there was no substantial variation between them. Hence, it can be said that RSM-CCD optimization provides reliable results for optimizing the synthesis conditions of the adsorbent (Ma et al., 2020).

Table 4.17: Optimum Synthesis Process of PKSAC-GO-Fe

| PKSAC/GO | Iron | Color Removal | Efficiency | Adsorption Capacity | |
|-----------|-------|---------------|-------------------|---------------------|-----------|
| I KSAC/GO | Oxide | Pred. | Exp. | Pred. | Exp. |
| 0.2/0.8 | 45% | 59.1% | 61.7% | 47.4 mg/g | 49.5 mg/g |

Pred.: Predicted; Exp.: Experimental

4.9.2 Effects of Adsorption Operational Parameters using Optimized Ternary Composite

The adsorption performance of the optimized PKSAC-GO-Fe composite in treating printing wastewater was evaluated by considering the initial pH of the wastewater (pH 3-11), adsorbent dosage (1-5 g/L), and contact time (2-6 hours). The responses evaluated are color removal efficiency and adsorption capacity. The experimental results under different adsorption operational conditions are depicted in Table 4.18. From Table 4.18, 100.0% color removal efficiency was obtained at pH 1.74 with 3 g/L of optimized PKSAC-GO-Fe for 4 hours. Meanwhile, the maximum adsorption capacity of 291.3 mg/g was recorded at pH 3 using 1 g/L of optimized PKSAC-GO-Fe for 6 hours.

Table 4.18: Adsorption of Printing Wastewater using Optimized PKSAC-GO-Fe

| Run | Initial pH of the Solution | Adsorbent Dosage (g/L) | Time (h) | Color Removal Efficiency (%) | Adsorption Capacity (mg/g) |
|-----|-------------------------------|---------------------------|-------------|------------------------------------|----------------------------------|
| 1 | 7.0 | 3.0 | 4.0 | 64.4 | 63.1 |
| 2 | 11.0 | 5.0 | 6.0 | 61.4 | 36.1 |
| 3 | 7.0 | 3.0 | 4.0 | 66.6 | 65.3 |
| 4 | 3.0 | 1.0 | 6.0 | 99.1 | 291.3 |
| 5 | 7.0 | 0.4 | 4.0 | 35.6 | 282.7 |
| 6 | 3.0 | 1.0 | 2.0 | 99.0 | 291.0 |
| 7 | 11.0 | 1.0 | 2.0 | 34.0 | 99.9 |
| 8 | 7.0 | 3.0 | 4.0 | 59.1 | 57.9 |
| 9 | 7.0 | 3.0 | 6.6 | 81.0 | 79.3 |
| 10 | 7.0 | 3.0 | 4.0 | 51.1 | 50.1 |
| 11 | 11.0 | 1.0 | 6.0 | 42.2 | 124.0 |
| 12 | 1.7 | 3.0 | 4.0 | 100 | 97.9 |
| 13 | 7.0 | 5.6 | 4.0 | 78.2 | 40.8 |
| 14 | 7.0 | 3.0 | 1.4 | 67.8 | 66.4 |
| 15 | 12.3 | 3.0 | 4.0 | 24.7 | 24.2 |
| 16 | 7.0 | 3.0 | 4.0 | 59.3 | 58.1 |
| 17 | 3.0 | 5.0 | 6.0 | 100.0 | 58.8 |
| 18 | 3.0 | 5.0 | 2.0 | 99.4 | 58.4 |
| 19 | 11.0 | 5.0 | 2.0 | 56.2 | 33.0 |
| 20 | 7.0 | 3.0 | 4.0 | 72.8 | 71.3 |

4.9.2.1 Effect of Initial pH of the Solution

The effectiveness of the adsorption process is greatly influenced by the pH of the sample solution and the types of functional groups present in the wastewater. In adsorption experiments, the pH_{pzc} refers to the pH at which the adsorbent surface has no net charge. In this study, the optimized PKSAC-GO-Fe composite had a pH_{pzc} of 5.1 (Figure 4.31). This means that when the initial solution pH is lower than 5.1, the composite surface becomes positively charged, and when the solution pH is greater than 5.1, the surface becomes negatively charged. The pH ranges from 3 to 11 were considered in this study. Printing wastewater may contain various functional groups, which contribute to variations in removal efficiencies at different pH levels. As shown in Figures 4.32 (a) and 4.33 (a), when 1 g/L of optimized PKSAC-GO-Fe composite was applied for a contact

time of 4 hours, color removal efficiency and adsorption capacity decreased from 84.5% (284.4 mg/g) to 22.1% (121.1 mg/g) as the pH increased from 3 to 11. A similar decreasing trend was observed at different adsorbent dosages. For instance, color removal efficiency and adsorption capacity were higher under acidic conditions at pH 3 (91.7%; 45.8 mg/g) compared to neutral pH (69.9%; 40.4 mg/g) and alkaline pH (49.1%; 35.0 mg/g) using 5 g/L of optimized PKSAC-GO-Fe composite under the same contact time. From the experimental results, it can be deduced that the printing wastewater sample contained a higher amount of anionic functional groups than cationic functional groups. As a result, higher performance can be achieved under acidic conditions attributed to the electrostatic interaction between positively charged adsorbent surface and anionic pollutants (Sridhar et al., 2022).

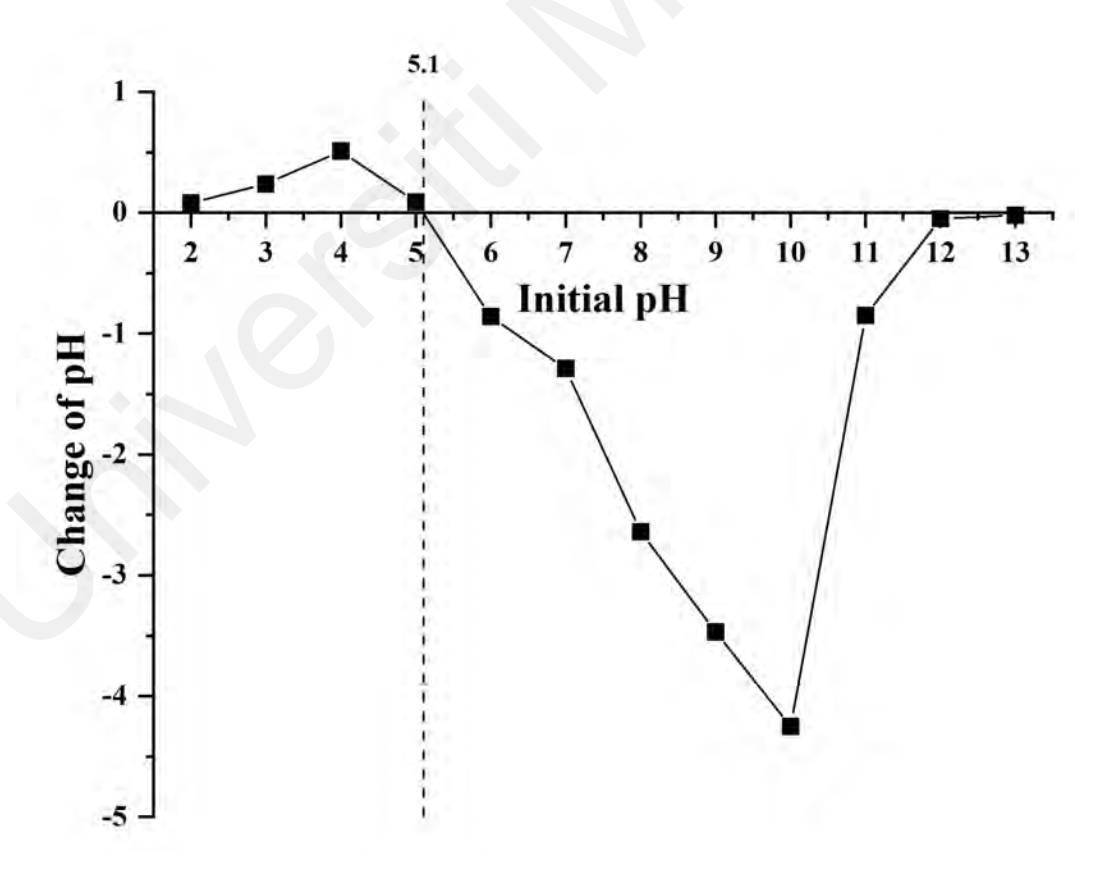


Figure 4.31: pH_{pzc} of Optimized PKSAC-GO-Fe Composite

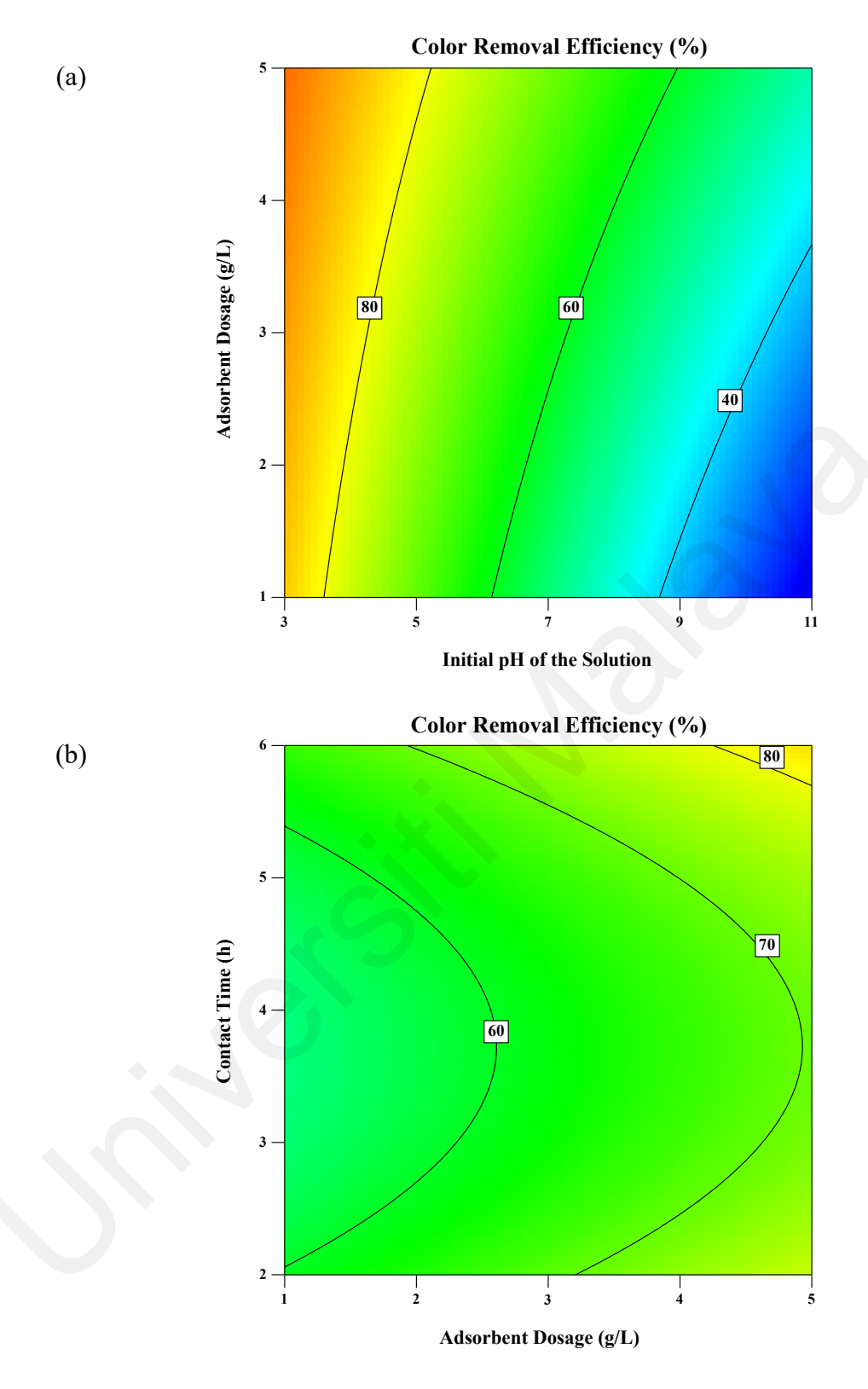
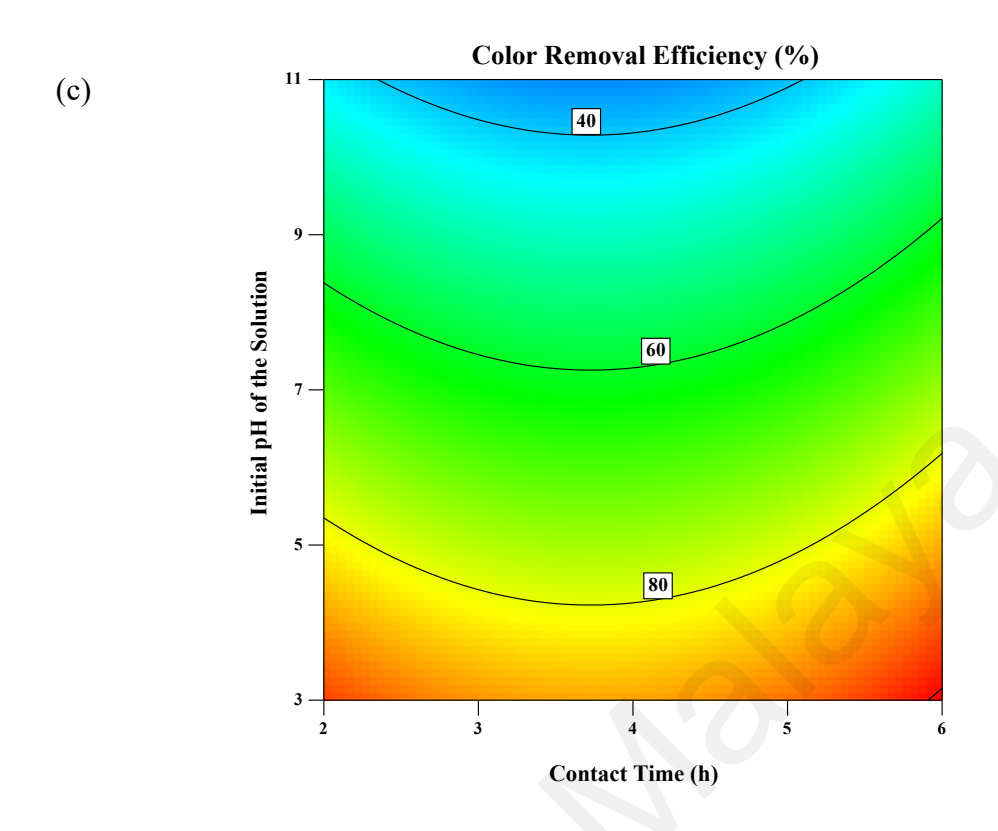


Figure 4.32: Interactive Effects of (a) pH and Adsorbent Dosage, (b) Adsorbent Dosage and Contact Time, and (c) Contact Time and pH on Color Removal Efficiency in Treating Actual Printing Wastewater using Optimized PKSAC-GO-Fe

Figure 4.32: Continued



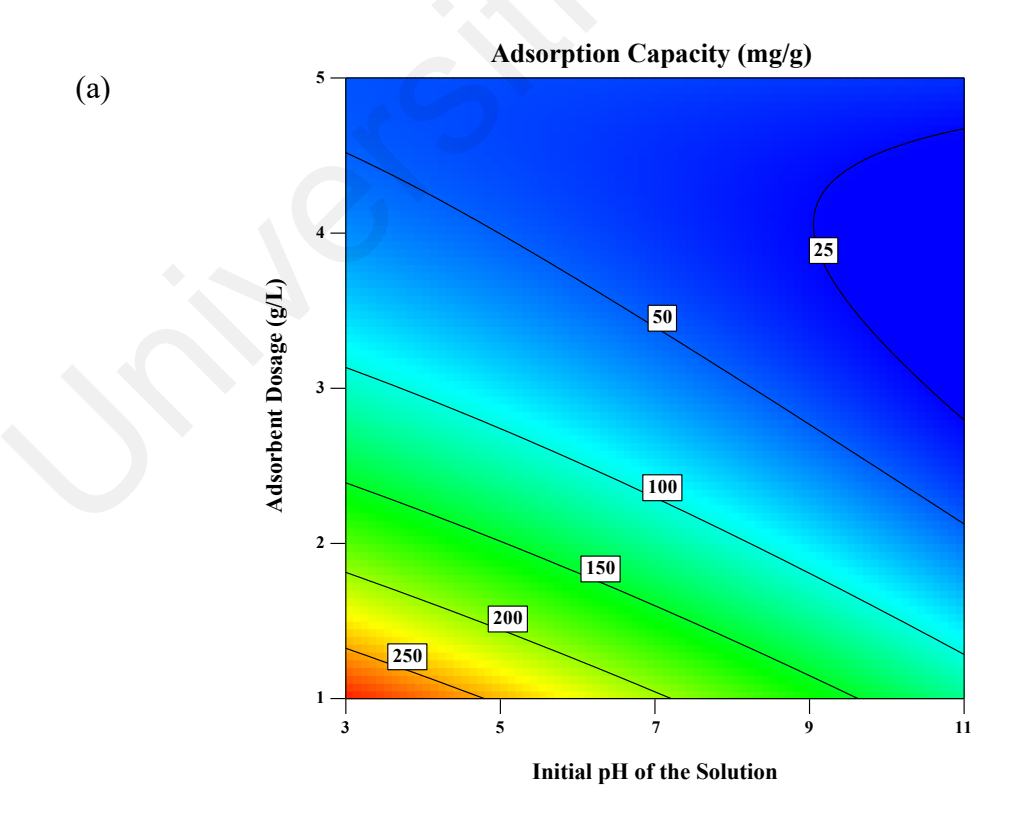
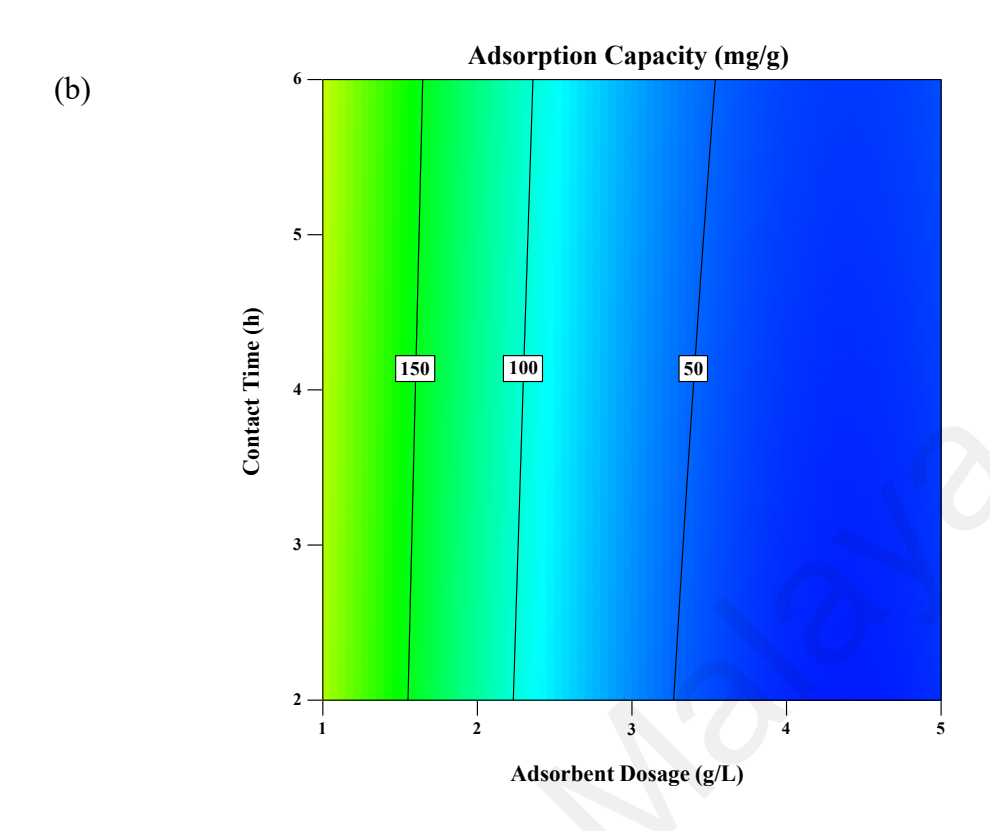
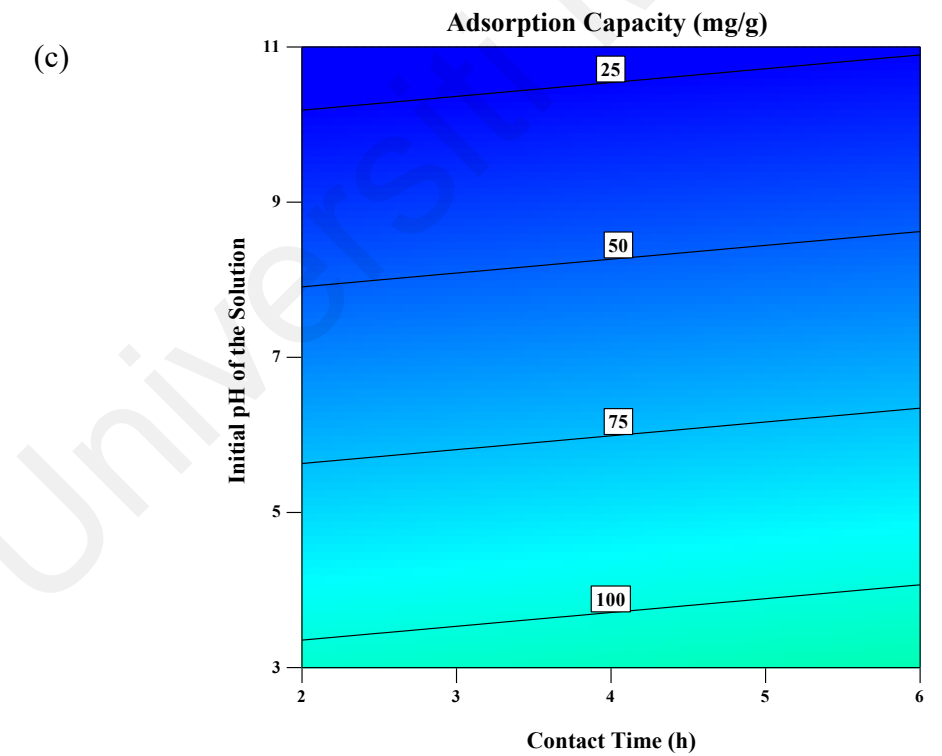


Figure 4.33: Interactive Effects of (a) pH and Adsorbent Dosage, (b) Adsorbent Dosage and Contact Time, and (c) Contact Time and pH on Adsorption Capacity in Treating Actual Printing Wastewater using Optimized PKSAC-GO-Fe

Figure 4.33: Continued





4.9.2.2 Effect of Adsorbent Dosage

In this study, the dosage of optimized PKSAC-GO-Fe composite was varied from 1 to 5 g/L in treating actual printing wastewater. Under acidic conditions (pH 3), color removal efficiency increased from 84.4% to 91.8% (Figure 4.32 (a)), while adsorption capacity decreased from 285.3 mg/g to 45.8 mg/g (Figure 4.33 (a)) at a contact time of 4 hours as the dosage of optimized composite increased from 1 to 5 g/L. The enhancement in color removal efficiency can be attributed to the increased number of active sites and adsorption surface area available at higher adsorbent dosages (Kumari et al., 2022; Lawal et al., 2018; W. Zhang et al., 2020). In contrast, due to the total surface area reduction and increased diffusion path length that caused by the aggregation of adsorption sites, a higher adsorbent dosage has led to a lower adsorption capacity (Bhattacharyya et al., 2018). In addition, the use of adsorption sites may not be maximized and could become saturated when higher adsorbent dosages are used (Ruscasso et al., 2021). This finding aligns with previous literature on the removal of various pollutants (Zhao & Zhou, 2016).

4.9.2.3 Effect of Contact Time

Contact time affects how long time is the interaction duration between the adsorbent and pollutants, is a crucial parameter in adsorption processes. In this study, the effect of contact time was investigated over a range of 2 to 6 hours. Figures 4.32 (c) and 4.33 (c) depict the effects of initial pH of the solution and contact time on color removal efficiency and adsorption capacity of printing wastewater using optimized PKSAC-GO-Fe composite. As shown in Figures 4.32 (c) and 4.33 (c), when 3 g/L of adsorbent was used, color removal efficiency and adsorption capacity were 95.2% (103.7 mg/g) and 100.0% (111.5 mg/g), respectively, for an adsorption contact time of 2 and 6 hours at pH 3. Similar trends were observed at neutral pH (7) and alkaline pH (11). At pH 7, as contact time increased from 2 to 6 hours, color removal efficiency and adsorption capacity slightly increased from 68.8% (59.8 mg/g) to 74.2% (67.9 mg/g). Under alkaline conditions (pH

11), color removal efficiency was 42.5% and 48.0%, while adsorption capacity was 16.6 mg/g and 24.1 mg/g for 2 and 6 hours of contact time, respectively. Only slight enhancements in color removal efficiency and adsorption capacity were recorded over 4 hours (pH 3: 4.8%; 7.8 mg/g, pH 7: 5.4%; 8.1 mg/g, pH 11: 5.5%; 7.5 mg/g). Initially, the adsorption process was rapid, with significant pollutant removal observed within the first 2 hours due to the high availability of active sites. As time progressed, the rate of adsorption slowed down, approaching equilibrium as the active sites became occupied (Munagapati et al., 2018).

4.9.2.4 Optimization Study

Considering the natural pH of printing wastewater (pH 7.2), the chemical cost of adjusting the solution pH, the need for post-treatment pH adjustment before discharge, the cost of the adsorbent, and time factors, as well as balancing between color removal efficiency and adsorption capacity, the optimum conditions were established to be pH 7.2 using 2.7 g/L of optimized PKSAC-GO-Fe for 2 hours. 70.2% color removal efficiency and an adsorption capacity of 76.4 mg/g were achieved in treating printing wastewater under the aforementioned conditions.

4.9.3 Mechanism Study of Optimized Ternary Composite

4.9.3.1 Kinetics Study

In this study, the rate-limiting steps and mechanisms of optimized PKSAC-GO-Fe involved in treating printing wastewater were identified through kinetics studies. Three models were employed: pseudo-first-order (P-F-O), pseudo-second-order (P-S-O), and intra-particle diffusion (I-P-D), with both linear and non-linear forms evaluated. The results are shown in Table 4.19 and Figure 4.34.

For the P-F-O model, the linear form provided a rate constant k_1 of 0.05 min⁻¹ and an R^2 of 0.7444 while the non-linear form showed a better fit with an R^2 of 0.9586 with k_1

of 0.16 min⁻¹. The calculated q_e were 74.2 mg/g and 71.3 mg/g for linear and non-linear P-F-O, respectively which deviate by 2.9% and 6.9% from the experimental data (76.4 mg/g). On the other hand, both the linear and non-linear forms of P-S-O provided an excellent fit, with R^2 values of 0.9975 and 0.9827, respectively The R^2 are the highest among the three kinetic models, indicating that the adsorption process follows the P-S-O kinetic model, suggesting that the adsorption is primarily governed by a chemisorption process (Khalil et al., 2024; Yaqub et al., 2024). The predicted q_e values of 79.8 mg/g and 75.6 mg/g are close to the experimental value of 76.4 mg/g, further supporting the validity of this kinetic model to describe the adsorption of actual printing wastewater using optimized PKSAC-GO-Fe composite (Kanwal et al., 2024). The linear form of I-P-D provided a rate constant k_i of 2.19 mg g^{-1} min^{-0.5} with an R^2 of 0.9723. The non-linear form yielded a higher k_i value of 5.29 mg g^{-1} min^{-0.5} but a lower R^2 of 0.7037. These results suggest that I-P-D model plays a role in the adsorption process, but it is not the sole rate-limiting step (Pandey et al., 2025).

In summary, the superior fit of the P-S-O model suggests that the adsorption of pollutants onto optimized PKSAC-GO-Fe is primarily governed by chemisorption, indicating chemical interactions between the adsorbate molecules and the active sites on the adsorbent surface. The I-P-D model also contributes to understanding the adsorption mechanism, indicating that diffusion within the adsorbent pores plays a significant role but is not the sole rate-limiting step. These findings are consistent with previous research (Khamwichit et al., 2022; Ouettar et al., 2023; Teshager et al., 2022).

Table 4.19: Kinetic Parameters of Printing Wastewater Adsorption onto Optimized PKSAC-GO-Fe

| Kinetic Model | Parameter | Unit | Linear | Non-Linear |
|---------------|---------------------------|--|-----------------------|-----------------------|
| Experiment | qe (experimental) | mg g ⁻¹ | 76.4 | |
| P-F-O | \mathbf{k}_1 | min ⁻¹ | 0.05 | 0.16 |
| | q_{e} | mg g ⁻¹ | 74.2 | 71.3 |
| | \mathbb{R}^2 | - | 0.7444 | 0.9586 |
| P-S-O | \mathbf{k}_2 | g mg ⁻¹ min ⁻¹ | 1.90×10 ⁻³ | 3.92×10 ⁻³ |
| | q_{e} | mg g ⁻¹ | 79.8 | 75.6 |
| | \mathbb{R}^2 | - | 0.9975 | 0.9827 |
| I-P-D | \mathbf{k}_{i} | mg g ⁻¹ min ^{-0.5} | 2.19 | 5.29 |
| | c | - | 52.98 | 26.91 |
| | \mathbb{R}^2 | - | 0.9723 | 0.7037 |

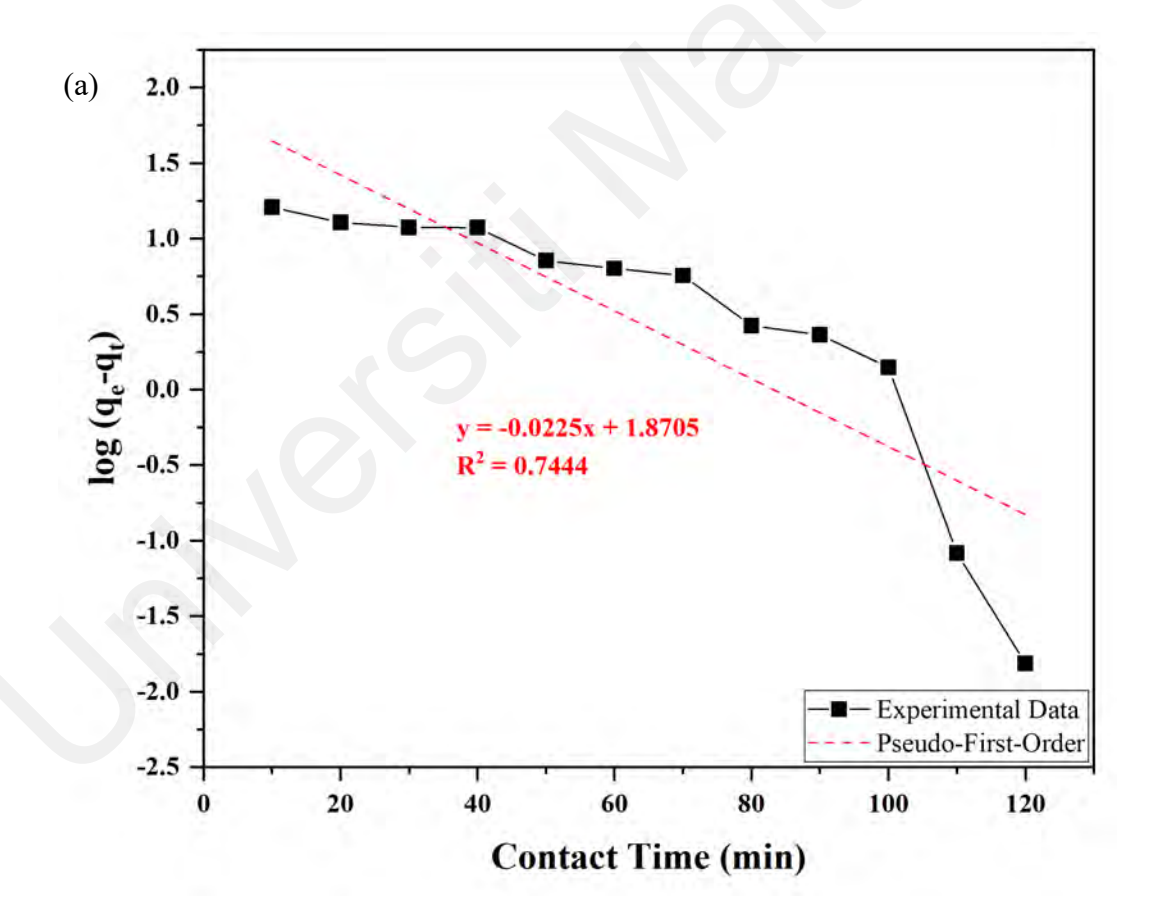
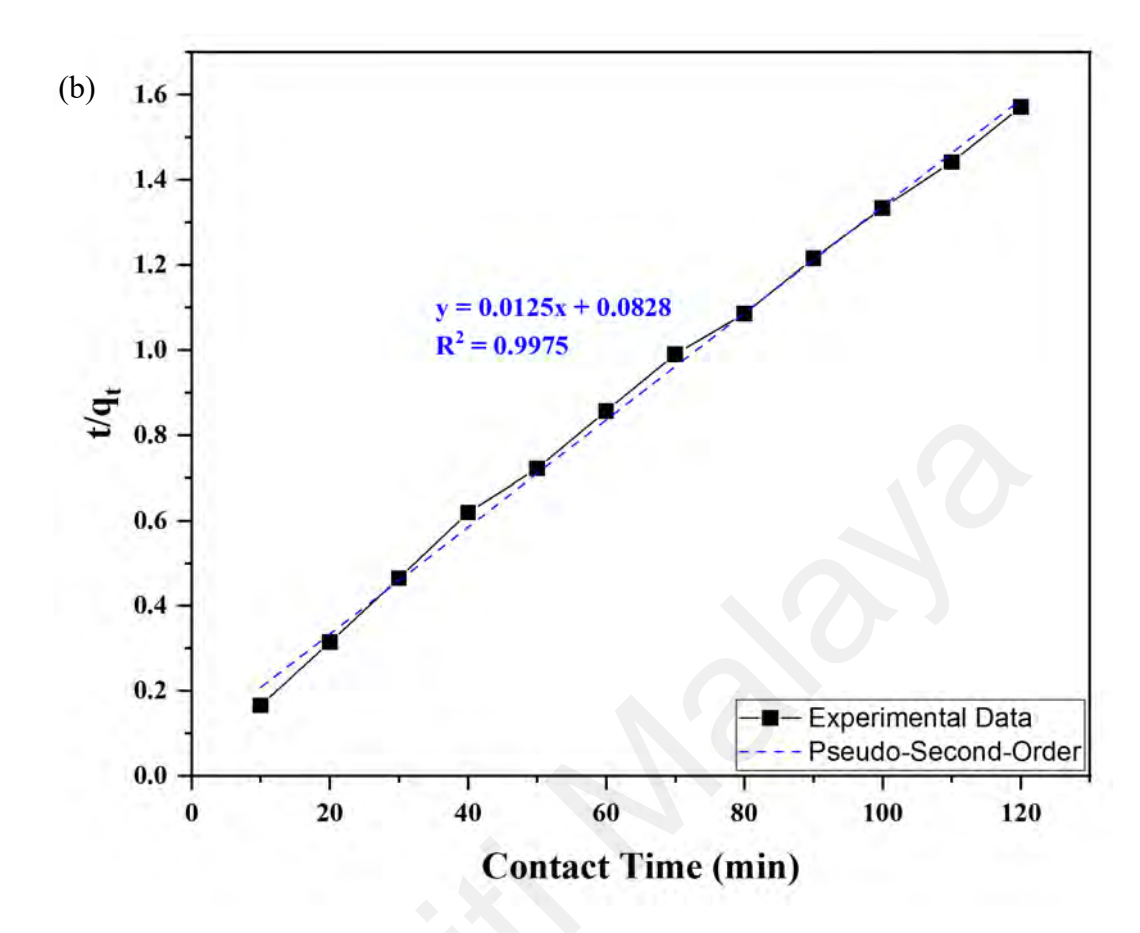


Figure 4.34: Linear Kinetic Plots for (a) P-F-O, (b) P-S-O, and (c) I-P-D, and (d) Non-Linear Kinetic Plot in Treating Actual Printing Wastewater

Figure 4.34: Continued



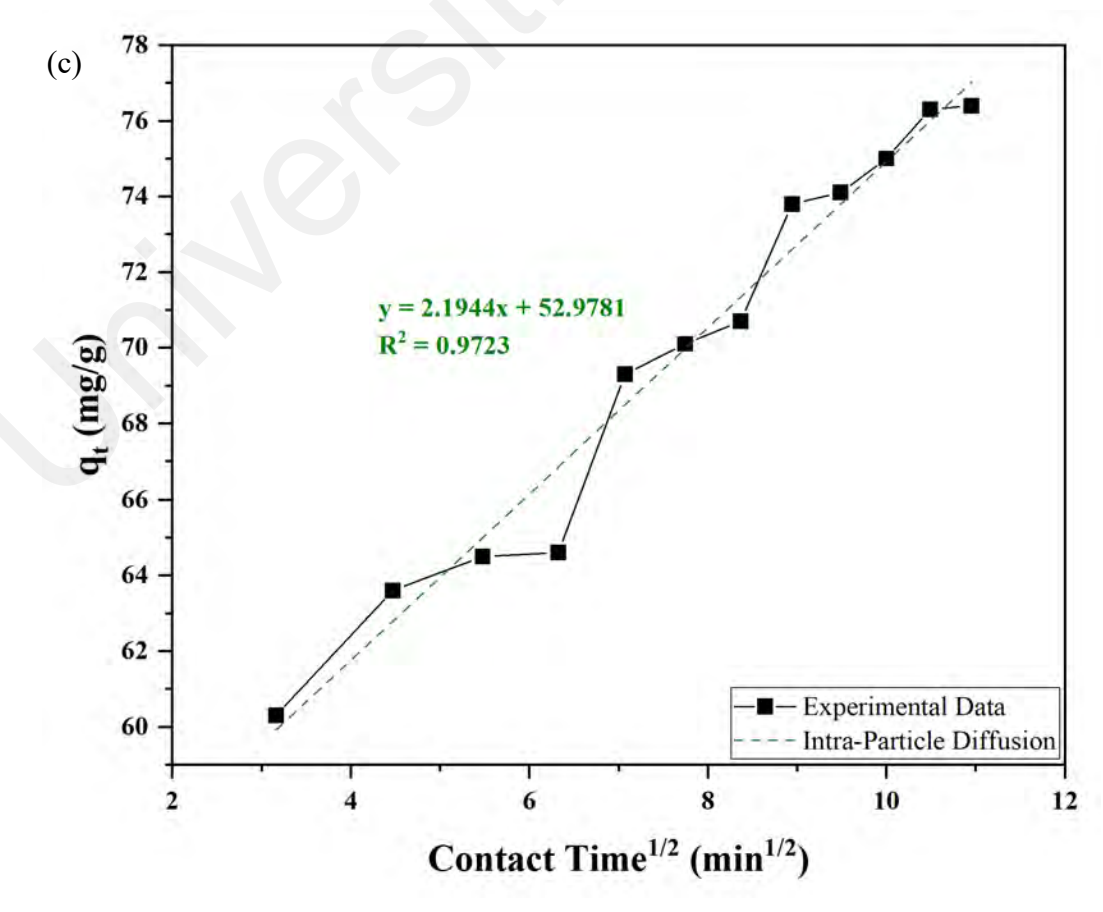
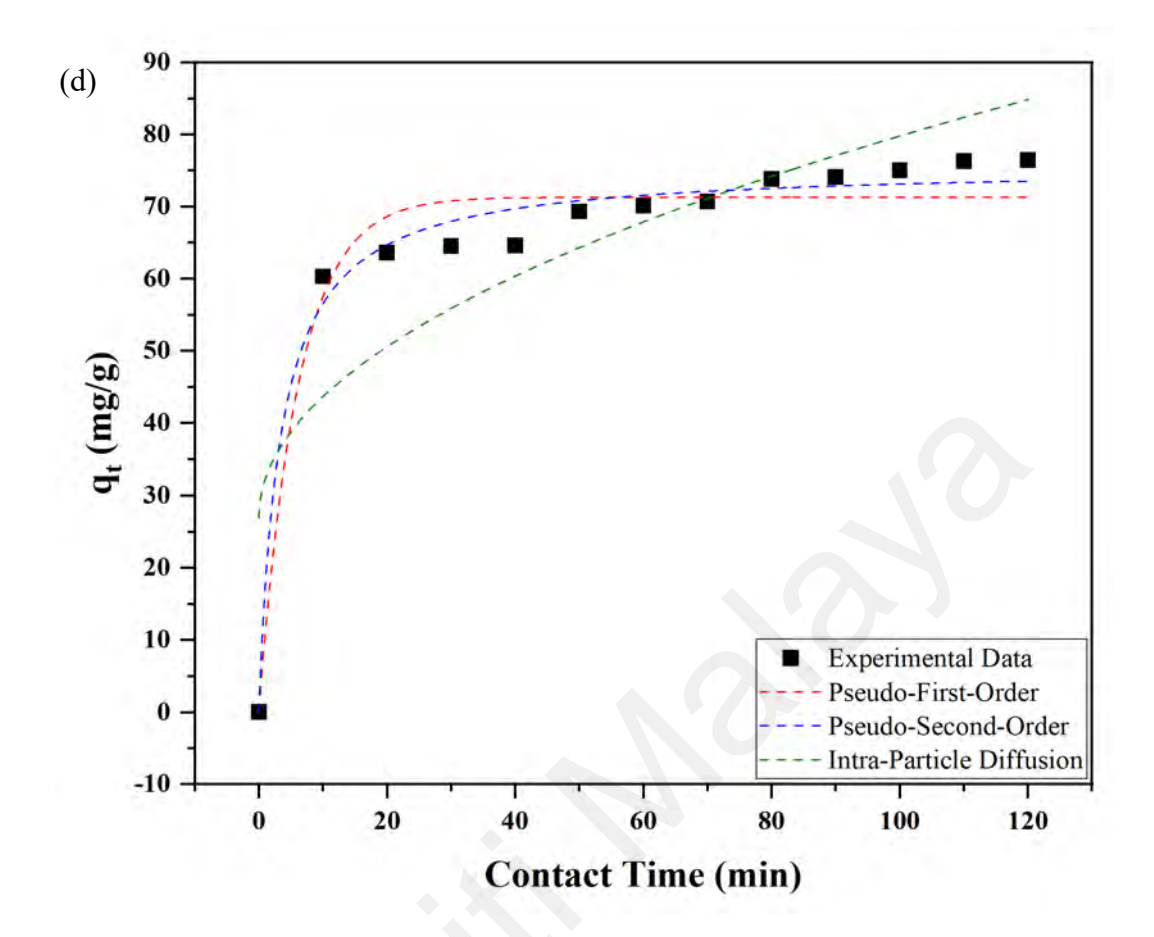


Figure 4.34: Continued



4.9.3.2 Isotherms Study

The study of adsorption isotherms is crucial for understanding how pollutants interact with adsorbents at equilibrium. This section focuses on the adsorption isotherms of printing wastewater onto the optimized PKSAC-GO-Fe adsorbent. The isotherms were fitted using Langmuir, Freundlich, and Temkin models, with the results depicted in Table 4.20 and Figure 4.35.

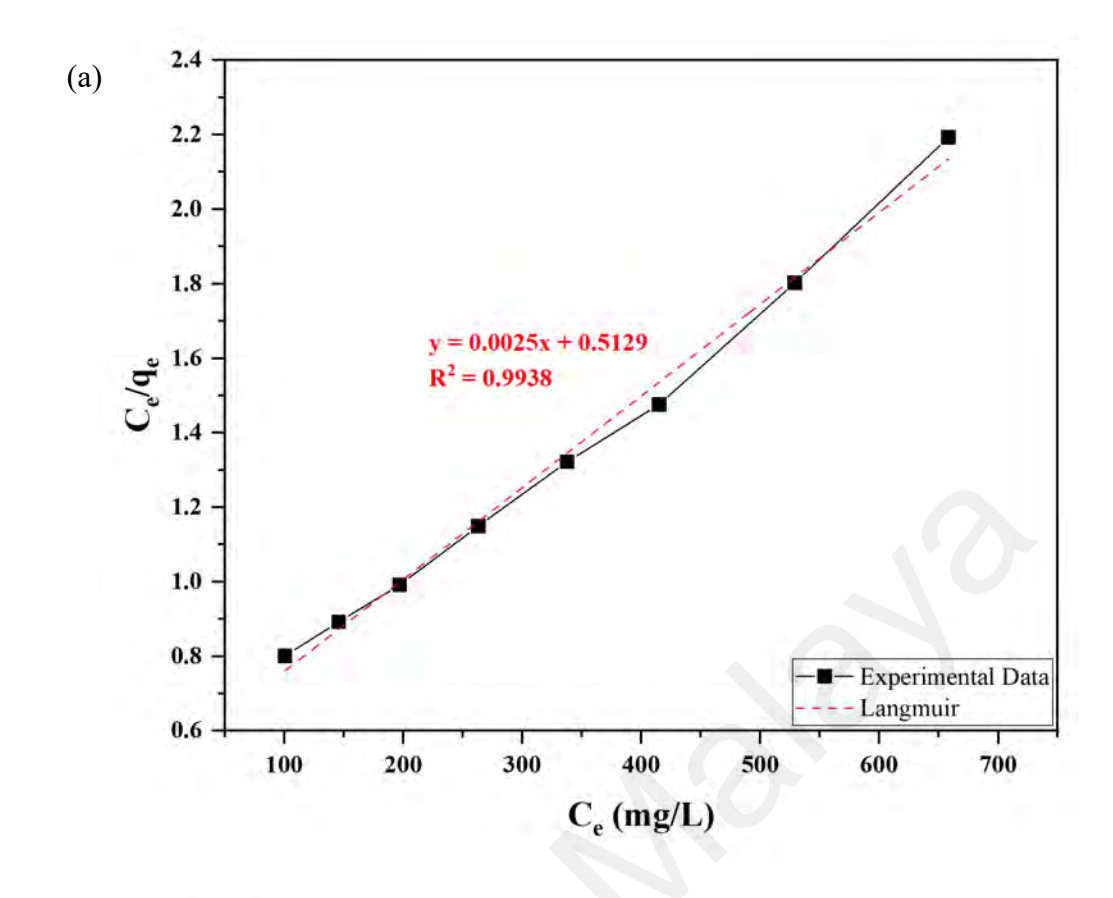
As shown in Table 4.20, the Langmuir model provided a Langmuir constant (K_L) of 0.0048 L/mg and a maximum adsorption capacity (Q_{max}) of 406.5 mg/g, with an R^2 of 0.9938 in its linear form. The non-linear form yielded similar results, with a Q_{max} of 410.7 mg/g and a K_L of 0.0047 L/mg, and an R^2 of 0.9965. The separation factor (R_L) values were 0.12 and 0.13 for the linear and non-linear forms, respectively, indicating favorable adsorption (Algethami et al., 2024; Kalam et al., 2021). These results suggest that the

Langmuir model best describes the adsorption process, indicating that the adsorption of printing wastewater onto the optimized PKSAC-GO-Fe composite occurs as a monolayer on a homogeneous surface (Elgarahy et al., 2023). For the Freundlich isotherm, the linear form showed a Freundlich constant (K_F) of 15.80 mg¹⁻ⁿ L^n g⁻¹ and an adsorption intensity (n) of 2.13, with an R^2 of 0.9554. The non-linear form provided a better fit with a K_F of 21.11 mg¹⁻ⁿ L^n g⁻¹ and n of 2.38, with an R^2 of 0.9805. For the Temkin model, the linear form yielded a Temkin constant (A) of 0.04 L g⁻¹, a constant related to adsorption heat (B) of 98.00, and a constant related to adsorption energy (b) of 25.30 J mol⁻¹, with an R^2 of 0.9843. The non-linear form showed similar parameters with an A of 0.04 L g⁻¹, B of 97.99, and b of 25.30 J mol⁻¹, with an R^2 of 0.9941.

Overall, the Langmuir isotherm model provides the best fit to the experimental data, as evidenced by the highest R² values in both linear and non-linear forms. This suggests that the adsorption of printing wastewater onto optimized PKSAC-GO-Fe is predominantly monolayer, occurring on a homogeneous surface with uniform adsorption sites. The findings are in line with previously reported studies (Hao et al., 2022; Kapoor et al., 2024; Sen et al., 2024).

Table 4.20: Isotherm Parameters of Printing Wastewater Adsorption onto Optimized PKSAC-GO-Fe

| Isotherm Model | Parameter | Unit | Linear | Non-Linear |
|----------------|----------------|---------------------|--------|------------|
| Langmuir | Qmax | mg g ⁻¹ | 406.5 | 410.7 |
| | K_{L} | L mg ⁻¹ | 0.0048 | 0.0047 |
| | $R_{ m L}$ | - | 0.12 | 0.13 |
| | \mathbb{R}^2 | - | 0.9938 | 0.9965 |
| Freundlich | K _F | $mg^{1-n}L^ng^{-1}$ | 15.80 | 21.11 |
| | n | - | 2.13 | 2.38 |
| | \mathbb{R}^2 | - | 0.9554 | 0.9805 |
| Temkin | A | L g ⁻¹ | 0.04 | 0.04 |
| | В | - | 98.00 | 97.99 |
| | ь | J mol ⁻¹ | 25.30 | 25.30 |
| | \mathbb{R}^2 | - | 0.9843 | 0.9941 |



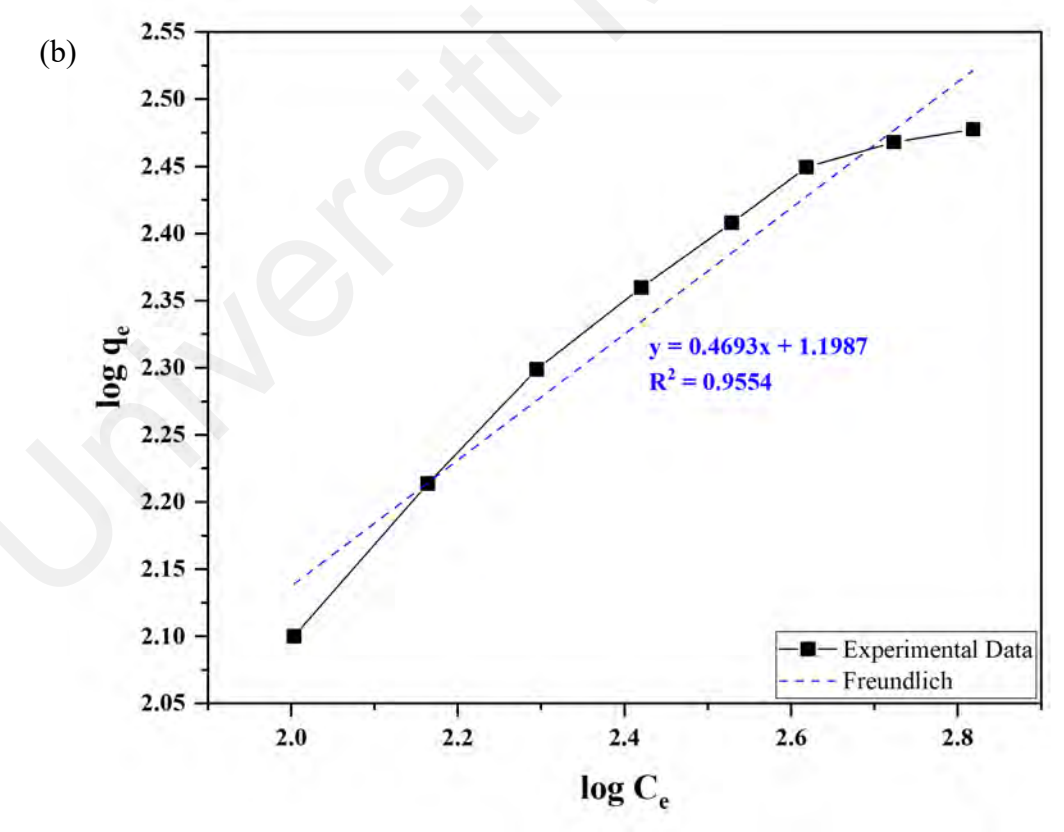
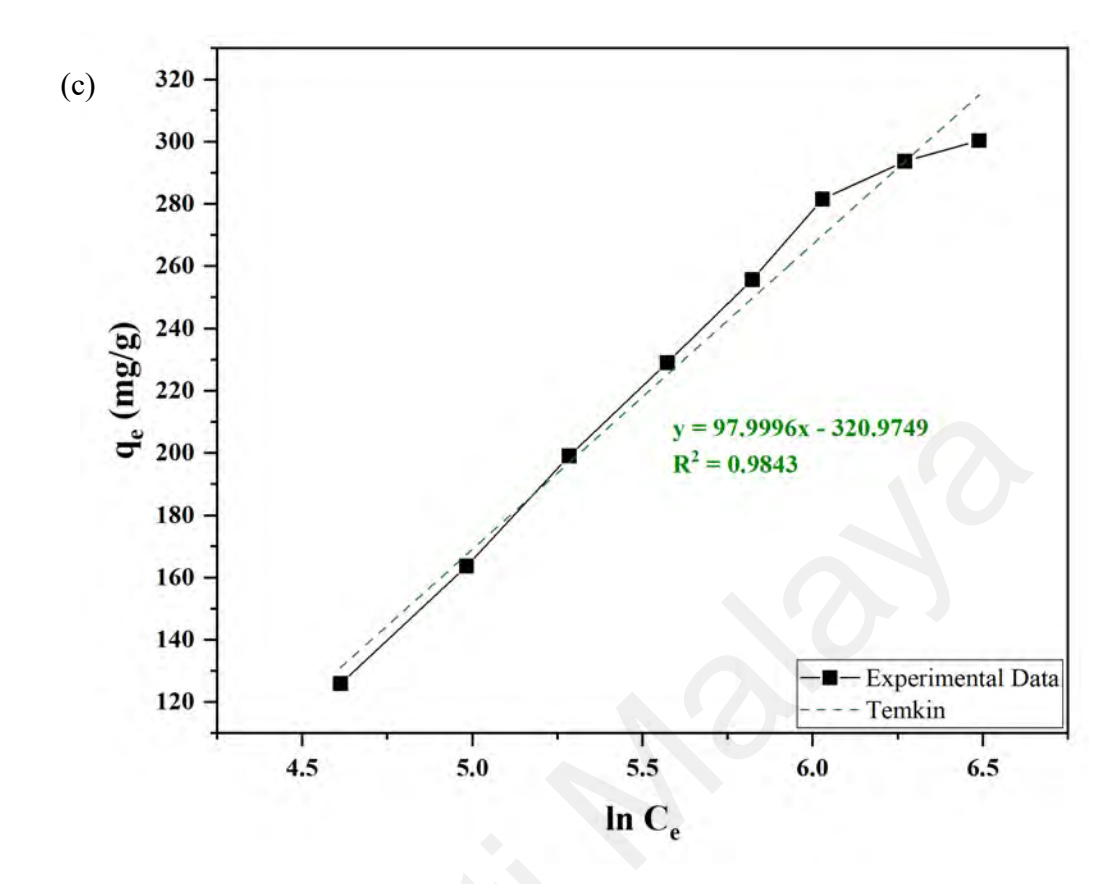
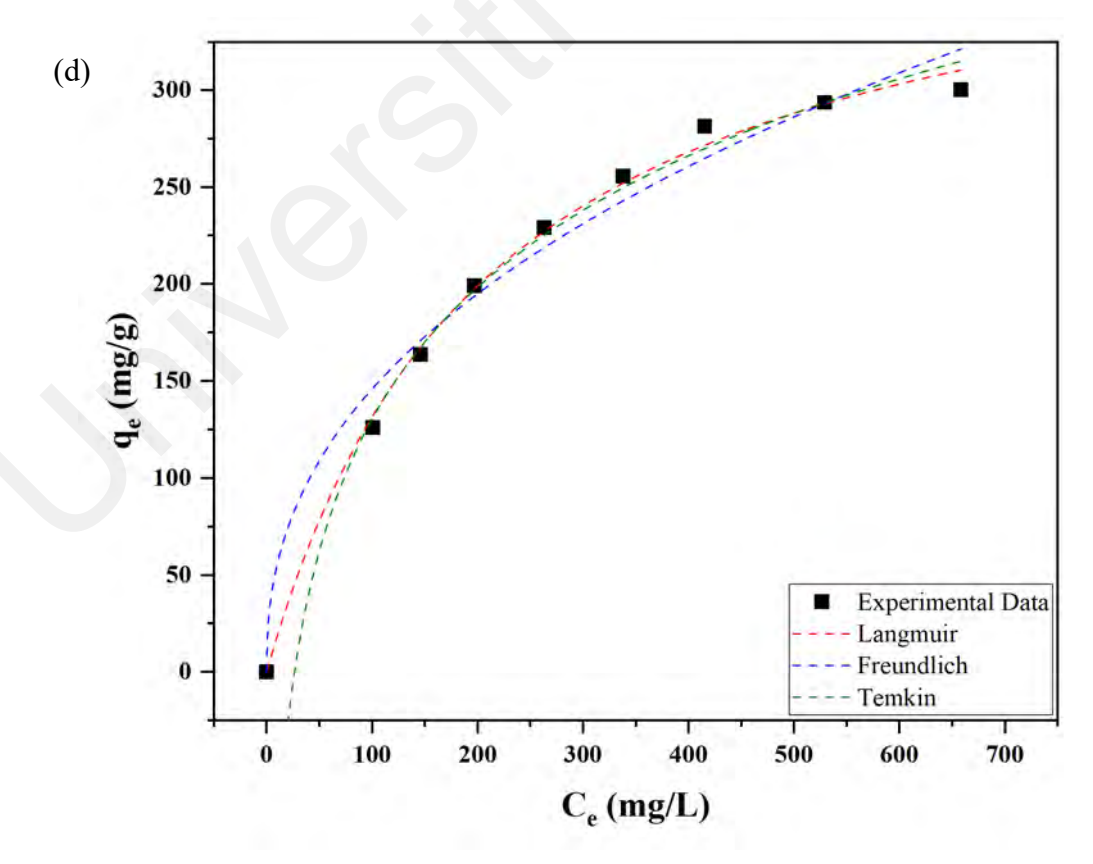


Figure 4.35: Linear Isotherm Plots for (a) Langmuir, (b) Freundlich, and (c) Temkin Models, and (d) Non-Linear Isotherm Plot in Treating Actual Printing Wastewater

Figure 4.35: Continued





4.9.3.3 Thermodynamics Study

Thermodynamic studies provide valuable insights into the nature and feasibility of adsorption processes. This section focuses on the thermodynamic parameters of printing wastewater adsorption using optimized PKSAC-GO-Fe. The thermodynamic results are depicted in Table 4.21 and Figure 4.36.

According to the thermodynamic results, it was found that all of the ΔG° values were negative, which indicates that the adsorption process is spontaneous (Hashem et al., 2024; Waghmare et al., 2023). The spontaneity was determined to decrease with increasing temperature, with ΔG° values ranging from -3.00 kJ/mol at 25°C to -1.20 kJ/mol at 65°C. Since higher temperatures reduce the adsorption performance, the observed phenomenon can be related to an exothermic process. On the other hand, the ΔH° value of -16.60 kJ/mol also suggests that printing wastewater adsorption is an exothermic process (Karim et al., 2024). A lower temperature range is preferred, as higher temperatures may disrupt the adsorbate-adsorbent interactions.

In addition, a decrease in randomness at the solid-liquid interface during adsorption was indicated by negative ΔS° value of -45.77 J/mol·K (S. Liu et al., 2020). This means that the adsorbate molecules are more orderly arranged on the adsorbent surface. Besides that, this decrease in randomness with a finite activation energy of 8.4-83.7 kJ/mol suggests that the adsorbate molecules have a strong interaction with the adsorbent surface, aligning well with the chemisorption mechanism indicated by the kinetics study (Acharya et al., 2013).

In short, the thermodynamic study of printing wastewater adsorption demonstrated that the process is spontaneous and exothermic. It is associated with a decrease in randomness at the solid-liquid interface. The negative ΔG° values indicate that the adsorption process is favorable across the studied temperature range with spontaneity decreasing with

increasing temperature. The exothermic nature of the process was confirmed by negative ΔH° value as lower temperatures achieved higher adsorption performance. It is also in line with the kinetics study that suggested a chemisorption mechanism. The negative ΔS° value signifies a more orderly arrangement of pollutants on the adsorbent surface, consistent with the chemisorption mechanism.

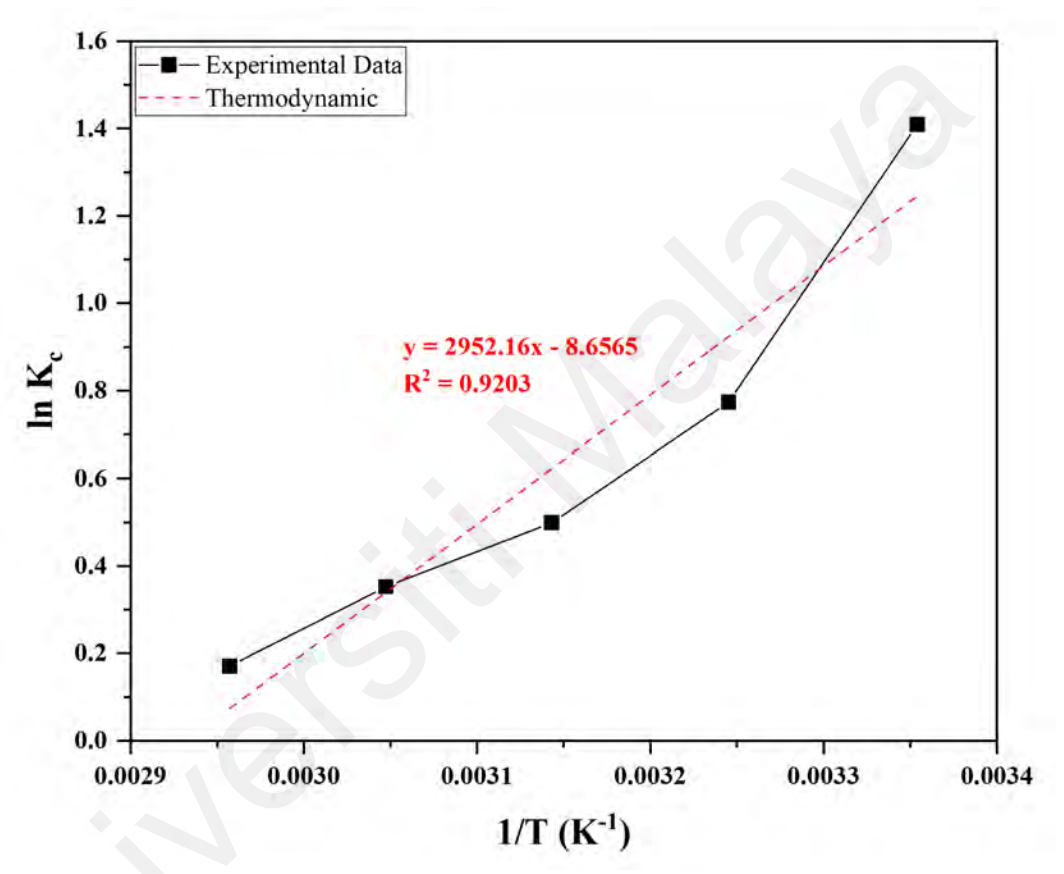


Figure 4.36: Van't Hoff Plot of Printing Wastewater Adsorption using Optimized PKSAC-GO-Fe

Table 4.21: Thermodynamic Study of Printing Wastewater Adsorption onto Optimized PKSAC-GO-Fe

| T (K) | ΔG° (kJ/mol) | ΔH° (kJ/mol) | ΔS° (J/mol·K) |
|--------|--------------|--------------|---------------|
| 298.15 | -3.00 | -16.60 | -45.77 |
| 308.15 | -2.54 | | |
| 318.15 | -1.86 | | |
| 328.15 | -1.60 | | |
| 338.15 | -1.20 | | |

4.9.4 Reusability Study

The reusability of an adsorbent plays a significant role in determining its practical application in wastewater treatment. This section evaluates the reusability of optimized PKSAC-GO-Fe over multiple cycles, as shown in Figure 4.37. The experimental findings show a gradual decline in both color removal efficiency and adsorption capacity over five cycles in treating printing wastewater.

Initially, in the first cycle, the color removal efficiency and the adsorption capacity were determined to be 70.2% and 76.4 mg/g, respectively. At the end of the fifth cycle, these values had decreased by 12% to 61.8% and 67.2 mg/g, respectively. This observation can be attributed to several factors, including, first, the blockage or deactivation of active sites caused by multiple uses, which in turn reduces its adsorption performance (Y. Zhang et al., 2023). Besides that, the degradation of the adsorbent structure over time also affects its ability to adsorb pollutants (Alsawy et al., 2022). In addition, incomplete desorption can leave residual adsorbates on the adsorbent surface and hence diminish its performance in the subsequent cycles. Despite the observed decline, the adsorbent retained 88.0% of its initial capacity and efficiency after five cycles, indicating the good reusability of the optimized PKSAC-GO-Fe composite. This implies that the adsorbent maintains its effectiveness over time, which is essential for real-world wastewater treatment applications.

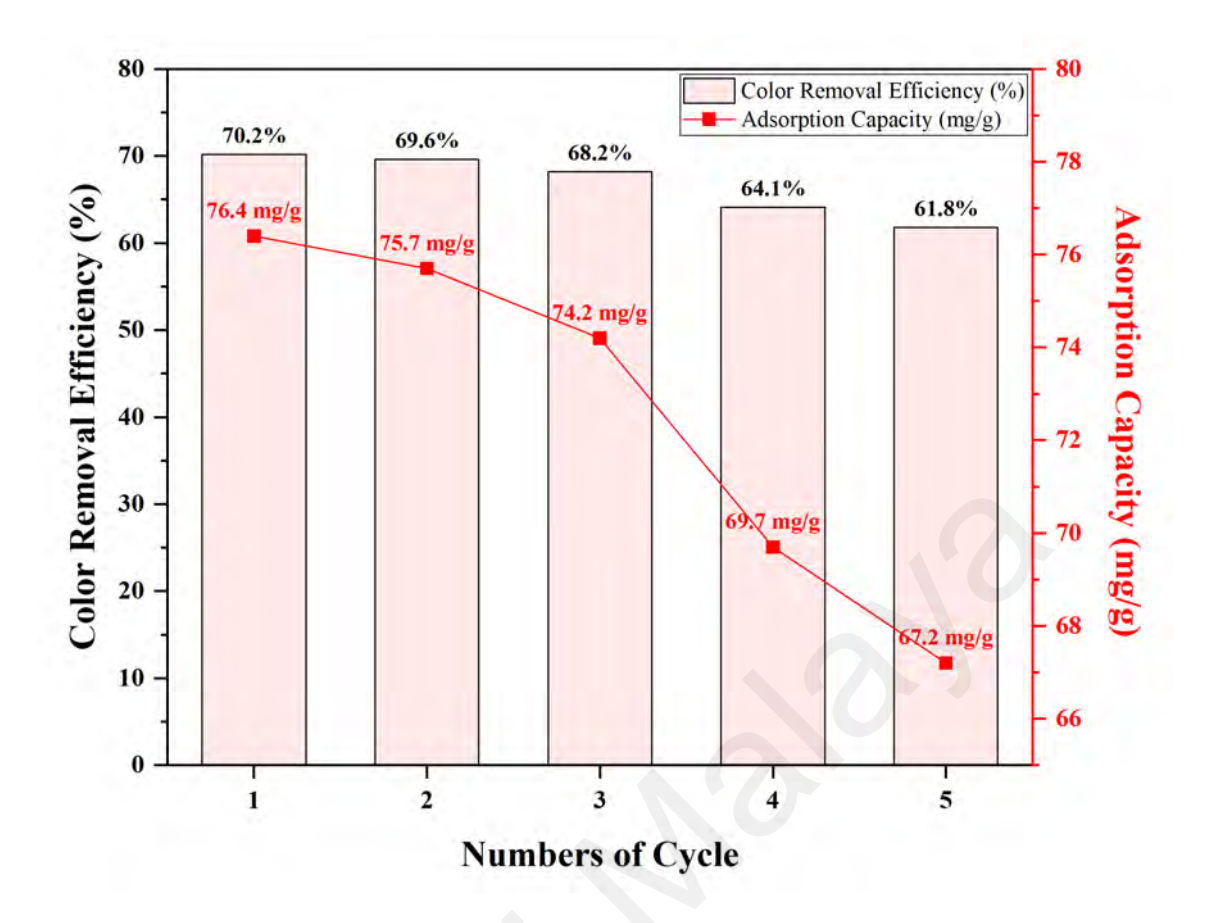


Figure 4.37: Reusability of Optimized PKSAC-GO-Fe

4.9.5 Model Validation using Various Types of Actual Wastewater

To validate the effectiveness of the optimized PKSAC-GO-Fe composite, its performance was validated on various actual wastewater samples, focusing on color removal efficiency, adsorption capacity, and COD removal efficiency.

As depicted in Figure 4.38, the results showed high color removal efficiency and adsorption capacity for printing wastewater (70.2% and 76.4 mg/g, respectively), along with a significant COD removal efficiency of 44.9%. This indicates that the adsorbent is highly effective for pollutants typically found in printing wastewater. For plastic fabrication wastewater, the adsorbent demonstrated moderate efficiency with 42.0% color removal, 56.5 mg/g adsorption capacity, and 24.1% COD removal efficiency. In the case of landfill leachate, the performance was lower, with 7.9% color removal efficiency, 6.1

mg/g adsorption capacity, and 8.7% COD removal efficiency, likely due to the complex mixture of pollutants and high organic load in the leachate. Batik wastewater showed the lowest adsorption performance among all tested samples, with only 0.7% color removal efficiency and 1.9 mg/g adsorption capacity, but had a relatively higher COD removal efficiency of 28.0%. Textile wastewater results were promising, with 54.7% color removal efficiency, 19.8 mg/g adsorption capacity, and 35.2% COD removal efficiency. For POME, the composite achieved a color removal efficiency of 26.1%, an adsorption capacity of 27.6 mg/g, and a COD removal efficiency of 25.9%.

Overall, the PKSAC-GO-Fe composite demonstrated excellent performance for certain wastewater types, such as printing and textile wastewater, without pre-treatment. However, its performance was limited to more complex wastewater samples like landfill leachate and batik wastewater. These findings suggest that adsorption alone may not be sufficient for treating all industrial wastewater types. To enhance its applicability, combining the PKSAC-GO-Fe composite with advanced treatment methods, such as membrane filtration or biological processes, could increase the removal rate. This approach could address the limitations of adsorption by targeting a wider range of pollutants and improving overall treatment performance. Further research should focus on optimizing these hybrid systems for broader industrial use and higher treatment efficiencies.

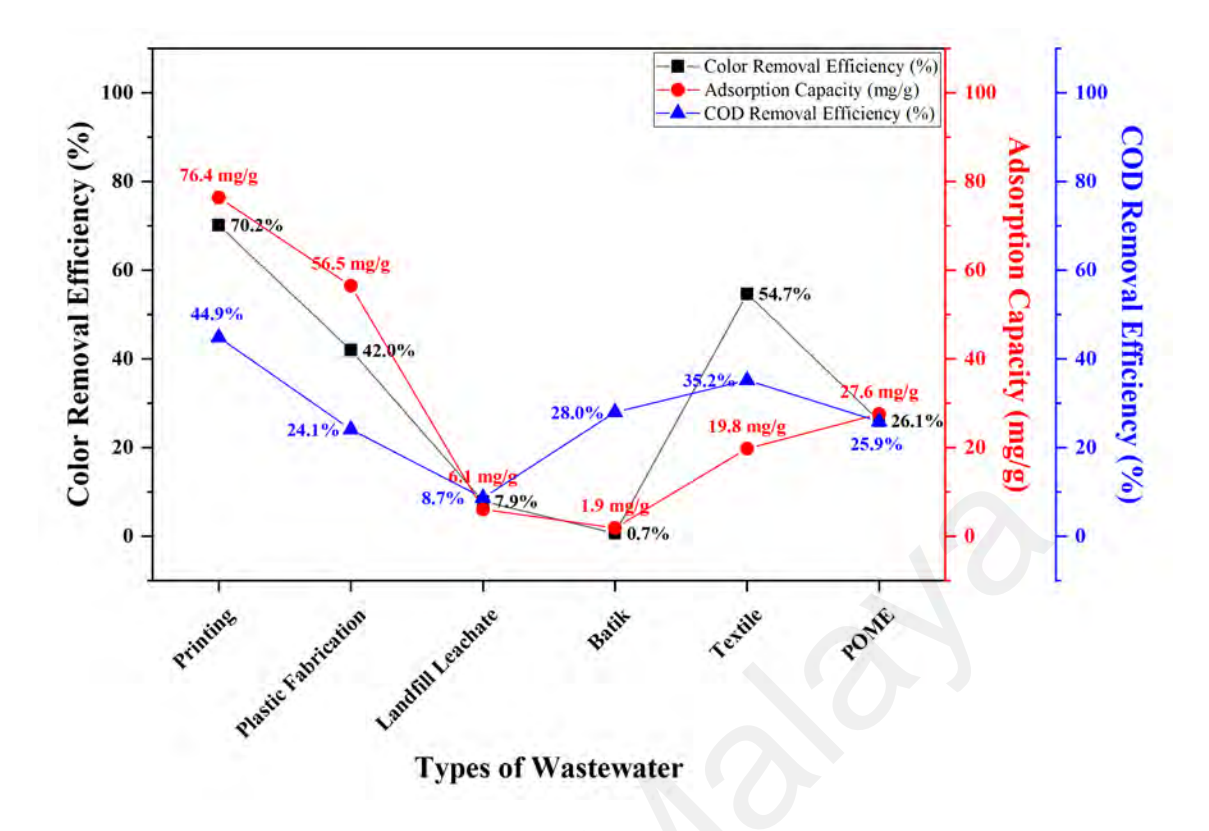


Figure 4.38: Adsorption Performance Validation using Various Types of Actual Wastewater

4.10 Comparison of Physicochemical Characteristics and Adsorption Performance of Ternary Composite Before and After Synthesis Process Optimization

The comparison of the PKSAC-GO-Fe composite before and after optimizing the synthesis process for treating printing wastewater shows substantial enhancements in physicochemical characteristics and adsorption performance. These improvements are likely due to differences in the formulation used during synthesis process. The optimized formulation utilized a PKSAC/GO ratio of 0.2/0.8 with 45% iron oxide loading, compared to the ratio of 0.5/0.5 and 30% iron oxide before optimization. This adjustment significantly enhanced the characteristics and performance of the composite, as summarized in Table 4.22.

Table 4.22: Comparison of PKSAC-GO-Fe Before and After Synthesis Process Optimization

| Parameter | Before | After | | | | |
|--|--------------|--------------|--|--|--|--|
| 1 at ameter | Optimization | Optimization | | | | |
| Formulation | | | | | | |
| PKSAC/GO | 0.5/0.5 | 0.2/0.8 | | | | |
| Iron oxide loading amount (%) | 30% | 45% | | | | |
| Physicochemical Characteristics | | | | | | |
| BET surface area (m ² /g) | 280.39 | 219.43 | | | | |
| Langmuir surface area (m ² /g) | 309.97 | 299.01 | | | | |
| Average pore diameter (nm) | 9.99 | 6.41 | | | | |
| Pore volume (cm ³ /g) | 0.35 | 0.31 | | | | |
| Elemental composition (%) | 35.02% C | 15.99% C | | | | |
| | 49.73% O | 43.71% O | | | | |
| | 15.25% Fe | 40.30% Fe | | | | |
| Magnetization (emu/g) | 33.74 | 43.78 | | | | |
| Point of zero charge | 5.6 | 5.1 | | | | |
| Performance | | | | | | |
| Color removal efficiency (%) | 52.2% | 70.2% | | | | |
| Adsorption capacity (mg/g) | 56.8 mg/g | 76.4 mg/g | | | | |
| COD removal efficiency (%) | 34.7% | 44.9% | | | | |
| Reusability after 5th cycle (%) | 41.7% | 61.8% | | | | |
| Reduction of reusability after 5th cycle (%) | 20.1% | 12.0% | | | | |

As shown in Table 4.22, the optimized composite exhibited a decrease in BET surface area from 280.39 m²/g to 219.43 m²/g (a reduction of 21.7%) and a decrease in Langmuir surface area from 309.97 m²/g to 299.01 m²/g (a reduction of 3.5%). Additionally, the average pore diameter decreased from 9.99 nm to 6.41 nm (a reduction of 35.8%), and pore volume dropped from 0.35 cm³/g to 0.31 cm³/g (a reduction of 11.4%). These reductions can be ascribed to the increased iron oxide loading on the surface. Despite the reductions in surface area, pore volume, and pore diameter, the experimental results demonstrated that the adsorption performance was not hindered. In fact, the optimized PKSAC-GO-Fe composite exhibited higher performance even with a relatively lower surface area and pore volume. The experimental findings are well in line with kinetics study where the process is predominantly chemisorption, as the surface functional groups contribute more than physical properties like surface area and pore volume. This was

further validated through computational approaches, including quantum chemical studies and machine learning

Figure 4.39 shows that the optimized PKSAC-GO-Fe has more sheet-like and agglomerated structures due to higher impregnation of GO and iron oxide. Elemental composition analysis revealed a significant reduction in carbon content from 35.02% to 15.99%, coupled with a dramatic increase in iron content from 15.25% to 40.30%. This indicates that the optimized composite has a higher amount of iron oxide, likely deposited on the carbon surface, which could block some carbon atoms. The saturation magnetization increased from 33.74 emu/g to 43.78 emu/g, enhancing post-treatment magnetic separation. The point of zero charge decreased from pH 5.6 to 5.1, indicating a slightly more acidic surface due to the higher GO impregnation ratio, as GO has a pH_{pzc} of 2.1.

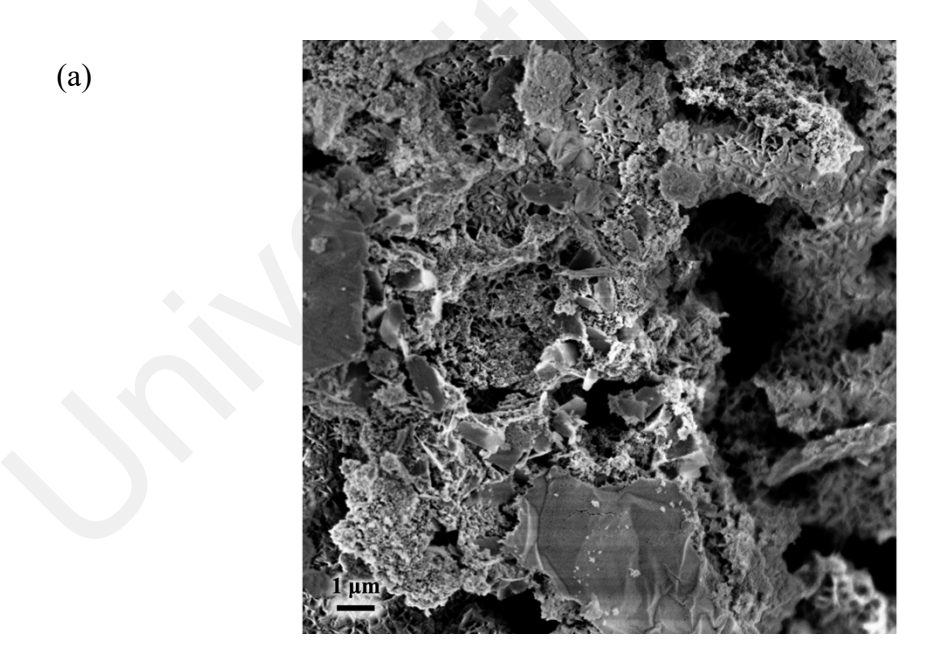
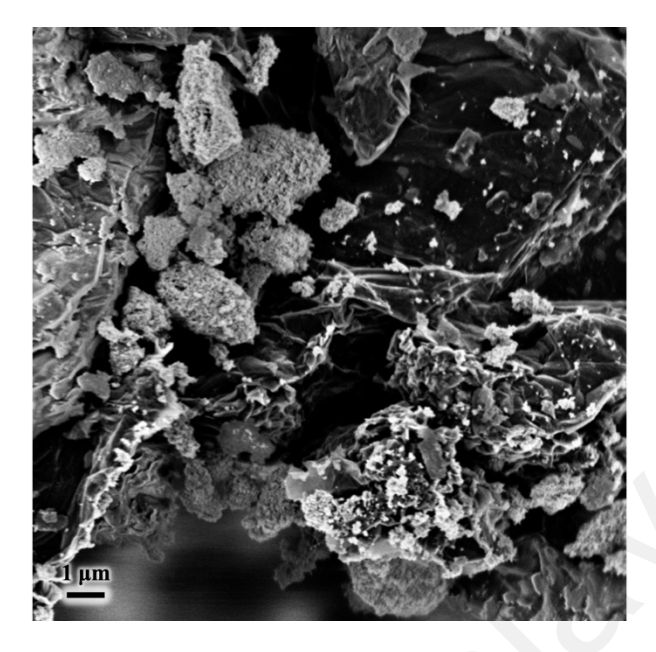


Figure 4.39: FESEM Images of PKSAC-GO-Fe (a) Before and (b) After Synthesis Process Optimization

Figure 4.39: Continued





In terms of adsorption performance, the optimized composite showed a significant increase in color removal efficiency from 52.2% to 70.2%. The adsorption capacity improved from 56.8 mg/g to 76.4 mg/g, representing a 34.5% increase. This improvement can be attributed to the higher graphene oxide and iron oxide content, providing more active sites for adsorbing pollutants from printing wastewater. COD removal efficiency also improved from 34.7% to 44.9%, indicating better overall pollutant removal performance. The reusability of the adsorbent improved remarkably, with the efficiency remaining after the fifth cycle increasing by 48.2% (from 41.7% to 61.8%). The reduction in reusability loss after the fifth cycle was determined to be decreased from 20.1% (before optimization) to 12.0% (after optimization). This signifies that the synthesis process optimization is very important to enhance the durability and stability of the composite.

Overall, after the optimization of the synthesis process for treating printing wastewater, substantial enhancements were obtained in both the physicochemical characteristics and adsorption performance. It was proved that, after optimization, the ternary composite demonstrated higher color removal efficiency, increased adsorption

capacity, better COD removal efficiency, and enhanced reusability compared to the composite before optimization. These improvements make the optimized PKSAC-GO-Fe a more effective and practical adsorbent for actual wastewater treatment applications.

4.11 Economic Evaluation

The economic evaluation of PKSAC-GO-Fe before and after synthesis process optimization is presented in Table 4.23. This study aims to assess the economic benefits besides the enhanced adsorption performance of the optimized composite. The basis used in the production cost calculation was based on small-to-medium enterprises (SME) of 1000 kg per batch.

As shown in Table 4.23, before optimization, the production cost for PKSAC-GO-Fe composite was determined to be 4.75 USD/kg. Optimization resulted in a 41.7% reduction in production costs, which dropped to 2.77 USD/kg. This can be related to synthesis process optimization, where the PKSAC/GO ratio was adjusted from 0.5/0.5 to 0.2/0.8 and the iron oxide amount was increased from 30% to 45%. These changes substantially increased the yield by 100.8% from 2333 kg to 4684 kg of PKSAC-GO-Fe per 1000 kg of raw materials. A higher yield led to overall reduced production costs per unit of adsorbent, which demonstrate the economical advantage of the optimized formulation.

In the case of adsorption performance, the adsorption capacity of the PKSAC-GO-Fe composite before optimization was 56.8 mg/g for treating printing wastewater. It was increased to 76.4 mg/g after optimization, which is equivalent to a 34.5% improvement. This increase in adsorption capacity means that the optimized composite can remove more pollutants, enhancing its overall adsorption performance under identical adsorption conditions.

In terms of cost per kilogram of pollutants removal, the PKSAC-GO-Fe before optimization costs 83.63 USD, while the optimized composite costs 36.25 USD. This dramatic 56.7% reduction signifies the enhanced cost-effectiveness of the optimized composite. The decreased cost per unit of pollutant removal is related to both lower production costs and higher adsorption capacity.

Besides that, a case study was conducted on a SME with wastewater generation of 1 ton/day. This study aimed to treat industrial wastewater with a 2000 mg/L COD level to meet the Malaysian discharge standard for industrial effluent (Standard A), which requires a COD level of ≤ 80 mg/L (*Environmental Quality (Industrial Effluents) Regulations* 2009). A comparison of the daily treatment cost required for COD removal in a SME using PKSAC-GO-Fe (before and after optimization) and CACs is presented in Figure 4.40. As shown in Figure 4.40, the optimized PKSAC-GO-Fe has the lowest cost of 19.84 USD/day. It showed significant cost savings compared to PKSAC-GO-Fe before optimization (44.03 USD) and various CACs (CAC 1: 36.60 USD; CAC 2: 241.38 USD; CAC 3: 489.85 USD), which represent treatment cost reductions of 54.9%, 45.8%, 91.8%, and 95.9%, compared to PKSAC-GO-Fe, CAC 1, CAC 2, and CAC 3, respectively.

These findings revealed that in addition to improving the adsorption performance, the optimization also made them more economical and feasible for actual applications. A significant reduction in both production and treatment costs suggest that the optimized PKSAC-GO-Fe composite is a more viable option for treating industrial wastewater. In short, the comparison between PKSAC-GO-Fe composite before and after optimization of the synthesis process exhibits substantial improvements in both economic feasibility and adsorption performance. Overall, the optimized composite exhibits a 41.7% reduction in production costs and a 34.5% increase in adsorption capacity, resulting in a 56.7% reduction in treatment costs.

Table 4.23: Economic Evaluation of PKSAC-GO-Fe Before and After Synthesis Process Optimization of PKSAC-GO-Fe

| Adsorbents | Chemicals / Materials | Unit Cost (USD/ ton) | Amount Used | Cost (USD) | Net Cost (USD) | Overhead Cost (USD) | Total Cost (USD) | Yield | Total Cost (USD/kg Adsorbent) | Cost (USD/kg Dye Removal) |
|-------------|--------------------------------------|-------------------------------|----------------|---------------|-------------------|---------------------------|------------------------|---|-------------------------------------|------------------------------------|
| PKSAC-GO-Fe | PKSAC | 1200.00 | 500 kg | 600.00 | 9637.05 | 1445.56 | 11082.61 | 2333 kg / | 4.75 | 83.63 |
| | GO | 5497.11 | 500 kg | 2748.55 | | | | 1000 kg raw | | |
| | CH ₃ COOH | 350.00 | 1010 L | 353.50 | | | | | | |
| | HC1 | 150.00 | 2500 L | 375.00 | | | | material | | |
| | FeCl ₃ ·6H ₂ O | 220.00 | 2000 kg | 440.00 | | | | | | |
| | FeCl ₂ ·4H ₂ O | 270.00 | 1000 kg | 270.00 | | | | | | |
| | NH ₄ OH | 250.00 | 3400 L | 850.00 | | | | | | |
| | Ethanol | 800.00 | 5000 L | 4000.00 | | | | | | |
| Optimized | PKSAC | 1200.00 | 200 kg | 240.00 | 11281.19 | 1692.18 | 12973.36 | 4684 kg / 1000 kg raw material | 2.77 | 36.25 |
| PKSAC-GO-Fe | GO | 5497.11 | 800 kg | 4397.69 | | | | | | |
| | CH ₃ COOH | 350.00 | 1010 L | 353.50 | | | | | | |
| | HC1 | 150.00 | 2500 L | 375.00 | | | | | | |
| | FeCl ₃ ·6H ₂ O | 220.00 | 3000 kg | 660.00 | | | | | | |
| | FeCl ₂ ·4H ₂ O | 270.00 | 1500 kg | 405.00 | | | | | | |
| | NH ₄ OH | 250.00 | 3400 L | 850.00 | | | | | | |
| | Ethanol | 800.00 | 5000 L | 4000.00 | | | | | | |
| CAC 1 | Biomass-based AC | 1200.00 | - | 1200.00 | - | - | 1200.00 | - | 1.20 | 101.69 |
| CAC 2 | Therapeutically applied AC | 13320.00 | - | 13320.00 | - | - | 13320.00 | - | 13.32 | 611.01 |
| CAC 3 | Chemically pure AC | 28060.00 | - | 28060.00 | - | - | 28060.00 | - | 28.06 | 1275.45 |

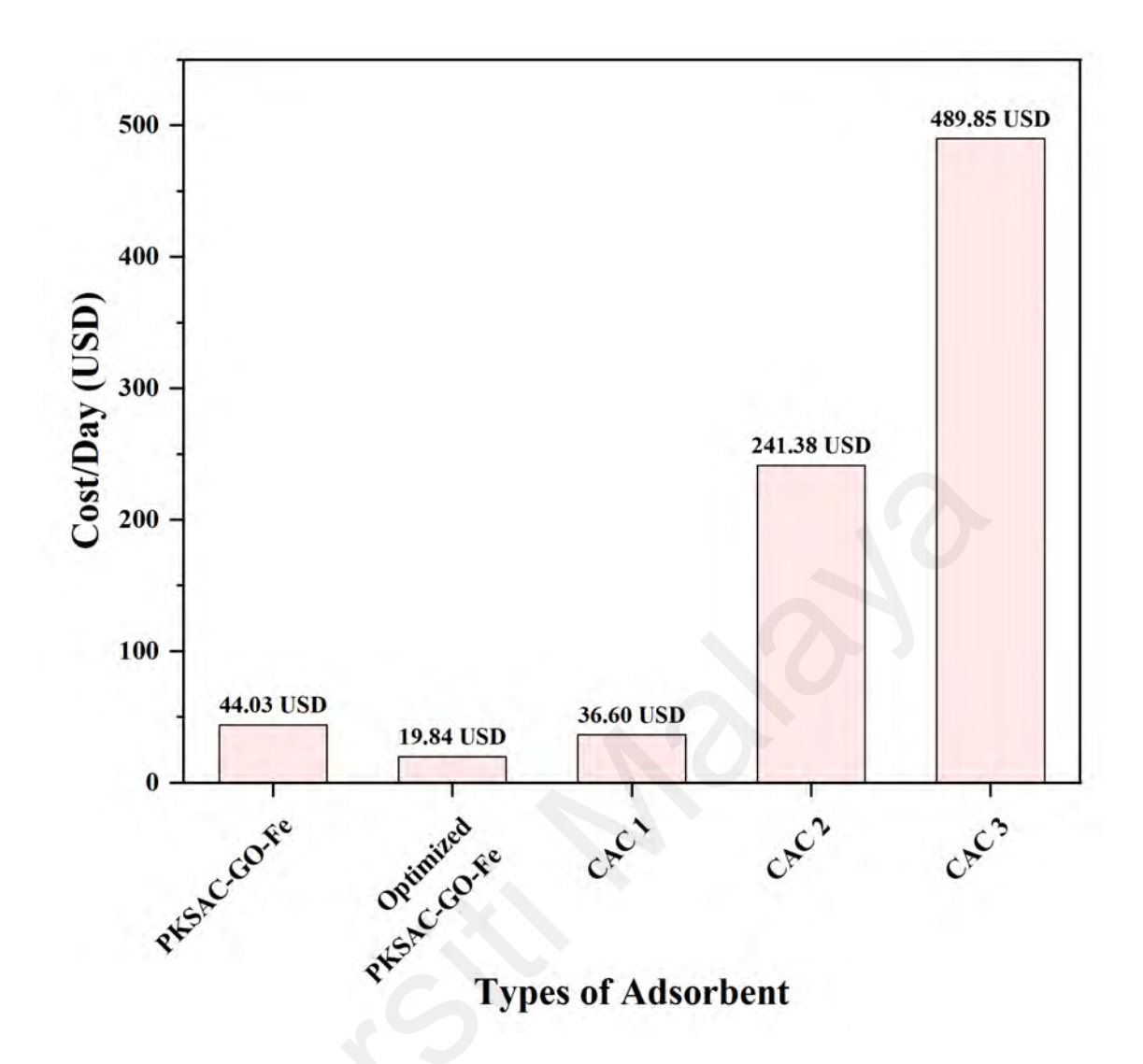


Figure 4.40: Cost Required for COD Removal Per Day

4.12 Environmental Evaluation

4.12.1 Carbon Dioxide Emissions Reduction

An environmental benefits analysis was studied, and the findings are summarized in Table 4.24. The comparison was made between baseline (coal-based) (Gu et al., 2018) and PKS (biomass-based) (Alhashimi & Aktas, 2017) activated carbon production, specifically focusing on the reduction in CO₂ emissions. The analysis was conducted considering a 10 kg quantity of raw materials and the respective yields for coal-based AC (25.0%) (Kim et al., 1996) and PKSAC (47.9%) (Ulfah et al., 2019). The analysis shows a remarkable reduction of 31.0% (from 45.8 kg CO₂ eq to 31.6 kg CO₂ eq) when using biomass-based precursors and hence signifies the potential of this greener alternative for AC development. With the utilization of renewable biomass sources, the process demonstrates a more sustainable and environmentally friendly approach to AC production compared to traditional coal-based methods.

Table 4.24: CO₂ Emissions from Coal-Based and PKS-Based AC Production

| Parameter | Coal-Based AC (baseline) | PKSAC | |
|-------------------------|--|--|--|
| Description | Production of AC using | Production of AC using | |
| | fossil fuels (coal) | biomass | |
| Average emission factor | 18.3 kg CO ₂ eq/kg AC | 6.6 kg CO ₂ eq/kg AC | |
| | produced | produced | |
| Total emission | Baseline emissions | PKSAC emissions | |
| | = baseline emission factor | = biomass AC emission | |
| | × mass of AC | factor × mass of PKSAC | |
| | $= 18.3 \text{ kg CO}_2 \text{ eq/kg AC}$ | $= 6.6 \text{ kg CO}_2 \text{ eq/kg AC}$ | |
| | produced × 2.50 kg | produced × 4.79 kg | |
| | $=45.8 \text{ kg CO}_2 \text{ eq}$ | $= 31.6 \text{ kg CO}_2 \text{ eq}$ | |
| Reduction in emission | Reduction in emissions | | |
| | = baseline emissions - PKSAC emissions | | |
| | $= (45.8-31.6) \text{ kg CO}_2 \text{ eq}$ | | |
| | $= 14.2 \text{ kg CO}_2 \text{ eq}$ | | |
| | ≈ 31.0% reduction | | |

4.12.2 Phytotoxicity Study

It is crucial to study the possible effect of PKSAC-GO-Fe-treated wastewater on plant growth, which can be done through a phytotoxicity study. The phytotoxicity study was performed using 100 mg/L AB113 dye solution as wastewater pollutants. Red bean seeds were chosen as the test species in this study due to their sensitivity to environmental stressors as well as their relevance to agricultural contexts. For comparison purposes, ultrapure water was used as a benchmark, which represents ideal growth conditions for the seeds.

The growth conditions of red bean seeds were observed over seven consecutive days, as shown in Figure 4.41 and Table 4.25. Seeds germinated in the untreated solution (Sample 1) exhibited significant inhibition and delayed growth compared to those germinated in ultrapure water (Control). Seeds germinated in the PKSAC-GO-Fe-treated wastewater (Sample 2) displayed growth patterns similar to those in ultrapure water, indicating a reduction in phytotoxicity in the PKSAC-GO-Fe-treated solution (Miyah et al., 2023). The seed germination rate was 100.0% for both the control and treated solutions, higher than the 80.0% observed before adsorption treatment. Although there was an 80.0% germination rate for seeds exposed to AB113 dye before adsorption, they had almost no leaves by the 7th day.

On the 14th day of the phytotoxicity study, all of the samples exhibited the same growth pattern as on the 7th day. For example, no further seed germination was recorded for the raw wastewater sample. However, there was a slight plant length increment from 2-3 cm to 5-6 cm observed as well as some leaf started to grow. On the other hand, the plant growth of ultrapure water and PKSAC-GO-Fe-treated samples demonstrated an increment in plant length from 5-6 cm to 9-10 cm with more leaves by the 14th day.

In summary, the phytotoxicity study demonstrated the effectiveness of PKSAC-GO-Fe in mitigating the harmful effects of pollutants on plant growth. The comparable growth performance of red bean seeds in the PKSAC-GO-Fe-treated solution to those in ultrapure water underscores the potential of the PKSAC-GO-Fe composite as a safe and efficient adsorbent for wastewater treatment applications.

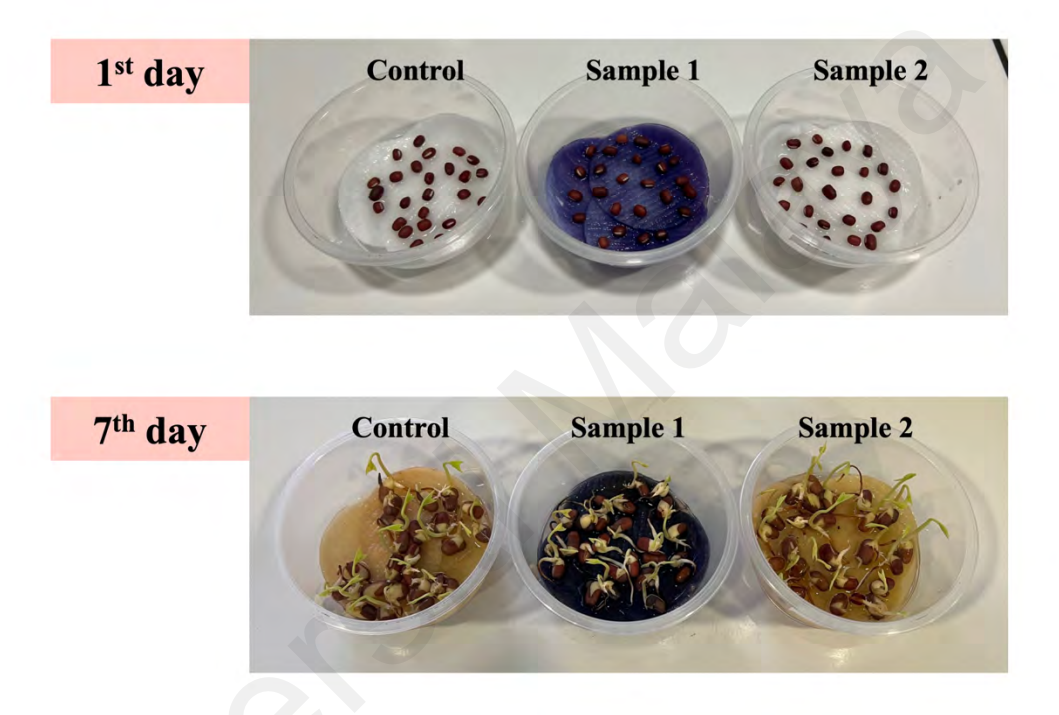


Figure 4.41: Phytotoxicity Assessment of PKSAC-GO-Fe

Table 4.25: Growth Conditions of Red Bean Seeds

| Types of Sample | Control | Sample 1 | Sample 2 | |
|------------------------|-----------------|----------------|--------------------|--|
| Description | Ultrapure water | Raw wastewater | Treated wastewater | |
| Germination rate | 100% | 80% | 100% | |
| Leaf growth | Yes | No | Yes | |
| Plant length | 5-6 cm | 2-3 cm | 5-6 cm | |

4.12.3 Leaching and Stability Study

Understanding the leaching behavior of iron oxide-containing adsorbents is crucial for assessing their environmental impact and potential for large-scale water treatment applications. This study investigates the leaching of iron ions from various iron oxide-containing adsorbents used in this study, including PKSAC-Fe, PKSAC-GO-Fe, and optimized PKSAC-GO-Fe. According to the WHO Guidelines for Drinking-Water Quality (*Guidelines for drinking-water quality*, 1996), iron concentrations are considered insignificant when below 0.3 mg/L, while concentrations ranging from 0.3 to 3 mg/L are deemed acceptable. Notably, all tested iron oxide-containing adsorbents demonstrated negligible iron ions leaching into the aqueous solution, as summarized in Table 4.26. This highlights the remarkable stability and potential reusability of these adsorbents for wastewater treatment applications.

Table 4.26: Leaching of Iron Ions into Aqueous Solution

| Types of Sample | Concentration of Iron Ions (mg/L) | Remarks |
|-----------------------|-----------------------------------|--------------------------|
| Ultrapure water | 0.000 | Control |
| PKSAC-Fe | 0.000 | - |
| PKSAC-GO-Fe | 0.000 | - |
| Optimized PKSAC-GO-Fe | 0.001 | <0.3 mg/L (unnoticeable) |

4.12.4 Possible Brick Formation using Spent Adsorbent

The evaluation of three key parameters, namely LOI, water absorption, and compressive strength, provided valuable insights into the potential of incorporating spent adsorbent into brick production. The brick properties with their respective compositions are shown in Table 4.27 and Figure 4.42.

As can be seen in Table 4.27 and Figure 4.42 (a), the LOI analysis revealed an increment in LOI values from 8.1% to 9.6% with an increase in the composition of spent adsorbent from 0% to 15%. This increase can be attributed to the presence of organic

matter within the spent adsorbent, which undergoes combustion during the calcination process, resulting in higher LOI values, attributed to the volatilization of these organic constituents (Ukwatta & Mohajerani, 2017). However, the significant LOI value observed in the reference brick (100% red brick powder; 0% spent adsorbent) is associated with the dehydroxylation and the breakdown of the organic content (Adazabra et al., 2023).

Besides that, the water absorption values exhibited a noticeable increase as the composition of spent adsorbent increased. This is due to the porous nature of the spent adsorbent, which allows greater amounts of water to be absorbed compared to conventional bricks. However, it should be noted that, the water absorption values, ranges from 6.5% to 7.6%, as reported in this study is comparable lower compared to previously reported literature (Adazabra et al., 2023; Barbieri et al., 2013; Demir, 2008; Eliche-Quesada et al., 2012; Velasco et al., 2015), which indicates an enhanced resistance to environmental factors and satisfactory permeability of bricks (Adazabra et al., 2023).

On the other hand, the mechanical strength of the fired brick samples showed a decreasing trend with increasing spent adsorbent composition. This decrease in mechanical strength can be attributed to the lower structural integrity and cohesion of the bricks due to the incorporation of spent adsorbent particles, attributed to the presence of more open porosities. Based on the results (ranging from 10.09 MPa to 14.06 MPa), all samples exhibit a compressive strength of > 10 MPa, which met the building standards specified by GB/T 2542-2012, UNE-67.046-88, and GB/T 5101-2003, which stipulate a minimum compressive strength of 10 MPa for structural construction materials (Adazabra et al., 2023; Chen et al., 2011; Eliche-Quesada & Leite-Costa, 2016).

Overall, the results indicate that while the incorporation of spent adsorbent into brick production may lead to increased LOI and water absorption values, but it still retains the mechanical strength of the bricks up to the addition of 15% of spent adsorbent. Further

optimization of the composition and processing parameters may be required to balance these competing factors and maximize the potential of spent adsorbent in brick production.

Table 4.27: Properties of Brick Formed using Different Formulations

| Formulations | Red Brick (%) | Spent Adsorbent (%) | LOI (%) | Compressive Strength (MPa) | Water Absorption (%) |
|--------------|---------------------|---------------------|------------|-------------------------------|----------------------|
| RB100-SA00 | 100 | 0 | 8.1 | 14.06 | 6.5 |
| RB95-SA05 | 95 | 5 | 8.7 | 12.23 | 6.8 |
| RB90-SA10 | 90 | 10 | 9.0 | 11.38 | 7.1 |
| RB85-SA15 | 85 | 15 | 9.6 | 10.09 | 7.6 |

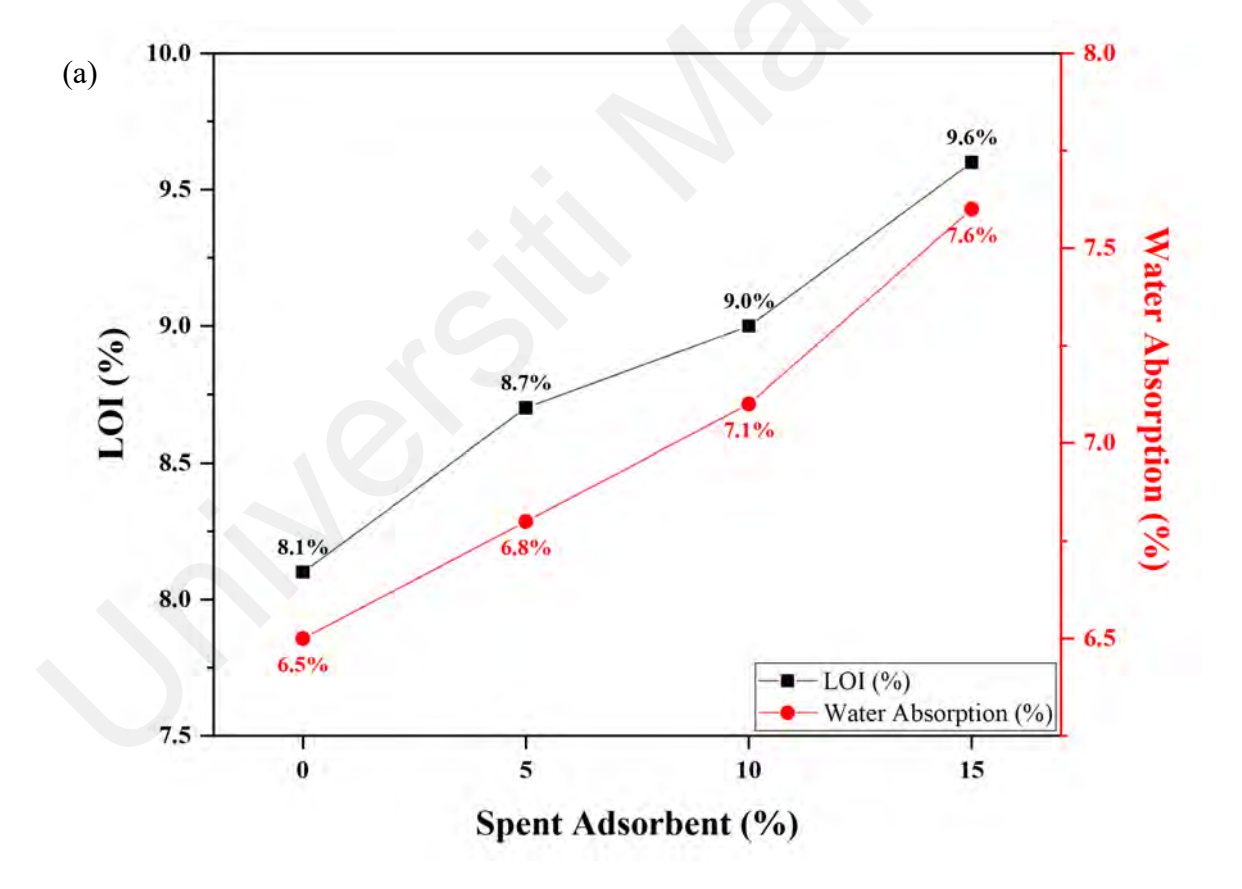
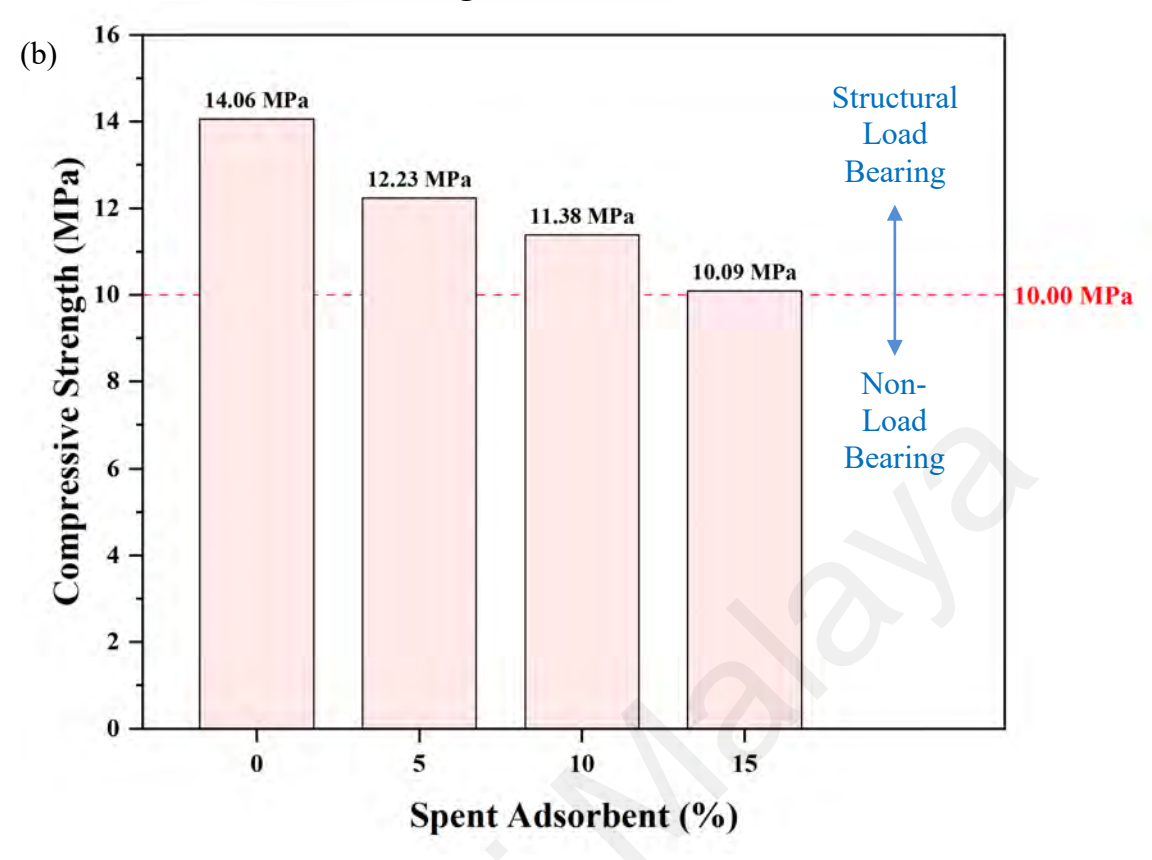


Figure 4.42: Plots of (a) LOI and Water Absorption and (b) Compressive Strength of Bricks as a Function of Spent Adsorbent Composition

Figure 4.42: Continued



Overall, this thesis covers the synthesis and optimization of a ternary composite comprising PKSAC, GO, and iron oxide for the treatment of synthetic and actual industrial wastewater. The research work involved the synthesis process, physicochemical characterization, and adsorption performance evaluation. The two main responses targeted were color removal efficiency and adsorption capacity. The ternary composite synthesis process was optimized at a ratio of PKSAC/GO of 0.2/0.8 and 45% iron oxide loading amount. Enhanced functionality and adsorption performance after GO and iron oxide impregnation into PKSAC were validated by physicochemical characterization, including FTIR, XRD, FESEM/EDX, and BET analyses. Besides that, the optimized composite also demonstrated excellent reusability and stability. The adsorption process using the PKSAC-GO-Fe composite was determined to be predominated by chemisorption, as supported by adsorption kinetic studies, as well as quantum and machine learning approaches. Moreover, economic and environmental

aspects were also thoroughly investigated. In conclusion, a ternary composite with enhanced performance was successfully developed in this study. As shown by the experimental and computational results, the PKSAC-GO-Fe composite has the potential to be an efficient adsorbent for wastewater treatment, which can contribute to circular economy and zero waste concepts.

CHAPTER 5: CONCLUSION AND RECOMMENDATIONS

5.1 Conclusion

This thesis covers a ternary composite comprising palm kernel shell activated carbon, graphene oxide, and iron oxide for dye wastewater treatment. The synthesis process of the ternary composite was optimized at PKSAC/GO ratio of 0.2/0.8 and 45% iron oxide loading. With the aforementioned optimization, substantial enhancements in the physicochemical characteristics and overall adsorption performance were observed.

The impregnation of GO and iron oxide to PKSAC added new surface functional groups and magnetic properties, confirmed by various physicochemical characterizations, such as FESEM, BET, XRD, and VSM analyses. FESEM images showed successful impregnation, with the composite having porous, sheet-like, and agglomerated structures. Although the surface area slightly decreased, the optimized composite retained high magnetization and stability.

From experimental studies, the ternary composite showed better adsorption performance than raw PKSAC and other PKSAC-based adsorbents. The effects of operational parameters, including the initial pH of the solution, adsorbent dosage, and contact time, have been thoroughly evaluated and optimized for treating synthetic and actual industrial wastewater. Besides that, the ternary composite also showed enhanced adsorption performance and reusability compared to commercial activated carbons. It can be applied to both batch and continuous processes, depending on industrial needs.

The adsorption mechanisms of the ternary composite were then studied via experimental and computational approaches. The experimental results reveal that the adsorption kinetics follow a pseudo-second-order model, which is a chemisorption-dominated process. The Langmuir isotherm model best describes the adsorption isotherm,

suggesting that the process was primarily monolayer in nature. The thermodynamic analysis showed that the adsorption process was exothermic and spontaneous. On the other hand, quantum chemical analysis indicated that the introduction of various functional groups which were contributed by the impregnation of graphene oxide and iron oxide, played a significant role in enhancing the adsorption process.

From an economical standpoint, the study demonstrated that the optimized composite is the most feasible adsorbent compared to commercial activated carbon, as well as PKSAC-GO-Fe before optimization. In addition, the use of PKSAC, a biomass-based activated carbon has resulted in lower carbon dioxide emissions compared to conventional coal-based activated carbon. This result highlights the environmental benefits of utilizing biomass-derived adsorbents. Besides that, the ternary composite also meets the WHO guidelines for drinking-water quality for iron ion leaching as well as exhibits no phytotoxicity, making it safe for environmental applications. Moreover, spent adsorbent has been incorporated into the brick formation. With this, in addition to secondary pollution mitigation, it also supports the ideas of zero waste and circular economy. Therefore, it can be said that the ternary composite synthesized in this study is a highly efficient, sustainable, and cost-effective solution for wastewater treatment applications.

5.2 Recommendations for Future Work

The following aspects should be addressed and considered in the future which will help to develop a more in-depth understanding of the ternary composite and its potential applications:

1. The ternary composite can be tested in a large adsorption system, for example, a pilot wastewater plant. With this, the practicality and effectiveness in real-world scenarios can be determined. This requires testing the process under industrial

- conditions to determine its feasibility and performance beyond laboratory settings.

 Additionally, the varying composition of industrial wastewater could reduce its efficiency, requiring site-specific adjustments.
- 2. Most of the current studies are conducted on a lab-scale basis, so the challenges in the collection and transportation of biomass precursors are rarely considered or discussed. Hence, in this case, a feasible route for the collection and transportation of precursors needs to be figured out. Palm kernel shells, for example, can be collected from the oil palm processing industries. Besides that, the consistency and equality of quality of precursors between batches during the mass production of adsorbents are yet to be noted and verified.
- 3. The potential applications of the ternary composite should be studied including areas such as the removal of other pollutants (e.g., heavy metals and rare earth elements), gas adsorption (e.g., carbon dioxide capture), catalyst support, soil remediation, energy storage, and advanced filtration systems. This could provide additional environmental protection and resource recovery benefits beyond dye wastewater treatment.
- 4. Developing adsorbents from other wastes such as plastic waste, marine waste, hazardous waste, and food waste could be possibly explored. Besides that, combining different precursors may result in higher performances and contain various functional groups from different precursors that can help in the adsorption process between adsorbent and adsorbate.
- 5. Integrating the adsorption process with other treatment technologies like membrane filtration, oxidation, and flocculation could further enhance its performance. Through the use of combined methods, a wide variety of complex wastewater could be treated more efficiently with the collective advantages of

- different technologies. However, it may require infrastructure upgrades and in turn will increase the overall cost and complexity, which should be a future focus.
- 6. The phytotoxicity study showed that the ternary composite can effectively remove the toxicity of pollutants from wastewater through adsorption. It is reflected in the growth patterns and germination rates. Further analysis of the cultured plants can be done to confirm that PKSAC-GO-Fe-treated wastewater can safely be used for plant cultivation, ensuring no toxic substances are transferred to humans upon consumption.
- 7. As pollutants adsorbed onto spent adsorbents may be released into the atmosphere at high temperatures. Hence, the smoke generated during the firing process of bricks containing spent adsorbents must be carefully monitored and managed. Advanced technologies, such as installing filtration systems at the smoke discharge point, should be implemented alongside real-time analysis of the smoke's content to prevent potential air pollution.

5.3 Contributions of the Study

This thesis presents a substantial advancement in the treatment of wastewater containing dyes. It was demonstrated that the ternary composite, which was synthesized by impregnating palm kernel shell activated carbon with graphene oxide and iron oxide, contributed to an improvement in the adsorption performance. In this way, it makes a contribution to the Sustainable Development Goals, and at the same time, offers a sustainable solution for the treatment of actual industrial wastewater. The following contributions are highlighted to emphasize the significance of this research:

1. PKSAC-GO-Fe, a ternary composite material that combines the advantages of the individual materials of PKSAC, GO, and iron oxide, is studied. This combination

- improves the physicochemical characteristics and adsorption performance for treating dye wastewater.
- 2. This study utilizes palm kernel shells, which are a waste product from the oil palm sector. With this, the study addresses the dual challenges of waste reduction and cost minimization. In simple words, wastes are transformed into a valuable resource through this approach, which contributes to sustainable waste management practices and reduces the overall environmental footprint.
- 3. The work provides a detailed analysis of adsorption mechanisms through both experimental and computational approaches. In addition to the experimental approach, the computational approach like quantum chemical analysis and machine learning was also studied. The interactions between pollutants and the functional groups present on the composite surface have been analyzed using quantum chemical studies. Feature importance analysis via machine learning, on the other hand, was conducted to relate the most significant properties to the adsorption process.
- 4. The study demonstrated the practical application of the PKSAC-GO-Fe composite in treating various actual industrial wastewater. This study also explores the applicability and feasibility of the continuous process, in addition to the batch process. Experimental results have proven that the ternary composite can be applied in different adsorption settings depending on treatment needs, regulations, and economic considerations.
- 5. By evaluating the economic feasibility of the ternary composite, it gives an overview of practical applications as well as provides a roadmap for scaling up of the technology.
- The study covers in-depth evaluations regarding various environmental aspects.
 This includes carbon dioxide emissions, iron leaching, and phytotoxicity studies.

With these considerations, the utilization of PKSAC-GO-Fe is in accordance with the SDGs with minimal environmental harm.

7. Besides that, this study also includes an innovative approach to managing spent adsorbents, which is repurposing them into brick production. This secondary application in brick industries supports circular economy practices and adds an additional benefit to the wastewater treatment process.

Overall, the findings of this work contribute to the advancement of the field of dye wastewater treatment. This research contributes to the development of wastewater management solutions that are more effective and environmentally friendly. The following aspects are evaluated, including physicochemical characteristics, adsorption performance, adsorption mechanisms, environmental impact, and economic feasibility. These contributions are substantial not only for academic research but also for the practical implementation of sustainable water treatment systems in actual scenarios.

5.4 Potential Applications

This study has demonstrated the successful impregnation of GO and iron oxide into PKSAC. The ternary composite significantly enhances physicochemical characteristics and adsorption performance, compared to other PKSAC-based adsorbents. Besides that, the ternary composite can effectively be used to treat synthetic and actual industrial wastewater. The stability, reusability, and applicability of the ternary composite in various adsorption settings have been validated. Hence, the ternary composite developed in this study demonstrated significant potential for real-world applications, highlighting the value of using renewable biomass sources for adsorbent development.

REFERENCES

- Abd-Elhamid, A. I., Kamoun, E. A., El-Shanshory, A. A., Soliman, H. M. A., & Aly, H. F. (2019). Evaluation of graphene oxide-activated carbon as effective composite adsorbent toward the removal of cationic dyes: Composite preparation, characterization and adsorption parameters. *Journal of Molecular Liquids*, 279, 530-539.
- Abdel-Ghani, N. T., El-Chaghaby, G. A., Rawash, E. A., & Lima, E. C. (2019). Magnetic activated carbon nanocomposite from Nigella sativa L. waste (MNSA) for the removal of Coomassie brilliant blue dye from aqueous solution: Statistical design of experiments for optimization of the adsorption conditions. *Journal of Advanced Research*, 17, 55-63.
- Abdelfattah, I., Ismail, A. A., Sayed, F. A., Almedolab, A., & Aboelghait, K. M. (2016). Biosorption of heavy metals ions in real industrial wastewater using peanut husk as efficient and cost effective adsorbent. *Environmental Nanotechnology, Monitoring & Management*, 6, 176-183.
- Abdi, G., Alizadeh, A., Amirian, J., Rezaei, S., & Sharma, G. (2019). Polyamine-modified magnetic graphene oxide surface: Feasible adsorbent for removal of dyes. *Journal of Molecular Liquids*, 289.
- Abdulsalam, K. A., Giwa, A.-R. A., & Adelowo, J. M. (2020). Optimization studies for decolourization of textile wastewater using a sawdust-based adsorbent. *Chemical Data Collections*, 27, 100400.
- Abuelnoor, N., AlHajaj, A., Khaleel, M., Vega, L. F., & Abu-Zahra, M. R. M. (2021). Activated carbons from biomass-based sources for CO₂ capture applications. *Chemosphere*, 282, 131111.
- Acharya, J., Kumar, U., & Meikap, B. C. (2013). Thermodynamic characterization of adsorption of lead(II) ions on activated carbon developed from tamarind wood from aqueous solution. *South African Journal of Chemical Engineering*, 18(1), 70-76.
- Adazabra, A. N., Viruthagiri, G., & Yirijor, J. (2023). Combined effects of biomass bottom ashes and spent charcoal on characteristics of fired clay bricks. *Construction and Building Materials*, 399, 132570.
- Adegoke, K. A., Adesina, O. O., Okon-Akan, O. A., Adegoke, O. R., Olabintan, A. B., Ajala, O. A., Olagoke, H., Maxakato, N. W., & Bello, O. S. (2022). Sawdust-biomass based materials for sequestration of organic and inorganic pollutants and potential for engineering applications. *Current Research in Green and Sustainable Chemistry*, 5, 100274.
- Aghashiri, A., Hashemian, S., & Fotooh, F. K. (2022). Mesoporous LaFeO₃ nanoparticles decorated onto activated carbon from agricultural paste (Synthesis, characterization and adsorption properties). *Journal of Molecular Structure*, 1260, 132822.

- Ahmad, A. A., & Hameed, B. H. (2010). Effect of preparation conditions of activated carbon from bamboo waste for real textile wastewater. *Journal of Hazardous Materials*, 173(1-3), 487-493.
- Ahmad, M. A., Eusoff, M. A., Oladoye, P. O., Adegoke, K. A., & Bello, O. S. (2021). Optimization and batch studies on adsorption of Methylene blue dye using pomegranate fruit peel based adsorbent. *Chemical Data Collections*, 32, 100676.
- Ahmad, R., & Ansari, K. (2022). Novel in-situ fabrication of L-methionine functionalized bionanocomposite for adsorption of Amido Black 10B dye. *Process Biochemistry*, 119, 48-57.
- Ahmad, T., & Danish, M. (2022). A review of avocado waste-derived adsorbents: Characterizations, adsorption characteristics, and surface mechanism. *Chemosphere*, 296, 134036.
- Ajibade, P. A., & Nnadozie, E. C. (2023). Synthesis, characterization, and structural studies of biochar capped magnetic iron oxide and its potentials as adsorbents for organic dyes. *Case Studies in Chemical and Environmental Engineering*, 8, 100473.
- Akhdhar, A. (2023). A Novel, Simple, and Reliable Spectrophotometric Determination of Total Hexavalent Chromium by Complexation with a New Reagent of Thiazole Linked to 2H-Chromen-2-One. *International Journal of Analytical Chemistry*, 2023, 2042221.
- Akkoz, Y., & Coskun, R. (2024). Cellulose- supported sulfated-magnetic biocomposite produced from hemp biomass: Effective removal of cationic dyes from aqueous solution. *International Journal of Biological Macromolecules*, 257, 128747.
- Akter, M., Rahman, F. B. A., Abedin, M. Z., & Kabir, S. M. F. (2021). Adsorption Characteristics of Banana Peel in the Removal of Dyes from Textile Effluent. *Textiles*, *1*(2), 361-375.
- Al-Odayni, A. B., Alsubaie, F. S., Abdu, N. A. Y., Al-Kahtani, H. M., & Saeed, W. S. (2023). Adsorption Kinetics of Methyl Orange from Model Polluted Water onto N-Doped Activated Carbons Prepared from N-Containing Polymers. *Polymers*, 15, 1983.
- Al-Tohamy, R., Ali, S. S., Li, F., Okasha, K. M., Mahmoud, Y. A., Elsamahy, T., Jiao, H., Fu, Y., & Sun, J. (2022). A critical review on the treatment of dye-containing wastewater: Ecotoxicological and health concerns of textile dyes and possible remediation approaches for environmental safety. *Ecotoxicology and Environmental Safety*, 231, 113160.
- Algethami, J. S., Alhamami, M. A. M., Alqadami, A. A., Melhi, S., & Seliem, A. F. (2024). Magnetic hydrochar grafted-chitosan for enhanced efficient adsorption of malachite green dye from aqueous solutions: Modeling, adsorption behavior, and mechanism analysis. *International Journal of Biological Macromolecules*, 254, 127767.

- Alhashimi, H. A., & Aktas, C. B. (2017). Life cycle environmental and economic performance of biochar compared with activated carbon: A meta-analysis. *Resources, Conservation and Recycling*, 118, 13-26.
- Ali, S. I., Lalji, S. M., Haneef, J., Ahsan, U., Khan, M. A., & Yousaf, N. (2021). Estimation of asphaltene adsorption on MgO nanoparticles using ensemble learning. *Chemometrics and Intelligent Laboratory Systems*, 208.
- Ali, S. S., Al-Tohamy, R., & Sun, J. (2025). Disruptive technology for integrating bioremediation and biodiesel production from persistent toxic aromatic wastes using termite gut yeasts. *Environmental Chemistry and Ecotoxicology*, 7, 462-493.
- Aljeboree, A. M., Abdulrazzak, F. H., Saleh, Z. M., Abbas, H. A., & Alkaim, A. F. (2023). Eco-Friendly Adsorption of Cationic (Methylene Blue) and Anionic (Congo Red) Dyes from Aqueous Solutions Using Sawdust. *Engineering Proceedings*, 59(1).
- Aljeboree, A. M., Alshirifi, A. N., & Alkaim, A. F. (2017). Kinetics and equilibrium study for the adsorption of textile dyes on coconut shell activated carbon. *Arabian Journal of Chemistry*, 10, S3381-S3393.
- Almoisheer, N., Alseroury, F. A., Kumar, R., Almeelbi, T., & Barakat, M. A. (2019). Synthesis of Graphene Oxide/Silica/Carbon Nanotubes Composite for Removal of Dyes from Wastewater. *Earth Systems and Environment*, *3*(3), 651-659.
- AlMomani, F., & Örmeci, B. (2020). Assessment of algae-based wastewater treatment in hot climate region: Treatment performance and kinetics. *Process Safety and Environmental Protection*, 141, 140-149.
- Alsawy, T., Rashad, E., El-Qelish, M., & Mohammed, R. H. (2022). A comprehensive review on the chemical regeneration of biochar adsorbent for sustainable wastewater treatment. *npj Clean Water*, 5(1).
- Alsharief, H. H., Alatawi, N. M., Al-bonayan, A. M., Alrefaee, S. H., Saad, F. A., El-Desouky, M. G., & El-Bindary, A. A. (2024). Adsorption of Azorubine E122 dye via Na-mordenite with tryptophan composite: batch adsorption, Box–Behnken design optimisation and antibacterial activity. *Environmental Technology*, 45(17), 3496-3515.
- Alsukaibi, A. K. D. (2022). Various Approaches for the Detoxification of Toxic Dyes in Wastewater. *Processes*, 10(10).
- Altıntıg, E., Altundag, H., Tuzen, M., & Sarı, A. (2017). Effective removal of methylene blue from aqueous solutions using magnetic loaded activated carbon as novel adsorbent. *Chemical Engineering Research and Design*, 122, 151-163.
- Altintig, E., Onaran, M., Sarı, A., Altundag, H., & Tuzen, M. (2018). Preparation, characterization and evaluation of bio-based magnetic activated carbon for effective adsorption of malachite green from aqueous solution. *Materials Chemistry and Physics*, 220, 313-321.

- Amri, A. E., Bensalah, J., Idrissi, A., Lamya, K., Ouass, A., Bouzakraoui, S., Zarrouk, A., Rifi, E. H., & Lebkiri, A. (2022). Adsorption of a cationic dye (Methylene bleu) by Typha Latifolia: Equilibrium, kinetic, thermodynamic and DFT calculations. *Chemical Data Collections*, 38, 100834.
- Anastopoulos, I., Pashalidis, I., Hosseini-Bandegharaei, A., Giannakoudakis, D. A., Robalds, A., Usman, M., Escudero, L. B., Zhou, Y., Colmenares, J. C., Núñez-Delgado, A., & Lima, É. C. (2019). Agricultural biomass/waste as adsorbents for toxic metal decontamination of aqueous solutions. *Journal of Molecular Liquids*, 295, 111684.
- Angelova, R., Baldikova, E., Pospiskova, K., Maderova, Z., Safarikova, M., & Safarik, I. (2016). Magnetically modified Sargassum horneri biomass as an adsorbent for organic dye removal. *Journal of Cleaner Production*, 137, 189-194.
- Ansari, S. A., Shakeel, A., Sawarkar, R., Maddalwar, S., Khan, D., & Singh, L. (2023). Additive facilitated co-composting of lignocellulosic biomass waste, approach towards minimizing greenhouse gas emissions: An up to date review. *Environmental Research*, 224, 115529.
- Aravindhan, S., Bharath Kumar, G., Saravanan, M., & Arumugam, A. (2024). Delonix regia biomass as an eco-friendly biosorbent for effective Alizarin Red S textile dye removal: Characterization, kinetics, and isotherm studies. *Bioresource Technology Reports*, 25, 101721.
- Ariza-Pineda, F. J., Macias-Quiroga, I. F., Hinojosa-Zambrano, D. F., Rivera-Giraldo, J. D., Ocampo-Serna, D. M., & Sanabria-Gonzalez, N. R. (2023). Treatment of textile wastewater using the Co(II)/NaHCO₃/H₂O₂ oxidation system. *Heliyon*, 9(12), e22444.
- Aryee, A. A., Gao, C., Han, R., & Qu, L. (2022). Functionalized magnetic biocomposite based on peanut husk for the efficient sequestration of basic dyes in single and binary systems: Adsorption mechanism and antibacterial study. *Journal of Environmental Chemical Engineering*, 10(4), 108205.
- Arzate, S., Pfister, S., Oberschelp, C., & Sánchez-Pérez, J. A. (2019). Environmental impacts of an advanced oxidation process as tertiary treatment in a wastewater treatment plant. *Science of The Total Environment*, 694, 133572.
- Asfaram, A., Fathi, M. R., Khodadoust, S., & Naraki, M. (2014). Removal of Direct Red 12B by garlic peel as a cheap adsorbent: kinetics, thermodynamic and equilibrium isotherms study of removal. *Spectrochimica Acta Part A: Molecular and Biomolecular Spectroscopy*, 127, 415-421.
- Astuti, W., Sulistyaningsih, T., Kusumastuti, E., Thomas, G., & Kusnadi, R. Y. (2019). Thermal conversion of pineapple crown leaf waste to magnetized activated carbon for dye removal. *Bioresource Technology*, 287, 121426.
- Banerjee, S., & Chattopadhyaya, M. C. (2017). Adsorption characteristics for the removal of a toxic dye, tartrazine from aqueous solutions by a low cost agricultural byproduct. *Arabian Journal of Chemistry*, 10, S1629-S1638.

- Barbieri, L., Andreola, F., Lancellotti, I., & Taurino, R. (2013). Management of agricultural biomass wastes: Preliminary study on characterization and valorisation in clay matrix bricks. *Waste Management*, 33(11), 2307-2315.
- Bellaj, M., Aziz, K., El Achaby, M., El Haddad, M., Gebrati, L., Kurniawan, T. A., Chen, Z., Yap, P.-S., & Aziz, F. (2024). Cationic and anionic dyes adsorption from wastewater by clay-chitosan composite: An integrated experimental and modeling study. *Chemical Engineering Science*, 285.
- Bello, O. S., Adegoke, K. A., Sarumi, O. O., & Lameed, O. S. (2019). Functionalized locust bean pod (*Parkia biglobosa*) activated carbon for Rhodamine B dye removal. *Heliyon*, 5(8), e02323.
- Bener, S., Atalay, S., & Ersöz, G. (2020). The hybrid process with eco-friendly materials for the treatment of the real textile industry wastewater. *Ecological Engineering*, 148, 105789.
- Bentéjac, C., Csörgő, A., & Martínez-Muñoz, G. (2021). A comparative analysis of gradient boosting algorithms. *Artificial Intelligence Review*, *54*(3), 1937-1967.
- Bhardwaj, M., Tewari, S., Kumari, N., Bhardwaj, A., Misra, N., Shukla, S., Dwivedi, J., & Sharma, S. (2024). Adsorption of Pb(II) and Cd(II) by functionalized graphene oxide (GO-MBT): Mechanisms, antibacterial activity, and DFT studies. *Inorganic Chemistry Communications*, 164, 112464.
- Bhateria, R., & Jain, D. (2016). Water quality assessment of lake water: a review. Sustainable Water Resources Management, 2(2), 161-173.
- Bhattacharyya, A., Banerjee, B., Ghorai, S., Rana, D., Roy, I., Sarkar, G., Saha, N. R., De, S., Ghosh, T. K., Sadhukhan, S., & Chattopadhyay, D. (2018). Development of an auto-phase separable and reusable graphene oxide-potato starch based cross-linked bio-composite adsorbent for removal of methylene blue dye. *International Journal of Biological Macromolecules*, 116, 1037-1048.
- Bhattacharyya, A., Ghorai, S., Rana, D., Roy, I., Sarkar, G., Saha, N. R., Orasugh, J. T., De, S., Sadhukhan, S., & Chattopadhyay, D. (2021). Design of an efficient and selective adsorbent of cationic dye through activated carbon graphene oxide nanocomposite: Study on mechanism and synergy. *Materials Chemistry and Physics*, 260, 124090.
- Bhatti, H. N., Sadaf, S., Aleem, A. (2015). Treatment of textile effluents by low cost agricultural wastes: Batch Biosorption Study. *The Journal of Animal & Plant Sciences*, 25(1), 284-289.
- Bogush, A. A., Kim, J. K., & Campos, L. C. (2007). Removal of arsenic, nitrate, persistent organic pollutants and pathogenic microbes from water using redox-reactive minerals. In I. A. M. Ahmed & K. A. Hudson-Edwards (Eds.), *Redox-reactive Minerals: Properties, Reactions and Applications in Clean Technologies* (Vol. 17, pp. 405-442). Mineralogical Society.

- Bouabbaci, S., Chougui, A., Asli, B., Mokhtar, A., Belouatek, A., Boukoussa, B., & Abboud, M. (2024). Preparation and characterization of activated carbon from pine bark biomass for malachite green removal. *International Journal of Environmental Analytical Chemistry*, 1-24.
- Bouhadjra, K., Lemlikchi, W., Ferhati, A., & Mignard, S. (2021). Enhancing removal efficiency of anionic dye (Cibacron blue) using waste potato peels powder. *Scientific Reports*, 11, 2090.
- Bouras, H. D., RedaYeddou, A., Bouras, N., Chergui, A., Favier, L., Amrane, A., & Dizge, N. (2021). Biosorption of cationic and anionic dyes using the biomass of *Aspergillus parasiticus* CBS 100926^T. *Water Science & Technology*, 83(3), 622-630.
- Brito, C. H. V., Gloria, D. C. S., Santos, E. B., Domingues, R. A., Valente, G. T., Vieira, N. C. S., & Gonçalves, M. (2023). Porous activated carbon/graphene oxide composite for efficient adsorption of pharmaceutical contaminants. *Chemical Engineering Research and Design*, 191, 387-400.
- Çağlar, E., Donar, Y. O., Sinağ, A., BiroğLu, İ., Bilge, S., Aydincak, K., & Pliekhov, O. (2018). Adsorption of anionic and cationic dyes on biochars, produced by hydrothermal carbonization of waste biomass: effect of surface functionalization and ionic strength. *Turkish Journal of Chemistry*, 42, 86-99.
- Cao, W., & Zhang, W. (2020). Low temperature selective catalytic reduction of nitric oxide with an activated carbon-supported zero-valent iron catalyst. *RSC Advances*, 10(69), 42613-42618.
- Cazetta, A. L., Pezoti, O., Bedin, K. C., Silva, T. L., Paesano Junior, A., Asefa, T., & Almeida, V. C. (2016). Magnetic Activated Carbon Derived from Biomass Waste by Concurrent Synthesis: Efficient Adsorbent for Toxic Dyes. *ACS Sustainable Chemistry & Engineering*, 4(3), 1058-1068.
- Cemin, A., Ferrarini, F., Poletto, M., Bonetto, L. R., Bortoluz, J., Lemee, L., Guegan, R., Esteves, V. I., & Giovanela, M. (2021). Characterization and use of a lignin sample extracted from Eucalyptus grandis sawdust for the removal of methylene blue dye. *International Journal of Biological Macromolecules*, 170, 375-389.
- Chand, P., Bafana, A., & Pakade, Y. B. (2015). Xanthate modified apple pomace as an adsorbent for removal of Cd (II), Ni (II) and Pb (II), and its application to real industrial wastewater. *International Biodeterioration & Biodegradation*, 97, 60-66.
- Chen, C., Hu, J., Shao, D., Li, J., & Wang, X. (2009). Adsorption behavior of multiwall carbon nanotube/iron oxide magnetic composites for Ni(II) and Sr(II). *Journal of Hazardous Materials*, 164(2-3), 923-928.
- Chen, Y., Zhang, Y., Chen, T., Zhao, Y., & Bao, S. (2011). Preparation of eco-friendly construction bricks from hematite tailings. *Construction and Building Materials*, 25(4), 2107-2111.

- Cheng, S., Shao, L., Ma, J., Xia, X., Liu, Y., Yang, Z., Yang, C., & Li, S. (2019). Simultaneous removal of phosphates and dyes by Al-doped iron oxide decorated MgAl layered double hydroxide nanoflakes. *Environmental Science: Nano*, 6(8), 2615-2625.
- Cheng, S., Zhang, L., Ma, A., Xia, H., Peng, J., Li, C., & Shu, J. (2018). Comparison of activated carbon and iron/cerium modified activated carbon to remove methylene blue from wastewater. *Journal of Environmental Sciences*, 65, 92-102.
- Cheruiyot, G. K., Wanyonyi, W. C., Kiplimo, J. J., & Maina, E. N. (2019). Adsorption of toxic crystal violet dye using coffee husks: Equilibrium, kinetics and thermodynamics study. *Scientific African*, 5, e00116.
- Cholico-Gonzalez, D., Ortiz Lara, N., Fernandez Macedo, A. M., & Chavez Salas, J. (2020). Adsorption Behavior of Pb(II), Cd(II), and Zn(II) onto Agave Bagasse, Characterization, and Mechanism. *ACS Omega*, 5(7), 3302-3314.
- Choong, T. S., Wong, T. N., Chuah, T. G., & Idris, A. (2006). Film-pore-concentration-dependent surface diffusion model for the adsorption of dye onto palm kernel shell activated carbon. *Journal of Colloid and Interface Science*, 301(2), 436-440.
- Daud, Z., Detho, A., Rosli, M. A., Abubakar, M. H., Samo, K. A., Rais, N. F. M., Abdul Halim, A., & Tajarudin, H. A. (2020). Ammoniacal nitrogen and COD removal from stabilized landfill leachate using granular activated carbon and green mussel (*Perna viridis*) shell powder as a composite adsorbent. *Desalination and Water Treatment*, 192, 111-117.
- Demir, I. (2008). Effect of organic residues addition on the technological properties of clay bricks. *Waste Management*, 28(3), 622-627.
- Deng, H., Lu, J., Li, G., Zhang, G., & Wang, X. (2011). Adsorption of methylene blue on adsorbent materials produced from cotton stalk. *Chemical Engineering Journal*, 172(1), 326-334.
- Deng, Y., Feng, C., Tang, L., Zeng, G., Chen, Z., & Zhang, M. (2019). Chapter 5 Nanohybrid Photocatalysts for Heavy Metal Pollutant Control. In L. Tang, Y. Deng, J. Wang, J. Wang, & G. Zeng (Eds.), Nanohybrid and Nanoporous Materials for Aquatic Pollution Control (pp. 125-153). Elsevier.
- Derakhshan, Z., Baghapour, M. A., Ranjbar, M., & Faramarzian, M. (2013). Adsorption of Methylene Blue Dye from Aqueous Solutions by Modified Pumice Stone: Kinetics and Equilibrium Studies. *Health Scope*, 2(3), 136-144.
- Dewangan, S. K., Toppo, D. N., & Kujur, A. (2023). Investigating the Impact of pH Levels on Water Quality: An Experimental Approach. *International Journal for Research in Applied Science and Engineering Technology*, 11(9), 756-759.
- Dhameliya, K. B., & Ambasana, C. (2023). Assessment of Wastewater Contaminants Caused by Textile Industries. *Journal of Pure and Applied Microbiology*, 17(3), 1477-1485.

- Dixit, U., Singh, K., Mohan, S., Singh, A. K., & Kumar, A. (2024). Surface activity, mechanisms, kinetics, and thermodynamic study of adsorption of malachite green dye onto sulfuric acid-functionalized *Moringa oleifera* leaves from aqueous solution. *Environmental Monitoring and Assessment*, 196, 78.
- Djelloul, C., Hasseine, A., & Hamdaoui, O. (2017). Adsorption of cationic dye from aqueous solution by milk thistle seeds: isotherm, kinetic and thermodynamic studies. *Desalination and Water Treatment*, 78, 313-320.
- Du, B., Li, W., Chai, L., Li, W., Wang, X., Chen, X., Zhou, J., & Sun, R.-C. (2023). Preparation of versatile lignin-based adsorbent for the removal of organic dyes and its application in wound healing. *Journal of Molecular Liquids*, 377, 121566.
- Du, J., Wu, Y., Dong, Z., Zhang, M., Yang, X., Xiong, H., & Zhao, L. (2022). Single and competitive adsorption between Indigo Carmine and Methyl orange dyes on quaternized kapok fiber adsorbent prepared by radiation technique. *Separation and Purification Technology*, 292, 121103.
- Duan, Z., Zhang, W., Lu, M., Shao, Z., Huang, W., Li, J., Li, Y., Mo, J., Li, Y., & Chen, C. (2020). Magnetic Fe₃O₄/activated carbon for combined adsorption and Fenton oxidation of 4-chlorophenol. *Carbon*, *167*, 351-363.
- El-Bindary, M. A., El-Deen, I. M., & Shoair, A. F. (2019). Removal of anionic dye from aqueous solution using magnetic sodium alginate beads. *Journal of Materials and Environmental Science*, 10(7), 604-617.
- El-Sayed, G. O. (2011). Removal of methylene blue and crystal violet from aqueous solutions by palm kernel fiber. *Desalination*, 272(1-3), 225-232.
- Elgarahy, A. M., Maged, A., Elwakeel, K. Z., El-Gohary, F., & El-Qelish, M. (2023). Tuning cationic/anionic dyes sorption from aqueous solution onto green algal biomass for biohydrogen production. *Environmental Research*, 216(Pt 1), 114522.
- Eliche-Quesada, D., Corpas-Iglesias, F. A., Pérez-Villarejo, L., & Iglesias-Godino, F. J. (2012). Recycling of sawdust, spent earth from oil filtration, compost and marble residues for brick manufacturing. *Construction and Building Materials*, 34, 275-284.
- Eliche-Quesada, D., & Leite-Costa, J. (2016). Use of bottom ash from olive pomace combustion in the production of eco-friendly fired clay bricks. *Waste Management*, 48, 323-333.
- Environmental Quality (Industrial Effluents) Regulations (2009).
- Eshghabadi, F., & Javanbakht, V. (2024). Preparation of porous metakaolin-based geopolymer foam as an efficient adsorbent for dye removal from aqueous solution. *Journal of Molecular Structure*, 1295.
- Etana, R., Angassa, K., & Getu, T. (2025). Dye removal from textile wastewater using scoria-based of vertical subsurface flow constructed wetland system. *Scientific Reports*, 15(1), 949.

- Faria, K. C., Gurgel, R. F., & Holanda, J. N. (2012). Recycling of sugarcane bagasse ash waste in the production of clay bricks. *Journal of Environmental Management*, 101, 7-12.
- Fatma, Hariani, P. L., Riyanti, F., & Sepriani, W. (2018). Desorption and re-adsorption of procion red MX-5B dye on alumina-activated carbon composite. *Indonesian Journal of Chemistry*, 18(2), 222-228.
- Fatombi, J. K., Osseni, S. A., Idohou, E. A., Agani, I., Neumeyer, D., Verelst, M., Mauricot, R., & Aminou, T. (2019). Characterization and application of alkalisoluble polysaccharide of *Carica papaya* seeds for removal of indigo carmine and Congo red dyes from single and binary solutions. *Journal of Environmental Chemical Engineering*, 7(5), 103343.
- Foroutan, R., Mohammadi, R., Farjadfard, S., Esmaeili, H., Saberi, M., Sahebi, S., Dobaradaran, S., & Ramavandi, B. (2019). Characteristics and performance of Cd, Ni, and Pb bio-adsorption using *Callinectes sapidus* biomass: real wastewater treatment. *Environmental Science and Pollution Research*, 26(7), 6336-6347.
- Foroutan, R., Mohammadi, R., Razeghi, J., & Ramavandi, B. (2019). Performance of algal activated carbon/Fe₃O₄ magnetic composite for cationic dyes removal from aqueous solutions. *Algal Research*, 40, 101509.
- Foroutan, R., Peighambardoust, S. J., Peighambardoust, S. H., Pateiro, M., & Lorenzo, J. M. (2021). Adsorption of Crystal Violet Dye Using Activated Carbon of Lemon Wood and Activated Carbon/Fe₃O₄ Magnetic Nanocomposite from Aqueous Solutions: A Kinetic, Equilibrium and Thermodynamic Study. *Molecules*, 26(8), 2241.
- Fraga, T. J. M., Ghislandi, M. G., Carvalho, M. N., & da Motta Sobrinho, M. A. (2020). One step forward: How can functionalization enhance the adsorptive properties of graphene towards metallic ions and dyes? *Environmental Research*, 184, 109362.
- Gadekar, M. R., & Ahammed, M. M. (2019). Modelling dye removal by adsorption onto water treatment residuals using combined response surface methodology-artificial neural network approach. *Journal of Environmental Management*, 231, 241-248.
- Gallios, G., Tolkou, A., Katsoyiannis, I., Stefusova, K., Vaclavikova, M., & Deliyanni, E. (2017). Adsorption of Arsenate by Nano Scaled Activated Carbon Modified by Iron and Manganese Oxides. *Sustainability*, 9(10).
- Gao, M., Wang, Z., Yang, C., Ning, J., Zhou, Z., & Li, G. (2019). Novel magnetic graphene oxide decorated with persimmon tannins for efficient adsorption of malachite green from aqueous solutions. *Colloids and Surfaces A: Physicochemical and Engineering Aspects*, 566, 48-57.
- Gemici, B. T., Ozel, H. U., & Ozel, H. B. (2021). Removal of methylene blue onto forest wastes: Adsorption isotherms, kinetics and thermodynamic analysis. *Environmental Technology & Innovation*, 22, 101501.

- Ghaedi, S., Seifpanahi-Shabani, K., & Sillanpaa, M. (2022). Waste-to-Resource: New application of modified mine silicate waste to remove Pb²⁺ ion and methylene blue dye, adsorption properties, mechanism of action and recycling. *Chemosphere*, 292, 133412.
- Ghaly, A. E., Ananthashankar, R., Alhattab, M., & Ramakrishnan, V. V. (2014). Production, Characterization and Treatment of Textile Effluents: A Critical Review. *Journal of Chemical Engineering & Process Technology*, 05(01), 1-18.
- Gözmen, B., Kayan, B., Gizir, A. M., & Hesenov, A. (2009). Oxidative degradations of reactive blue 4 dye by different advanced oxidation methods. *Journal of Hazardous Materials*, 168(1), 129-136.
- Gu, H., Bergman, R., Anderson, N., & Alanya-Rosenbaum, S. (2018). Life cycle assessment of activated carbon from woody biomass. *Wood and Fiber Science*, 50(3), 229-243.
- Guidelines for drinking-water quality. (1996). (2 ed., Vol. 2). Geneva: World Health Organization.
- Gulati, P., Sharma, A., & Gupta, M. (2016). Theoretical Study of Decision Tree Algorithms to Identify Pivotal Factors for Performance Improvement: A Review. *International Journal of Computer Applications*, 141, 19-25.
- Guo, F., Li, X., Jiang, X., Zhao, X., Guo, C., & Rao, Z. (2018). Characteristics and toxic dye adsorption of magnetic activated carbon prepared from biomass waste by modified one-step synthesis. *Colloids and Surfaces A: Physicochemical and Engineering Aspects*, 555, 43-54.
- Guo, J., Zhang, Q., Cai, Z., & Zhao, K. (2016). Preparation and dye filtration property of electrospun polyhydroxybutyrate—calcium alginate/carbon nanotubes composite nanofibrous filtration membrane. *Separation and Purification Technology*, *161*, 69-79.
- Habibi, N., Rouhi, P., & Ramavandi, B. (2017). Synthesis of adsorbent from Tamarix hispida and modified by lanthanum metal for fluoride ions removal from wastewater: Adsorbent characteristics and real wastewater treatment data. *Data in Brief*, 13, 749-754.
- Hafsa, N., Rushd, S., Al-Yaari, M., & Rahman, M. (2020). A Generalized Method for Modeling the Adsorption of Heavy Metals with Machine Learning Algorithms. *Water*, 12(12).
- Hamadi, A., Yeddou-Mezenner, N., Lounis, A., Ali, R. M., & Hamad, H. (2021). Upgrading of agro-industrial green biomass residues from chocolate industry for adsorption process: diffusion and mechanistic insights. *Journal of Food Science and Technology*, 58(3), 1081-1092.
- Hameed, B. H. (2009). Evaluation of papaya seeds as a novel non-conventional low-cost adsorbent for removal of methylene blue. *Journal of Hazardous Materials*, 162, 939-944.

- Hameed, B. H., & Ahmad, A. A. (2009). Batch adsorption of methylene blue from aqueous solution by garlic peel, an agricultural waste biomass. *Journal of Hazardous Materials*, 164, 870-875.
- Han, L., Sun, H., Sun, K., Yang, Y., Fang, L., & Xing, B. (2021). Effect of Fe and Al ions on the production of biochar from agricultural biomass: Properties, stability and adsorption efficiency of biochar. *Renewable and Sustainable Energy Reviews*, 145, 111133.
- Han, X., Wang, W., & Ma, X. (2011). Adsorption characteristics of methylene blue onto low cost biomass material lotus leaf. *Chemical Engineering Journal*, 171(1), 1-8.
- Hao, S., Zhang, Q., Wang, Y., Zhang, W., & Huang, J. (2022). Preparation and Adsorption Properties of Green Sustainable Biomass Carbon Microspheres. *Industrial & Engineering Chemistry Research*, 61(30), 11249-11261.
- Harif, S., Aboulhassan, M. A., & Bammou, L. (2021). Overview of Wastewater Characteristics of Cardboard Industry. *Scientific Study and Research: Chemistry and Chemical Engineering*, 22, 1-011.
- Hashem, H. M., El-Maghrabey, M., & El-Shaheny, R. (2024). Inclusive study of peanut shells derived activated carbon as an adsorbent for removal of lead and methylene blue from water. *Scientific Reports*, 14(1), 13515.
- Holkar, C. R., Jadhav, A. J., Pinjari, D. V., Mahamuni, N. M., & Pandit, A. B. (2016). A critical review on textile wastewater treatments: Possible approaches. *Journal of Environmental Management*, 182, 351-366.
- Holliday, M. C., Parsons, D. R., & Zein, S. H. (2022). Agricultural Pea Waste as a Low-Cost Pollutant Biosorbent for Methylene Blue Removal: Adsorption Kinetics, Isotherm And Thermodynamic Studies. *Biomass Conversion and Biorefinery*, 14, 6671-6685.
- Hossain, M. F., & Park, J. Y. (2016). Plain to point network reduced graphene oxide-activated carbon composites decorated with platinum nanoparticles for urine glucose detection. *Scientific Reports*, 6, 21009.
- Hosseinzadeh, H., & Ramin, S. (2018). Effective removal of copper from aqueous solutions by modified magnetic chitosan/graphene oxide nanocomposites. *International Journal of Biological Macromolecules*, 113, 859-868.
- Hossen, A., Chowdhury, T., & Mondal, M. I. H. (2022). Purification of textile dyecontained wastewater by three alternative promising techniques: Adsorption, Biodegradation and Advanced Oxidation Processes (AOPs) - A review. *Journal* of Textile Engineering & Fashion Technology, 8(3), 96-98.
- Husain, S., Yusup, M., Haryanti, N. H., Suryajaya, Saukani, M., Rodiansono, Arjo, S., & Riyanto, A. (2021). Characteristics of zinc ferrite nanoparticles (ZnFe₂O₄) from natural iron ore. *IOP Conference Series: Earth and Environmental Science*, 758(1), 012001.

- Ibrahim, S. M., Al-Harby, N. F., El-Molla, S. A., & Ibrahim, E. S. (2024). New combined experimental and DFT studies for adsorption of sole Azo-dye or binary cationic dyes from aqueous solution. *Scientific Reports*, 14(1), 14756.
- International Filtration News. (2009). I. Eagle Publications.
- Izwan Anthonysamy, S., Ahmad, M. A., & E.M. Yahaya, N. K. (2023). Insight the mechanism of MgAl/layered double hydroxide supported on rubber seed shell biochar for Remazol Brilliant Violet 5R removal. *Arabian Journal of Chemistry*, 16(4), 104643.
- Jain, S. N., & Gogate, P. R. (2017). Acid Blue 113 removal from aqueous solution using novel biosorbent based on NaOH treated and surfactant modified fallen leaves of Prunus Dulcis. Journal of Environmental Chemical Engineering, 5(4), 3384-3394.
- Jain, S. N., Tamboli, S. R., Sutar, D. S., Jadhav, S. R., Marathe, J. V., Shaikh, A. A., & Prajapati, A. A. (2020a). Batch and continuous studies for adsorption of anionic dye onto waste tea residue: Kinetic, equilibrium, breakthrough and reusability studies. *Journal of Cleaner Production*, 252.
- Jain, S. N., Tamboli, S. R., Sutar, D. S., Jadhav, S. R., Marathe, J. V., Shaikh, A. A., & Prajapati, A. A. (2020b). Batch and continuous studies for adsorption of anionic dye onto waste tea residue: Kinetic, equilibrium, breakthrough and reusability studies. *Journal of Cleaner Production*, 252, 119778-119778.
- Jawad, A. H., & Abdulhameed, A. S. (2020). Mesoporous Iraqi red kaolin clay as an efficient adsorbent for methylene blue dye: Adsorption kinetic, isotherm and mechanism study. *Surfaces and Interfaces*, 18, 100422.
- Jawad, A. H., Saud Abdulhameed, A., Wilson, L. D., Syed-Hassan, S. S. A., Alothman, Z. A., & Rizwan Khan, M. (2021). High surface area and mesoporous activated carbon from KOH-activated dragon fruit peels for methylene blue dye adsorption: Optimization and mechanism study. *Chinese Journal of Chemical Engineering*, 32, 281-290.
- Jiang, D., Li, H., Cheng, X., Ling, Q., Chen, H., Barati, B., Yao, Q., Abomohra, A., Hu, X., Bartocci, P., & Wang, S. (2023). A mechanism study of methylene blue adsorption on seaweed biomass derived carbon: From macroscopic to microscopic scale. *Process Safety and Environmental Protection*, 172, 1132-1143.
- Jiang, W., Zhang, L., Guo, X., Yang, M., Lu, Y., Wang, Y., Zheng, Y., & Wei, G. (2021). Adsorption of cationic dye from water using an iron oxide/activated carbon magnetic composites prepared from sugarcane bagasse by microwave method. *Environmental Technology*, 42(3), 337-350.
- Jiang, Y., Gong, J. L., Zeng, G. M., Ou, X. M., Chang, Y. N., Deng, C. H., Zhang, J., Liu, H. Y., & Huang, S. Y. (2016). Magnetic chitosan-graphene oxide composite for anti-microbial and dye removal applications. *International Journal of Biological Macromolecules*, 82, 702-710.
- Jiang, Z., & Hu, D. (2019). Molecular mechanism of anionic dyes adsorption on cationized rice husk cellulose from agricultural wastes. *Journal of Molecular Liquids*, 276, 105-114.

- Joshi, P., Sharma, O. P., Ganguly, S. K., Srivastava, M., & Khatri, O. P. (2022). Fruit waste-derived cellulose and graphene-based aerogels: Plausible adsorption pathways for fast and efficient removal of organic dyes. *Journal of Colloid and Interface Science*, 608(Pt 3), 2870-2883.
- Juela, D., Vera, M., Cruzat, C., Astudillo, A., & Vanegas, E. (2022). A new approach for scaling up fixed-bed adsorption columns for aqueous systems: A case of antibiotic removal on natural adsorbent. *Process Safety and Environmental Protection*, 159, 953-963.
- Jumasiah, A., Chuah, T. G., Gimbon, J., Choong, T. S. Y., & Azni, I. (2005). Adsorption of basic dye onto palm kernel shell activated carbon: sorption equilibrium and kinetics studies. *Desalination*, 186(1-3), 57-64.
- Kalam, S., Abu-Khamsin, S. A., Kamal, M. S., & Patil, S. (2021). Surfactant Adsorption Isotherms: A Review. *ACS Omega*, 6(48), 32342-32348.
- Kalenskii, A., Ivanov, A., Sevostyanov, D. B., Zvekov, A., & Krechetov, A. (2023). The Adsorption Performance of Porous Activated Carbons Prepared from Iron (II) Precursors Precipitated on the Porous Carbon Matrix Thermolysis. *Magnetochemistry*, 9, 151.
- Kanwal, S., Devi, P., Ahmed, Z., & Qambrani, N. A. (2024). Adsorption isotherm, kinetic and thermodynamic studies for adsorption of fluoride on waste marble powder. *Desalination and Water Treatment*, 319.
- Kapoor, R. T., Rafatullah, M., Siddiqui, M. R., & Alam, M. (2024). Adsorptive potential of coconut fruit shell biochar as low-cost adsorbent for sequestration of rhodamine B dye: kinetics, thermodynamics and phytotoxicity studies. *Biomass Conversion and Biorefinery*.
- Kapoor, R. T., & Sivamani, S. (2023). Adsorptive Potential of Orange Peel Biochar for Removal of Basic Red 46 Dye and Phytotoxicity Analysis. *Chemical Engineering & Technology*, 46(4), 756-765.
- Karim, A. B., Mounir, B., Hachkar, M., Bakasse, M., & Yaacoubi, A. (2017). Adsorption/desorption behavior of cationic dyes on Moroccan clay: equilibrium and mechanism. *Journal of Materials and Environmental Sciences*, 8(3), 1082-1096.
- Karim, M. A., Ahmed, S., Hossain, D., Hossain, Hossain, A., Rahman, S., Dipti, S. S., Abul, K., Azad, & Rahman, M. H. (2024). Adsorption Isotherms and Kinetics Studies on Adsorption of Malachite Green onto Activated Charcoal from Aqueous Solution. *Journal of Science and Engineering Papers*, 01, 18-25.
- Kassimi, A. E., Achour, Y., Himri, M. E., Laamari, M. R., Haddad, M. E. (2021). High Efficiency of Natural Safiot Clay to Remove Industrial Dyes from Aqueous Media: Kinetic, Isotherm Adsorption and Thermodynamic Studies. *Biointerface Research in Applied Chemistry*, 11(5), 12717-12731.
- Kaur, S., Rani, S., & Mahajan, R. K. (2013). Adsorption Kinetics for the Removal of Hazardous Dye Congo Red by Biowaste Materials as Adsorbents. *Journal of Chemistry*, 2013, 628582.

- Kausar, A., Rehman, S. U., Khalid, F., Bonilla-Petriciolet, A., Mendoza-Castillo, D. I., Bhatti, H. N., Ibrahim, S. M., & Iqbal, M. (2022). Cellulose, clay and sodium alginate composites for the removal of methylene blue dye: Experimental and DFT studies. *International Journal of Biological Macromolecules*, 209(Pt A), 576-585.
- Khalil, A., Mangwandi, C., Salem, M. A., Ragab, S., & El Nemr, A. (2024). Orange peel magnetic activated carbon for removal of acid orange 7 dye from water. *Scientific Reports*, 14(1), 119.
- Khalse, N. M., & De, M. (2024). Adsorptive desulfurization of thiophenic sulfur compounds using nitrogen modified graphene. *Separation and Purification Technology*, 331.
- Khamwichit, A., Dechapanya, W., & Dechapanya, W. (2022). Adsorption kinetics and isotherms of binary metal ion aqueous solution using untreated venus shell. *Heliyon*, 8(6), e09610.
- Khan, A. A., Chaudhari, O., & Chandra, R. (2024). A review of ensemble learning and data augmentation models for class imbalanced problems: Combination, implementation and evaluation. *Expert Systems with Applications*, 244.
- Khan, S., & Malik, A. (2014). Environmental and Health Effects of Textile Industry Wastewater. In A. Malik, E. Grohmann, & R. Akhtar (Eds.), *Environmental Deterioration and Human Health: Natural and anthropogenic determinants* (pp. 55-71). Springer Netherlands.
- Kim, S.-H., Kim, D.-S., Moradi, H., Chang, Y.-Y., & Yang, J.-K. (2023). Highly porous biobased graphene-like carbon adsorbent for dye removal: Preparation, adsorption mechanisms and optimization. *Journal of Environmental Chemical Engineering*, 11(2), 109278.
- Kim, S. C., Hong, I. K., Choi, I.-S., & Kim, C.-H. (1996). Coal Based Activated Carbon Manufacturing Process. *Journal of Industrial and Engineering Chemistry*, 2(2), 116-121.
- Kittappa, S., Jais, F. M., Ramalingam, M., Mohd, N. S., & Ibrahim, S. (2020). Functionalized magnetic mesoporous palm shell activated carbon for enhanced removal of azo dyes. *Journal of Environmental Chemical Engineering*, 8(5), 104081.
- Kobayashi, Y., & Yoshida, K. (2021). Quantitative structure-property relationships for the calculation of the soil adsorption coefficient using machine learning algorithms with calculated chemical properties from open-source software. *Environmental Research*, 196, 110363.
- Köseoğlu, E., & Akmil-Başar, C. (2015). Preparation, structural evaluation and adsorptive properties of activated carbon from agricultural waste biomass. *Advanced Powder Technology*, 26(3), 811-818.

- Kousha, M., Daneshvar, E., Sohrabi, M. S., Jokar, M., & Bhatnagar, A. (2012). Adsorption of acid orange II dye by raw and chemically modified brown macroalga Stoechospermum marginatum. *Chemical Engineering Journal*, 192, 67-76.
- Krishanamoorthi, S., Sivakumar, V., Saravanan, K., & Sriram Prabhu, T. V. (2009). Treatment and Reuse of Tannery Waste Water by Embedded System. *Modern Applied Science*, 3.
- Kumar, P. S., Ramalingam, S., Senthamarai, C., Niranjanaa, M., Vijayalakshmi, P., & Sivanesan, S. (2010). Adsorption of dye from aqueous solution by cashew nut shell: Studies on equilibrium isotherm, kinetics and thermodynamics of interactions. *Desalination*, 261(1-2), 52-60.
- Kumari, H., Sonia, Suman, Ranga, R., Chahal, S., Devi, S., Sharma, S., Kumar, S., Kumar, P., Kumar, S., Kumar, A., & Parmar, R. (2023). A Review on Photocatalysis Used For Wastewater Treatment: Dye Degradation. *Water, Air, & Soil Pollution, 234*(6), 349.
- Kumari, M., Chaudhary, G. R., Chaudhary, S., & Umar, A. (2022). Transformation of solid plastic waste to activated carbon fibres for wastewater treatment. *Chemosphere*, 294, 133692.
- Kumbhar, P., Narale, D., Bhosale, R., Jambhale, C., Kim, J.-H., & Kolekar, S. (2022). Synthesis of tea waste/Fe₃O₄ magnetic composite (TWMC) for efficient adsorption of crystal violet dye: Isotherm, kinetic and thermodynamic studies. *Journal of Environmental Chemical Engineering*, 10(3), 107893.
- Kundu, A., Redzwan, G., Sahu, J. N., Mukherjee, S., Sen Gupta, B., & Hashim, M. A. (2014). Hexavalent Chromium Adsorption by a Novel Activated Carbon Prepared by Microwave Activation. *bioresources*, *9*(1), 1498-1518.
- Kyzas, G. Z., Deliyanni, E. A., & Lazaridis, N. K. (2014). Magnetic modification of microporous carbon for dye adsorption. *Journal of Colloid and Interface Science*, 430, 166-173.
- Kyzas, G. Z., & Kostoglou, M. (2014). Green Adsorbents for Wastewaters: A Critical Review. *Materials*, 7(1), 333-364.
- Lafi, R., Montasser, I., & Hafiane, A. (2019). Adsorption of congo red dye from aqueous solutions by prepared activated carbon with oxygen-containing functional groups and its regeneration. *Adsorption Science & Technology*, 37(1-2), 160-181.
- Lai, K. C., Hiew, B. Y. Z., Lee, L. Y., Gan, S., Thangalazhy-Gopakumar, S., Chiu, W. S., & Khiew, P. S. (2019). Ice-templated graphene oxide/chitosan aerogel as an effective adsorbent for sequestration of metanil yellow dye. *Bioresource Technology*, 274, 134-144.
- Langmuir, I. (1918). The adsorption of Gases on Plane Surfaces of Glass, Mica and Platinum. *Journal of the American Chemical Society*, 40(9), 1361-1403.

- Laurent, S., Forge, D., Port, M., Roch, A., Robic, C., Vander Elst, L., & Muller, R. N. (2008). Magnetic Iron Oxide Nanoparticles: Synthesis, Stabilization, Vectorization, Physicochemical Characterizations, and Biological Applications. *Chemical Reviews*, 108(6), 2064-2110.
- Lawal, I. A., Lawal, M. M., Akpotu, S. O., Azeez, M. A., Ndungu, P., & Moodley, B. (2018). Theoretical and experimental adsorption studies of sulfamethoxazole and ketoprofen on synthesized ionic liquids modified CNTs. *Ecotoxicology and Environmental Safety*, 161, 542-552.
- Lellis, B., Fávaro-Polonio, C. Z., Pamphile, J. A., & Polonio, J. C. (2019). Effects of textile dyes on health and the environment and bioremediation potential of living organisms. *Biotechnology Research and Innovation*, 3(2), 275-290.
- Li, A., Ge, W., Liu, L., & Qiu, G. (2022). Preparation, adsorption performance and mechanism of MgO-loaded biochar in wastewater treatment: A review. *Environmental Research*, 212(Pt B), 113341.
- Lima, G. L., Oliveira, R. W. L., de Jesus Neto, R. M., Gomes, A. M. d. S., Fiuza Junior, R. A., Andrade, H. M. C., & Mascarenhas, A. J. S. (2020). Single Step Synthesis of Magnetic Materials Derived from Biomass Residues. *Waste and Biomass Valorization*, *12*(2), 1039-1050.
- Liu, B., Zheng, H., Wang, Y., Chen, X., Zhao, C., An, Y., & Tang, X. (2018). A novel carboxyl-rich chitosan-based polymer and its application for clay flocculation and cationic dye removal. *Science of The Total Environment*, 640-641, 107-115.
- Liu, S., Ge, H., Cheng, S., & Zou, Y. (2020). Green synthesis of magnetic 3D bioadsorbent by corn straw core and chitosan for methylene blue removal. *Environmental Technology*, 41(16), 2109-2121.
- Liu, S., Ge, H., Wang, C., Zou, Y., & Liu, J. (2018). Agricultural waste/graphene oxide 3D bio-adsorbent for highly efficient removal of methylene blue from water pollution. *Science of The Total Environment*, 628-629, 959-968.
- Liu, S., Li, M., Liu, Y., Liu, N., Tan, X., Jiang, L., Wen, J., Hu, X., & Yin, Z. (2019). Removal of 17β-estradiol from aqueous solution by graphene oxide supported activated magnetic biochar: Adsorption behavior and mechanism. *Journal of the Taiwan Institute of Chemical Engineers*, 102, 330-339.
- Liu, W., Huang, J., Weatherley, A. J., Zhai, W., Liu, F., Ma, Z., Jiao, Y., Zhang, C., & Han, B. (2022). Identifying adsorption sites for Cd(II) and organic dyes on modified straw materials. *Journal of Environmental Management*, 301, 113862.
- Liu, Y., Li, J., Wu, L., Shi, Y., He, Q., Chen, J., & Wan, D. (2020). Magnetic spent bleaching earth carbon (Mag-SBE@C) for efficient adsorption of tetracycline hydrochloride: Response surface methodology for optimization and mechanism of action. *Science of the Total Environment*, 722, 137817.
- Liu, Y., Men, B., Hu, A., You, Q., Liao, G., & Wang, D. (2020). Facile synthesis of graphene-based hyper-cross-linked porous carbon composite with superior adsorption capability for chlorophenols. *Journal of Environmental Sciences*, 90, 395-407.

- Ma, C. M., Hong, G. B., & Wang, Y. K. (2020). Performance Evaluation and Optimization of Dyes Removal using Rice Bran-Based Magnetic Composite Adsorbent. *Materials*, 13, 2764.
- Mahamadi, C., Mawere, E., & Bloor, M. (2019). Continuous flow biosorptive removal of methylene blue and crystal violet dyes using alginate-water hyacinth beads. *Cogent Environmental Science*, 5(1).
- Mahapatra, S. S., & Vishwanathan, A. S. (2023). Single-wavelength colorimetric tests for low-cost estimation of bacterial activity, chemical oxygen demand, and turbidity in domestic wastewater. *Water Quality Research Journal*.
- Maier, H. R., Galelli, S., Razavi, S., Castelletti, A., Rizzoli, A., Athanasiadis, I. N., Sànchez-Marrè, M., Acutis, M., Wu, W., & Humphrey, G. B. (2023). Exploding the myths: An introduction to artificial neural networks for prediction and forecasting. *Environmental Modelling & Software*, 167.
- Malek, N. H. A., Yaacob, W. F. W., Wah, Y. B., Md Nasir, S. A., Shaadan, N., & Indratno, S. W. (2022). Comparison of ensemble hybrid sampling with bagging and boosting machine learning approach for imbalanced data. *Indonesian Journal of Electrical Engineering and Computer Science*, 29(1).
- Malenga, E. N., Mulaba-Bafubiandi, A. F., & Nheta, W. (2022). Application of the response surface method (RSM) based on central composite design (CCD) and design space (DS) to optimize the flotation and the desliming conditions in the recovery of PGMs from mine sludge. *Separation Science and Technology*, 57(18), 2960-2983.
- Marković, S., Stanković, A., Lopičić, Z., Lazarević, S., Stojanović, M., & Uskoković, D. (2015). Application of raw peach shell particles for removal of methylene blue. Journal of Environmental Chemical Engineering, 3(2), 716-724.
- Márquez, P., Gutiérrez, M. C., Toledo, M., Alhama, J., Michán, C., & Martín, M. A. (2022). Activated sludge process versus rotating biological contactors in WWTPs: Evaluating the influence of operation and sludge bacterial content on their odor impact. *Process Safety and Environmental Protection*, 160, 775-785.
- Martínez-López, S., Lucas-Abellán, C., Serrano-Martínez, A., Mercader-Ros, M. T., Cuartero, N., Navarro, P., Pérez, S., Gabaldón, J. A., & Gómez-López, V. M. (2019). Pulsed light for a cleaner dyeing industry: Azo dye degradation by an advanced oxidation process driven by pulsed light. *Journal of Cleaner Production*, 217, 757-766.
- Mas, J. F., & Flores, J. J. (2008). The application of artificial neural networks to the analysis of remotely sensed data. *International Journal of Remote Sensing*, 29(3), 617-663.
- Massima Mouele, E. S., Tijani, J. O., Badmus, K. O., Pereao, O., Babajide, O., Zhang, C., Shao, T., Sosnin, E., Tarasenko, V., Fatoba, O. O., Laatikainen, K., & Petrik, L. F. (2021). Removal of Pharmaceutical Residues from Water and Wastewater Using Dielectric Barrier Discharge Methods-A Review. *International Journal of Environmental Research and Public Health*, 18(4).

- Mazaheri, H., Ghaedi, M., Ahmadi Azqhandi, M. H., & Asfaram, A. (2017). Application of machine/statistical learning, artificial intelligence and statistical experimental design for the modeling and optimization of methylene blue and Cd(II) removal from a binary aqueous solution by natural walnut carbon. *Physical Chemistry Chemical Physics*, 19(18), 11299-11317.
- Mike Agbesi, A., & Ebenezer David Okwaning, A. (2017). Low-Cost Technologies for Mining Wastewater Treatment. *Journal of Environmental Science and Engineering B*, 6(8).
- Miyah, Y., Ssouni, S., Benjelloun, M., Mejbar, F., El-Habacha, M., Iaich, S., Arjdal, E. H., Lahrichi, A., & Zerrouq, F. (2023). DFT theoretical analysis and experimental approach combination to understand the toxic dye's adsorption mechanism on the corncob-activated carbon surface. *Journal of Molecular Structure*, 1288.
- Moghazy, R. M., Bakr, A. M., El-Wakeel, S. T., & El Hotaby, W. (2023). Porous cellulose microspheres loaded with dry Nile water algae for removal of MB dye and copper ions from aqueous media. *Polymer Engineering and Science*, 63(7), 2002-2014.
- Mohammed, R. R., & Chong, M. F. (2014). Treatment and decolorization of biologically treated Palm Oil Mill Effluent (POME) using banana peel as novel biosorbent. *Journal of Environmental Management*, 132, 237-249.
- Mojoudi, F., Hamidian, A. H., Zhang, Y., & Yang, M. (2019). Synthesis and evaluation of activated carbon/nanoclay/thiolated graphene oxide nanocomposite for lead(II) removal from aqueous solution. *Water Science & Technology*, 79(3), 466-479.
- Mosoarca, G., Vancea, C., Popa, S., Gheju, M., & Boran, S. (2020). *Syringa vulgaris* leaves powder a novel low-cost adsorbent for methylene blue removal: isotherms, kinetics, thermodynamic and optimization by Taguchi method. *Scientific Reports*, 10(1), 17676.
- Munagapati, V. S., Yarramuthi, V., Kim, Y., Lee, K. M., & Kim, D. S. (2018). Removal of anionic dyes (Reactive Black 5 and Congo Red) from aqueous solutions using Banana Peel Powder as an adsorbent. *Ecotoxicology and Environmental Safety*, 148, 601-607.
- Nasiri, R., & Arsalani, N. (2018). Synthesis and application of 3D graphene nanocomposite for the removal of cationic dyes from aqueous solutions: Response surface methodology design. *Journal of Cleaner Production*, 190, 63-71.
- Naskar, A., & Majumder, R. (2017). Understanding the adsorption behaviour of acid yellow 99 on *Aspergillus niger* biomass. *Journal of Molecular Liquids*, 242, 892-899.
- Naveed, S., Bhatti, I., & Ali, K. (2006). Membrane technology and its suitability for treatment of textile waste water in Pakistan. *Journal of Research (Science)*, 17(3), 155-164.

- Ndagijimana, P., Liu, X., Xu, Q., Lai, D., Wang, G., Pan, B., & Wang, Y. (2021). Cassava flour extracts solution to induce gelatin cross-linked activated carbon-graphene oxide composites: The adsorption performance of dyes from aqueous media. *Environmental Advances*, 5, 100079.
- Nethaji, S., Sivasamy, A., & Mandal, A. B. (2013). Preparation and characterization of corn cob activated carbon coated with nano-sized magnetite particles for the removal of Cr(VI). *Bioresource Technology*, 134, 94-100.
- Nguyen, T. T. V., Phan, A. N., Nguyen, T. A., Nguyen, T. K., Nguyen, S. T., Pugazhendhi, A., & Phuong, H. H. K. (2022). Valorization of agriculture waste biomass as biochar: As first-rate biosorbent for remediation of contaminated soil. *Chemosphere*, 307(3), 135834.
- Olusegun, S. J., Souza, T. G. F., Souza, G. d. O., Osial, M., Mohallem, N. D. S., Ciminelli, V. S. T., & Krysinski, P. (2023). Iron-based materials for the adsorption and photocatalytic degradation of pharmaceutical drugs: A comprehensive review of the mechanism pathway. *Journal of Water Process Engineering*, 51.
- Omwoyo, F. O., & Otieno, G. (2024). Optimization of Methylene Blue Dye Adsorption onto Coconut Husk Cellulose Using Response Surface Methodology: Adsorption Kinetics, Isotherms and Reusability Studies. *Journal of Materials Science and Chemical Engineering*, 12(02), 1-18.
- Onet, C. (2010). Characteristic of the untreated waste water produced by Food industry.
- Opoku, B. K., Isaac, A., Micheal, A. A., Bentum, J. K., & Muyoma, W. P. (2021). Characterization of Chemically Activated Carbons Produced from Coconut and Palm Kernel Shells Using SEM and FTIR Analyses. *American Journal of Applied Chemistry*, 9(3).
- Orooji, Y., Liang, F., Razmjou, A., Liu, G., & Jin, W. (2018). Preparation of anti-adhesion and bacterial destructive polymeric ultrafiltration membranes using modified mesoporous carbon. *Separation and Purification Technology*, 205(May), 273-283.
- Ouettar, L., Guechi, E. K., Hamdaoui, O., Fertikh, N., Saoudi, F., & Alghyamah, A. (2023). Biosorption of Triphenyl Methane Dyes (Malachite Green and Crystal Violet) from Aqueous Media by Alfa (*Stipa tenacissima* L.) Leaf Powder. *Molecules*, 28(8), 3313.
- Pandey, B., Singh, P., & Kumar, R. (2025). Ultrasonic-Assisted Adsorptive Uptake of Malachite Green Dye Onto Zn/Cu-Layered Double Oxide: Spectrophotometric and Smartphone-Based Detection. *Applied Organometallic Chemistry*, 39(2), e7981.
- Pang, J., Fu, F., Ding, Z., Lu, J., Li, N., & Tang, B. (2017). Adsorption behaviors of methylene blue from aqueous solution on mesoporous birnessite. *Journal of the Taiwan Institute of Chemical Engineers*, 77, 168-176.
- Pang, Y. L., Cheam, W. C., Chua, K. H., & Lim, S. (2020). Synthesis of iron modified sugarcane bagasse activated carbon for oxidation degradation of malachite green. *IOP Conference Series: Earth and Environmental Science*, 476(1), 012137.

- Pathania, D., Sharma, A., & Siddiqi, Z.-M. (2016). Removal of congo red dye from aqueous system using Phoenix dactylifera seeds. *Journal of Molecular Liquids*, 219, 359-367.
- Pavan, F. A., Camacho, E. S., Lima, E. C., Dotto, G. L., Branco, V. T. A., & Dias, S. L. P. (2014). Formosa papaya seed powder (FPSP): Preparation, characterization and application as an alternative adsorbent for the removal of crystal violet from aqueous phase. *Journal of Environmental Chemical Engineering*, 2(1), 230-238.
- Pawlak-Kruczek, H., Arora, A., Mościcki, K., Krochmalny, K., Sharma, S., & Niedzwiecki, L. (2020). A transition of a domestic boiler from coal to biomass Emissions from combustion of raw and torrefied palm kernel shells (PKS). *Fuel*, 263, 116718.
- Periyasamy, A. P. (2024). Recent Advances in the Remediation of Textile-Dye-Containing Wastewater: Prioritizing Human Health and Sustainable Wastewater Treatment. *Sustainability*, 16(2).
- Pessoa, N. T., Sales, D. C. S., Do Nascimento, G. E., Dos Santos, J. H. L., Silva, M., Napoleao, D. C., Rodriguez-Diaz, J. M., & Duarte, M. (2024). Effective adsorption of cadmium and nickel ions in mono and bicomponent systems using eco-friendly adsorbents prepared from peanut shells. *Environmental Research*, 247, 118220.
- Piccin, J. S., Gomes, C. S., Mella, B., & Gutterres, M. (2016). Color removal from real leather dyeing effluent using tannery waste as an adsorbent. *Journal of Environmental Chemical Engineering*, 4(1), 1061-1067.
- Poddar, K., Sarkar, D., Sahu, J. R., Patil, P. B., Pal, S. K., & Sarkar, A. (2023). Technoeconomic assessment of doxycycline recovery using rice straw biochar: A circular economic execution. *Chemosphere*, 338, 139504.
- Prabakaran, E., Pillay, K., & Brink, H. (2022). Hydrothermal synthesis of magnetic-biochar nanocomposite derived from avocado peel and its performance as an adsorbent for the removal of methylene blue from wastewater. *Materials Today Sustainability*, 18, 100123.
- Rafeeq, H., Afsheen, N., Rafique, S., Arshad, A., Intisar, M., Hussain, A., Bilal, M., & Iqbal, H. M. N. (2023). Genetically engineered microorganisms for environmental remediation. *Chemosphere*, 310, 136751.
- Ramakrishna, S. V., Annapurna, J., Satyavathi, B., Prakasham, R. S., & Venkata Mohan, S. (2001). Biotreatability studies of pharmaceutical wastewater using an anaerobic suspended film contact reactor. *Water Science and Technology*, 43(2), 271-276.
- Rao Vaddi, D., Malla, R., & Geddapu, s. (2024). Magnetic activated carbon: A promising approach for the removal of methylene blue from wastewater. *Desalination and Water Treatment*, 317.
- Reddy, M. C., Sivaramakrishna, L., & Reddy, A. V. (2012). The use of an agricultural waste material, Jujuba seeds for the removal of anionic dye (Congo red) from aqueous medium. *Journal of Hazardous Materials*, 203-204, 118-127.

- Ren, Z., Chen, F., Wang, B., Song, Z., Zhou, Z., & Ren, D. (2019). Magnetic biochar from alkali-activated rice straw for removal of rhodamine B from aqueous solution. *Environmental Engineering Research*, 25(4), 536-544.
- Renita, A. A., Amarnath, D. J., & Duraikannu, S. L. (2021). Synthesis of peanut-shell magnetized biocarbon for acid fuchsin dye removal. *Materials Today: Proceedings*, 43, 3075-3078.
- Ricci, A., Cataldi, A., Zara, S., & Gallorini, M. (2022). Graphene-Oxide-Enriched Biomaterials: A Focus on Osteo and Chondroinductive Properties and Immunomodulation. *Materials*, 15(6), 2229.
- Rodgers, E. M. (2021). Adding climate change to the mix: responses of aquatic ectotherms to the combined effects of eutrophication and warming. *Biology Letters*, 17(10), 20210442.
- Ruscasso, F., Bezus, B., Garmendia, G., Vero, S., Curutchet, G., Cavello, I., & Cavalitto, S. (2021). *Debaryomyces hansenii* F39A as biosorbent for textile dye removal. *Revista Argentina de Microbiología*, 53(3), 257-265.
- Saeed, A., Sharif, M., & Iqbal, M. (2010). Application potential of grapefruit peel as dye sorbent: kinetics, equilibrium and mechanism of crystal violet adsorption. *Journal of Hazardous Materials*, 179(1-3), 564-572.
- Saini, S., Tewari, S., Dwivedi, J., & Sharma, V. (2023). Biofilm-mediated wastewater treatment: a comprehensive review. *Materials Advances*, 4(6), 1415-1443.
- Salami, M., Pourahmad, J., & Zarei, M. H. (2023). Toxicity of para-phenylenediamine (PPD;1, 4 diaminobenzene) on isolated human lymphocytes: The key role of intracellular calcium enhancement in PPD-induced apoptosis. *Toxicology and Industrial Health*, 39(7), 388-397.
- Salema, A. A., Ani, F. N., Mouris, J., & Hutcheon, R. (2017). Microwave dielectric properties of Malaysian palm oil and agricultural industrial biomass and biochar during pyrolysis process. *Fuel Processing Technology*, *166*, 164-173.
- Salman, H. A., Kalakech, A., & Steiti, A. (2024). Random Forest Algorithm Overview. Babylonian Journal of Machine Learning, 2024, 69-79.
- Samaraweera, H., Alam, S. S., Nawalage, S., Parashar, D., Khan, A. H., Chui, I., Perez, F., & Mlsna, T. (2023). Facile synthesis and life cycle assessment of Iron oxide-Douglas fir biochar hybrid for anionic dye removal from water. *Journal of Water Process Engineering*, *56*, 104377.
- Samaraweera, H., Rivera, A., Carter, K., Felder, T., Nawalage, S., Chui, I., Perez, F., Khan, A. H., & Mlsna, T. (2023). Green iron oxide-modified biochar for methylene blue removal from aqueous solutions. *Groundwater for Sustainable Development*, 21, 100945.
- Saravanan, A., Kumar, P. S., & Rangasamy, G. (2022). Removal of Toxic Pollutants from Industrial Effluent: Sustainable Approach and Recent Advances in Metal Organic Framework. *Industrial & Engineering Chemistry Research*, 61(43), 15754-15765.

- Saroyan, H. S., Giannakoudakis, D. A., Sarafidis, C. S., Lazaridis, N. K., & Deliyanni, E. A. (2017). Effective impregnation for the preparation of magnetic mesoporous carbon: application to dye adsorption. *Journal of Chemical Technology & Biotechnology*, 92(8), 1899-1911.
- Saufi, H., Alouani, M. E. L., Aride, J., & Taibi, M. h. (2020). Rhodamine B biosorption from aqueous solution using *Eichhornia crassipes* powders: Isotherm, kinetic and thermodynamic studies. *Chemical Data Collections*, 25, 100330.
- Sayin, F. E., Karatas, O., Ozbay, I., Gengec, E., & Khataee, A. (2022). Treatment of real printing and packaging wastewater by combination of coagulation with Fenton and photo-Fenton processes. *Chemosphere*, 306, 135539.
- Sen, N., Shefa, N. R., Reza, K., Shawon, S., & Rahman, M. W. (2024). Adsorption of crystal violet dye from synthetic wastewater by ball-milled royal palm leaf sheath. *Scientific Reports*, *14*(1), 5349.
- Shaikh, W. A., Kumar, A., Chakraborty, S., Islam, R. U., Bhattacharya, T., & Biswas, J. K. (2022). Biochar-based nanocomposite from waste tea leaf for toxic dye removal: From facile fabrication to functional fitness. *Chemosphere*, 291, 132788.
- Shanmugam, S., Karthik, K., Veerabagu, U., Hari, A., Swaminathan, K., Al-Kheraif, A. A., & Whangchai, K. (2021). Bi-model cationic dye adsorption by native and surface-modified *Trichoderma asperellum* BPL MBT1 biomass: From fermentation waste to value-added biosorbent. *Chemosphere*, 277, 130311.
- Shao, Y., Liu, G. H., Wang, Y., Zhang, Y., Wang, H., Qi, L., Xu, X., Wang, J., He, Y., Li, Q., Fan, H., & Zhang, J. (2020). Sludge characteristics, system performance and microbial kinetics of ultra-short-SRT activated sludge processes. *Environment International*, 143, 105973.
- Sharma, A., Dipesh, Kumar, P., Vas, J. V., Medwal, R., & Srivastava, A. K. (2024). Exchange-coupling enhanced: Tailoring structural and magnetic properties of Dy iron garnet ferrite nanoparticles via La substitution for switching devices. *Journal of Materials Research*, 39(10), 1576-1593.
- Sherlala, A. I. A., Raman, A. A. A., Bello, M. M., & Buthiyappan, A. (2019). Adsorption of arsenic using chitosan magnetic graphene oxide nanocomposite. *Journal of Environmental Management*, 246, 547-556.
- Shokry, H., Elkady, M., & Hamad, H. (2019). Nano activated carbon from industrial mine coal as adsorbents for removal of dye from simulated textile wastewater: operational parameters and mechanism study. *Journal of Materials Research and Technology*, 8(5), 4477-4488.
- Siddiqui, S. I., Allehyani, E. S., Al-Harbi, S. A., Hasan, Z., Abomuti, M. A., Rajor, H. K., & Oh, S. (2023). Investigation of Congo Red Toxicity towards Different Living Organisms: A Review. *Processes*, 11(3).
- Singh, N., Riyajuddin, S., Ghosh, K., Mehta, S., & Dan, A. (2019). Chitosan-Graphene Oxide Hydrogels with Embedded Magnetic Iron Oxide Nanoparticles for Dye Removal. *ACS Applied Nano Materials*, *2*, 7379-7392.

- Singh, S., Parveen, N., & Gupta, H. (2018). Adsorptive decontamination of rhodamine-B from water using banana peel powder: A biosorbent. *Environmental Technology & Innovation*, 12, 189-195.
- Singh, U. S., Panwar, S., Jain, R. K., & Tripathi, Y. C. (2020). Physicochemical Analysis of Effluents from Agro-Based Paper Mill in Uttarakhand State of India. *International Journal of ChemTech Research*, 13(3), 174-180.
- Sirajudheen, P., Karthikeyan, P., Ramkumar, K., Nisheetha, P., & Meenakshi, S. (2021). Magnetic carbon-biomass from the seeds of Moringa oleifera@MnFe₂O₄ composite as an effective and recyclable adsorbent for the removal of organic pollutants from water. *Journal of Molecular Liquids*, 327, 114829.
- Song, Y., Wang, L., Qiang, X., Gu, W., Ma, Z., & Wang, G. (2023). An overview of biological mechanisms and strategies for treating wastewater from printing and dyeing processes. *Journal of Water Process Engineering*, 55.
- Sridhar, A., Ponnuchamy, M., Kapoor, A., & Prabhakar, S. (2022). Valorization of food waste as adsorbents for toxic dye removal from contaminated waters: A review. *Journal of Hazardous Materials*, 424(Pt B), 127432.
- Srinivasan, N., Thangavelu, K., Sekar, A., & Uthandi, S. (2020). Characteristics of Sago Processing Wastewater Effluents released from different Sago Factories in Salem and Namakkal District of Tami Nadu, India. *Madras Agricultural Journal*, 107.
- Stavrinou, A., Aggelopoulos, C. A., & Tsakiroglou, C. D. (2018). Exploring the adsorption mechanisms of cationic and anionic dyes onto agricultural waste peels of banana, cucumber and potato: Adsorption kinetics and equilibrium isotherms as a tool. *Journal of Environmental Chemical Engineering*, 6(6), 6958-6970.
- Su, G., Mohd Zulkifli, N. W., Ong, H. C., Ibrahim, S., Bu, Q., & Zhu, R. (2022). Pyrolysis of oil palm wastes for bioenergy in Malaysia: A review. *Renewable and Sustainable Energy Reviews*, 164.
- Su, H., Ye, Z., & Hmidi, N. (2017). High-performance iron oxide—graphene oxide nanocomposite adsorbents for arsenic removal. *Colloids and Surfaces A: Physicochemical and Engineering Aspects*, 522, 161-172.
- Sukhbaatar, B., Yoo, B., & Lim, J. H. (2021). Metal-free high-adsorption-capacity adsorbent derived from spent coffee grounds for methylene blue. *RSC Advances*, 11(9), 5118-5127.
- Supong, A., Bhomick, P. C., Baruah, M., Pongener, C., Sinha, U. B., & Sinha, D. (2019). Adsorptive removal of Bisphenol A by biomass activated carbon and insights into the adsorption mechanism through density functional theory calculations. *Sustainable Chemistry and Pharmacy*, 13, 100159.
- Swearingen, L. E. D., Bernard N. (1932). The Rate of Adsorption from Solution. *Journal of Physical Chemistry*, 36(2), 534-545.
- Taguchi, A., & Schüth, F. (2005). Ordered mesoporous materials in catalysis. *Microporous and Mesoporous Materials*, 77(1), 1-45.

- Taher, F. A., Kamal, F. H., Badawy, N. A., & Shrshr, A. E. (2018). Hierarchical magnetic/chitosan/graphene oxide 3D nanostructure as highly effective adsorbent. *Materials Research Bulletin*, 97, 361-368.
- Tan, K. B., Abdullah, A. Z., Horri, B. A., & Salamatinia, B. (2016). Adsorption mechanism of microcrystalline cellulose as green adsorbent for the removal of cationic methylene blue dye. *Journal of the Chemical Society of Pakistan*, 38(4), 651-664.
- Tatarchuk, T., Soltys, L., & Macyk, W. (2023). Magnetic adsorbents for removal of pharmaceuticals: A review of adsorption properties. *Journal of Molecular Liquids*, 384.
- Temkin, M., & Pyzhev, V. (1940). Kinetics of Ammonia Synthesis on Promoted Iron Catalysts. *Acta Physicochimica U.R.S.S.*, *12*, 327-356.
- Teshager, F. M., Habtu, N. G., & Mequanint, K. (2022). A systematic study of cellulose-reactive anionic dye removal using a sustainable bioadsorbent. *Chemosphere*, 303, 135024.
- Thakur, A. K., Singh, R., Teja Pullela, R., & Pundir, V. (2022). Green adsorbents for the removal of heavy metals from Wastewater: A review. *Materials Today: Proceedings*, 57, 1468-1472.
- Thangappan, R., Kalaiselvam, S., Elayaperumal, A., & Jayavel, R. (2014). Synthesis of graphene oxide/vanadium pentoxide composite nanofibers by electrospinning for supercapacitor applications. *Solid State Ionics*, 268, 321-325.
- Tran, H. N., You, S.-J., Nguyen, T. V., & Chao, H.-P. (2017). Insight into the adsorption mechanism of cationic dye onto biosorbents derived from agricultural wastes. *Chemical Engineering Communications*, 204(9), 1020-1036.
- Tu, M., Yu, J., Wang, J., Shi, X., Fu, Z., Hu, S., Zhong, M., & Fei, Z. (2023). Coral-like TiO₂/organosilane hybrid particles with rapid adsorption of methyl orange. *Separation and Purification Technology*, 309, 123000.
- Uba, G., Manogaran, M., Manogaran, M., Yakasai, H. M., Yasid, N. A., & Shukor, M. Y. (2022). Response Surface Method for the Optimization of *Pseudomonas* sp. strain DrY135 Growth on Acrylamide as a Nitrogen Source. *Bulletin of Environmental Science and Sustainable Management*, 6(2), 23-34.
- Uddin, M. T., Rahman, M. A., Rukanuzzaman, M., & Islam, M. A. (2017). A potential low cost adsorbent for the removal of cationic dyes from aqueous solutions. *Applied Water Science*, 7(6), 2831-2842.
- Ukwatta, A., & Mohajerani, A. (2017). Characterisation of fired-clay bricks incorporating biosolids and the effect of heating rate on properties of bricks. *Construction and Building Materials*, 142, 11-22.
- Ulfah, M., Raharjo, S., Hastuti, P., & Purnama, D. (2019). The influence of textural and chemical properties of palm kernel shell activated carbon on the adsorption capacity and desorption efficiency of β-carotene in a model system. *International Food Research Journal*, 26, 345-353.

- Vahdati-Khajeh, S., Zirak, M., Tejrag, R. Z., Fathi, A., Lamei, K., & Eftekhari-Sis, B. (2019). Biocompatible magnetic N-rich activated carbon from egg white biomass and sucrose: Preparation, characterization and investigation of dye adsorption capacity from aqueous solution. *Surfaces and Interfaces*, 15, 157-165.
- Van Tran, T., Cam Nguyen, D. T., Le, H. T. N., Nguyen, O. T. K., Nguyen, V. H., Nguyen, T. T., Bach, L. G., & Nguyen, T. D. (2019). A hollow mesoporous carbon from metal-organic framework for robust adsorbability of ibuprofen drug in water. *Royal Society of Chemistry*, 6(5), 190058.
- Velasco, P. M., Ortiz, M. P. M., Giró, M. A. M., Melia, D. M., & Rehbein, J. H. (2015). Development of sustainable fired clay bricks by adding kindling from vine shoot: Study of thermal and mechanical properties. *Applied Clay Science*, 107, 156-164.
- Wafti, N. S. A., Lau, H. L. N., Loh, S. K., Aziz, A. A., Rahman, Z. A., & May, C. Y. (2017). Activated Carbon from Oil Palm Biomass as Potential Adsorbent for Palm Oil Mill Effluent Treatment. *Journal of Oil Palm Research*, 29(2), 278-290.
- Waghmare, C., Ghodmare, S., Ansari, K., Dehghani, M. H., Amir Khan, M., Hasan, M. A., Islam, S., Khan, N. A., & Zahmatkesh, S. (2023). Experimental investigation of H₃PO₄ activated papaya peels for methylene blue dye removal from aqueous solution: Evaluation on optimization, kinetics, isotherm, thermodynamics, and reusability studies. *Journal of Environmental Management*, 345, 118815.
- Walker, M., Harvey, A. J., Sen, A., & Dessent, C. E. (2013). Performance of M06, M06-2X, and M06-HF density functionals for conformationally flexible anionic clusters: M06 functionals perform better than B3LYP for a model system with dispersion and ionic hydrogen-bonding interactions. *The Journal of Physical Chemistry A*, 117(47), 12590-12600.
- Wang, F., Li, L., Iqbal, J., Yang, Z., & Du, Y. (2022). Preparation of magnetic chitosan corn straw biochar and its application in adsorption of amaranth dye in aqueous solution. *International Journal of Biological Macromolecules*, 199, 234-242.
- Wang, J., Adelodun, A. A., Oh, J. M., & Jo, Y. M. (2020). TEPA impregnation of electrospun carbon nanofibers for enhanced low-level CO₂ adsorption. *Nano Convergence*, 7(1), 7.
- Wang, J., & Guo, X. (2020). Adsorption isotherm models: Classification, physical meaning, application and solving method. *Chemosphere*, 258, 127279.
- Wang, P., Cao, M., Wang, C., Ao, Y., Hou, J., & Qian, J. (2014). Kinetics and thermodynamics of adsorption of methylene blue by a magnetic graphene-carbon nanotube composite. *Applied Surface Science*, 290, 116-124.
- Wazzan, N., Soliman, K. A., & Halim, W. S. A. (2019). Theoretical study of gallium nitride nanocage as a carrier for 5-fluorouracil anticancer drug. *Journal of Molecular Modeling*, 25(9), 265.
- Wei, M., Marrakchi, F., Yuan, C., Cheng, X., Jiang, D., Zafar, F. F., Fu, Y., & Wang, S. (2022). Adsorption modeling, thermodynamics, and DFT simulation of tetracycline onto mesoporous and high-surface-area NaOH-activated macroalgae carbon. *Journal of Hazardous Materials*, 425, 127887.

- Wong, S., Ghafar, N. A., Ngadi, N., Razmi, F. A., Inuwa, I. M., Mat, R., & Amin, N. A. S. (2020). Effective removal of anionic textile dyes using adsorbent synthesized from coffee waste. *Scientific Reports*, 10(1), 2928.
- Wong, S., Yac'cob, N. A. N., Ngadi, N., Hassan, O., & Inuwa, I. M. (2018). From pollutant to solution of wastewater pollution: Synthesis of activated carbon from textile sludge for dye adsorption. *Chinese Journal of Chemical Engineering*, 26(4), 870-878.
- Wu, W., Cheng, K., Hu, Y., He, H., Wang, P., & Zhu, C. (2024). Adsorption and desorption mechanism of toluene gas by iron modified activated carbon fiber. *Chemical Physics*, 580.
- Xiang, V. M., & Ghazi, R. M. (2019). Adsorption of methylene blue from aqueous solution using palm kernel shell activated carbon. *AIP Conference Proceedings*, 2068, 020038.
- Xu, P., Zheng, M., Chen, N., Wu, Z., Xu, N., Tang, J., & Teng, Z. (2019). Uniform magnetic chitosan microspheres with radially oriented channels by electrostatic droplets method for efficient removal of Acid Blue. *Journal of the Taiwan Institute of Chemical Engineers*, 104, 210-218.
- Yadav, S., Rajput, P., Balasubramanian, P., Liu, C., Li, F., & Zhang, P. (2025). Machine learning-driven prediction of biochar adsorption capacity for effective removal of Congo red dye. *Carbon Research*, 4(1).
- Yadav, S., Yadav, A., Bagotia, N., Sharma, N., Sharma, A. K., & Kumar, S. (2022). Simultaneous adsorption of three anionic dyes at neutral pH from their individual and multi-component systems on a CTAB modified Pennisetum glaucum based carbon nanotube green composite: Adsorption mechanism and process optimization by Box-Behnken design model. *Journal of Molecular Liquids*, 358.
- Yan, H., Tao, X., Yang, Z., Li, K., Yang, H., Li, A., & Cheng, R. (2014). Effects of the oxidation degree of graphene oxide on the adsorption of methylene blue. *Journal of Hazardous Materials*, 268, 191-198.
- Yang, H., Huang, K., Zhang, K., Weng, Q., Zhang, H., & Wang, F. (2021). Predicting Heavy Metal Adsorption on Soil with Machine Learning and Mapping Global Distribution of Soil Adsorption Capacities. *Environmental Science & Technology*, 55(20), 14316-14328.
- Yang, J., Dong, Z., Jiang, C., Wang, C., & Liu, H. (2019). An overview of bromate formation in chemical oxidation processes: Occurrence, mechanism, influencing factors, risk assessment, and control strategies. *Chemosphere*, 237, 124521.
- Yang, N., Zhu, S., Zhang, D., & Xu, S. (2008). Synthesis and properties of magnetic Fe₃O₄-activated carbon nanocomposite particles for dye removal. *Materials Letters*, 62(4-5), 645-647.
- Yang, Z., Ju, X., Liao, H., Meng, Z., Ning, H., Li, Y., Chen, Z., & Long, J. (2021). Preparation of Activated Carbon Doped with Graphene Oxide Porous Materials and Their High Gas Adsorption Performance. *ACS Omega*, 6(30), 19799-19810.

- Yaqub, A., Zahid, M., Un Nisa, M., Iqbal, T., Hussain Shah, K., Samad Shah, N., & Daraz Khan, U. (2024). Sustainable removal of methylene blue dye from textile effluents by magnetized Tea waste and Peanut shells. *Chemical Engineering Science*, 120498.
- Yi, Y., Wang, X., Ma, J., & Ning, P. (2020). An efficient Egeria najas-derived biochar supported nZVI composite for Cr(VI) removal: Characterization and mechanism investigation based on visual MINTEQ model. *Environmental Research*, 189, 109912.
- You, X., Zhou, R., Zhu, Y., Bu, D., & Cheng, D. (2022). Adsorption of dyes methyl violet and malachite green from aqueous solution on multi-step modified rice husk powder in single and binary systems: Characterization, adsorption behavior and physical interpretations. *Journal of Hazardous Materials*, 430, 128445.
- Yu, L., Keffer, D. J., Hsieh, C.-T., Scroggins, J. R., Chen, H., Dai, S., & Harper, D. P. (2022). Lignin-Derived Magnetic Activated Carbons for Effective Methylene Blue Removal. *Industrial & Engineering Chemistry Research*, 61(32), 11840-11850.
- Zabneva, O. V., Smolin, S. K., Klimenko, N. A., Shvidenko, O. G., Grechanik, S. V., & Sinel'nikova, A. V. (2012). Structural and sorption properties of activated carbon modified with iron oxides. *Journal of Water Chemistry and Technology*, 34(6), 264-270.
- Zandi, M., Russell, N. V., Edyvean, R. G., Hand, R. J., & Ward, P. (2007). Interpretation of standard leaching test BS EN 12457-2: is your sample hazardous or inert? *Journal of Environmental Monitoring*, 9(12), 1426-1429.
- Zeeshan, M., Javed, T., Kumari, C., Thumma, A., Wasim, M., Taj, M. B., Sharma, I., Haider, M. N., & Batool, M. (2025). Investigating the interactions between dyes and porous/composite materials: A comprehensive study. *Sustainable Chemistry for the Environment*, 9.
- Zhang, C., Yuan, R., Chen, H., Zhou, B., Cui, Z., & Zhu, B. (2024). Advancements in Inorganic Membrane Filtration Coupled with Advanced Oxidation Processes for Wastewater Treatment. *Molecules*, 29(17).
- Zhang, H., Wang, X., Liang, H., Tan, T., & Wu, W. (2016). Adsorption behavior of Th(IV) onto illite: Effect of contact time, pH value, ionic strength, humic acid and temperature. *Applied Clay Science*, 127-128, 35-43.
- Zhang, H., Xing, L., Liang, H., Ren, J., Ding, W., Wang, Q., Geng, Z., & Xu, C. (2022). Efficient removal of Remazol Brilliant Blue R from water by a cellulose-based activated carbon. *International Journal of Biological Macromolecules*, 207, 254-262.
- Zhang, M., Zhang, M., Zeng, Q., Lin, D., & Zhang, N. (2023). Association of p-phenylenediamine exposure with alterations of pulmonary function, pruritus and health-related quality of life in hair dye factory workers: a cross-sectional study. *Scientific Reports*, 13(1), 2623.

- Zhang, N., Reguyal, F., & Sarmah, A. K. (2024). Effect of iron nanoparticles on chromium adsorption in aqueous solution using magnetic biochar: A site energy distribution analysis. *Environmental Pollution*, 346, 123593.
- Zhang, W., Lan, Y., Ma, M., Chai, S., Zuo, Q., Kim, K. H., & Gao, Y. (2020). A novel chitosan-vanadium-titanium-magnetite composite as a superior adsorbent for organic dyes in wastewater. *Environment International*, 142, 105798.
- Zhang, W., Qiu, X., Wang, C., Zhong, L., Fu, F., Zhu, J., Zhang, Z., Qin, Y., Yang, D., & Xu, C. C. (2022). Lignin derived carbon materials: current status and future trends. *Carbon Research*, *I*(14), 1-39.
- Zhang, W., Yang, Q., Luo, Q., Shi, L., & Meng, S. (2020). Laccase-Carbon nanotube nanocomposites for enhancing dyes removal. *Journal of Cleaner Production*, 242, 118425-118425.
- Zhang, Y., Guo, W., Liu, D., & Ding, Y. (2023). Tailoring abundant active-oxygen sites of Prussian blue analogues-derived adsorbents for highly efficient Yb(III) capture. *Journal of Hazardous Materials*, 445, 130457.
- Zhang, Y., Hui, C., Wei, R., Jiang, Y., Xu, L., Zhao, Y., Du, L., & Jiang, H. (2022). Study on anionic and cationic dye adsorption behavior and mechanism of biofilm produced by *Bacillus amyloliquefaciens* DT. *Applied Surface Science*, 573, 151627.
- Zhao, B., Xiao, W., Shang, Y., Zhu, H., & Han, R. (2017). Adsorption of light green anionic dye using cationic surfactant-modified peanut husk in batch mode. *Arabian Journal of Chemistry*, 10, S3595-S3602.
- Zhao, F., Tang, L., Jiang, H., Mao, Y., Song, W., & Chen, H. (2023). Prediction of heavy metals adsorption by hydrochars and identification of critical factors using machine learning algorithms. *Bioresource Technology*, 383, 129223.
- Zhao, H., Jia, J., Ying, J., He, M., Sun, Z., Zhang, X., Wang, Z., & Zhou, W. (2024). CO₂ selective adsorption over O₂ on N-doped activated carbon: Experiment and quantum chemistry study. *Applied Surface Science*, 656.
- Zhao, S., & Zhou, T. (2016). Biosorption of methylene blue from wastewater by an extraction residue of *Salvia miltiorrhiza Bge. Bioresource Technology*, 219, 330-337.
- Zheng, Y., Wang, J., Li, D., Liu, C., Lu, Y., Lin, X., & Zheng, Z. (2021). Insight into the KOH/KMnO₄ activation mechanism of oxygen-enriched hierarchical porous biochar derived from biomass waste by *in-situ* pyrolysis for methylene blue enhanced adsorption. *Journal of Analytical and Applied Pyrolysis*, 158, 105269.
- Zheng, Y., Yao, G., Cheng, Q., Yu, S., Liu, M., & Gao, C. (2013). Positively charged thin-film composite hollow fiber nanofiltration membrane for the removal of cationic dyes through submerged filtration. *Desalination*, 328, 42-50.

- Zhou, Q., Wu, Y., Chen, H., Zhu, G., Zhang, Y., Liang, D., Chen, G., & Tang, S. (2022). Preparation of *Quercus mongolica* leaf-derived porous carbon with a large specific surface area for highly effective removal of dye and antibiotic from water. *Arabian Journal of Chemistry*, 15(9), 104031.
- Zhu, X., Liu, Y., Zhou, C., Zhang, S., & Chen, J. (2014). Novel and High-Performance Magnetic Carbon Composite Prepared from Waste Hydrochar for Dye Removal. *ACS Sustainable Chemistry & Engineering*, 2(4), 969-977.

LIST OF PUBLICATIONS AND PAPERS PRESENTED

- 1. **Tan, Y. Y.**, Abdul Raman, A. A., Bello, M. M., & Buthiyappan, A. (2020). Magnetic graphene oxide-biomass activated carbon composite for dye removal. *Korean Journal of Chemical Engineering*, *37*(12), 2179-2191. https://doi.org/10.1007/s11814-020-0628-9
- Tan, Y. Y., Bello, M. M., & Abdul Raman, A. A. (2021). Towards cleaner production in palm oil industry: Advanced treatment of biologically-treated POME using palm kernel shell-based adsorbent. *Cleaner Engineering and Technology*, 2, 10079. https://doi.org/10.1016/j.clet.2021.100079
- Tan, Y. Y., Abdul Raman, A. A., Zainal Abidin, M. I. I., & Buthiyappan, A. (2023).
 Sustainable Dye Adsorption Using Novel Activated Carbon Prepared from Passion Fruit (Passiflora edulis) Leaf: Mechanism and Cost Analysis. *Industrial & Engineering Chemistry Research*, 62(36), 14507-14521.
 https://doi.org/10.1021/acs.iecr.3c01303
- Tan, Y. Y., Zainal Abidin, M. I. I., Buthiyappan, A., & Abdul Raman, A. A. (2023).
 Resource recovery from palm kernel shell and its application for wastewater treatment: a circular economy approach. IOP Conference Series: Earth and Environmental Science, 1281(1), 012017. https://doi.org/10.1088/1755-1315/1281/1/012017
- 5. **Tan, Y. Y.**, Abdul Raman, A. A., Zainal Abidin, M. I. I., & Buthiyappan, A. (2024). A review on sustainable management of biomass: physicochemical modification and its application for the removal of recalcitrant pollutants-challenges, opportunities, and future directions. *Environmental Science and Pollution Research*. https://doi.org/10.1007/s11356-024-33375-x
- 6. Tan. Y. Y., Buthiyappan, A., Abdul Raman, A. A., & Zainal Abidin, M. I. I. (2021). Palm Kernel Shell Derived Adsorbent for the Removal of Cationic Dye from Aqueous Solution. Kyoto University International Symposium on Education and Research in Global Environmental Studies in Asia 2021 (November 29-30, 2021).

- 7. **Tan. Y. Y.**, Abdul Raman, A. A., Buthiyappan, A., & Zainal Abidin, M. I. I. (2022). Potential Application of Crop Residue-Based Adsorbent for Dye Removal. *Kyoto University International Symposium on Education and Research in Global Environmental Studies in Asia 2022* (November 24-25, 2022).
- 8. **Tan, Y. Y.**, Abdul Raman, A. A., Zainal Abidin, M. I. I., & Buthiyappan, A. (2024). Hydrothermal conversion of waste human hair as a biomaterial for wastewater treatment. *The 14th International Symposium on Southeast Asian Water Environment (SEAWE-14)*. Wyndham Grand Bangsar Kuala Lumpur, Malaysia (December 3-5, 2024) Best Oral Presentation Award
- Tan, Y. Y., Araya, R., Buthiyappan, A., Zainal Abidin, M. I. I., & Abdul Raman, A. A. (2024). AI-Assisted Dye Adsorption Modeling Using Graphene and Iron Oxides Impregnated Biomass Activated Carbon. AI for Materials: 2024 Peking University "M-Talents" International Doctoral Students Academic Forum. Peking University, China (October 25-27, 2024) Best Poster Award
- 10. Solih, F. A., Buthiyappan, A., Abdul Raman, A. A., & **Tan, Y. Y.** (2023). Carbonaceous material from agricultural waste for treating colored wastewater: characterization and adsorption performance evaluations. *Chemical Papers*, 77(6), 2985-3001. https://doi.org/10.1007/s11696-023-02682-x
- 11. Tee, Y. Y., Tan, Y. Y., Zainal Abidin, M. I. I., Abdul Raman, A. A., & Buthiyappan, A. (2024). Innovative Approach to Dye Adsorption: A Comparative Study of Iron Impregnated Waste Human Hair-Based Activated Carbon. *International Journal of Environmental Science and Technology*. https://doi.org/10.1007/s13762-024-05928-7
- 12. Lim, T. L., Tan, Y. Y., Buthiyappan, A., Abdul Raman, A. A., Zainal Abidin, M. I. I., Ramesh, S., & Ibrahim, S. (2024). Green synthesis of lignocellulosic adsorbents for anionic dye removal from aqueous solution: characterization, optimization and kinetics studies. *Environment, Development and Sustainability*. https://doi.org/10.1007/s10668-024-05771-3